



TECHNISCHE
UNIVERSITÄT
WIEN

DISSERTATION

*TiO₂-based photocatalysis: role of defects during
photocatalytic hydrogen evolution and oxidation of
methanol*

Ausgeführt zum Zwecke der Erlangung des akademischen Grades einer Doktorin
der Naturwissenschaften unter der Leitung von

Prof. Dr. Dominik Eder

E165

Institut für Materialchemie

Eingereicht an der Technischen Universität Wien
Fakultät für Technische Chemie

von

Greta M. Haselmann

01529749

Getreidemarkt 9 / BC02 A20, 1060 Wien

Wien am:

Unterschrift

“Things are not quite so simple always as black and white.”

Doris Lessing

Abstract

Climate change caused by anthropogenic greenhouse gas emissions is currently one of the most pressing global issues. One promising mitigation strategy is the replacement of fossil fuels with renewable energy sources, e.g. solar fuels like H_2 obtained from photocatalytic water splitting.

In the first part of my work, I investigate the deactivation of TiO_2 loaded with Pt during photocatalytic H_2 evolution reaction (HER) from aqueous methanol solutions under UV irradiation. I attribute this deactivation to a shift in the reaction mechanism that favors the formation of a methyl formate intermediate and which is accompanied by an increased CO generation. Photocatalytic experiments and thorough ex situ characterization suggest that oxygen vacancies that are inherent to the metal oxide or photoinduced during the reaction stabilize this mechanism shift, possibly through electron back-donation by surface Ti^{3+} or higher selectivity for detrimental side reactions. I suggest that the ratio of Pt particles to oxygen vacancies is a critical factor for the stability of the H_2 generation rate. Furthermore, transmission electron microscopy (TEM) and X-ray photoelectron spectroscopy (XPS) suggest possible strong metal-support interaction (SMSI)-like encapsulation of Pt by suboxides invoked by an increasing degree of reduction during HER. This work shows that the complexity and dynamics of heterogeneous photocatalytic reactions are still not fully understood. Understanding individual steps of the HER at the example of the reference system of Pt-loaded TiO_2 will help in designing better photocatalysts. A novel liquid phase ATR-FTIR cell has been developed that allows for systematic studies at controlled parameters in order to identify possible different reaction pathways.

In the second part of this work, I am performing a broad comparative study of different synthesis routes for the novel photocatalyst black TiO_2 . Generally, the synthesis of black TiO_2 seems to need more specific conditions than often stated in literature rendering comparison across literature tedious to impossible. However, concluding from this work, surface amorphization independent of valence band modifications is the crucial parameter for the synthesis of highly active photocatalysts: H_2 -treated, largely amorphous TiO_2 followed by a rapid cooling step outperforms P25-type TiO_2 during photocatalytic H_2 production under visible light by a factor of 2. Identification of key features in this work for the outstanding photocatalytic performance of black TiO_2 can be applied to future material designs for improved photocatalytic performances.

Abstrakt (German)

Eine der wohl dringlichsten Herausforderungen unserer Zeit ist der Klimawandel. Hauptursache dafür sind anthropogene Treibhausgasemissionen, die durch das Verbrennen von fossilen Brennstoffen entstehen. Das Ersetzen dieser Brennstoffe durch erneuerbare Energiequellen, wie z.B. durch photokatalytisch hergestellten H_2 , ist eine vielversprechende mitigierende Strategie.

Im ersten Teil meiner Arbeit untersuche ich die Deaktivierung von mit Pt beladenem TiO_2 , während der photokatalytischen Produktion von H_2 . Ich schreibe diese Deaktivierung einer Verschiebung im Reaktionsgleichgewicht zu, bei der Methylformat als Intermediat begünstigt wird und die mit einer zunehmenden CO-Entwicklung einhergeht. Photokatalytische Experimente und eine umfassende ex situ Charakterisierung weisen auf einen stabilisierenden Effekt durch Sauerstofffehlstellen für diese Verschiebung hin, der möglicherweise durch Rückbindung der Elektronen von Oberflächen Ti^{3+} Zentren oder durch eine höhere Selektivität für nachteilige Nebenreaktionen entsteht. Das Verhältnis von Pt-Partikeln zu Sauerstofffehlstellen erscheint ein kritischer Faktor für die Stabilität der H_2 -Produktion zu sein. Darüberhinaus weisen Transmissions-elektronenmikroskopie (TEM) und Röntgenphotoelektronenspektroskopie (XPS) auf eine mögliche Enkapsulierung durch Suboxide hin, wie sie vom Phänomen der strong metal-support interactions (SMSI) bekannt ist. Eine neuartige ATR-FTIR-Flüssigzelle für systematische Studien unter kontrollierten Parametern wurde entwickelt, um ein besseres Verständnis der möglichen Reaktionswege während der photokatalytischen Produktion von H_2 zu gewährleisten und Systeme zukünftig effizienter gestalten zu können.

Im zweiten Teil meiner Arbeit, führe ich eine breit angelegte, vergleichende Studie verschiedener Synthesemethoden von schwarzem TiO_2 durch. Generell scheint die Synthese von schwarzem TiO_2 spezifischere Bedingungen zu benötigen als in der Literatur beschrieben sind, was einen Vergleich verschiedener Materialien langwierig bishin zu unmöglich macht. Basierend auf meiner Arbeit ist die Oberflächenamorphisierung unabhängig von Valenzbandmodifikationen der kritische Parameter für die erhöhte Performance des Photokatalysators: Großteils amorphes TiO_2 , das nach einer reduktiven H_2 -Behandlung rasch abgekühlt wird, entwickelt H_2 doppelt so schnell wie P25. Die Identifikation von Schlüsselmerkmalen für die herausragende photokatalytische Performance von schwarzem TiO_2 in dieser Arbeit können auf das Design zukünftiger Materialien angewandt werden.

Table of Contents

Abstract.....	i
Abstrakt (German).....	ii
Table of Contents.....	iii
List of Figures	viii
List of Tables.....	xv
List of abbreviations	xvii
1 Introduction & Background.....	1
1.1. The need for sustainable development.....	1
1.1.1. Climate Change – a global threat.....	1
1.1.2. Solar hydrogen production as alternative to fossil fuels	4
1.1.3. Perspective: H ₂ as future fuel	11
1.2. Materials requirements for a photocatalyst.....	12
1.2.1. Light absorption and charge excitation (Step 1)	12
1.2.2. Charge separation & transfer (Steps 2 & 3)	15
1.2.3. The co-catalyst: Pt.....	15
1.2.4. The photocatalyst: TiO ₂	19
1.3. Defects & Photocatalysis	25
1.3.1. General	25
1.3.2. How to create oxygen vacancies	29
1.3.3. Characterization of oxygen vacancies in metal oxides	30
1.3.4. Influence of oxygen vacancies on the photocatalytic performance ...	31
1.3.5. Black TiO ₂	34
2 Motivation	40
3 Methods & Procedures.....	42
3.1. Photocatalytic experiments.....	42
3.1.1. Reactor system for photocatalytic HER.....	42
3.1.2. Photocatalytic HER experiment.....	45

3.1.3.	Quantum yield calculations	48
3.2.	Reduction of TiO ₂	50
3.2.1.	High pressure reduction	50
3.2.2.	Aluminum reduction	51
3.2.3.	NaBH ₄ reduction.....	52
3.2.4.	H ₂ reduction followed by rapid cooling.....	53
3.3.	Characterization	54
3.3.1.	Electron microscopy	54
3.3.2.	Optical spectroscopy	57
3.3.3.	Adsorption studies.....	68
3.3.4.	X-ray diffraction (XRD)	70
3.3.5.	X-ray photoelectron spectroscopy (XPS).....	72
4	Preliminary studies and characterization	76
4.1.	HER: Blank experiments	76
4.2.	TEM: Electron beam-induced damage of TiO ₂ during TEM imaging	76
4.3.	Raman: Laser-induced phase transformation & defect formation.....	78
4.4.	XPS: Interpretation of typical XPS detail spectra for TiO ₂ at the example of P25	79
4.4.1.	C 1s.....	79
4.4.2.	O 1s	80
4.4.3.	Ti 2p	81
4.4.4.	VB.....	82
5	Deactivation.....	86
5.1.	Deactivation in general	86
5.2.	Role of defects.....	87
5.2.1.	Photocatalytic experiments	88
5.2.2.	Ex situ characterization	94
5.2.3.	Role of defects: discussion & conclusions	107
5.3.	Role of carbon monoxide	108
5.3.1.	Mechanistic perspective	108

5.3.2.	HER experiments with CO detection	112
5.3.3.	In situ ATR-FTIR – first experiments.....	115
5.3.4.	Conclusions	120
5.4.	Reversibility of deactivation.....	120
5.5.	Role of pH and anions	123
5.6.	Incipient wetness impregnation.....	127
5.6.1.	Induced SMSI.....	128
5.7.	Deactivation of pure TiO ₂ polymorphs and a mixture	129
5.7.1.	Stability	131
5.7.2.	Maximum activity values	132
5.7.3.	Conclusions	134
5.8.	Deactivation of Pt-loaded TiO ₂ during photocatalytic HER and methanol oxidation: conclusions & outlook.....	135
6	Black TiO₂.....	137
6.1.	TiO ₂ reduced at high H ₂ pressure	139
6.1.1.	Color.....	139
6.1.2.	DRS	141
6.1.3.	BET	142
6.1.4.	TEM.....	143
6.1.5.	Raman.....	145
6.1.6.	XRD.....	146
6.1.7.	XPS.....	148
6.1.8.	HER	152
6.1.9.	Discussion & Conclusions	154
6.2.	Aluminum-reduced TiO ₂	156
6.2.1.	Theoretical background	156
6.2.2.	Color & DRS	159
6.2.3.	BET	160
6.2.4.	TEM.....	160
6.2.5.	Raman.....	161

6.2.6.	XRD.....	162
6.2.7.	XPS.....	164
6.2.8.	HER.....	169
6.2.9.	Discussion & Conclusions	170
6.3.	NaBH ₄ -reduced P25.....	172
6.3.1.	Color & DRS.....	172
6.3.2.	BET	173
6.3.3.	TEM	173
6.3.4.	Raman	174
6.3.5.	XRD.....	175
6.3.6.	XPS.....	176
6.3.7.	HER.....	180
6.3.8.	Discussion & Conclusions	181
6.4.	H ₂ reduction followed by rapid cooling	183
6.4.1.	Color & DRS.....	183
6.4.2.	BET	184
6.4.3.	TEM	184
6.4.4.	Raman	185
6.4.5.	XRD.....	186
6.4.6.	XPS.....	187
6.4.7.	HER.....	188
6.4.8.	Discussion & Conclusions	190
6.5.	Discussion & Conclusions	192
6.5.1.	Reproducibility and performance of the reported black core-shell TiO ₂	192
6.5.2.	Identifying key characteristics	193
6.5.3.	Conclusion	195
6.6.	Outlook	196
References.....		197
Curriculum Vitae.....		211

List of publications.....	212
Acknowledgments.....	214

List of Figures

Figure 1-1. Scheme for the working principle of Earth's greenhouse effect. Incoming solar radiation gets partially converted into outgoing infrared radiation (red arrows). IR radiation is partially reflected back to Earth by greenhouse gases in the atmosphere, such as CO ₂ , CH ₄ , and NO _x leading to an increased temperature at the surface.	2
Figure 1-2. CO ₂ levels in the atmosphere over the past 10 000 year. Values since 1958 have been measured at Mauna Loa Observatory, Hawaii. CO ₂ levels before 1958 have been determined from ice-core analysis. The data was provided by the Scripps Institute of Oceanography of UC San Diego. ⁶	3
Figure 1-3. Generic potential energy diagram of an uncatalyzed (black) and catalyzed (green) reaction. Using a catalysts results in lower activation energy (E _a), while thermodynamic levels remain constant.	6
Figure 1-4. Schematic illustration of the steps and processes involved in heterogeneous photocatalytic reactions on the surface of a semiconducting nanoparticle.	7
Figure 1-5. Direct Z-scheme for overall water splitting using two semiconductor photocatalysts for the oxygen evolution reaction (OER) and hydrogen evolution reaction (HER), respectively.	9
Figure 1-6. Energetics of photocatalysis and photosynthesis. Reprinted with permission from ref. 34.	11
Figure 1-7. ASTM G173-03 solar reference spectrum adapted from ref. 39. Colored areas correspond to the different light regions: UV light (violet), visible light (green) and infrared light (red).	13
Figure 1-8. Relationship between band structure of semiconductor and redox potentials of water splitting. Reprinted with permission from ref. 41.	14
Figure 1-9. Energy band diagrams of metal and n-type semiconductor contacts. E _{vac} , vacuum energy; E _c , energy of conduction band minimum; E _v , energy of valence band maximum; ϕ_m , metal work function; ϕ_s , semiconductor work function; χ_s , electron affinity of the semiconductor. Reprinted with permission from ref. 72. Copyright 2012 American Chemical Society.	17
Figure 1-10. a) and d) Ball-stick model of unit cells of TiO ₂ rutile and anatase, respectively. b) and e) coordination polyhedra of the titanium atoms of TiO ₂ rutile and anatase, respectively. Adapted with permission from ref. 84. Copyright 2015 American Chemical Society. c) and f) Wulff construction of anatase and rutile,	

respectively. Reprinted figure with permission from ref. 82 and 83. Copyright 2001 and 1994 by the American Physical Society.	20
Figure 1-11. Proposed valence and conduction band alignment mechanisms for the anatase/rutile interface. Red arrows indicate the flow of electrons (holes) in the conduction band (valence band). Based on ref. 96.....	22
Figure 1-12. A series of reduced TiO ₂ with controllable reduction degree. The blue coloration is induced by F ⁺ color centers. Figure taken with permission from ref. 121 - Published by The Royal Society of Chemistry.	28
Figure 1-13. Schematic of the interaction of bulk and surface defects and with charge carriers. Bulk defects serve as recombination centers (cross), whereas surface defects enable an increased likelihood of surface reactions to occur.....	33
Figure 1-14. "(A) Schematic illustration of the structure and electronic DOS of a semiconductor in the form of a disorder-engineered nanocrystal with dopant incorporation. Dopants are depicted as black dots, and disorder is represented in the outer layer of the nanocrystal. The effect of disorder, which creases broadened tails of states extending into the otherwise forbidden band gap, is shown at the right. (B) A photo comparing unmodified white and disorder-engineered black TiO ₂ nanocrystals. (C and D) HRTEM images of TiO ₂ nanocrystals before and after hydrogenation, respectively. In (D), a short-dashed curve is applied to outline a portion of the interface between the crystalline core and the disordered outer layer (marked by white arrows) of black TiO ₂ ." from ref. 129. Reprinted with permission from AAAS.....	35
Figure 3-1. General flow scheme for the photocatalytic setup in our laboratory. Ar serves as carrier gas and is regulated by a mass flow controller (MFC). Two Ar cycles can be chosen A for purging and B for the reaction.....	43
Figure 3-3. Schematic illustration of reactor type 1 and 2.....	44
Figure 3-2. Emission spectra of a) 200 W super-pressure Hg lamp (Superlite SUV DC-P deep UV) provided by Lumatec and b) Solis TM High-Power LED ($\lambda = 365$ nm) provided by Thorlabs.....	45
Figure 3-4. Schematic of two-zone furnace for aluminum reduction of TiO ₂	52
Figure 3-5. Interaction of a high-energy electron beam with matter and corresponding signals that can be detected by scanning and transmission electron microscopy. Signal directions are relative and indicate the strongest intensity or position of detection.	56
Figure 3-6. Schematic energy levels of a diatomic molecule. Reprinted from ref. 195, Copyright 2003, with permission from Elsevier	58

Figure 3-7. Specular versus diffuse reflection. In specular reflection the angle of incidence equals the angle of reflection. In diffuse reflection additional refraction and diffraction processes occur.....	59
Figure 3-8. Experimental arrangement for measuring direct reflectivity spectra (a) and scheme of a typical integrating sphere used for diffuse reflectance measurements (b). Adapted with permission from ref. 197. Copyright 2005 John Wiley and Sons.....	60
Figure 3-9. Schematic setup of a Michaelson interferometer.....	62
Figure 3-10. Working principle of an ATR measurement. The incident IR beam reflects on the internal surface of the ATR element. An evanescent wave penetrates the sample, which absorbs energy and modifies the exiting beam. Modification in form of absorbance spectra can be recorded by a detector.	63
Figure 3-11. Optical setup consisting of a flow cell placed on a Si ATR crystal within a commercial FTIR spectrometer	64
Figure 3-12. Setup of a DRIFTS measurement cell. Reprinted from ref. 203 - Published by The Royal Society of Chemistry.....	66
Figure 3-13. Comparison of different light interaction for infrared absorption and Raman scattering. Based on ref. 197.....	67
Figure 3-14. Geometrical construction for derivation of Bragg's Law: Two parallel beams are diffracted at two different atoms in a crystal lattice. The path difference can be described as $2\delta = 2d \sin\theta$. Constructive interference (Bragg diffraction) occurs when the path difference equals an integer multiple of the wavelength of the incident radiation. ²⁰⁹	70
Figure 3-15. Exemplary diffractogram of P25 with the indexed anatase (A) and rutile (R) crystal facets. ²¹⁰	71
Figure 3-16. Setup of a X-ray photoelectron spectrometer.....	73
Figure 3-17. Correlation between kinetic energy (KE), binding energy (BE) and the work function of the sample and the spectrometer.....	74
Figure 4-1. TEM images of P25 recorded at a) 0 min b) 2 min and c) 5 min at a fixed sample position.....	77
Figure 4-2. TEM images of P25 recorded at a) 0 min b) 2 min and c) 7 min at a fixed sample position and reduced electron beam intensity.....	78
Figure 4-3. Laser-induced phase transformation and damages as observed during Raman measurements of TiO ₂ samples at different laser intensities. A dark spot appears at the measuring position with increasing intensity.	78
Figure 4-4. Laser-induced shift and peak broadening as observed during Raman measurements of TiO ₂ samples at different laser intensities. Samples did not appear damaged in the camera images (right side).	79

Figure 4-5. C 1s detail spectrum of P25.....	80
Figure 4-6. O 1s detail spectrum of P25.	81
Figure 4-7. Ti 2p detail spectrum of P25.....	82
Figure 4-8. Molecular-orbital diagram for anatase. Reprinted with permission from ref. 172. Copyright 2001 American Chemical Society.	83
Figure 4-9. VB spectrum of P25 with a) individual components as suggested by ref. 133 and b) determination of the valence band maximum (VBM).	84
Figure 5-1. Exemplary graphs for a stable (a), a gradual deactivating (b), and a fast deactivating (c) HER experiment of Pt-loaded P25 under UV light irradiation.	86
Figure 5-2. Photocatalytic HER experiment under UV light in aqueous methanol solutions of P25 loaded with 0.4 wt.% Pt. The red trace is for a sample that was pretreated with ultrasound (US, 1 min) prior to the experiment. ²³⁴	88
Figure 5-3. Investigation of different US treatments on HER: a) increasing the duration of the US pretreatment from 1 (black) to 30 min (red), b) performing the US pretreatment in water (red) instead of aqueous methanol solution (black).	90
Figure 5-4. HER experiments at varying UV intensities and fixed Pt loadings. a) 10-fold decrease of UV intensity (orange) of 0.4 wt.% Pt-loaded P25 with and without US pretreatment. b) 3-fold increase of UV intensity (orange) for 0.75 wt.% Pt-loaded P25. ²³⁴	91
Figure 5-5. HER for pristine P25 (black) and P25 oxidized in air at 400 °C for 5 h (green). ²³⁴	92
Figure 5-6. Gas evolution rates during photocatalytic HER for a series of P25 loaded with different amounts of Pt. Black traces represent experiments without US pretreatment. Red traces represent experiments with US pretreatment. Deactivation is observed at low Pt loadings independent of the pretreatment with US (e.g., 0.25 wt %) but not at high Pt loadings (≥ 0.75 wt %). ²³⁴	93
Figure 5-7. Powder XRD patterns of Pt-loaded P25, pristine P25 as well as P25 subjected to US in water and methanol solution for reference. ²³³	96
Figure 5-8. Tauc plots of dry P25 (black), P25 treated with US in methanol (magenta) and water solutions (blue), P25 treated with UV (orange) as well as the dry pre-calcined P25 (green) (all without Pt). As the US and UV-treated samples are recovered from aqueous solutions, pristine P25 and the calcined P25 are also measured after dispersion in aqueous methanol solutions (violet, grey).	97
Figure 5-9. Absorption spectra for P25 and P25 loaded with different amounts of P25 recovered after HER experiments: a) no US pretreatment, b) US pretreatment.	98

Figure 5-10. FTIR spectra of P25 loaded with different amounts of Pt recovered after HER experiments, as well as P25 subjected to US in water and 50 vol.% methanol solution for reference.....	99
Figure 5-11. Raman spectra of P25 and UV and/or US irradiated P25: complete Raman spectra (left) and close-up of E_g mode (right).....	100
Figure 5-12. Raman spectra of P25 and Pt-loaded P25 recovered after HER experiments: (left) complete spectra with typical P25 Raman modes (left) and close-up of E_g mode at 146 cm^{-1} (right). The E_g modes show an increasing peak broadening and shift with an increasing Pt loading. ²³³	100
Figure 5-13. XPS Pt 4f spectra of pristine P25 and Pt-loaded P25 recovered after photocatalytic experiments as well as Pt-loaded P25 poisoned with O_2 . The spectra show weak signals for the low loadings in the range of metallic Pt (Pt 4f _{7/2} , 70.8 eV; Pt 4f _{5/2} , 74.1 eV). A pronounced shoulder in the 1.5 wt % loaded samples at $\sim 72.8\text{ eV}$ indicates a partial oxidation of Pt. ²³³	101
Figure 5-14. TEM images of a stable (a) and deactivated (b) Pt-loaded P25 sample recovered after photocatalytic HER experiment.....	104
Figure 5-15. DRIFTS study for CO adsorption on 0.5 wt.% Pt loaded P25 recovered after a HER experiment. Insert: close-up of the Pt-CO bonding region.	106
Figure 5-16. Gas evolution curves for H_2 , CO_2 (multiplied by 10) and CO (multiplied by 100) of a deactivating (a) and a stable sample (b).....	113
Figure 5-17. H_2 generation rates for different methanol concentrations for Pt-loaded P25 (0.25 wt %).	115
Figure 5-18. SEM images of P25 film spin-coated onto a Si single crystal: a) top view b) profile view.....	116
Figure 5-19. Time-dependent absorbance difference spectra of Pt-loaded P25 films on Si crystals (8 wt.%, as determined by ICP-MS) during 60 min UV irradiation.....	117
Figure 5-20. Time-dependent absorbance difference spectra of Pt-loaded P25 films on Si crystals (4 wt.%, as determined by ICP-MS) during 60 min UV irradiation.....	118
Figure 5-21. Investigations of reversibility of deactivation: a) recycled experiment (teal) b) recycled experiment with additional Pt deposition (green) and one-step photodeposition of corresponding Pt amount (blue). The black trace represents the first experiment.....	121
Figure 5-22. Difference in chloride ions and pH between a deactivating (e.g. 0.4 wt.%, red trace) and a stable Pt loading (e.g. 1.5 wt.%, black trace) at otherwise fixed parameters.....	125

Figure 5-23. H ₂ (solid), CO ₂ (dash), and CO generation (dots) for 0.4 wt.% Pt-loaded P25 with addition of either (a) HCl, (b) NaCl, (c) or HI. Green traces correspond to $\Delta[\text{Cl}^-]/\Delta\text{pH}$. Magenta traces correspond to a 10-fold excess of $\Delta[\text{Cl}^-]/\Delta\text{pH}$.	126
Figure 5-24. TEM images of (a) photodeposited Pt, (b) IW075-TiO ₂ and (c) IW075-TiO ₂ followed by H ₂ treatment.	128
Figure 5-25. Photocatalytic HER experiments for P25 with Pt deposited with different methods: photodeposition (black), incipient wetness impregnation (IW075-TiO ₂ , red) and (c) incipient wetness impregnation followed by H ₂ treatment (blue).	129
Figure 5-26. H ₂ evolution rates for (a) anatase, (b) rutile, (c) a 80:20 mixture of anatase and rutile, and (d) P25 under UV irradiation at loadings ranging between 0.1 wt.% (exception 0.02 wt.% Pt for rutile) and 1.0 wt.% Pt (exception 3.0 wt.% Pt for P25).	130
Figure 6-1. Images of different TiO ₂ samples before (top) and after (bottom) treatment in 40 bar H ₂ atmosphere for 5 days at 200 °C.	139
Figure 6-2. Tauc plots of (a) high-pressure reduced self-made aNC, (b) anatase, (c) rutile and (d) P25 and their pristine precursors.	141
Figure 6-3. TEM images of a) aNC b) H ₂ -treated aNC, c) commercial anatase, d) H ₂ -treated commercial anatase.	143
Figure 6-4. TEM images of a) commercial rutile b) H ₂ -treated rutile, c) P25, d) H ₂ -treated P25.	144
Figure 6-5. Raman spectra of P25, rutile, anatase, aNC before (black) and after (red) H ₂ treatment at 40 bar for 5 days at 200 °C. Right: Close-ups of the E _g modes.	145
Figure 6-6. XRD patterns of P25, rutile, anatase, aNC before (black) and after (red) H ₂ treatment at 40 bar. for 5 days at 200 °C.	147
Figure 6-7. C 1s detail spectra of aNC, anatase, rutile and P25 before (bottom) and after (top) H ₂ treatment at 40 bar for 5 days at 200 °C.	149
Figure 6-8. O 1s detail spectra aNC, anatase, rutile and P25 before (bottom) and after (top) H ₂ treatment at 40 bar for 5 days at 200 °C.	149
Figure 6-9. Ti 2p detail spectra of aNC, anatase, rutile and P25 before (bottom) and after (top) H ₂ treatment at 40 bar for 5 days at 200 °C. H ₂ -treated rutile was measured second time because of some charging effects, a little different intensity due to measurement.	150
Figure 6-10. VB detail spectra of aNC, anatase, rutile and P25 before (bottom) and after (top) H ₂ treatment at 40 bar for 5 days at 200 °C.	151

Figure 6-11. HER experiments under UV light of aNC, anatase, rutile and P25 before (black) and after (red) H ₂ treatment at 40 bar for 5 days at 200 °C.....	153
Figure 6-12. HER experiments under visible light of aNC, anatase, rutile and P25 before (black) and after (red) H ₂ treatment at 40 bar for 5 days at 200 °C.....	154
Figure 6-13. Ellingham diagram for TiO ₂ , Ti ₂ O ₃ and Al ₂ O ₃ based on data shown in ref. 297.	157
Figure 6-14. Quartz glass reaction tube with TiO ₂ and aluminum powder after aluminum reduction process.	159
Figure 6-15. Tauc plots and images of P25 and Al-reduced P25.	160
Figure 6-16. TEM images of pristine P25 (a), grey (b), light blue (c), blue (d) and dark blue P25 reduced for 12 h (e) and 24 h (f).	161
Figure 6-17. Raman spectra of pristine P25 and aluminum- reduced samples. a) typical spectral range from 110 cm ⁻¹ to 1000 cm ⁻¹ with close-up of the E _g mode. b) spectra between 1000 cm ⁻¹ and 3000 cm ⁻¹	162
Figure 6-18. XRD patterns of pristine P25 and aluminum-reduced samples.....	163
Figure 6-19. XPS survey spectra of P25 and aluminum-reduced P25. The red line marks Ti LMM edge and Na 1s signal.	165
Figure 6-20. C 1s detail spectra of P25 and aluminum-reduced P25. Right: close-up of BE region between 290 and 296 eV.	167
Figure 6-21. O 1s detail spectra of P25 and aluminum-reduced P25.....	168
Figure 6-22. Ti 2p detail spectra of P25 and aluminum-reduced P25.....	168
Figure 6-23. VB spectra of P25 and aluminum-reduced P25.....	169
Figure 6-24. HER experiments for P25 and aluminum-reduced P25 under UV (left) and visible light irradiation (right).....	170
Figure 6-25. Tauc plots and images of P25 and NaBH ₄ -reduced P25.	172
Figure 6-26. TEM images of P25 and P25 reduced with NaBH ₄ at 300 °C.....	173
Figure 6-27. TEM images of P25 and P25 reduced with NaBH ₄ at 350 °C.....	174
Figure 6-28. TEM images of P25 and P25 reduced with NaBH ₄ at 400 °C.....	174
Figure 6-29. Raman spectra of P25 and NaBH ₄ -reduced P25. Right: close-up of E _g mode.....	174
Figure 6-30. XRD patterns of P25 and NaBH ₄ -reduced P25. Right: close-up of E _g mode.....	175
Figure 6-31. Na 1s and B 1s detail spectra for P25 and NaBH ₄ -reduced P25.....	177
Figure 6-32. C 1s, O 1s and Ti 2p detail spectra for P25 and NaBH ₄ -reduced P25.	179
Figure 6-33. VB spectra for P25 and NaBH ₄ -reduced P25.	179
Figure 6-34. HER experiments for P25 and NaBH ₄ -reduced P25 under UV (left) and visible light (right) irradiation.	180

Figure 6-35. Tauc plots and images of sol-gel TiO ₂ , He-TiO ₂ and H ₂ -TiO ₂	183
Figure 6-36. TEM images of sol-gel TiO ₂ (a,d), He-TiO ₂ (b,e), and H ₂ -TiO ₂ (c,f). ...	184
Figure 6-37. Raman spectra of sol-gel TiO ₂ , HeTiO ₂ , and H ₂ -TiO ₂	185
Figure 6-38. XRD patterns of sol-gel TiO ₂ , He-TiO ₂ , and H ₂ -TiO ₂	186
Figure 6-39. (a) C 1s and (b) O 1s detail spectra of sol-gel TiO ₂ , He-TiO ₂ , and H ₂ -TiO ₂	187
Figure 6-40. (a) Ti 2p and (b) VB detail spectra of sol-gel TiO ₂ , He-TiO ₂ , and H ₂ -TiO ₂	188
Figure 6-41. HER experiments for sol-gel TiO ₂ , He-TiO ₂ , H ₂ -TiO ₂ , and a commercial rutile reference under both UV and visible light irradiation. Additionally, a P25 reference is plotted for the visible light experiments.....	188

List of Tables

Table 1-1. Work function values for common co-catalysts and TiO ₂ . Values are taken from ref.15 and 73.....	18
Table 1-2. Overview over selected literature reporting on photocatalytic HER experiments of P25 in aqueous methanol solutions using Pt as a co-catalyst at loadings ranging from 0 to 2.1 wt.%. ca. signalizes when values were not explicitly reported in text but in a figure.	24
Table 3-1. Amounts of acid or salt added during each HER experiment for investigations of the influence of pH and anion.....	47
Table 3-2. Calculated photon fluxes, qp , for each emission region of the 200 W super-pressure Hg lamp (Superlite SUV DC-P deep UV). Theoretical power values at each emission region are provided by Lumatec. The average energy of a photon, E , of each emission region is calculated from Planck's relation,.....	50
Table 3-3. Color variation of aluminum-reduced P25 with corresponding Al:P25 ration and duration of reduction treatment.....	52
Table 4-1. BE values, fwhm and area % of the individual components of the C 1s detail spectrum of P25.	80
Table 4-2. BE values, fwhm and area % of the individual components of the O 1s detail spectrum of P25.	81
Table 4-3. BE values, fwhm and area % of the individual components of the Ti 2p detail spectrum of P25.	82
Table 4-4. BE values, fwhm and area % of the individual components of the VB spectrum of P25.....	84
Table 4-5. Reported VBM values in literature for commercial TiO ₂ samples.	85

Table 4-6. Reported VBM values in literature for self-synthesized TiO ₂ samples. .	85
Table 4-7. Reported VBM values in literature for black TiO ₂ samples.	85
Table 5-1. Overview on the photocatalytic activities and corresponding quantum yields (QY) for all materials shown in this work correlated to their pretreatment using ultrasound (US) and (if applicable) the observed deactivation. ²³³	94
Table 5-2. Overview of BET measurements, band gap calculations from DRS, and phase composition from XRD patterns for the different Pt-loaded P25 samples and their references.	98
Table 5-3. Data from the particle size distribution for different Pt loadings on P25.	103
Table 5-4. IR absorbance band positions and assignments for in situ ATR-FTIR measurements of Pt-loaded P25 in aqueous methanol solution. Faint bands are labeled with an asterisk (*).	119
Table 5-5. H ₂ evolution rates for HER experiments of anatase (A), rutile (R), a 80:20 mixture of anatase and rutile (A+R), and P25. Values are rounded to steps of 50 μmol h ⁻¹ . <i>D</i> -quick deactivation, <i>d</i> -slow deactivation, <i>s</i> -stable, <i>s</i> *- stable with slow initial kinetics.	132
Table 6-1. BET surface areas for aNC, anatase, rutile and P25 before and after 40 bar H ₂ atmosphere for 5 days at 200 °C of one specific sample batch.....	142
Table 6-2. Average crystallite sizes aNC, anatase, rutile and P25 before and after 40 bar H ₂ atmosphere for 5 days at 200 °C as calculated from the Scherrer equation. A – anatase, R – rutile.	Error! Bookmark not defined.
Table 6-3. Band gap values as estimated from Tauc plots for the various aluminum-reduced P25 samples with reaction parameters.....	160
Table 6-4. Calculated fractions of anatase and rutile for pristine and aluminum-reduced P25. Based on ref. 241.	164
Table 6-5. Quantifications from survey spectra for P25 and aluminum-reduced P25.....	166
Table 6-6. Elemental composition quantified from XPS survey measurements for P25 and a sample of P25 reduced with NaBH ₄ at 400 °C after three washing steps.	176
Table 6-7. Elemental composition from survey spectra for P25 and NaBH ₄ -reduced P25.	177
Table 6-8. Elemental composition of sol-gel TiO ₂ , He-TiO ₂ , and H ₂ -TiO ₂ quantified from XPS survey spectra.....	187
Table 6-9. Comparison of characterization results between literature references and this work for the synthesis of black TiO ₂	191

List of abbreviations

Abbreviation	Full name
aNC	anatase nanocrystals
approx.	approximately
at. %	atomic percent
ATR	Attenuated total reflectance
BE	binding energy
BET	Brunauer-Emmett-Teller
BF	bright field
ca.	circa
CB	conduction band(s)
CCD	charge-coupled device
CPS	counts per second
DF	dark field
DFT	density functional theory
DRS	diffuse reflectance spectroscopy
e.g.	example given
ED	electron diffraction
EDX	energy-dispersive X-ray spectroscopy
eV	electron volt
FTIR	Fourier-transform infrared spectroscopy
fwhm	full width at half maximum
GC	gas chromatography
GHG	greenhouse gas
HER	hydrogen evolution reaction
(HR)TEM	(high resolution) transmission electron microscopy or microscope
i.a.	inter alia
ICP-MS	inductively coupled plasma mass spectrometry
IEP	isoelectric point
IPCC	International Panel on Climate Change
KE	Kinetic energy
KM	Kubelka-Munk
MO	molecular orbital
PEC	photoelectrochemical
PSD	particle size distribution
QY	quantum yield
SEM	scanning electron microscopy or microscope
SMSI	strong metal-support interaction
STM	scanning tunneling microscope
STS	scanning tunneling spectroscopy
TCD	thermal conductivity detector
TPB	triple phase boundary
TTIP	Titanium tetraisopropoxide
UHV	ultra-high vacuum

US	ultrasound
UV	ultraviolet
VB	valence band(s)
VBM	valence band maximum
vis	visible
WGS	water-gas shift
XPS	X-ray photoelectron spectroscopy
XRD	X-ray diffraction or X-ray diffractogram

1 Introduction & Background

1.1. The need for sustainable development

With the rapid growth of both economy and population that Earth is facing, we quickly approach the limits of our planet. The need for action has in part been acknowledged by politics in form of the United Nations Framework Convention on Climate Change in 1992 and the Kyoto Protocol from 1997. Just in 2015, the United Nations Development Programme brought the Sustainable Development Goals into life (*formally*: “Transforming our World: the 2030 Agenda for Sustainable Development”), which comprises 17 independent goals that include social, economic and environmental aspects for a sustainable, future-oriented society. One could argue about which is the most pressing issue; however, what is safe to say is that without strong, world-wide actions in the environmental and energy sector, we will face an unprecedented global crisis.

1.1.1. Climate Change – a global threat

In his book “Age of Sustainable Development”, Jeffrey D. Sachs comprehensively illustrates the different aspects of a sustainable society including climate change. He identified several aspects that make climate change as threatening as it is:¹

- 1) *Climate change is global and thus needs to be mitigated on a global scale.* This is particularly challenging, as the global power distributions are currently shifting between West and East and there is no clear global leader which could unify nations.
- 2) *Climate change is highly-related to our energy-based economy.* The burning of fossil fuels is the main source of energy as well as greenhouse gas emission that lead to global warming.
- 3) *Climate change has drastic consequences on a global scale with respect to ecosystems.* Ocean acidification, desertification, extreme weather (to name a few) lead to disturbed or malfunctioning ecosystems.
- 4) *Climate change is a slow process to us.* While the climate changes rapidly on the scale of Earth’s history, we are usually not affected by the consequences in our everyday life. Some of the effects will only be felt by next generations. Thus, it is easy to ignore.
- 5) *Climate change is complex.* The factors that influence climate are manifold and the remedies not always straight-forward.

Chapter 1 – Introduction & Background

- 6) *Climate change mitigation strategies do not agree with business goals of powerful lobbies like the oil industry.* The realization of mitigation strategies therefore needs the support of politics and the general public. Solutions need to be cost-competitive for the industry to build economic pressure.

Climate change is based on the greenhouse effect (Figure 1-1). Solar irradiation is absorbed by the Earth, which in turn releases infrared (IR) radiation upon heating. IR radiation is partially reflected back to Earth by greenhouse gases (GHG) in the atmosphere, such as CO_2 , CH_4 , and NO_x , leading to an increased temperature at the surface.. Overall, this results in an atmosphere and climate that is essential for life as we know it. Now, increasing the amount of GHG increases Earth's temperature.² The main GHG is CO_2 making up 77% of the total warming effect by the greenhouse effect, followed by methane and nitrous oxides. Already in 1896 Nobel Prize laureate Svante Arrhenius investigated the effect that CO_2 has on the global temperature and found that a doubling of CO_2 in Earth's atmosphere would result in a roughly 5-6 °C increase of the global temperature (corrected in 1906 to roughly 2 °C). And he investigated this only using absorption studies of lunar IR irradiation, no ice core analysis or other advanced analysis method.^{1, 3-4}

The anthropogenic origin of climate change is out of question: Increasing GHG emissions are the main cause for climate change. The main GHG is CO_2 . The main source of CO_2 emissions is the burning of fossil fuels (85% of total CO_2 emissions in 2010).⁵ In 1958, Charles Keeling set up a monitoring station of atmospheric CO_2 levels at the Mauna Loa Observatory in Hawaii, which is still in operation. Together with ice core analysis prior to 1958, the atmospheric CO_2 levels in Earth's

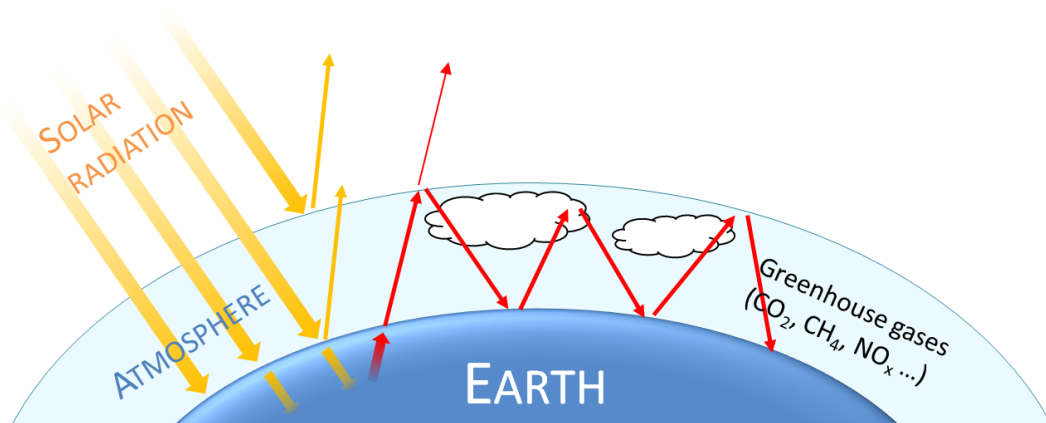


Figure 1-1. Scheme for the working principle of Earth's greenhouse effect. Incoming solar radiation gets partially converted into outgoing infrared radiation (red arrows). IR radiation is partially reflected back to Earth by greenhouse gases in the atmosphere, such as CO_2 , CH_4 , and NO_x leading to an increased temperature at the surface.

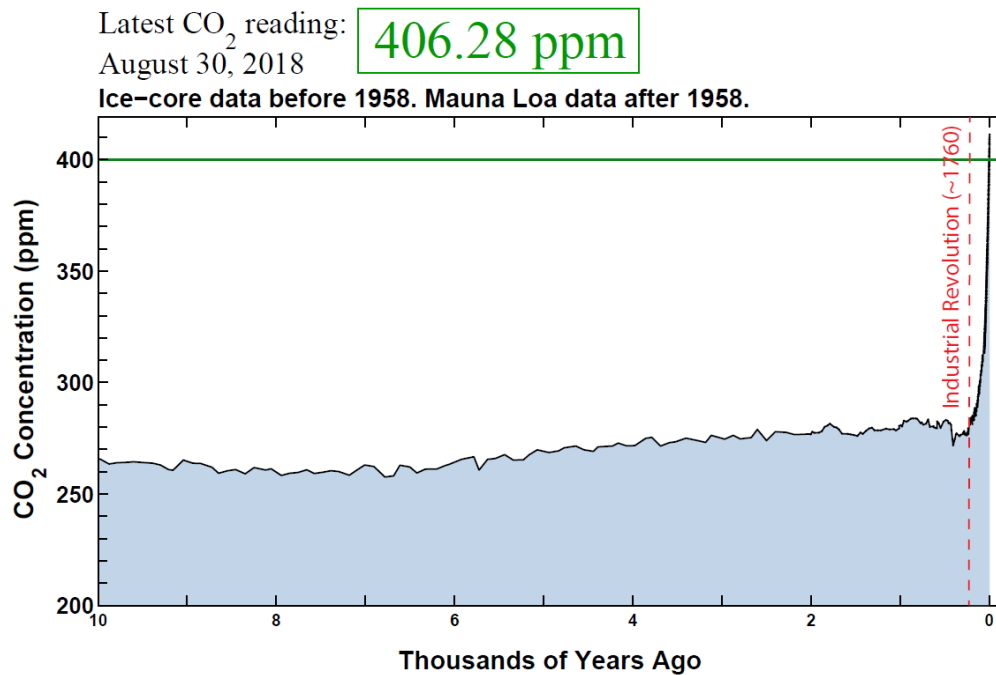


Figure 1-2. CO₂ levels in the atmosphere over the past 10 000 year. Values since 1958 have been measured at Mauna Loa Observatory, Hawaii. CO₂ levels before 1958 have been determined from ice-core analysis. The data was provided by the Scripps Institute of Oceanography of UC San Diego.⁶

atmosphere over the past millennia have been able to be plotted and paint an alarming picture; clearly showing an unprecedented sharp increase, ever since the Industrial Revolution started (Figure 1-2).⁶⁻⁷

We know climate change is real, it is a threat to our civilization and it is caused by humans. However, the need to reduce GHG emission opposes a continuously growing and developing global community. A review published by economist Nicholas Stern (Stern review) showed that the costs of taking action against climate change now outweigh the costs caused by the impacts of climate change. Furthermore, he states that if we do not act against the rising global temperature, a more than 50% chance is given that the temperature rise exceeds 5% which is "equivalent to the temperature increase from the last ice age until today". Climate stabilization would need an emission reduction by 80%, when his report was published in 2006.⁸

Two strategies can and need to be used in order to deal with this challenge: adaptation and mitigation. Adaptation is necessary as we already experience the consequences of climate change and they will continue to intensify within the next decades according to future projections. However, only mitigation strategies will give long-term solutions towards an environmentally sustainable society. Scientists will play a key role in finding strategies for decarbonization. One would be

to increase the efficiency of already available technologies. Another is to replace the main cause of CO₂ emissions: the burning of fossil fuels for energy gain. Ideally, renewable resources, i.e. solar, wind, or water power, should become our primary source of energy and they have experienced tremendous research interest over the past years. Nuclear power is also an alternative for a low-carbon technology; however, the risks connected to misuse make this a less appealing energy source (e.g. Fukushima accident).¹

The advantage of solar energy in comparison to other renewables (wind, water, biomass, geothermal) is the comparatively high power density of solar technologies. Differences in economic and power efficiencies between the different renewable energy sources are difficult to quantify due to the absence of a shared metric. However, power density (in W m⁻²) has arisen as a basis for comparing different renewable energy sources. The power density of solar technologies, e.g., for photovoltaics, outperforms those of other renewables by 1 to 2 orders of magnitude, making it a highly desirable, renewable, primary energy source (e.g. 10 W m⁻² for photovoltaics compared to 2 W m⁻² for wind and 0.2 W m⁻² for hydro power).⁹ Theoretically, there is more energy provided in one hour of sunlight than is consumed world-wide in a year.¹⁰ Another advantage is the abundance of sunlight, although intensity varies globally. The attractiveness of using solar energy to replace fossil fuels led to the development of solar fuels, such as H₂.

1.1.2. Solar hydrogen production as alternative to fossil fuels

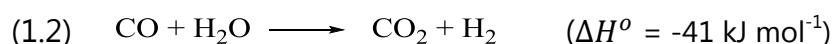
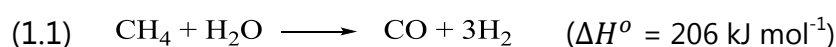
The main source of our energy is simultaneously the main cause of anthropogenic CO₂ emissions: the burning of fossil fuels. Next to the detrimental consequences to Earth, fossil fuels are also an energy source that is limited both in its global abundance leading to political tensions as well as in its total amount as fuels are much faster consumed than replenished by natural processes.

1.1.2.1. Why H₂?

H₂ is a promising candidate to replace fossil fuels: with 120 MJ kg⁻¹ it has the highest specific energy density of all known substances, while the only by-product upon burning with O₂ is water.¹¹⁻¹² H₂ is also the most abundant element on Earth, although not by occurring in its elemental form but rather by being bound in chemical compounds. These features already led to the development of H₂-based engines, e.g. the internal H₂ combustion engine and the H₂ fuel cell, which actually show higher efficiencies than conventional engines. However, these technologies cannot yet compete on an economical level with fossil fuel-based technology. Furthermore, while the actual fuel cell and H₂ combustion

engine might be emission-free, production of H₂ is based on industrial processes that actually rely on the burning of fossil fuels and release CO₂.¹¹⁻¹⁴

H₂ is still mainly produced by steam reforming of hydrocarbons, e.g. methane. Steam reforming is a gas-phase, high pressure (15-40 kbar) and high temperature (650-950 °C) treatment of hydrocarbons with water steam over Ni-based catalysts. For methane, this reaction produces H₂ and CO in a ratio of 3:1 (equation ((1.1))). In a second step at lower temperature, further H₂ is produced by the reaction of water steam with CO which oxidizes to CO₂ (so-called water-gas shift (WGS) reaction) (equation (1.2)).¹⁵⁻¹⁶



Thus, a way to produce H₂ in a sustainable and efficient manner has to be developed in order to render it a valid replacement for fossil fuels. Otherwise, the GHG emission problem would just be shifted to an earlier step in the energy production chain.

There has been a large research interest in different synthetic routes for sustainable H₂ production over the past decades that Dutta summarized 2014 in a review on the production, storage and use of H₂, e.g., steam reforming of glycerol, fermentation of biomass, or electrochemical oxidations by microbes or in alkaline media.¹⁴ However, water has been the most interesting resource for H₂ across literature due to its abundance and ultimate eco-friendliness. The fundamental idea of H₂ production from water is to basically split an H₂O molecule and reduce protons to H₂ and oxidize hydroxyls to O₂ gas.¹⁴ In combination with solar light as primary energy source, solar water splitting has arisen as a new field experiencing tremendous recent research effort studying the mechanisms, key properties of materials and applicability of this new technology: photocatalytic water splitting.

1.1.2.2. *Photocatalytic water splitting*

In 1972, Honda and Fujishima showed the first successful photolysis of water using a photoelectrochemical (PEC) cell consisting of a Pt (H₂ evolution) and TiO₂ (O₂ evolution) electrode.¹⁷ Ever since, tremendous research interest has developed in the field of heterogeneous photocatalysis with the main body of (early) work focused on PEC setups. Later, dispersions of semiconductor nanopowders have gained popularity due to their simplicity of handling and application (i.e.

Chapter 1 – Introduction & Background

powder + water + sun = H_2). Homogenous photocatalysis, using dye complexes and enzymes, may exhibit higher turn-over numbers, selectivities and efficiencies, however, usually applications currently lack the prospects to be applied in industrial technologies as for heterogeneous systems. The simple handling and application of semiconducting powder films or dispersions gives a consequential advantage for large-scale industrial applications as is required for H_2 to become the fundament for future energy generation.¹⁸⁻²⁵ Thus, this work focuses on heterogeneous photocatalysis principles and applications using powder dispersions of semiconducting nanoparticles, which, I will discuss in the following sections.

The same working principle applies for heterogeneous photocatalysis as for heterogeneous catalysis: the activation energy of a reaction is lowered by the presence of a catalyst leading to an increased rate of reaction. This means that the kinetics of a reaction change through an alternative reaction path, while the thermodynamics remain unaltered (Figure 1-3). Importantly, the (photo-)catalyst is not consumed and is recycled during the reaction.²⁶

Heterogeneous photocatalysis thus differs from heterogeneous catalysis mainly in the “mode of activation”: catalysis proceeds through thermal activation, whereas photocatalysts are activated through photons.^{21, 26} Photocatalysis thus operates at much milder conditions, i.e. ambient conditions, than catalysis which often needs high temperatures or high pressure as discussed for the WGS reaction (section 1.1.2.1). Furthermore, photocatalysts open up new reaction pathways and in this way alter reaction selectivities. They also allow completely new reactions of mole-

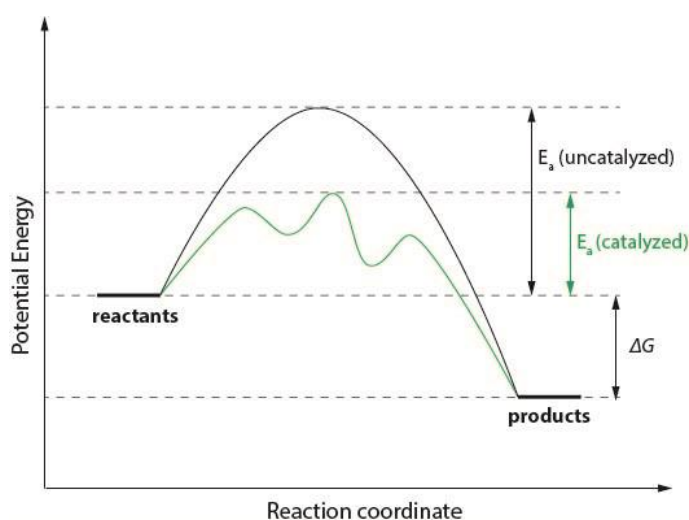


Figure 1-3. Generic potential energy diagram of an uncatalyzed (black) and catalyzed (green) reaction. Using a catalysts results in lower activation energy (E_a), while thermodynamic levels remain constant.

cules that are conventionally considered unreactive, as in the case of H_2O .

In the following, I will discuss the working principles of a photocatalytic reaction on a semiconductor particle at the example of the overall water splitting reaction ((Figure 1-4 and equations (1.3)-(1.6)). Metal oxides represent a common class of semiconductors and following examples in this work will mainly be based on Pt-loaded TiO_2 which has developed as a benchmark photocatalyst ever since 1972.

Before the actual photocatalytic reaction can occur, reactants have to diffuse through the bulk liquid and adsorb onto the surface of the photocatalyst just as in heterogeneous catalysis. Upon excitation by light, an electron-hole pair is formed in the semiconductor, if the energy of the incident photons is larger than the band gap of the semiconductor ($h\nu > E_g$). An electron can get promoted to the conduction band (CB), which leaves behind a hole in the valence band (VB) (Step 1, equation (1.3)). The separated charges can either recombine, thereby remain inactive for the further reaction, or stay separated and migrate to the surface (Step 2), where they partake in either an oxidation or reduction reaction (Step 3). In the case of water oxidation, two molecules of water need to consume four photogenerated holes to create one molecule of O_2 and four protons (equation (1.4)). This half-reaction is also called the oxygen evolution reaction, or OER. On the reduction site of the reaction, the generated protons can be reduced to H_2 by consumption of photogenerated electrons (equation (1.5)). Analogous to the OER, this half-reaction is called the hydrogen evolution reaction, or HER.

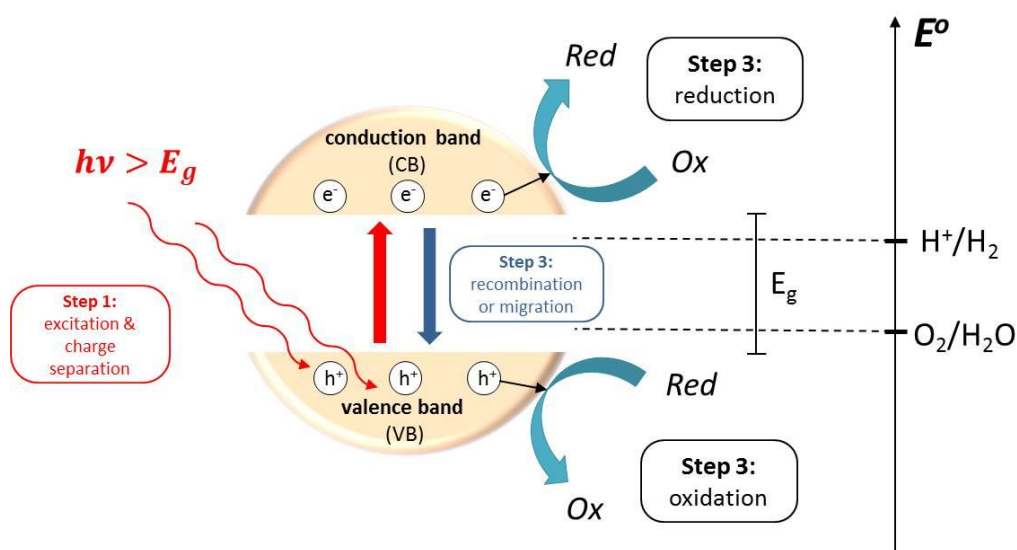
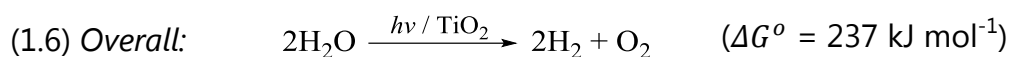
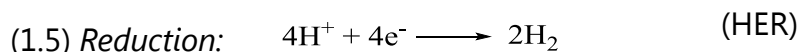
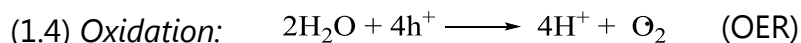


Figure 1-4. Schematic illustration of the steps and processes involved in heterogeneous photocatalytic reactions on the surface of a semiconducting nanoparticle.

Chapter 1 – Introduction & Background

Overall, two molecules of water split into two molecules of H₂ and one molecule of O₂ (equation (1.6)). The photocatalytic reaction is completed with desorption and back-diffusion into the bulk liquid by the products.^{21, 23, 26}



The overall reaction is endergonic and requires 237 kJ mol⁻¹ ("up-hill" reaction).²⁷ Thus, the back reaction is actually thermodynamically favorable and needs to be suppressed for a successful water splitting reaction. Co-catalysts, such as Pt, facilitates are used to facilitate charge separation (see section 1.2.3). Next to the back reaction, there is another limiting factor: the OER is a complex reaction that requires the consumption of four holes compared to the two-electron HER, making the OER the kinetically slow and limiting half-reaction. Furthermore, the driving force for the half-reactions is determined by the potential difference between the position of the CB and VB and the standard potential of the respective redox couple, i.e. for HER: E°(H⁺/H₂) = 0 V vs. NHE and for the OER: E°(O₂/H₂O) = +1.23 V vs. NHE.²⁸ Thus, the VB should be positioned at more positive potentials as for the OER and the CB should be at more negative potentials than that for the HER. The specific material requirements and challenges in photocatalyst design are discussed in section 1.2.

Finding a material, that is a good photocatalyst for both O₂ and H₂ evolution is challenging. The so-called Z-scheme offers a solution to the problem to fulfill all material requirements for both half-reactions, while still being able to absorb visible light (Figure 1-5). Here, two photocatalysts, one for the OER and one for the HER, are connected at their interface. The internal electric field that is established, band bending effects and Coulomb repulsion hinder that photogenerated electrons transfer from the HER photocatalyst, e.g. TiO₂, to the OER photocatalyst, e.g. WO₃, and vice versa in case of photogenerated holes. Thus, a research focus for photocatalytic water splitting is to find efficient photocatalysts for either of the half-reactions, so that they can be combined in a second step via the Z-scheme.²⁹ In my work, I focus on the HER of water splitting which I will discuss in more detail in the following section.

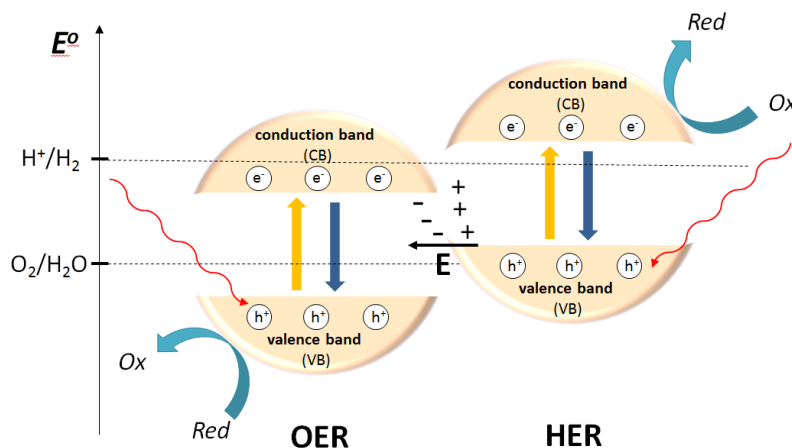


Figure 1-5. Direct Z-scheme for overall water splitting using two semiconductor photocatalysts for the oxygen evolution reaction (OER) and hydrogen evolution reaction (HER), respectively.

1.1.2.3. *HER: H₂ production in the presence of organic molecules (sacrificial water splitting)*

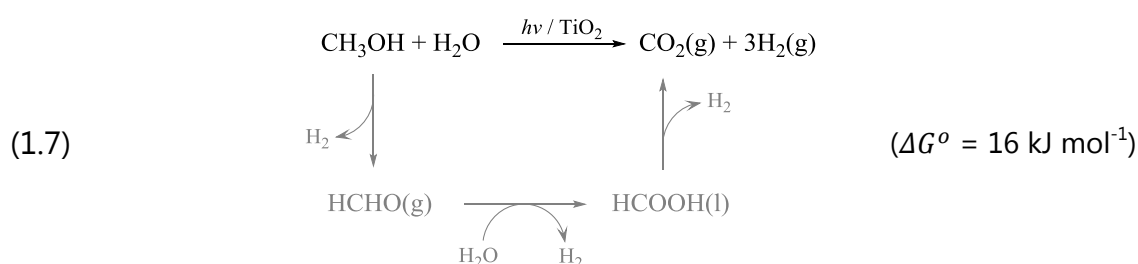
From the reaction scheme for overall water splitting (equations (1.3)-(1.6)), two things are noteworthy: 1) the reaction is energetically unfavorable and 2) the oxidation of water requires four holes, whereas the reduction consumes only two electrons. This leads to an kinetically unfavorable reaction for overall water splitting and reaction rates that are often negligible in practical applications. One strategy to improve the efficiency with respect to H₂ production has been to add a so-called sacrificial agent, in form of an organic substance such as an acid or alcohol, which is more readily oxidized and leads to more favorable thermodynamics.³⁰ Very often, methanol is used as it is a simple molecule and abundant in chemical laboratories. Methanol is oxidized stepwise upon consumption of holes on the surface of the photocatalyst, e.g. TiO₂, with formaldehyde and formic acid as intermediates (equation (1.7)). CO₂ and H₂ are the final products with a stoichiometric ratio of 1:3.³⁰⁻³²

While still being an endergonic reaction, the change in Gibb's free energy dropped from 237 kJ mol⁻¹ for overall water splitting to 16 kJ mol⁻¹ for HER in the presence of methanol.³³ The actual pathways and possible side reactions during the photooxidation of methanol are quite complex and will be discussed in more detail in the context of mechanistic investigations in Chapter 5. In most cases, the presence of methanol during the HER has been wrongfully neglected. This might be due to the misleading term of a sacrificial agent which implies that the alcohol does not play an active role in the overall reaction, but is passively eliminated by the oxidation reaction. However, from the reaction scheme it is clear that a major

Chapter 1 – Introduction & Background

part of the produced H_2 actually originates from methanol, when it is used as sacrificial agent. Therefore, this process is – strictly speaking – not water splitting in the original sense; however, methanol and other sacrificial agents enable us to look at a photocatalytic system with respect to the proton reduction ability which enables mechanistic studies as well as investigation of critical parameters for a good H_2 evolution photocatalyst. In lack of a better alternative, the term sacrificial agent is still used today, in particular when the focus of the research lies on the H_2 production activity of photocatalyst and co-catalyst and not so much on the actual proton source. Photoreforming or photooxidation of methanol may be more accurate terms that describe the same process as sacrificial water splitting.

From a sustainability perspective, the usage of methanol only makes sense if it is produced from a sustainable source, e.g. from biomass, and if the overall CO_2 emission during the production and usage of H_2 is significantly less than upon burning of fossil fuels.



1.1.2.4. Criticism: Photocatalysis vs. Photosynthesis

Overall water splitting shows some parallels to the natural process of photosynthesis. While in natural photosynthesis sugars (energy) and O_2 are generated from water, CO_2 and sunlight, water splitting stores solar energy in form of solar fuels like H_2 and O_2 . Thus, the described reaction for photocatalytic overall water splitting is also referred to as "artificial photosynthesis".^{10, 23}

In a recent review, Osterloh pointed out the often vaguely used terminology of photocatalysis (Figure 1-6). As defined above, any catalytic reaction involves solely an increase in reaction speed, while the thermodynamics remain unchanged. Thus, photocatalytic reactions are those that are thermodynamically downhill ($\Delta G < 0$) and where a photocatalyst increases the reaction rate by lowering the activation energy. This means that there is no net storage of energy in these kinds of reactions and the back reaction is energetically unfavorable. On the other side, if a reaction is thermodynamically uphill ($\Delta G > 0$) a photo-induced reaction should rather be called photosynthetic. Here, the photons provide the energy for the reaction to occur rather than lowering the activation energy. As the forward

reaction is energetically unfavorable, the back reaction logically is favored and needs to be suppressed. In these systems, energy is stored in the form of chemical bonds.³⁴

This distinction has not been applied throughout the community and in order to avoid possible points of confusion, I will keep the term of photocatalysis for this thesis. Still, it should be kept in mind that there might be different thermodynamic driving forces in photo-induced reactions.

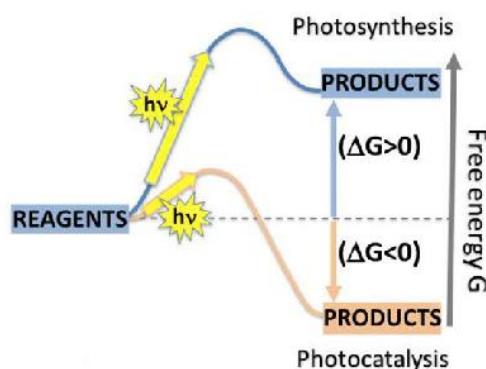


Figure 1-6. Energetics of photocatalysis and photosynthesis.
Reprinted with permission from ref. 34.

1.1.3. Perspective: H₂ as future fuel

Even if a sustainable H₂ production is established, there are still further steps and accompanying challenges that need to be faced before we can realize a hydrogen-based economy. Production is only a part of the usage chain, which also involves storage, distribution.

While the gravimetric energy density of H₂ is the highest amongst all known substances, its volumetric energy density is very low and in particular low in comparison with gasoline. Thus, for H₂ to be used in everyday life, e.g. for cars, it needs to be stored at densities that are higher than its liquid energy density rendering traditional storage in pressurized tanks obsolete and uneconomical. New storage options have to be explored and there have already been promising materials reported such as magnesium alloys, boron- or nitrogen-based compounds, metal hydrides or metal-organic frameworks. A major challenge in the development of storage materials is to balance the capacity of H₂ that a material can absorb (which is determined by the bond strength: the stronger, the higher the capacity) and a high cycling capability (which would require fast kinetics and rather weak

bonding of H_2). Furthermore, distribution infrastructure has to be established, such as H_2 fueling stations and pipelines. All of which need to pass certain safety requirements as H_2 is a highly flammable and very light gas that can easily leak without noticing.¹³⁻¹⁴

The realization of a hydrogen-based economy will largely depend on the research developments in the next years, public education and acceptance about the risks and safety of the technologies as well as policies to implement and support new technologies.

1.2. Materials requirements for a photocatalyst

The following section will first discuss specific material requirements for photocatalysts and co-catalyst, which is followed by a more detailed discussion about the materials used in this work: TiO_2 as semiconductor loaded with Pt as co-catalyst.

1.2.1. Light absorption and charge excitation (Step 1)

First of all, a photocatalyst needs to possess a suitable band gap in order to be photo-excitabile and able to split charges: this is the case for semiconductors. Metal oxides such as TiO_2 ,²⁰ ZnO ,³⁵ ZrO_2 ,³⁶ and CeO_2 ³⁷ have been widely used, with TiO_2 being by far the most studied material.

The suitability of a band gap is defined by several aspects:

- 1) *The band gap should be small enough for maximum absorption of solar light irradiation.* Ideally, we would like our experiments to run under sunlight. Most metal oxides are wide band gap semiconductors. For example, TiO_2 has a band gap of 3.0 to 3.2 eV, which corresponds to a wavelength of roughly 400 nm.³⁸ This means UV irradiation is needed to excite TiO_2 . However, from the solar spectrum, it is clearly evident that only about 5% of the total solar irradiation lies in the range of UV light (Figure 1-7).³⁹ Thus, narrower band gaps that result in visible light absorption result in a much more efficient energy uptake from solar irradiation. A strategy to increase absorption is band gap engineering via doping or introduction of defects, which will be discussed in more detail in section 1.3.

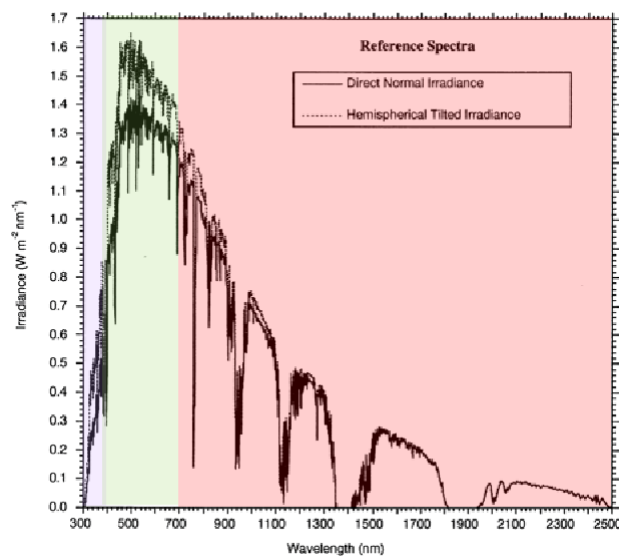
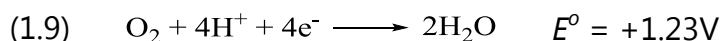
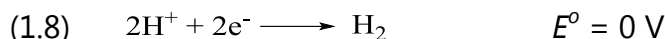
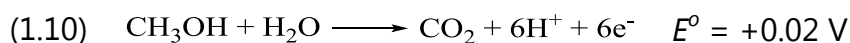


Figure 1-7. ASTM G173-03 solar reference spectrum adapted from ref. 39. Colored areas correspond to the different light regions: UV light (violet), visible light (green) and infrared light (red).

- 2) *The band gap needs to be large enough.* The overall photocatalytic reaction can be considered as a redox reaction. The standard reduction potential of a redox couple tells us the potential needed for a reaction to occur. So for overall water splitting, we consider the HER and OER half-reactions:²⁸



The potential difference is 1.23 V. So the potential difference between the electrons in the CB and the holes in the VB has to be at least 1.23 V for the water splitting reaction to occur. Furthermore, a certain overpotential needs to exist between the CB/VB and the redox potentials of the half-reactions to provide a large enough driving force for a reaction to occur. On the other side, if methanol is used as sacrificial agent, the potential difference between proton reduction and methanol oxidation to CO_2 is only 0.02 V resulting in a much larger potential driving force for the oxidation reaction of methanol compared to OER (equation (1.10)).⁴⁰



- 3) Furthermore, the band positions of the semiconductor have to be appropriate. This means that the CB needs to lie at a more negative potential than the proton reduction reaction and the VB needs to be more positive than the water oxidation reaction (Figure 1-8). The higher the potential difference between the electronic bands of the semiconductor and redox potential of the half-reaction, the higher the driving force for the respective reaction. Figure 1-8 shows the band gap values of common semiconductors used in photocatalysis as well as their VB and CB position compared to the redox potential of water oxidation and reduction.⁴¹

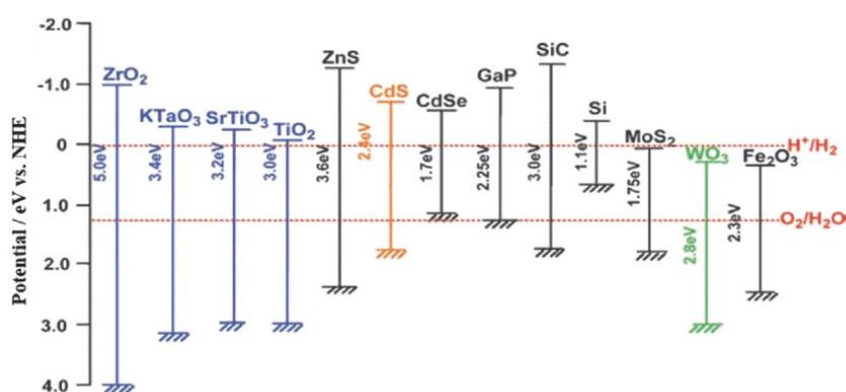


Figure 1-8. Band positions of common semiconductors with respect to the redox potentials of proton reduction and water oxidation. Reprinted with permission from ref. 41.

The listed values are the standard reduction potentials, which are typically reported at a pH of 0. For overall water splitting a pH of 7 is more likely, while during photooxidation of methanol, the optimum pH lies between 3-5.⁴²⁻⁴⁴ The redox potentials are pH-dependent, so while the overall potential difference remains the same, the absolute energy value might shift in position (e.g. at pH 7: $E^\circ(\text{H}^+/\text{H}_2) = -0.41 \text{ V}$; $E^\circ(\text{O}_2/\text{H}_2\text{O}) = +0.82 \text{ V}$; $E^\circ(\text{CH}_3\text{OH}/\text{CO}_2) = +0.38 \text{ V}$).⁴⁵ Pourbaix diagrams based on the Nernst equation can be used to estimate the redox potential at a certain pH. Furthermore, the band positions of a semiconductor depend on the surface charge due to band bending phenomena (section band bending). The surface charge, again, is dictated by the pH and characteristic isoelectric point of a material. Thus, redox potential values and positions of the CB and VB for the semiconductors should be seen as guideline and need to be evaluated for a specific system. While I did not investigate the exact band alignment in the case of methanol photooxidation in this work, the vast lit-

erature on the photooxidation of methanol confirms that the VB of TiO_2 is sufficiently deep enough to allow for the oxidation reaction and should not show a strong pH dependence in the regime I am using (pH 3-5). Still, these are important parameters to keep in mind, when comparing literature.

1.2.2. Charge separation & transfer (Steps 2 & 3)

Once an electron-hole pair is separated into electrons and holes, recombination needs to be avoided so that the individual charge carriers can transfer to the adsorbed reactants at the surface of the photocatalyst. Certain material properties can reduce the likelihood of recombination events

- 1) The material should be defect-free (includes vacancies, interstitials, dopants, grain boundary, ...). Recombination may happen, if a charge carrier is trapped at a defect site. The localization of the charge without possibility to react leads to a higher probability that it is eventually recombining again to an electron-hole pair. In section 1.3.4, I will discuss the role of defects in photocatalytic reaction in more detail. I will show, that defects can sometimes also have a beneficial effect on the performance of a photocatalyst depending on their concentration and location.
- 2) The material should have small transfer paths (e.g. nanowires, nanotubes). The faster the charge carriers reach the surface, the higher is the probability that trapping or recombination does not occur.
- 3) Heterostructures within a material can facilitate the separation of charges. An example is the synergistic effect in P25, a mixed-phase TiO_2 , which will be discussed in section 1.2.4.1).
- 4) Additional extraction of the charge carriers from the semiconductor by either an applied electric current (PEC cell) or by using a co-catalyst leads to a higher degree of separation and lower recombination rates. Furthermore, the co-catalyst can facilitate charge transfer. The working principle of a co-catalyst will be described in the following section.

1.2.3. The co-catalyst: Pt

Co-catalysts serve as electron traps and active sites for proton reduction and are usually deposited as nanoparticles onto the surface of the photocatalyst, in particular for the HER.⁴⁶ Oxidation reactions on the other side can be performed without additionally co-catalysts, because the VB levels of most photocatalysts

are deep enough to provide a large enough potential difference and driving force for the OER.

Common co-catalysts are either metals (e.g. Pt,^{15, 47-51} Pd,⁴⁷⁻⁵⁰ Ag,^{15, 49} Au,^{15, 48, 51} Rh,⁴⁷⁻⁵⁰ Ru,^{47, 50} Ni,⁴⁷⁻⁴⁸ Ir^{48, 50}) or metal oxides (e.g. CuO⁵², NiO⁵²⁻⁵³). Co-catalysts are mainly deposited from acid or salt precursors via an impregnation^{43, 51, 54-63} or photodeposition method^{54, 64-69}. In particular, hexachloroplatinic acid (H₂PtCl₆) is conventionally used for the deposition of Pt. The impregnation method involves an oxidation step of adsorbed PtCl₄²⁻ to PtO, followed by a reduction in H₂ atmosphere to metallic Pt. This procedure needs high temperatures and several steps. Photodeposition on the other side simply uses the fact, that H₂PtCl₆ completely reduces to metallic Pt under UV irradiation.⁷⁰ In this work, in situ photodeposition is used as one-step method to deposit Pt nanoparticles during the HER reaction.

As can be seen in Figure 1-8, the CB levels of TiO₂ and many other semiconductors are very close to the reduction potential of protons. Thus, the driving force for H₂ production to occur is relatively low and actually, in the case of TiO₂, only small – if any – amounts of H₂ are produced from methanol solutions and basically zero gas evolves in pure water solutions. Depositing metal particles with higher work functions than the semiconductor, such as Pt, Au, Ag, onto the photocatalyst, e.g. TiO₂ induces so-called band bending, which allows for better charge separation and thus largely enhanced reaction rates.

1.2.3.1. *Band bending & Schottky barrier*

Band bending and the formation of a Schottky-barrier between the metal and metal oxide are the working principle between enhanced charge separation by a co-catalyst and improved performance of a photocatalyst.

In 2012, Zhang and Yates published a very comprehensive and well-written review about the principles of band bending, ways to measure its extent and implications in the context of photocatalysis. They pointed out that although band bending is well known in solid state physics and electrochemistry, there has been a lack of research considering these effects in the area of photocatalysis.⁷¹⁻⁷²

Band bending occurs in semiconductors when they come in contact with another conductive material (e.g. metal or other semiconductor) with a different work function. The extent and direction of band bending depends on the Fermi level difference between the semiconductor and the metal, which is determined by their work functions. Figure 1-9 shows a schematic depiction of upward and

downward bend bending upon contact of a semiconductor with a metal of a different work function. If the work function of the metal, ϕ_m , is larger than that of the semiconductor, ϕ_s , ($\phi_m > \phi_s$), the Fermi level of the metal is at a lower potential compared to the semiconductor. In order to establish an equilibrium, electrons flow from the semiconductor to the metal until both Fermi levels are aligned. This creates a Helmholtz double layer at the interface that is negatively charged in the metal and positively in the semiconductor. The poor screening ability in semiconductors due to low concentration of charge carriers leads to space charge layers that is, in this case, poor in electrons and therefore also called depletion layer. Due to repulsion of the semiconductor bands in the depletion area by the negatively charged metal interface, the potential energy of the bands increases and an upward band bending occurs. In case of a metal and an n-type semiconductor and $\phi_m > \phi_s$ (e.g. Pt and TiO_2) the potential barrier at the hetero-

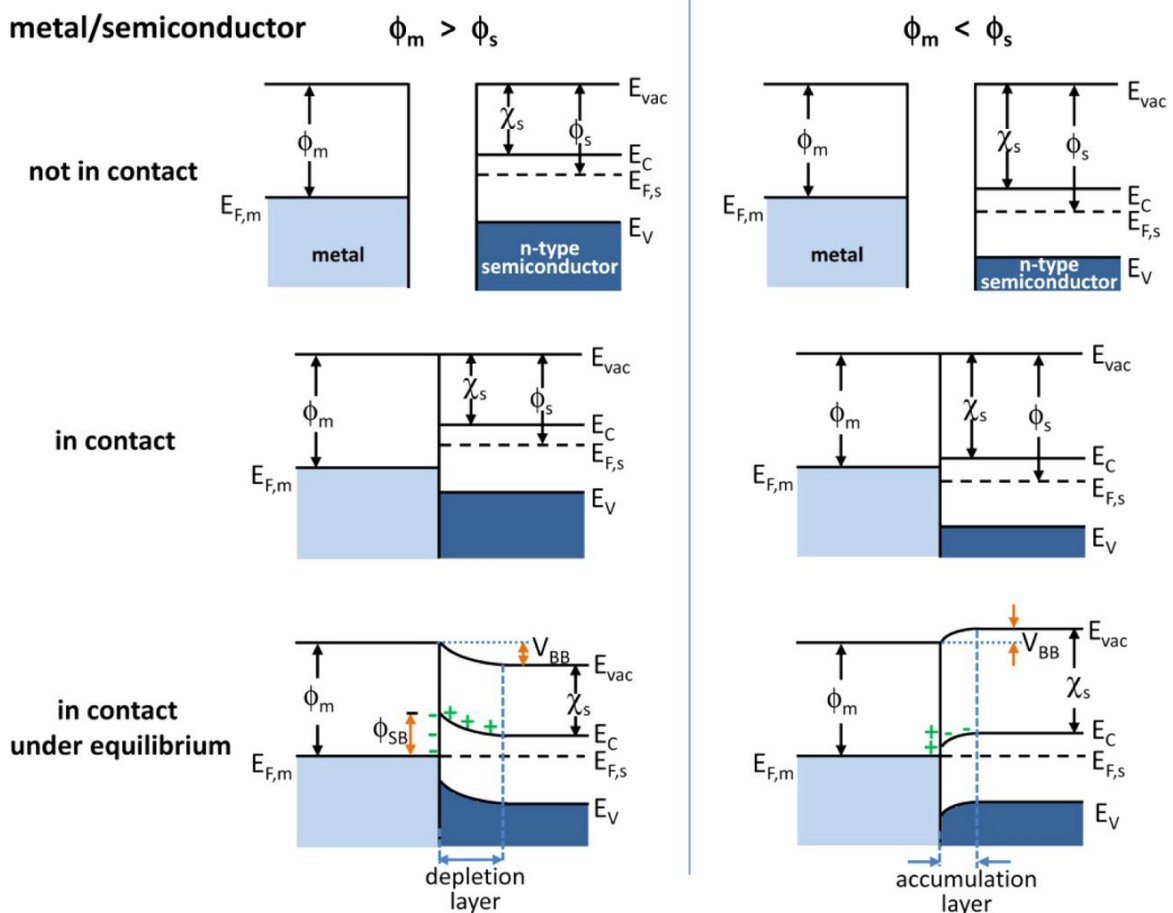


Figure 1-9. Energy band diagrams of metal and n-type semiconductor contacts. E_{vac} , vacuum energy; E_C , energy of conduction band minimum; E_V , energy of valence band maximum; ϕ_m , metal work function; ϕ_s , semiconductor work function; χ_s , electron affinity of the semiconductor. Reprinted with permission from ref. 72. Copyright 2012 American Chemical Society.

Chapter 1 – Introduction & Background

junction is also called Schottky barrier.⁷²

If $\phi_m < \phi_s$, the processes are reversed: electrons flow from the metal to the semiconductor resulting in an accumulation layer in the semiconductor and a downward band bending. Instead of a Schottky barrier, an ohmic contact is established.⁷²

Band bending is interesting for photocatalytic reactions, these potential differences can be used for charge separation and reduction of undesired recombination. In case of an upward bend (Schottky barrier, $\phi_m > \phi_s$), electrons accumulate in the metal, while holes are available to react on the semiconductor surface. This configuration is desirable for H₂ reduction applications, as the proton reduction occurs on the co-catalyst (Pt) and oxidation of water or organic molecules on the semiconductor (TiO₂) surface.⁷²

As the difference in the work functions determines the extent of band bending and therefore the charge separation, it can be inferred that a higher work function of the metal co-catalyst results in less recombination and thus better photocatalytic performance with respect to H₂ production. Table 1-1 lists the work functions of commonly used co-catalyst during photocatalytic HER experiments. Pt has the highest work function with $\phi_{Pt} = 5.65$ eV, which explains why it leads to the highest performances in HER experiments on TiO₂ ($\phi_{TiO_2} = 4.6-4.7$ eV).^{15, 73}

metal	ϕ / eV
<i>Pt</i>	5.65
<i>Ir</i>	5.27
<i>Ni</i>	5.15
<i>Pd</i>	5.12
<i>Au</i>	5.10
<i>Rh</i>	4.98
<i>Ru</i>	4.71
<i>Ag</i>	4.26
<i>TiO₂</i>	4.6-4.7

Table 1-1. Work function values for common co-catalysts and TiO₂. Values are taken from ref.15 and 73.

Band bending further depends on several factors such as particle size, dopant concentration and the dielectric constant of a material.⁷² Generally, band bending should be considered whenever two different Fermi levels are in contact with each other, which is also true for surface states of different Fermi position or for adsorbants during surface reactions.

1.2.3.2. *Is Pt as co-catalyst sustainable?*

While Pt shows high performance and good properties as a co-catalyst, it also is a precious metal with finite availability and high price. Thus, it will face issues in any large scale industrial application and cannot be considered sustainable at the current state of technology. Cheaper and more abundant co-catalysts are the matter of high research interest. Metal oxides, such as NiO or CuO, are a popular alternative. Also other novel materials are being discovered: In 2015, ternary pyrite-type cobalt phosphosulphide (CoPS) has been reported as a high-performance Earth-abundant catalyst for the PEC production of H₂.⁷⁴

I did not explore any alternative to Pt in my research as a large focus was a) to investigate the mechanism of H₂ evolution via the photooxidation of methanol (Chapter 5) and b) to compare differently synthesized TiO₂ to literature and identify key characteristics for improved performance (Chapter 6). While some of my findings might be system-specific, the hope is that a better or complete understanding of a reference system as Pt-loaded TiO₂ is, will lead to better understanding for newly developed technologies and materials.

1.2.4. **The photocatalyst: TiO₂**

TiO₂ is likely the most studied metal oxide across literature.^{20, 24, 38, 42, 75} Its Earth abundance, stability, non-toxicity and inexpensiveness together with other physicochemical properties (e.g. semiconductivity) led to its use in various applications ranging from cosmetics⁷⁶ and paints⁷⁷ to electrical devices⁷⁸ and gas sensors⁷⁹. The following section will discuss some fundamental knowledge about the structure and most common phases of TiO₂ (anatase and rutile), as well as reported performance in HER reactions comparable to this work. A special focus will be given to the mixed-phase TiO₂, P25.

TiO₂ has three major polymorphs which, in order of abundance, are: rutile, anatase, and brookite. Rutile and anatase are the by far most studied polymorphs and, in particular, anatase has shown the highest photocatalytic activities amongst the different forms of TiO₂. In general, anatase is kinetically favored at temperatures below approximately 600-700 °C on which it transforms into the thermodynamically favored rutile phase.²¹ Brookite is a metastable phase that can be obtained from the hydrolysis of K₂Ti₄O₉.⁸⁰ However, stability can vary with particle size: Anatase, for example, has been reported to be most stable for particle sizes below ca. 14 nm.⁸¹

Chapter 1 – Introduction & Background

Figure 1-10 shows the ball-stick models of the unit cells, coordination polyhedra and Wulff reconstructions of the equilibrium shapes of an anatase and rutile crystal. Ti is surrounded by six O atoms in a distorted (elongated along the z-axis) octahedron in both anatase and rutile. For anatase, octahedra are rather edge-sharing, whereas octahedra in rutile are connected at the corners and alternating by 90° along their long axis. Anatase has a tetragonal bipyramidal form with (101), (011) and (001) as the dominating facets. Rutile commonly occurs in a prismatic, often needle-like form with the dominating low-energy facets of (110) and (100). The atomic connectivity between O and Ti differs with the different facets and will not be discussed in detail here. Generally for all facets, exposed Ti^{4+} atoms may serve as Lewis acid sites, while O^{2-} ions are Lewis bases.^{38, 82-84}

TiO_2 is an n-type semiconductor. Its VB is mainly composed of O 2p orbitals; the CB of Ti 3d orbitals. This is discussed in more detail in a later section (section 4.4.4). The optical band gaps are 3.0 eV (415) nm for rutile and 3.2 eV (385 nm) for anatase, making them wide band gap semiconductors that absorb in the UV light range.³⁸ Interestingly, the nature of the optical transition in rutile and anatase, i.e. whether it is direct or indirect, seems to be a matter of controversy. While a majority of reports consider the band gap of anatase as indirect⁸⁵⁻⁸⁸, it has also been described as direct in nanoparticles⁸⁹. Rutile is even more controversial across literature, with reports stating its indirect nature⁸⁵⁻⁸⁶, while others treat it as a direct band gap semiconductor⁸⁷⁻⁸⁸. Also, the type of transition also depends on

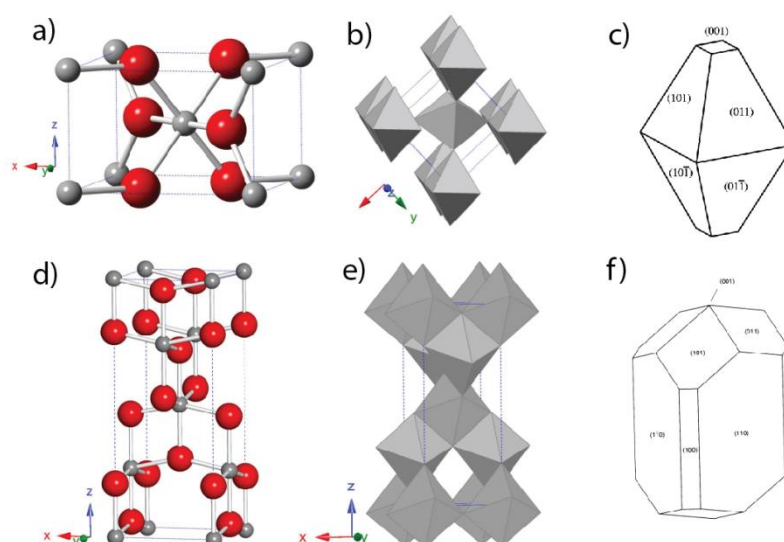


Figure 1-10. Ball-stick models of unit cells of a) rutile and d) anatase; coordination polyhedra of b) rutile and e) anatase. Adapted with permission from ref. 84. Copyright 2015 American Chemical Society. Wulff construction of c) rutile and f) anatase. Reprinted figure with permission from ref. 82 and 83. Copyright 2001 and 1994 by the American Physical Society.

the proximity to the absorption edge as stated for rutile.⁹⁰ For my analyses, treating both band gaps as indirect seemed to be most appropriate. In particular, Tauc plot analysis in Chapter 6 agreed well with literature values, when rutile is treated as indirect semiconductor.

1.2.4.1. *P25 – the benchmark: synergistic effects*

Mixed-phase TiO₂ outperforms the pure polymorphs anatase and rutile in photocatalytic applications.⁹¹ In particular, P25-type TiO₂ in combination with Pt as co-catalyst has evolved as standard reference in most photocatalytic applications.

P25 (originally by Evonik, formerly Degussa) is synthesized by flame-spray pyrolysis from, for example, a TiCl₄ precursor.⁹² It is typically stated to consist of 80% anatase and 20% rutile phase, while the presence of a minor amorphous phase due to the synthesis method is often neglected.⁹³ In 2010, Ohtani et al. determined the ratio of anatase:rutile:amorphous phase by selective dissolution to be 78:14:8. These values may vary even within the same sample batch and cannot be applied to the P25 used in this work, although it can be seen as reference or guiding value.⁹⁴

There has been some controversy about the reasons behind the synergistic effect of a close interface between anatase and rutile in the past. While at first rutile was thought to serve as electron sink⁹², there have been several studies that investigated the electron flow under UV illumination and band alignment of the two polymorphs.^{91, 95-96} Scanlon et al. convincingly show that the VB and CB is shifted to lower energies compared to rutile, which leads to a higher electron affinity of the anatase phase and thus, better charge separation as supported by EPR studies (Figure 1-11).⁹⁶ Rutile can act as sort of visible light antenna as its band gap slightly extends into the visible light, whereas charge separation occurs due to band bending at the interface of both metal oxides (Figure 1-11). As anatase has the higher work function as rutile, its VB is bent upwards, whereas that of rutile bends upward (section 1.2.3.1). This results in an improved charge separation and higher photocatalytic performance.

However, although there seems to be profound evidence on the reasons for the synergistic effects in P25, other work casts doubt whether there is synergy at all. Ohtani et al. isolated the different phases of P25 by selective dissolution and reconstructed the original P25 by physically mixing the isolated fractions and commercial amorphous powder. The photocatalytic performance varied -11 to +19% of the original P25, which suggests the lack of strong interparticle interaction. Fur-

thermore, the isolated phases could even show higher activities than the original P25 depending on the type of photocatalytic experiment.⁹⁴

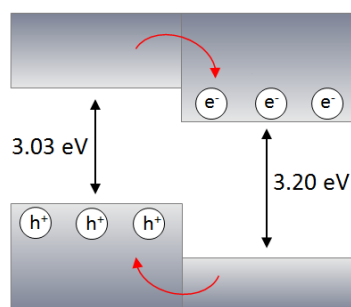


Figure 1-11. Proposed valence and conduction band alignment mechanisms for the anatase/rutile interface. Red arrows indicate the flow of electrons (holes) in the conduction band (valence band). Based on ref. 96.

1.2.4.2. *TiO₂ in HER*

TiO₂ and, in particular P25, has become a benchmark in any photocatalytic application including the HER.^{20, 24, 38, 42} Applications based on the photoassisted degradation of organic molecules can be found in waste water treatment⁹⁷, bacterial disinfection⁹⁸, self-cleaning surfaces⁹⁹, and protective coatings¹⁰⁰. Band alignment investigations between anatase and rutile by Scanlon et al. suggest that the CB of rutile is at a higher position, which would result in a better driving force for the HER for rutile (section 1.2.4.1).⁹⁶ However, anatase is the generally the most active TiO₂ phase for photocatalytic applications. One explanation for the better performance of anatase is a significantly lower recombination rate compared to rutile.¹⁰¹⁻¹⁰²

For this work, it has been of interest to compare values obtained in my system to literature values. The performance of a photocatalyst depends on many variables, to name a few: incoming light flux & direction, the reactor setup, temperature, amount and type of sacrificial agent/co-catalyst. Thus, although there are many publications on the photocatalytic HER over TiO₂, the number of suitable references decreases tremendously, once they are narrowed down to the specific conditions used in this work. Table 1-2 (p.24) gives an overview of selected publications including critical reaction conditions for HER over Pt-loaded TiO₂ in water or aqueous methanol solutions. The listed values show some range in the reported absolute values but can still serve as approximate references for my experiments. For example, values around 4 mmol of H₂ per hour and per gram of photocatalyst

are reported for TiO₂ loaded with 0.5 wt.% Pt.^{57, 103} For 1.0 wt.% Pt loaded TiO₂ H₂ evolution rates ranged between 6 and 11 mmol h⁻¹ g⁻¹ of photocatalyst.^{54, 67, 103}

1.2.4.3. *Deactivation of TiO₂*

Chapter 5 of this thesis will introduce and investigate deactivation of the TiO₂ loaded with Pt as co-catalyst by in situ photodeposition during the photooxidation of methanol and HER. I first observed deactivation during my master studies and some preliminary work has been already published in my master thesis. To my knowledge, this type of deactivation has not been observed in literature before – or not discussed in depth. A few studies do observe a degradation in the H₂ rate during HER or degradation of organic compounds.^{51, 104-107} For example, the group of Prof. Verykios showed a deactivation during the photooxidation of methanol that, they assigned to active site poisoning by photogenerated oxygen due to the degradation or absence of the sacrificial agent.¹⁰⁴⁻¹⁰⁵ Furthermore, Kozlova et al. found differences in stabilities of Pt deposited using impregnation followed NaBH₄ reduction compared to photodeposited Pt.¹⁰⁷ The photodeposited Pt showed a deactivation in rate during oxidation of an organophosphorous compound due to agglomeration of Pt particles during the reaction. However, these explanations have not been coherent with my observations as will be shown in detail in Chapter 5. Pan et al. photooxidized benzyl alcohol over Pt-loaded TiO₂ in an aerobic environment and observed a decrease in the absolute H₂ produced after each run for a series of experiments.¹⁰⁸ They suggested that oxygen vacancies form under UV illumination, which serve as recombination site and reduce the photocatalytic performance. The role and influence of defects during photocatalysis is a major focus of this work and will be introduced in the following section.

Reference (year)	methanol / vol. %	Dispersion / g L ⁻¹	Pt loading / wt. %	Pt deposition method	Light source	Activity H ₂ / mmol h ⁻¹ g ⁻¹	CO observed (Y/N/not mentioned)?	Additional information
55 (2007)	25	1.5 (300 mg in 200 mL)	0.02	Impregnation from H ₂ PCl ₆	300 W Xe lamp	online GC : ca. 3 (Fig. 14)	N	
55 (2007)	25	1.5 (300 mg in 200 mL)	0.1	Impregnation from H ₂ PCl ₆	300 W Xe lamp	online GC : ca. 4.7 (Fig. 14)	N	
270 (2000)	12.5	2.5 (1 g in 400 mL)	0.1	H ₂ PCl ₆ (not specified)	400 W high-P Hg lamp	GC : 0.55	Y	
55 (2007)	25	1.5 (300 mg in 200 mL)	0.2	Impregnation from H ₂ PCl ₆	300 W Xe lamp	online GC : ca. 4.8 (Fig. 14)	N	
269 (2005)	0.004-0.0012	0.8 (300 mg in 400 mL)	0.3	Impregnation from H ₂ PCl ₆	450 W medium-P Hg lamp (inner irradiation), (emission spectrum given)	GC : 1-3 (Fig. 3)	N	30-60°C
269 (2005)	2.5	0.8 (300 mg in 400 mL)	0.3	Impregnation from H ₂ PCl ₆	450 W medium-P Hg lamp (inner irradiation), (emission spectrum given)	GC : 25.6	N	30-60°C
51 (2010)	25	1.0 (1 g in 1 L)	0.3	Impregnation from H ₂ PCl ₆	150 W metal halide (solar; inner); (30 mW cm ⁻²)	online-GC : 1.1	mentioned, not studied	
55 (2007)	25	1.5 (300 mg in 200 mL)	0.5	Impregnation from H ₂ PCl ₆	300 W Xe lamp	online GC : ca. 4.5 (Fig. 14)	N	
196 (2013)	25	0.8 (100 mg in 120 mL)	0.5	not mentioned	300 W Hg lamp	GC : 0.75	not mentioned	
196 (2013)	25	0.8 (100 mg in 120 mL)	0.5	not mentioned	AM 1.5G solar light-sim (cut-off by 400 nm); (100 mW cm ⁻²)	GC : none	not mentioned	
103 (2013)	25	1.0 (200 mg in 200 mL)	0.5	photodeposition from H ₂ PCl ₆ + heat treatment	8 Philips CLEO 15 W (300-400nm, max at 365 nm)	GC : ca. 3.8 (Fig. 10)	not mentioned	pH 5
66 (2014)	0.12	1.0 (60 mg in 60 mL)	0.5 (?)	photodeposition from H ₂ PCl ₆	Photodeposition: Philips fluorescence Hg-lamp (UV(A)); (1.0 mW cm ⁻²) Photocat: 365 nm LED (Thorlabs); (44 mW cm ⁻²)	online MS : 1.2 (Fig. 2 Inset)	N	
55 (2007)	25	1.5 (300 mg in 200 mL)	1	Impregnation from H ₂ PCl ₆	300 W Xe lamp	online GC : ca. 3.3 (Fig. 14)	N	
191 (2014)	25	0.4 (50 mg in 120 mL)	1	not mentioned	300 W Xe lamp	GC : 0.9	not mentioned	
103 (2013)	25	1.0 (200 mg in 200 mL)	1	photodeposition from H ₂ PCl ₆ + heat treatment	8 Philips CLEO 15 W (300-400nm, max at 365 nm)	GC : 11	not mentioned	pH 5
103 (2013)	25	1.0 (200 mg in 200 mL)	2.1	photodeposition from H ₂ PCl ₆ + heat treatment	8 Philips CLEO 15 W (300-400nm, max at 365 nm)	GC : 14	not mentioned	pH 5

Table 1-2. Overview over selected literature reporting on photocatalytic HER experiments of P25 in aqueous methanol solutions using Pt as a co-catalyst at loadings ranging from 0 to 2.1 wt.%. ca. signalizes when values were not explicitly reported in text but in a figure.

1.3. Defects & Photocatalysis

Defects – deviations from order – are the reactive centers of materials and dictate their structural and electronic properties. Defects, for example, can induce ionic and electronic conductivity, thereby giving rise to ionic conductors used in solid state fuel cells or the n-type semiconductivity in TiO_2 . The influence on the electronic structure is of particular interest in photocatalysis as defects may serve as recombination sites and induce band gap narrowing due to new electronic states that result in an increased absorption. As I will show later, defects can have a negative or beneficial impact on a reaction depending on their nature and location (see section 1.3.4). Next to their impact on the electronic structure of a material, surface defects are of particular interest regarding (photo-)catalytic applications as they usually serve as nucleation and adsorption sites. For example, water, methanol and Pt all favor the adsorption at surface oxygen vacancies, which leads to competitive adsorption behavior as I will discuss in section 1.3.4.1.

Thus, understanding and knowing the defect chemistry of your material is critical for a complete understanding of a reaction. Applying this knowledge and controlling defects is a powerful tool in tuning the properties of a material and increasing efficiencies of reactions. This purposeful tuning is also known as “defect engineering”.¹⁰⁹⁻¹¹²

In the following section, I will give an overview about fundamental concepts in defect chemistry with a special focus on oxygen vacancies in TiO_2 , ways to introduce defects as well as typical methods for characterization and the corresponding challenges. An overview on the impact of oxygen vacancies in photocatalysis is given at the end with a particular emphasis on black TiO_2 .

1.3.1. General

Defects are present in any crystalline material and can be defined as deviation from the long-range periodicity in crystals. Their presence can be explained thermodynamically by applying the equation for Gibb’s free energy (equation (1.11)): The gain in entropy by creating disorder and a higher degree of freedom outweighs the energy it costs to create a defect due to bond breaking or rearranging ($T\Delta S > \Delta H$). This leads to a negative change in Gibb’s free energy ($\Delta G < 0$), so that defects form spontaneously at temperatures above 0 K in any material.¹⁰⁹

$$(1.11) \quad \Delta G = \Delta H - T\Delta S$$

Chapter 1 – Introduction & Background

Defects can be categorized according to their dimensionality:

- **0-D:** point defects: *vacancies, interstitials, substitutionals*
- **1-D:** linear defects: *edges, screws, steps*
- **2-D:** planar defects: *grain boundaries, surfaces*
- **3-D:** extended defects: *pores, cracks*

The defect with the lowest energy of formation typically dominates and dictates the defect chemistry, which is usually a vacancy defect.¹⁰⁹ The different possibilities of metal charged states and bonds make the defect structure in metal oxides more complex than in metals.¹¹⁰ While adsorbed H and subsurface defects have experienced more attention in recent research¹¹³⁻¹¹⁴, I will focus on oxygen vacancies the dominant defect in metal oxides at the example of TiO_2 .

Point defects in binary systems like metal oxides typically come in pairs in order to maintain an overall neutral charge in the crystal and conserve stoichiometry. For example, a vacancy in a sublattice leads to a charge misbalance that needs to be compensated by a vacancy, interstitial or substitution. They are categorized into intrinsic and extrinsic point defects: Intrinsic point defects are either vacancies or interstitials and are those present during the thermodynamic equilibrium of a crystal. They can be further sub-divided into Schottky (vacancy in both anion and cation sublattice) and Frenkel defects (cation is displaced to interstitial lattice site and creates a vacancy). The anti-Frenkel defect is a special case of the Frenkel defect that can be found in fluorite structures, in which an anion moves to an interstitial site instead of a cation. This is less common due to generally unfavorable energetics as anions typically occupy more space than cations. Extrinsic point defects are formed, when a foreign atom (often of different oxidation state than the host) is introduced into the crystal lattice. For example, if CaCl_2 is added to NaCl , one Ca^{2+} ion can substitute for two Na^+ ions and thus creates a vacancy in the cation sublattice.¹¹⁵ Furthermore, ZrO_2 stabilized by CaO is an important example, in which Ca^{2+} substitutes a Zr^{4+} ion.¹¹⁶ An oxygen vacancy is created in turn for charge compensation. If these extrinsic defects are introduced voluntarily, it is called doping and the foreign atom is a dopant. For example, the introduction of hydrogen into the crystal lattice of TiO_2 can be seen as doping of TiO_2 with H.^{42,}

109

Nonstoichiometry is a different type of defect state, where the structural formula of a compound cannot be expressed by integers anymore (e.g. nonstoichiometric $\text{TiO}_2 = \text{TiO}_{1.998}$). Charge neutrality is ensured by redistribution of the charge across

the crystal lattice and changes in the oxidation states within the crystal.¹⁰⁹ For example, upon reduction metal oxides lose an oxygen atom and form an oxygen vacancy with two excess electrons in their crystal lattice.¹¹⁰ This will be discussed in more detail in the context of color centers and conductivity (section 1.3.1.1).

The Kröger-Vink notation is commonly used to describe defect equilibria in solids. These equilibria can also be used to establish defect diagrams (Brouwer diagram), which illustrate the dominating defect at a certain set of conditions (*e.g.* partial oxygen pressure, T , concentration).^{109, 117-118} However, these diagrams are highly specific and need well-controlled parameters. Reaction systems as in the HER are very complex and corresponding diagrams have not been established.

Point defects are mobile species and can diffuse through a material via vacancy hopping or interstitial diffusion. The diffusion coefficient depends strongly on temperature, and also on the defect density and lattice structure. Diffusivity is much higher along grain boundaries and dislocations. Diffusion is not only material but also phase-specific and can be mediated by adsorbates. At the same time, defects, such as a bridging oxygen vacancy in TiO_2 can mediate diffusion of alkoxy-species¹¹⁹ or of hydrogen atoms¹²⁰ on bridge-bonded oxygens. In particular the alkoxy-shuttling is interesting in the context of HER from methanol solutions. This shuttling could accelerate the diffusion of organic reactants across the metal oxide surface to reactive sites, *e.g.* at the triple phase boundary (TPB) between co-catalyst, metal oxide and reaction solution, and enhance oxidation and thus overall performance of the photocatalyst.

1.3.1.1. *Color centers & conductivity*

The influence of oxygen vacancies on the electronic structure of a material is determined by the binding environment in a crystal.¹¹⁰ For example, in the case of the ionic MgO crystal, electrons stay trapped in the vacancy resulting in a neutrally charged oxygen vacancy, whereas for covalently bonded SiO_2 a Si-Si bond is formed upon loss of an oxygen atom, resulting in a double positively charged oxygen vacancy. TiO_2 (and other transition metal oxides) represents an intermediate case between ionic and covalent binding, where the excess charge of the vacancy is redistributed into empty 3d orbitals. Thus, upon loss of an oxygen atom in TiO_2 , Ti^{4+} is reduced to Ti^{3+} and the oxygen vacancy can be regarded as singly positively charged. The detection of Ti^{3+} centers is thus an indirect measure of the presence of oxygen vacancies in TiO_2 . However, as discussed by Minato et al., there has been some controversy in literature about whether electrons are local-

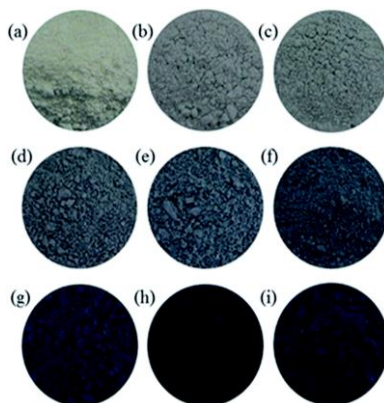


Figure 1-12. Reduced TiO₂ with increasing degree of reduction. The blue coloration is induced by F⁺ color centers. Figure taken with permission from ref. 121 - Published by The Royal Society of Chemistry.

ized or delocalized. Despite the lack of a strong conclusion, delocalization seems to occur at least to some extent.¹¹³

A feature of all of these differently trapped electrons is that they can cause visible light absorption and generate color in the defective materials. For example, reduced TiO₂ typically results in a blue coloration due to the newly introduced Ti 3d donor states (Figure 1-12).¹²¹ Therefore, these defect sites are also called color or F centers (from German for color: "*Farbe*"). Depending on the different electronic environments, one may distinguish between F, F⁺ and F⁺⁺ color centers for neutral, singly, and doubly charged oxygen vacancies, respectively. Further color center types are the F₂ dimer center, in the case of an oxygen di-vacancy, and the V-type color center, due to a trapped hole.^{110, 122-125}

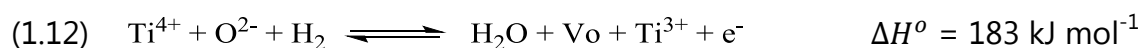
Another feature introduced by the formation of shallow donor states in the Ti 3d orbital results in an n-type electronic conduction in oxygen deficient TiO₂. For stoichiometric TiO₂ (oxygen-treated), the activation energy for conduction was found to be 0.5 eV below 700 K and 1.62 eV above 700 K. For H₂-treated TiO₂, the conductivity was 4-5 orders of magnitude higher, with an activation energy for conduction of about 0.1-0.2 eV.¹²⁶ Regonini et al. confirmed these values in another study using impedance spectroscopy in 2012.¹²⁷ They investigated stoichiometric TiO₂ as well as Magnéli phases, confirming the activation energy for electronic conduction of only about 0.14 ± 0.1 eV for oxygen-deficient TiO₂ that increased to 0.77 ± 0.08 eV above 250 °C.

1.3.2. How to create oxygen vacancies

Understanding and knowing the nature and effects of defects in certain materials is the first step, applying that knowledge and controlling them the second. Oxygen vacancies have desirable properties, such as increasing absorption and conductivity, in particular with respect to photocatalytic applications. For example, introduction of color centers that can absorb in the visible light may increase the performance of TiO₂ under solar light, the ultimate goal for a sustainable energy source. Furthermore, increased conductivity may also lead to higher photocurrents and thus higher H₂ production rates. Therefore, oxygen vacancies have become a focus of research interest not only in conventional catalysis but also for photocatalysis.^{111, 114, 128} A recent example is black TiO₂, a hydrogen-treated form of TiO₂ that showed remarkable activities for H₂ evolution under solar light.¹²⁹

Xiong et al. give a comprehensive overview about common methods to introduce oxygen vacancies into TiO₂ by loss of O₂ including high temperature annealing in vacuum¹³⁰⁻¹³¹, reductive thermal treatment in H₂¹³², and bombardment with high-energy particles (Ar⁺ sputtering,¹³³ neutron bombardment,¹³⁴ plasma treatment,¹³⁵ Knotek-Feibelman mechanism¹³⁶⁻¹³⁷ (section 4.2)).¹²⁸ The introduction of dopants, e.g. Fe³⁺,¹³⁸ can be used to generate oxygen vacancies as discussed in context of the extrinsic defects (section 1.3.1). Also, the combustion of organic compounds has been shown to act reductively on the TiO₂ substrate.¹³⁹⁻¹⁴⁰ At last, irradiation of TiO₂ by either UV^{56, 141-145} or ultrasound (US)^{49, 146-151} has been found to create oxygen vacancies and reduce the material. This is of particular interest, as UV irradiation is prevalent in photocatalysis and US is commonly used to disperse materials. Indeed, I found a detrimental effect of both types of irradiation during my HER experiments, which will be discussed in more detail in Chapter 5 in context with deactivation.

Chapter 6 concentrates on the deliberate introduction of defects into the TiO₂ crystal lattice using – amongst other methods – H₂ thermal treatments. In hydrogen thermal treatment, an oxygen vacancy is typically created under formation of water and Ti³⁺ (equation (1.12)).¹⁵²



Haerudin et al. published a combined volumetric and IR study in which the defect formation upon thermal treatment of TiO₂ in a H₂ flow was investigated.¹⁵² They distinguished two different temperature regimes: At T < 400°C, the number of oxygen vacancies increased with the temperature and duration of reduction and showed a dependence on the water vapor pressure. These defects were located

on the surface. At $T > 400\text{ }^{\circ}\text{C}$, bulk defects form due to a suggested saturation and defect formation is less dependent on water vapor pressure. Other synthesis routes applied in Chapter 6 for defect creation are less common and more specific to the case of black TiO_2 and will be discussed in a later section (1.3.5).

1.3.3. Characterization of oxygen vacancies in metal oxides

Defect concentrations are usually very dilute and thus defects are very difficult to observe and characterize. Tuller and Bishop summarized the most common techniques to characterize defects in materials giving a short description and application of the technique.

Surface-sensitive techniques such as atomic force microscopy (AFM),¹⁵³⁻¹⁵⁵ scanning tunneling microscopy or spectroscopy (STM/STS),^{119, 130, 155} or X-ray photoelectron spectroscopy¹⁵⁶⁻¹⁵⁸ can give valuable insight into the surface morphology, electronic structure, and qualitative defect concentration. However, clearly they are with their own limitations, e.g. needing ultra-high vacuum (UHV), that do not always render them suitable for applications. A common technique that is not listed by Tuller and Bishop is electron paramagnetic resonance (EPR), which measures the unpaired electron in Ti^{3+} .^{95, 159} Furthermore, photoacoustic spectroscopy is a powerful tool to characterize defects and distinguish between bulk and surface defects.^{145, 160}

Optical absorption spectroscopy (e.g. Raman¹⁶¹⁻¹⁶² or infrared spectroscopy¹⁶³⁻¹⁶⁴), X-ray diffraction¹⁶⁵⁻¹⁶⁶ or impedance spectroscopy¹²⁶⁻¹²⁷ can give insight into the electronic structure and crystal strain induced by defects. These are averaging techniques that are usually more available but may not give specific enough or only indirect evidence for the presence of defects.

The quantification of defects still remains challenging. Theoretical *ab initio* calculations are thus a critical tool to support investigations of defect structure, thermodynamics, charging and diffusion but are mostly only valid at 0K.^{112, 167} Volumetric adsorption studies have proven valid in determining absolute values of defect concentrations in materials.¹⁵² However, these are specific to H_2 treatment and not necessarily transferrable to other systems.

It becomes evident that more than one characterization method is needed to establish a solid picture of the defect chemistry of a material. Most characterization techniques are not suitable for in situ studies of defects, making them elusive species that are difficult to get a clear picture of.

Defect characterization has been a major challenge of this work. I used a wide array of techniques to characterize my photocatalysts, including: optical absorption, X-ray photoelectron spectroscopy, X-ray diffraction, and transmission electron microscopy (TEM). However, seemingly “common” techniques, such as Raman and TEM, showed defect formation that was induced during the measurement itself. The principles and challenges of these methods in characterizing defects in my materials are discussed in Chapter 3 and 4. Apparent contradicting results or the lack of direct evidence had to be counteracted with a comprehensive set of available characterization techniques complemented by phenomenological, experimental observations.

1.3.4. Influence of oxygen vacancies on the photocatalytic performance

Simply spoken, we obtain high performances for a photocatalytic reaction if we have a lot of reactants consuming a lot of charge carriers. Thus, increasing the amount of available charge carriers or reactants will result in higher photocatalytic performances. In the following, I will first discuss the influence of oxygen vacancies on the adsorption behavior and reactivity of adsorbants with respect to HER. The second part of this section will be about the influence of defects on absorption and recombination and its impact on photocatalytic performances.

1.3.4.1. Influence on reactants: Adsorption & reactivity of adsorbants

At the surface, reactants need to be available for the charge carriers. Defect sites are adsorption sites for reactants, including their intermediates. Thus, the adsorption behavior and defect chemistry of a material strongly influence the energetics of a reaction.

Studies of the adsorption behavior of water and methanol in the presence of oxygen vacancies have shown that both molecules preferably adsorb at oxygen vacancies on the metal oxide surface via a dissociative mechanism.¹⁶⁷⁻¹⁷¹ Guo et al. used isotope labeling combined with theoretical calculations to show that methanol adsorption and dissociation outcompetes that of water due to the facile desorption of methoxy species and the high reverse energy barrier for C-H recombination, which prevents an unfavorable back reaction as in the case of water.¹⁷¹ Han et al. further investigated the interactions of methanol in the presence of Pt using theoretical calculations. They found that in the presence of Pt clusters, the dissociation and adsorption of methanol is further enhanced due to the availability of more binding sites at the triple phase boundary (TPB).¹⁶⁸ Furthermore, Pt also favorably adsorbs at surface vacancies, so that a competition between Pt and

methanol is expected. Han et al. showed that Pt outperforms methanol when competing for adsorption sites.¹⁶⁸ No interference is thus expected during in situ photodeposition of Pt in the presence of methanol as performed in this work.

An example where oxygen vacancies not only influence the adsorption behavior but also reaction selectivities has been given by Wu and van de Krol for the photocatalytic reaction of NO over defective TiO₂.¹³⁸ The authors showed that stabilization of a large amount of oxygen vacancies in TiO₂ by Fe³⁺ led to a tetrahedral coordination of Ti. This changed the photooxidation of NO to nitrate species that occurs on octahedrally coordinated Ti to a photoreduction reaction of NO to N₂ and O₂ on the defective TiO₂.

1.3.4.2. *Influence on charge carriers*

Critical factors for charge carrier generation are the ability to absorb light by the photocatalyst and a successful separation of electron-hole pairs. Thus, finding strategies to 1) increase absorption or 2) decrease recombination are approaches to increase the amount of charge carriers available for surface reactions. Generally, it should be considered that oxygen vacancies can be introduced deliberately, but may also be generated during the reaction by combustion of organic compounds or by photoreduction processes (section 1.3.2).

A strategy to increase absorption is doping with acceptor and/or donor atoms. The introduced donor or acceptor states below the CB or above the VB result in a narrowing of the band gap or formation of localized interband gap states and thus an increased absorption. Doping is a common technique to introduce additional donor and/or acceptor states below the CB or above the VB. In the case of oxygen vacancies, the same principles apply and reduced TiO₂ is also sometimes called self-doped TiO₂. While increasing absorption, these defects are recombination sites for photogenerated electrons and holes. Thus, there is generally an optimum doping amount at which the beneficial effect of increased absorption outweighs the detrimental effect of a higher recombination rate.^{42, 172-174} Also, the overall impact of an increased absorption should be investigated. For example Tan et al. showed that the visible light response was not significantly improved upon introduction of oxygen vacancies.¹⁷⁵ The overall improvement of photocatalytic activity in the UV range of defective SrTiO₃ was attributed to reduced charge recombination. Also, Chen et al. showed that the activity of their defective black TiO₂ for only visible and IR light was only 1% of the overall activity, which suggest a minor impact of the absorption properties on the improved activity.¹²⁹

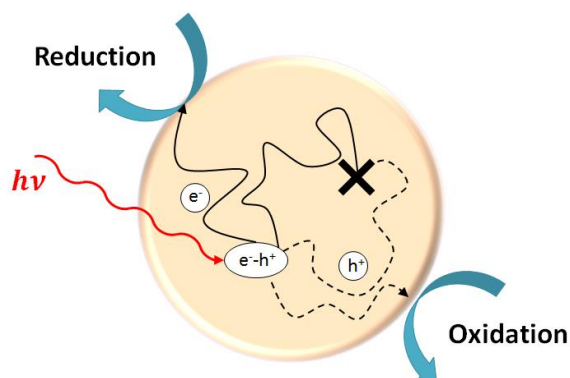


Figure 1-13. Schematic of the interaction of bulk and surface defects and with charge carriers. Bulk defects serve as recombination centers (cross), whereas surface defects enable an increased likelihood of surface reactions to occur.

The second aspect of introducing oxygen vacancies is that they serve as electron traps. Depending on the location and number this can be beneficial or detrimental to the photocatalytic activity. While surface defects can serve as adsorption site and directly transfer trapped charges, thus separating electron-hole pairs, bulk defects more often lead to recombination of charge carriers (Figure 1-13).²¹ Kong et al. used positron annihilation to determine the relative concentration ratio of bulk to surface defects.¹⁷⁶ They showed an increase in photocurrent and degradation of benzene under UV with an increasing ratio of surface to bulk defects. In agreement, Leshuk et al. showed a decreasing photocatalytic activity for degradation of the dye methylene blue when the number of bulk defects increased.¹⁷⁷ Yan et al. used different calcination temperatures (400-700 °C) to adjust the surface to bulk defect ratio.¹⁶⁰ However, in this case it is difficult to factor out the influence of the surface area changes. Since calcination also increases crystallite size, the authors added another factor including the surface area to intensity ratio in order to make values more comparable. The resulting volume specific factor, R , showed an increasing photoactivity in the photoreforming of methanol as well as photodegradation of phenethyl alcohol for an increasing amount of surface defects. However, Maeda et al. did not find a significant relationship between the surface defect density and activity for overall water splitting experiments and even suggested that any surface defect might be detrimental to the photocatalytic activity.⁶⁴

These reports suggest that for photocatalytic experiments besides overall water splitting a higher surface to bulk defect ratio results in a better photocatalytic performance. Still, qualitative and, even more, quantitative measurement of de-

fects are required for a clear understanding of the impact of defects on photocatalytic reactions.

1.3.4.3. *The optimum amount of oxygen vacancies*

Absolute numbers for Ti^{3+} or V_o defect density in correlation to the photocatalytic activity are very rarely reported. Most commonly, the relative ratio of surface to bulk Ti^{3+} was determined using either XPS¹⁷⁸ or positron annihilation^{176, 178}. Two (independent) publications found that a thermal treatment in H_2 atmosphere¹³², air and N_2 at 550°C ¹⁷⁹ resulted in an optimum activity for the photooxidation of organic compounds. In addition, Haerudin et al. used volumetric adsorption to determine the absolute oxygen vacancy density in P25 treated by a H_2 thermal treatment at different temperatures, which could be correlated to the mentioned publications.¹⁵² However, they only quantified the vacancies up to temperatures of 475°C , where they found a total of $10.0 \times 10^{18} \text{ g}^{-1}$ of oxygen vacancies corresponding to $18.2 \text{ vacancies nm}^{-2}$. Thus, there seems to be an optimum number of oxygen vacancies that is, however, yet unquantified and needs to be indirectly determined for each setup.

1.3.5. **Black TiO_2**

Black TiO_2 is a novel form of defective TiO_2 that showed high H_2 production rates under simulated solar light making it a highly desirable candidate for sustainable energy applications. The following sections will discuss the original work by Chen and Mao as well as the reported properties of black TiO_2 collected from literature that attempted to reproduce this material.

1.3.5.1. *First reports on black TiO_2*

In 2011, Chen et al. were the first to report on so-called black TiO_2 .¹²⁹ They showed that after TiO_2 was treated in a high pressure hydrogen atmosphere for several days at elevated temperatures (20 bar H_2 , 200°C , 5 days), it appeared black in color and showed very high photocatalytic activities under simulated solar light for both photocatalytic dye degradation and sacrificial water splitting. A unique core-shell morphology was identified as key parameter for the high activity consisting of a crystalline TiO_2 core (8 nm) surrounded by a thin ($\sim 1 \text{ nm}$) disordered outer layer (Figure 1-14). XPS analysis and theoretical calculations showed that the introduced disordered layer generates extended VB tail and mid-gap states that narrow the band gap to only 1.54 eV resulting in the strong visible light absorption and the unusual black color. However, photocatalytic activities under visible and IR light were found to account for only 1% of the overall activity for H_2 generation under simulated solar light, which indicates that the increased

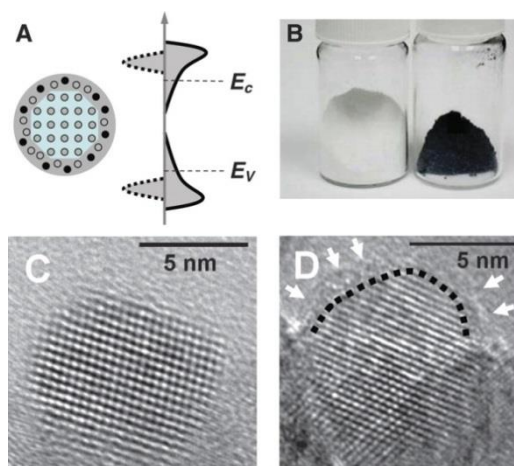


Figure 1-14. (A) Schematic illustration of proposed core-shell morphology of hydrogenated black TiO_2 with a corresponding diagram of the density of states in black TiO_2 compared to unmodified TiO_2 . (B) Images of TiO_2 nanocrystals before (white) and after hydrogenation (black). HRTEM images of TiO_2 nanocrystals C) before and D) after hydrogenation" from ref. 129. Reprinted with permission from AAAS.

absorption might not be the critical parameter for the high performance of black TiO_2 . From theoretical calculations, the key function of the introduced VB tail states is found in strong localization and trapping of photoexcited holes, which reduces their spatial overlap with delocalized electrons. Thereby, recombination of electron-hole pairs decreases and photocatalytic activity increases.^{129, 180} This effect is amplified as holes are drawn to the energetically higher VB tail states and, thus, their traps. Overall, according to Chen et al., the creation of VB tail states by introduction of disorder in the outer layers of a TiO_2 crystal leads to highly reduced recombination rates as well as an improved visible light absorption of black TiO_2 .

Further theoretical studies were conducted to investigate the process of disorder formation upon hydrogenation and the nature of the newly-formed VB states.¹⁸⁰ Calculated energies for the generation of the observed VB mid gap states only conformed with the experimental conditions after introduction of H_2 into their models, supporting a stabilizing effect of H that was suggested in the first report. Upon hydrogenation, the H_2 molecule assists in breaking the strong Ti-O bond (6.87 eV) by acting as a sort of "scissor" and forms new Ti-H and O-H bonds. The authors found that this process is energetically more favorable at the surface due to an increased number of degrees of freedom of surface atoms, while a disordered phase is unstable in bulk material leading to a stable crystalline core and under certain conditions favorable disordered outer layer. The additional VB states are formed by 1) a mixture of Ti 3d and H 1s orbitals with influence of the O 2p orbitals of neighboring oxygen atoms and 2) the distortion that is caused by

the incorporation of H atoms into the crystal lattice. Ti^{3+} centers which are usually introduced upon the creation of oxygen vacancies and which would lead to Ti 3d donor levels below the CBM (and the typical blue color for hydrogenated TiO_2) were not found in this material. This is in line with calculations that show that the CBM is quite insensitive to changes in the bonding environment or lattice disorder upon incorporation of H.¹⁸⁰ Also impurities like C were excluded by XPS analysis.¹⁸¹

1.3.5.2. *Overview of reported properties of black TiO_2*

Since the first report, many groups started investigating this novel material. This led to the development of almost as many different synthesis methods with sometimes seemingly contradictory characteristics between different black TiO_2 . Chen et al. published a comprehensive review on black nanomaterials in 2015, in which they systemized the large variety of synthesis routes into four different main approaches for synthesis (five, if H_2 plasma treatment is counted as independent from other hydrogenation treatments): 1) hydrogenation treatments with a large variety of conditions, including reduction with hydrogen plasma, 2) chemical reductions, 3) chemical oxidations, and 4) electrochemical reductions.¹⁸² While all of these materials have reported to show an improved photocatalytic activity, the properties (even starting with the color) and characterizations are often not congruent. In their review, Chen et al. listed 62 references and comprised a table with an overview of some key characteristics of black TiO_2 and the findings in literature.

Here, I further summarized this very comprehensive table and will cross-correlate certain properties in order to see whether certain trends can be observed between different properties (e.g. color and existence of a disordered shell):

1) Color

Very different color ranges are reported from yellow, greenish, brown to blue, gray, and black. Generally, materials with a disordered outer shell are black, sometimes reported as gray or dark brown. However, for some black materials the typical shell was not observed.

2) Disordered outer shell (32 not studied, 19 yes, 11 no)

32 references – almost half of the cited literature – did not study the presence of a disordered outer shell. 19 references found a disordered shell (synthesis approaches: high and ambient pressure hydrogenation, H_2 plasma, chemical reduction (aluminum, NaBH_4), electrochemical reduction),

whereas 13 references did not see a disordered shell (synthesis approaches: high and ambient pressure hydrogenation, chemical reduction (Zn and CaH_2) chemical oxidation). Treatment with H_2 under high pressure and for a longer time period, similar to the first report, did not always result in a disordered outer shell.¹⁸³⁻¹⁸⁵ While this was explained by a higher treatment temperature (450-500°C) in some cases¹⁸⁴⁻¹⁸⁵, Danon et al. also found an effect by the reactor material that was used and suggested that chromium doping by stainless steel reactors may cause a black color.¹⁸³ Additionally, treatments that did not involve H_2 , as for example chemical reduction with aluminum, also resulted in a disordered outer shell and black material which questions the argumentation that H_2 is needed for the introduction of disorder as well as the cause of the dark color. Still, a disordered shell is more often observed than not.

3) Presence of Ti^{3+} (8 not studied, 43 yes, 11 no)

A majority of reports confirms the presence of Ti^{3+} (43 yes, 11 no). Chen et al. did not see any Ti^{3+} in the original black TiO_2 that they reported on in 2011 and explain that the introduced disorder is rather due to H incorporation into the lattice than the creation of Ti^{3+} . Still, many reports that used a hydrogenation treatment confirmed the presence of Ti^{3+} as well as a disordered outer shell.

4) Presence of V_O (13 not studied, 47 yes, 2 no)

Only two reports denied the presence of oxygen vacancies. However, one of them is the original work by Chen et al. from 2011.

5) Presence and increase of surface Ti-OH (25 not studied, 23 yes, 6 no)

Again, a large number of references (25) did not investigate an increase in hydroxylation. When investigated, 23 references (including Chen et al.) showed the presence or increase of Ti-OH independent of the presence of a disordered outer shell. 6 reports did not see Ti-OH or even reported on a decrease of these groups.

6) Presence of Ti-H (43 not studied, 9 yes, 10 no)

The presence of hydride species – interesting for any hydrogenation approach – is not very well studied with a majority of reports not investigating these groups. Still, 10 references deny the presence of Ti-H, while 9 references confirm the presence of such species, resulting in no clear pic-

ture about Ti-H. Whenever Ti-H was observed and the existence of a shell was investigated, surface disorder was present.

7) Shift of VB (47 not studied, 7 yes, 8 no)

Although described as one of the key characteristics in the first report by Chen et al., a large majority of the cited references (47) did not study VB modifications. The remaining reports show no preference for whether a shift should be observed (7) or not (8). However, whenever a shift of the VB was observed, there was also a core-shell structure. The other way around, out of the 19 reports that show a core-shell morphology, only 7 studied the presence of VB modifications and 2 out of these did not see a shift in VB states. Wang et al. explained the absence of VB modifications although they observe a core-shell morphology for their aluminum-reduced TiO₂ due to reoxidation of the shell.¹⁸⁶ Additionally, Naldoni et al. argue that the reoxidized outer shell protects the crystalline core from further oxidation preventing any changes in the XPS detail spectra.¹⁸⁷ However, they still see a clear VB shift and tail states, which Wang et al. argued would vanish upon oxidation. As hydrogen has a stabilizing impact on the shell as suggested by Chen et al., it could be hypothesized that methods involving H₂ treatment result in shells that are more stable against reoxidation and thus VB modifications can be observed.^{129, 180} However, in another report using H₂ plasma for reduction, where the presence of Ti-H was identified by XPS and a shell was clearly observed in TEM images, no VB modification was seen.¹⁸⁸ The question why one shell should reoxidize and another should not, although shell thicknesses seem to be identical or at least very comparable and materials show a black color in all cases, is not yet answered.

8) Electrical conductivity (35 not studied, 27 increase)

Electrical conductivity was either not studied (35) or it increased (27), showing a clear trend for this characteristic.

In summary, different approaches to synthesize black TiO₂ resulted in materials with a large color variety (yellow, greenish, brown to blue, gray, and black). Materials with a disordered outer shell are mainly black, sometimes reported as gray or dark brown. However, a black color was also observed in the absence of disorder. The presence of a disordered outer shell – although a critical parameter in the first report on black TiO₂ – is surprisingly not very well investigated. Still, there is a

slight preference in literature for observing surface amorphization. A large majority of the materials show the presence of Ti^{3+} and oxygen vacancies rendering these species relatively unspecific. While less studied, Ti-OH is also more often seen than not. Hydride formation and VB modifications are – again surprisingly – not well investigated and reports do not show a preference for the presence or absence of either, which makes a possible cross-correlation between VB modifications, color and a disordered outer layer difficult from the presented literature. The electrical conductivity increased whenever it was studied.

Concluding from this summary, it is clear that there are a lot of open questions to what exactly is the key characteristic that improves photocatalytic activity and generates black TiO_2 and why there is such a wide spread of apparent characteristics. In my work, I picked two hydrogenation and two chemical reduction approaches in order to comparatively investigate the properties of the resulting materials and narrow down key characteristics for improved performance as well as answering the question to the origin of the sometimes differing reports. The results are discussed in Chapter 6 of this thesis.

2 Motivation

Climate change caused by anthropogenic GHG emissions is currently one of the most pressing issues of our civilization. The main source of GHG is the burning of fossil fuels, contributing to about 85% of overall emissions. Furthermore, the rapidly growing demand for energy due to an ever expanding global population is further opposed by the political and geographical limitations of conventional fuels, such as oil. One mitigation strategy to overcome these challenges is the replacement of fossil fuels with renewable energy sources. A clean alternative is H_2 as it only produces H_2O as by-product upon burning, while having the highest specific energy density of all known substances. However, H_2 is conventionally obtained from unsustainable industrial processes, i.e. steam reforming of methane.

Fundamental research is needed in order to obtain H_2 in a sustainable manner and making is competitive and applicable in our economy. Photocatalytic water splitting – resulting in O_2 and H_2 that, for example, could be used in a fuel cell – has recently attracted great interest as a possible way for sustainable H_2 production. However, the overall process is limited by a complex four-step oxidation reaction as well as undesired recombination events of charge carriers and the back reaction to water. To circumvent these limiting factors, sacrificial agents can be used to focus solely on the HER. A reference system for HER is TiO_2 loaded with Pt as co-catalyst in aqueous methanol solutions.

Defects have been shown to have a large impact on photocatalytic reactions in both a beneficial and detrimental way. During the course of my master thesis, I found that the reference system of Pt-loaded P25 showed unstable behavior at certain conditions. One main motivation of this thesis is therefore to further investigate and understand the origins of this “deactivation”. In particular, I aim at evaluating a possible dependence of deactivation on defects that are induced during and prior to the photocatalytic reaction. The results of these studies will be shown in Chapter 5.

A literature example for the beneficial impact of defects on HER is the novel material black TiO_2 . In the original report in 2011, the introduction of a disordered outer layer resulted in an improved charge separation and photocatalytic performance. However, many publications that aimed at reproducing this material have been published that show a likewise improved performance but differing charac-

teristics. Thus, the second main motivation of this thesis is to narrow down a key characteristic of black TiO_2 in order to understand beneficial features for future photocatalyst design. These results will be shown in Chapter 6.

3 Methods & Procedures

This chapter covers experimental procedures, including photocatalytic experiments and synthesis of reduced TiO_2 , as well as techniques applied for physico-chemical characterization of the photocatalysts, including a brief theoretical background about the working principles of each characterization method as well as a description about the instrumentation and conditions used in this work.

3.1. Photocatalytic experiments

This section focuses on the photocatalytic reactor setup for the performed HER reactions. First, an overview about the equipment is given including light source and detector details, followed by experimental procedures for the HER experiments, which I divided according to the two large results chapters on deactivation and reduced TiO_2 . Finally, quantum yield and its calculation are discussed. Generally, distilled water is used in all experiments.

A detailed discussion about the development and validation of our various reactor designs has been published by Dr. Alexey Cherevan in his PhD thesis.¹⁸⁹

3.1.1. Reactor system for photocatalytic HER

I use water-cooled, top-irradiated quartz glass reactors that are connected to an Ar flow (99.999% purity) as shown in Figure 3-1. General flow scheme for the photocatalytic setup in our laboratory. Ar serves as carrier gas and is regulated by a mass flow controller (MFC). Two Ar cycles can be chosen A for purging and B for the reaction.. Gaseous products are detected by an on-line gas analyzing unit with a condenser and CaCl_2 trap connected upstream in between the reactor and detector in order to condense any water vapor that might develop during the reaction. The reaction solution is stirred at a fixed speed for all experiments by magnetic stirring. A thermal mass flow controller (Q-Flow 140 Series, MCC Instruments) is used to control the Ar flow. Interconnected three-way valves allow to switch between Ar cycle A (only Ar lining and detector for purging and equilibration) and Ar cycle B (including the reactor).

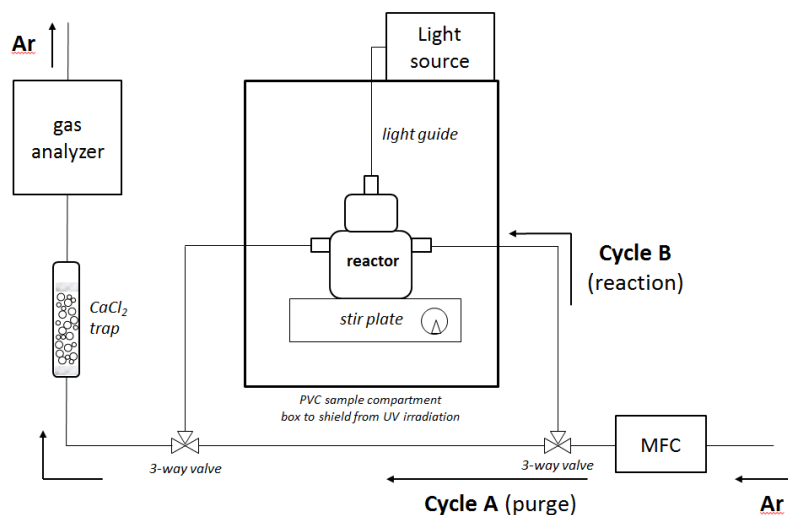


Figure 3-1. General flow scheme for the photocatalytic setup in our laboratory. Ar serves as carrier gas and is regulated by a mass flow controller (MFC). Two Ar cycles can be chosen A for purging and B for the reaction.

3.1.1.1. Reactors

Two different reactors which mainly differ in size from each other are used during this work (Figure 3-2). Reactor 1 is larger in volume (200 mL reaction solution) than reactor 2 (10 mL reaction solution). Due to the larger reaction volume, more photocatalyst is used in reactor 1 and equilibration times are longer, which adds to the total time of the experiment (~6 h) but results in sufficient amounts of recovered photocatalysts for further characterization. In contrast, only small amounts of photocatalyst are needed for reactor 2, which makes this the better choice for performance studies of materials that are low in amount, as is sometimes the case for the self-synthesized TiO_2 in Chapter 6. The condenser as shown in Figure 3-2 for the reactor type 1 has been proven unnecessary for the small reactor. Also, the gas inlet glass tube does not immerse into the reaction solution. Purging with Ar of the reaction solution is achieved by using a syringe needle prior to connecting the Ar tubing. Additionally, experiments are much shorter (~3 h) allowing for a higher data output.

For the deactivation chapter, mainly reactor 1 is used with the exception of studies on the pH and anion effect. Experiments of Chapter 6 were exclusively performed in reactor 2.

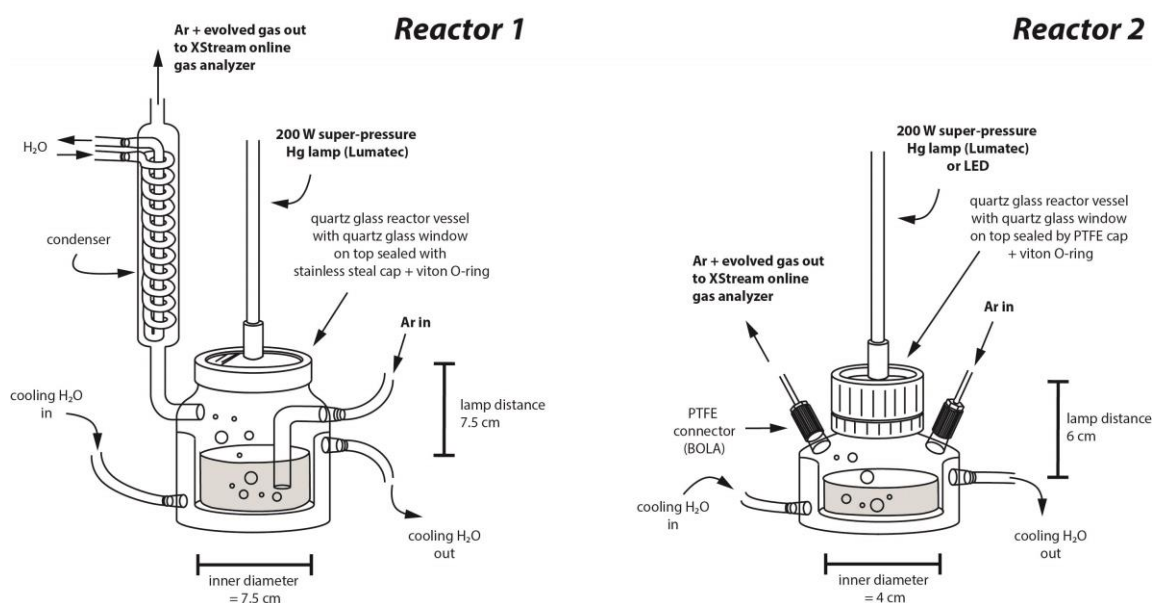


Figure 3-2. Schematic illustration of reactor type 1 and 2.

3.1.1.2. Gas detection

I use an on-line gas analyzer by Emerson (X-STREAM general purpose gas analyzer, Emerson) for identification of the gaseous products. The analyzer is equipped with three different detectors: a non-dispersive IR photometer, a thermal conductivity detector (TCD) and a paramagnetic detector for analysis of CO₂, H₂ and O₂, respectively. For experiments, involving CO detection an additional IR photometer is used. The identity of the gases was confirmed using an on-line micro-GC coupled to the outlet of the gas analyzer.

3.1.1.3. Light sources

A 200 W super-pressure Hg lamp ($\lambda = 240\text{-}500\text{ nm}$, $I = 30\text{ mW cm}^{-2}$, Superlite SUV DC-P deep UV, Lumatec) equipped with an optical fiber light guide is used unless noted otherwise. Figure 3-3 shows the emission spectrum of this light source. Two modes, i.e. visible light and UV light mode, can be chosen. The visible light mode includes wavelengths from 400-700 nm, whereas the UV light mode covers a wavelength range of 240 to 500 nm, which includes a small fraction of blue light. We observe a gradual decrease in intensity with ageing of the lamp, which leads to small variations in absolute activity values with time and, in particular, a slightly varying Pt loading dependence of deactivation in Chapter 5. The light intensity is measured using a thermo detector (S310C, Thorlabs) coupled to a power energy meter (PM100D, Thorlabs).

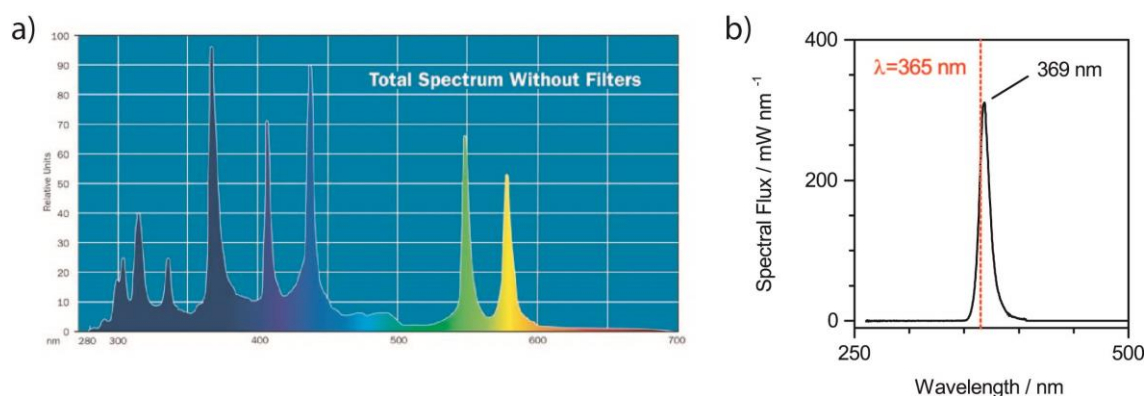


Figure 3-3. Emission spectra of a) 200 W super-pressure Hg lamp (Superlite SUV DC-P deep UV) provided by Lumatec and b) Solis™ High-Power LED ($\lambda = 365$ nm) provided by Thorlabs.

For recent investigations, such as the presented results on the deactivation behavior of pure phase polymorphs of TiO_2 (section 5.7), a single wavelength LED ($\lambda = 365$ nm, $P = 4.0$ W, Solis™ High-Power LED, Thorlabs) is used. The LED allows for easier handling and better control of the irradiated wavelength and will be used in future work for experiments both under UV (365 nm LED) and visible light (445 nm LED) irradiation.

3.1.2. Photocatalytic HER experiment

Two slightly different experimental procedures are applied for the two reactor types, which mainly differ in the time needed for equilibration and the mass and volume of photocatalyst and reaction solution.

3.1.2.1. Deactivation (Reactor 1)

TiO_2 (50 mg, Aeroxide® P-25 by Acros Organics) is suspended in a 50 vol.% aqueous methanol solution (200 mL, HPLC grade, VWR) in the quartz glass reaction vessel described above under continuous stirring. The suspension is deaerated with Ar for 15 min at a gas flow of 100 mL min^{-1} , after which H_2PtCl_6 is added as Pt precursor (section 3.1.2.3). The solution is purged for another 30 min at 100 mL min^{-1} , followed by equilibration in the dark at 30 mL min^{-1} for 1 h. The flow of 30 mL min^{-1} was kept constant during the remaining experiment. UV light was turned on for 2 h, after which the system was allowed to equilibrate again for about another 1.5 h until the baseline of the detection system was reached. Samples were dried until all solvent was evaporated (> 36 hrs) at 60°C for further analysis.

Chapter 3 – Methods & Procedures

3.1.2.1.1. *Ultrasound pretreatment*

For the US pretreatment, the TiO_2 suspension in aqueous methanol, was ultrasonicated for 1 min or 30 min in an ultrasonic bath (VWR Ultrasonic cleaner, 45 kHz, 80 W) before addition of the Pt precursor.

3.1.2.1.2. *Pure phase experiments*

Reactor type 1 with slightly lower volume and without condenser is used for pure phase experiments, with a photocatalyst dispersion of 0.2 g L^{-1} and a total reaction volume of 100 mL (50 vol.% methanol). The light source for these experiments is a single wavelength LED ($\lambda = 365 \text{ nm}$, section 3.1.1.3). Otherwise, the same experimental steps described above are followed. TiO_2 photocatalysts are: Aeroxide® P-25 by Acros Organics; anatase nanopowders (99.7%, $<25 \text{ nm}$ in size, Sigma-Aldrich); rutile nanopowders (99.5%, $<100 \text{ nm}$ in size, Sigma-Aldrich); and a physical mixture of anatase and rutile.

The mixture of anatase and rutile is prepared by suspending both commercial nanopowders in a weight ratio of 80:20 (anatase:rutile) in 100 mL distilled water. The suspension is stirred at 500 rpm for 3 h and dried in vacuum at 70°C until all solvent is evaporated.

3.1.2.1.3. *Role of pH and anions (reactor 2)*

Differences in pH or the concentration of anions may influence the stability of H_2 generation rates.

The general procedure follows that for reactor 2 (section 3.1.1). Only either HCl, NaCl or HI is added together with H_2PtCl_6 (0.4 wt.% Pt equivalent) to the reaction suspension. Two different experiments are conducted for each HCl, NaCl, and HI, in which the salt or acid amount is 1) equivalent to the difference in H^+ or Cl^- concentrations between 0.4 wt.% Pt-loaded P25 (deactivating) and 1.5 wt.% Pt-loaded P25 (stable), $\Delta[\text{Cl}^-]/\Delta\text{pH}$, or 2) a 10-fold excess of this concentration difference $10\times\Delta[\text{Cl}^-]/\Delta\text{pH}$. Then, the HER experiment is performed as described above.

Table 3-1 lists the amounts of acid or salt added during each experiment. Calculations of these amounts are as follows:

For a loading of 1.5 wt.% Pt on 10 mg TiO_2 , I use $187.6 \text{ }\mu\text{L}$ H_2PtCl_6 solution (4.1 mM), which equals $1.2 \times 10^{-6} \text{ mol}$ of free Cl^- ions if I assume full dissociation. For 0.4 wt.% loaded P25 on 10 mg TiO_2 , I use $50 \text{ }\mu\text{L}$ H_2PtCl_6 solution (4.1 mM), which corresponds to $4.6 \times 10^{-6} \text{ mol}$ of Cl^- . $\Delta[\text{Cl}^-]$ would thus be $3.4 \times 10^{-6} \text{ mol}$ Cl^- ions.

Experiment	H ₂ PtCl ₆ (4.1 mM) / μL		HCl (0.12 M) / μL		NaCl (0.10 M) / μL		HI (0.08 M) / μL
$\Delta[Cl^-]/\Delta pH$	50	+	28	or	34	or	45
$10x(\Delta[Cl^-]/\Delta pH)$	50	+	280	or	340	or	450

Table 3-1. Amounts of acid or salt added during each HER experiment for investigations of the influence of pH and anion.

For simplicity, I did not calculate the difference in H⁺ concentration and based the concentration difference on Cl⁻ ions for both $\Delta[Cl^-]$ and ΔpH . Although, this is quite a simplification, pH measurements show good agreement of the pH of solutions after addition of the various acids, while the pH for NaCl addition remains constant.

3.1.2.2. Reduced TiO₂ (Reactor 2)

The photocatalyst (10 mg, 4 mg in case of aluminum-reduced TiO₂) is suspended in a 50 vol.% aqueous methanol solution (10 mL, HPLC grade, VWR) in the quartz glass reaction vessel described above under continuous stirring. The suspension is deaerated with Ar for 10 min at a gas flow of 100 mL min⁻¹, after which H₂PtCl₆ is added as Pt precursor (section 3.1.2.3). A loading of 1 wt.% Pt was used for all experiments in Chapter 6.

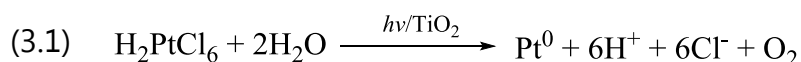
The solution is purged for another 20 min at 100 mL min⁻¹, followed by equilibration in the dark at 30 mL min⁻¹ for 50 min. The flow is kept constant at 30 mL min⁻¹ during the remaining experiment. UV light is turned on for 1 h, after which the system is allowed to equilibrate again for about another hour until the baseline of the detection system was reached. Then, visible light was turned on for 1 h. After equilibration and reaching baseline levels, the samples are filtrated and dried in air for further characterization.

3.1.2.3. Pt deposition

Different deposition methods have been reported with incipient wetness and photodeposition being the most common across literature (section 1.2.3). Using in situ photodeposition allows following the HER right from the point when all active ingredients (photocatalyst and co-catalyst) come together. Incipient wetness impregnation is used in some preliminary experiments for comparison to this technique regarding stability and activity (section 5.6).

3.1.2.3.1. *In situ photodeposition of Pt*

Pt is deposited by in situ photodeposition from aqueous H_2PtCl_6 solution (hexachloroplatinic acid, 8 wt.% in H_2O , Fluka) that has previously been reported to completely decompose to Pt^0 under UV irradiation following equation (3.1).^{70, 190}



Under the assumption of complete decomposition, amounts of a diluted stock solution of H_2PtCl_6 (4.1 mM) corresponding to the desired wt.% are added to the TiO_2 suspensions prior to UV illumination (e.g., 250 μL stock solution for 0.4 wt.% Pt on 50 mg TiO_2).

3.1.2.3.2. *Incipient wetness impregnation*

For incipient wetness impregnation, TiO_2 (P25, 200 mg) is suspended in distilled water (15 mL). 1.0 mL or 1.9 mL of H_2PtCl_6 (4.1 mM, diluted from 8 wt.% in H_2O stock solution provided by Fluka) is added to the TiO_2 suspension corresponding to a Pt loading of 0.4 or 0.75 wt.%, respectively. The suspension is stirred for 24 h and dried at 100 °C for 2 h. The resulting yellow powder is calcined in O_2 at 350 °C for 3 h, followed by a reduction in H_2 gas at 350 °C for 1 h. The sample was cooled down in H_2 atmosphere, purged with He and recovered from the furnace.

3.1.3. Quantum yield calculations

The quantum yield (QY) indicates how much of the potential energy available by incident light is actually used in a reaction, i.e. the number of reacted electrons per incident photons.

$$(3.2) \quad QY = \frac{\# \text{ of reacted electrons}}{\# \text{ of incident photons}}$$

For the HER, the number of reacted electrons can be computed from the amount of H_2 that is generated (equation (1.8)). For this, the rate of H_2 evolution, r_{H_2} (mol h^{-1}), is multiplied by a factor of 2, as two moles of electrons react to produce one H_2 molecule which gives us the rate of how many moles of electrons are produced per hour, r_{e^-} (mol h^{-1}) (equation (3.5)).

$$(3.3) \quad r_{e^-} = 2 r_{\text{H}_2}$$

As we are able to quantify the amount of electrons produced from the reaction rates, we now need to determine the amount of photons that are incident on the system. This can be quantified in terms of the photon flux, q_p (in photons h^{-1}), which is defined as the power, P (in J h^{-1}), divided by energy of a photon, E (in J photon^{-1}) (equation (3.4)). The total incident photon flux of the UV mode is the sum of the fluxes of the different light regions (UVC, UVB, UVA, blue light). Calculated photon fluxes, q_p , for each emission region of the 200 W super-pressure Hg lamp are listed in Table 3-2. Note, that these calculations are typically done with a single-wavelength light source. However, we use the average emission of the entire source.

$$(3.4) \quad q_p = P/E$$

Theoretical power values at each emission region are provided by Lumatec and are listed in Table 3-2. The average energy of a photon, E , of each emission region is calculated from Planck's relation (equation (3.5)), where h is Planck's constant ($6.626 \times 10^{-34} \text{ J s}$), and ν is the frequency of the photon which equals the speed of light, c ($2.998 \times 10^8 \text{ m s}^{-1}$), divided by its wavelength, λ . For λ , I use the average wavelength of a photon at each emission region.

$$(3.5) \quad E = h\nu = \frac{hc}{\lambda}$$

q_p has to be adjusted for the time-dependent decrease in light intensity of the Hg lamp by an ageing factor, a . This ageing factor is the ratio of the measured light power, P_{real} (in W), to the theoretical power, P_o (3.9 W), and assumes a homogeneous decrease in intensity across the emission spectrum (equation (3.6)). For example, for a measured light intensity of 1.2 W, the ageing factor is 0.31.

$$(3.6) \quad a = \frac{P_{real}}{P_o}$$

We can now put together the rate of the reacted electrons and the rate of incident photons (note, that the time-dependence cancels out in this step) to obtain an overall equation for the QY. r_{e^-} is multiplied by the Avogadro constant, N_A ($6.022 \times 10^{23} \text{ mol}^{-1}$) to convert from the reacted moles to the total number of electrons that react per hour. This gives an overall reaction equation for the QY of:

$$(3.7) \quad QY = \frac{r_{e^-} N_A}{a q_p}$$

Chapter 3 – Methods & Procedures

As the Hg lamp UV mode extends into the blue light, we can either consider the QY for wavelengths that can theoretically be absorbed by the material (*e.g.* $\lambda < 400$ nm) or all incident photons ($\lambda = 240$ -500 nm) depending on which information one wants to obtain. Both QY are considered and labeled accordingly with $QY_{\lambda=240-500\text{nm}}$ and $QY_{\lambda<400\text{nm}}$.

Note, that the calculated values in any case represent only apparent QY and generally underestimate the theoretically possible QY. This is caused by a general overestimation of the amount of incident photons due to scattering effects in the suspension that are difficult to quantify and that result in a lower number of photons reaching the photocatalyst.^{25, 27}

Range	λ / nm	P / J s ⁻¹	λ_{ave} / nm	E / J	q_p / photons h ⁻¹
<i>UVC</i>	240-280	0.100	260	7.64×10^{-19}	4.71×10^{20}
<i>UVB</i>	280-320	0.800	300	6.62×10^{-19}	4.35×10^{21}
<i>UVA</i>	320-400	1.300	360	5.52×10^{-19}	8.48×10^{21}
<i>blue light</i>	400-500	1.700	450	4.41×10^{-19}	1.39×10^{22}
<i>UV + blue light</i>	240-500	3.900			2.72×10^{22}
<i>UV</i>	240-400	2.200			1.33×10^{22}

Table 3-2. Calculated photon fluxes, q_p , for each emission region of the 200 W super-pressure Hg lamp (Superlite SUV DC-P deep UV). Theoretical power values at each emission region are provided by Lumatec. The average energy of a photon, E , of each emission region is calculated from Planck's relation,

3.2. Reduction of TiO₂

In the following section, four different synthesis procedures based on literature for the fabrication of black TiO₂ (section 1.3.5) are described, including: the original approach using high pressures of H₂ and medium temperatures (200 °C)¹²⁹, two chemical reduction approaches using aluminum¹⁸⁶ and NaBH₄¹⁹¹, as well as another H₂ treatment based on cooling rates after synthesis¹⁸⁷. In the case of the aluminum reduction, some theoretical background is given in more detail for better understanding of the concept behind synthesis. If necessary, differing conditions between my work and the literature references are discussed. Syntheses of precursors are described in separate subsections of the respective approach.

3.2.1. High pressure reduction

The following procedure is based on the work of Chen et al.:¹²⁹ Self-made anatase nanocrystals (see below), commercial anatase nanopowder (99.7%, <25 nm in

size, Sigma-Aldrich), rutile (99.5%, <100 nm in size, Sigma-Aldrich) and P25 (Aeroxide, Sigma) are used as starting materials. Between 80 and 100 mg of TiO_2 are placed in a PTFE-sealed, stainless steel high-pressure reactor (model: BR-700 by Berghof Products + Instruments GmbH, max. pressure: 200 bar, max. T: 300 °C; built: 2010, serial #: 115) with an inner PTFE lining of ~800 mL in volume. For reduction, the reactor is first purged with N_2 of at least 10 bar to ensure that there is no air in the system, then filled with 40 bar of H_2 gas and heated at 200 °C for 5 days. Some pressure is usually lost during the course of the synthesis reaching a final value of ~30 bar. This is still above the reaction pressure in the reference paper and should suffice for the reduction of TiO_2 . After the H_2 treatment and cooling down of the reactor, H_2 is released into the venting system and the reactor is purged with N_2 again to ensure the absence of H_2 before retrieving the samples.

3.2.1.1. *Anatase nanocrystals*

Anatase nanocrystals are prepared from titanium tetraisopropoxide (TTIP, $\geq 97.0\%$, Sigma-Aldrich) as precursor using Pluronic[®] F127 (Sigma-Aldrich) as organic template according to the experimental procedure by Chen et al.¹²⁹ For this, TTIP, F127, HCl (37%, VWR), distilled water and absolute ethanol (ACS grade, Chem-Lab NV) are mixed in a molar ratio of 1:0.005:0.5:15:40. More precisely, F127 is first mixed with absolute ethanol in a small beaker followed by addition of TTIP, HCl and H_2O in this order. The solution turns from milky to almost clear, when HCl is added. The solution is then stirred for 24 h at 40 °C, while being covered with a small watchglass to avoid evaporation of the solvent during which TiO_2 precipitates as white solid. The suspension is transferred to a ceramic boat and heated for 24 h at 110 °C resulting in a light-yellow powder. In a final step, the powder is heated to 500 °C at a ramp of 0.3 °C min^{-1} and held at that temperature for 6 h to remove the organic template and crystallize the TiO_2 powder.

3.2.2. **Aluminum reduction**

The synthesis of the aluminum-reduced samples is based on a previous report by Wang et al.¹⁸⁶: P25 (Aeroxide[®] P-25, Acros Organics, BET 55 $\text{m}^2 \text{g}^{-1}$) and Al powder (laborladen.de, <55 μm , BET 0.3 $\text{m}^2 \text{g}^{-1}$) are placed in ceramic boats in a glass tube (3 cm i.d.) and evacuated to a base pressure of $\sim 10^{-4}$ bar (Figure 3-4). Al powder is heated to 800 °C (10 °C min^{-1}). P25 is heated to 500 °C (5 °C min^{-1}). Reduction times vary between 6, 12, and 24 h. The line to the vacuum pump is open for about 60 min to allow possibly adsorbed species to desorb from the glass tube, after which it is closed to allow the pressure to equilibrate. The ratio of Al to P25 is varied by two orders of magnitude in order to increase the degree of re-

Chapter 3 – Methods & Procedures

duction and are classified by their color after treatment for further characterization as listed in **Table 3-3**.

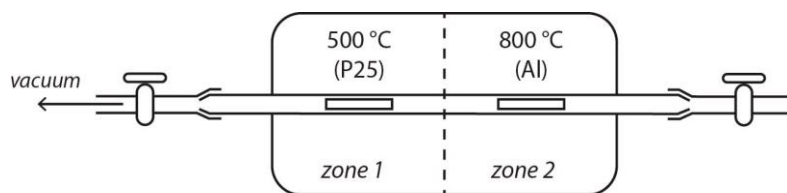


Figure 3-4. Schematic of two-zone furnace for aluminum reduction of TiO_2 .

color	Al : P25	reduction t / h
white (P25)	-	-
grey	21	6
light blue	25	6
blue	539	6
dark blue	605	12
dark blue	521	24

Table 3-3. Color variation of aluminum-reduced P25 with corresponding Al:P25 ration and duration of reduction treatment.

Note, that the original paper used a base pressure of maximum 10^{-6} bar. Unfortunately, this has not been realized in my setup during the course of this work. While the influence of the vacuum quality is not clear and has not been discussed in the reference, my results show that reduction is possible at these pressures.

Note, that the heating rate, type of aluminum, ratio of Al to TiO_2 , were all not specified in the original paper. The authors have been contacted, but did not reply up to this point in time.

3.2.3. NaBH_4 reduction

The following reduction of TiO_2 by dry mixing with NaBH_4 is based on the publication by Tan et al.¹⁹¹ P25 and NaBH_4 are mixed in a ratio of 1 : 0.375, respectively, (e.g. 200 mg P25 and 75 mg NaBH_4) and ground in an agate mortar for ~15 minutes, after which no further improvement of mixing is observable. The white to greyish powder is transferred to a ceramic boat and placed into a tube furnace. The oven is first flushed with Ar for 60 min, followed by heating (10 °C min^{-1}) to 300, 350 or 400 °C and dwelling at that temperature for 1 h. Afterwards samples

are washed with thorough amounts of ethanol ($3 \times \sim 100$ mL) and warm water (75°C , $3 \times \sim 150$ mL), followed by filtration and drying in air.

Note, that XPS surveys showed remaining salt in the samples after washing, which was removed by two additional washes. For each additional washing, NaBH_4 -treated TiO_2 was stirred in warm water (~ 500 mL for 50 mg sample) for 1 h, followed by filtration and drying in air.

3.2.4. H_2 reduction followed by rapid cooling

The following procedure is based on the work by Naldoni et al. in which rapid cooling after H_2 treatment of an amorphous precursor froze the metastable, disordered outer shell and resulted in black TiO_2 .¹⁸⁷

3.2.4.1. H_2 treatment

The sol-gel derived, mainly amorphous TiO_2 powders are first oxidized in O_2 for 1 h at 200°C in order to obtain fully stoichiometric TiO_2 , followed by reduction at 500°C in H_2 for 2 h. Afterwards, the clamp oven is opened immediately to allow for the fastest possible cooling in H_2 . As reference, He gas is used instead of H_2 . Samples treated in H_2 atmosphere were dark grey after hydrogenation with a slight lightening to a grey color during cooling, while the reference treated in He atmosphere remained white throughout the experiment. The cooling rate followed an expected exponential decay with an approximate initial rate of $30^\circ\text{C min}^{-1}$. After cooling down, the reaction tube is purged with inert gas before samples are retrieved.

Note, that the cooling rate in this setup compares relatively well with the reported $50^\circ\text{C min}^{-1}$.¹⁸⁷ There is no detailed information about how the reported rate is achieved and whether it is a controlled and linear drop until room temperature is established. Realizing a fast cooling rate is definitely a key factor for this synthesis approach and would need further equipment than the one that has been available during this work.

3.2.4.2. Amorphous precursor from sol-gel route

Two different routes to synthesize an amorphous precursor are performed. However, results in section 6.4 are based on the TiCl_4 precursor which avoids contamination by carbon residues, while being partially rutile.

3.2.4.2.1. Titanium(IV) butoxide (TBOT)-derived

TBOT (4g, 97%, abcr) is stirred in 10 mL of absolute ethanol in atmosphere until hydrolysis is completed. While characterization shows no crystalline phases in

these materials, they turn black upon heat treatment (no H₂) indicating the presence of carbon residues and rendering these precursors inadequate for synthesis of black TiO₂.

3.2.4.2.2. *TiCl₄-derived*

Titanium tetrachloride (TiCl₄, 99%, Merck) was chosen as sol-gel precursor to avoid carbon residues after synthesis that can also cause a darkening of the materials after calcination. The synthesis is based on the work of Addamo et al.¹⁹² TiCl₄ is added dropwise in a volume ratio of 1:10 into distilled water at 0 °C under Ar atmosphere during which vigorous HCl evolution is observed. The suspension is boiled for about 2 h and washed with copious amounts of water. The obtained white powder was dried at 60°C in air (BET surface area: 125.6 ± 8.3 m² g⁻¹; some rutile phase present).

3.3. Characterization

This section will give theoretical insight into the different methods applied for characterization of the photocatalysts. Electron microscopy is used for morphological and structural analysis at the nanoscale. In particular, transmission electron microscopy is a critical tool for the characterization of black TiO₂ and important measuring parameters are discussed in an extra section on damage induced by the electron beam. A section on absorption spectroscopy covers diffuse reflectance, infrared and Raman spectroscopy providing optical parameters and further structural insight, i.e. strain effects by defect formation and fingerprinting. Furthermore, infrared is the tool of choice for the mechanistic studies conducted in Chapter 5 and different setups are discussed. Surface-sensitive techniques, such as adsorption studies with N₂ and CO as well as X-ray photoelectron spectroscopy are discussed towards the end of the section. X-ray diffraction complements these techniques with macroscale structural information, such as phase composition.

3.3.1. Electron microscopy

Electron microscopy is based on the interaction of electrons with matter to magnify objects at resolutions within the nanoscale range. Electron microscopes were first developed to overcome the resolution limitations of optical microscopes (200 nm) whose resolution is – according to Abbe's Law – limited by the wavelength of light. This resolution limit is overcome by using a high-energy electron

beam in electron microscopy as electrons show wave-like behavior with wavelengths much shorter than visible light as first postulated by de Broglie.¹⁹³

The incident high-voltage electron beam triggers various processes when interacting with an object as shown in Figure 3-5. The variety of processes shows the different detection possibilities and the respective variety of information one can draw depending on which detection method is chosen. In general, any electron microscope consists of:

- an electron source (e.g. W filament, LaB₆ cathode, field-emission gun) coupled to an electron accelerator (SEM: 0.1-30 kV, TEM: up to 400 kV)
- an electromagnetic lens system: that is used to focus and control the electron beam by adjustment of their electric current
- and the detection system (e.g. CCD camera)

Electron microscopy techniques require ultra-high vacuum (UHV) in order to avoid collision of electrons with other gas molecules.¹⁹³

The two main methods of microscopy used in general are: transmission electron microscopy (TEM), in which electrons that transmit through a thin sample are imaged, and scanning electron microscopy (SEM), which detects secondary or backscattered electrons that are ejected while scanning over the surface of a sample. The resolution of TEM (~0.1 nm) is generally one order of magnitude higher than for SEM (~1-10 nm).¹⁹³⁻¹⁹⁴

In this work, mainly TEM has been used for the nanoscale investigations of (Pt-loaded) TiO₂ and reduced TiO₂ to observe morphological and structural changes in the individual crystals. SEM has been used for characterization of the spin-coated Si crystals for in situ ATR-FTIR experiments.

3.3.1.1. *Transmission electron microscopy (TEM)*

TEM analysis allows for a comprehensive microstructural characterization of materials. Depending on the mode of operation, either a direct image of the sample or its diffraction pattern can be obtained. For conventional imaging, transmitted electrons that do not get scattered can pass through the sample and are detected by either an imaging device (e.g. a fluorescent screen) or a sensor (e.g. a charge-coupled device (CCD)). Imaging can further be subdivided into bright-field (BF) and dark-field (DF) imaging. BFTEM can be considered the standard mode of imaging and considers information of the whole electron beam, whereas in DFTEM

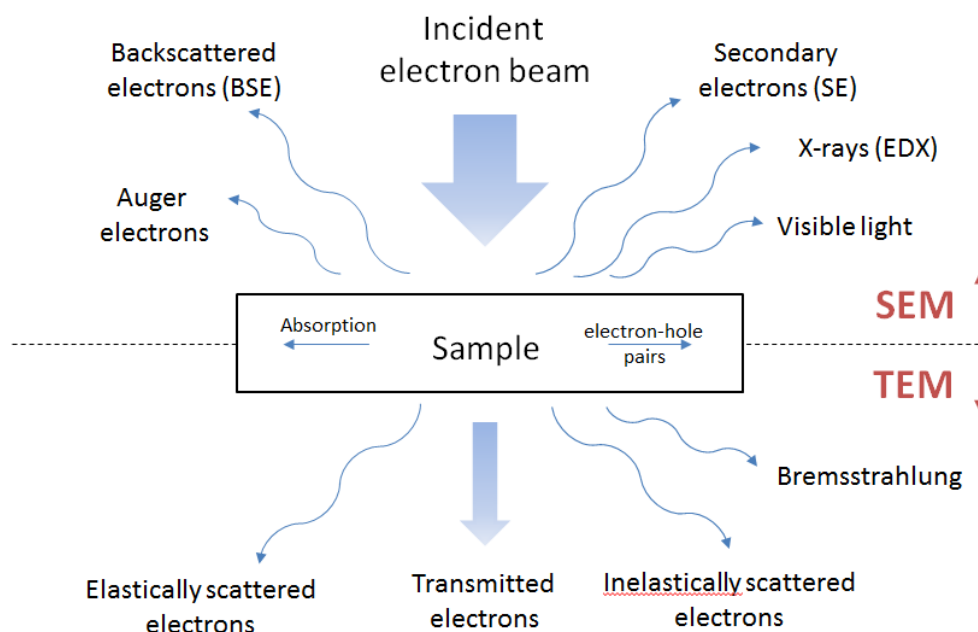


Figure 3-5. Interaction of a high-energy electron beam with matter and corresponding signals that can be detected by scanning and transmission electron microscopy. Signal directions are relative and indicate the strongest intensity or position of detection.¹⁹⁴

only selected diffracted beams are imaged, which can give information about distribution of a certain crystallite or facet in a sample.

Image contrast in TEM is due to mass-thickness differences, i.e. the atomic number of an element, as well as different diffraction or absorption of the electron beam. For diffraction mode, diffracted electrons are detected and used for crystallographic analysis. While electron diffraction (ED) patterns are less quantitative than bulk X-ray techniques, such as XRD (section 3.3.4), the use of electrons allows for crystallographic analysis on a more microstructural level. Furthermore, analytical TEM, such as energy-dispersive x-ray spectrometry (EDX) or electron energy-loss spectrometry (EELS), can give even chemical information about the elemental composition and bonding environment of atoms in a sample.¹⁹⁴

While TEM is a powerful tool, there are still some limitations for its use, for example: samples have to be electron transparent, which means less than 100 nm in thickness (dependent on the material), and need to be able to withstand vacuum conditions (difficult for biological samples). Furthermore, the maximum theoretically possible resolution for TEM imaging as expected from the wavelength of the electron is limited by chromatic and mainly spherical aberration.¹⁹⁴

In this work, TEM images were obtained on a Zeiss Libra FE 200 and a FEI Tecnai F20 both operated at an acceleration voltage 200 kV. For sample preparation, powders were first dispersed in ethanol and, subsequently, dropping the suspension onto copper grids coated with a holey carbon film (200 mesh, Science Services GmbH, München). As I observed effects by ultrasonication in the photocatalytic experiments, I avoided additional ultrasonication during dispersion of the samples.

3.3.1.2. *Scanning electron microscopy (SEM)*

In contrast to imaging a single spot by TEM, a raster scan of a focused electron beam across the sample is performed during SEM resulting in a 3D image. Topographical and morphological information is obtained by detection of secondary electrons (inelastically scattered) and backscattered electrons (elastically scattered), whereas chemical information is collected by detecting ejected Auger electrons and X-rays which allows for EDX analysis. Similar to TEM, image contrast depends on the mass of the elements which allows differentiating between different materials. For measurements, samples generally need to be conductive as well as able to withstand the vacuum atmosphere.

In this work, a FEI Quanta 250 FEG SEM operated at an acceleration voltage between 3 and 10 kV was used for characterization of the spin-coated TiO₂ films on Si crystals for in situ ATR-FTIR experiments (section 3.3.2.2.3). For sample preparation, powders were placed to adhesive carbon tape fixed on an aluminum sample holder.

3.3.1.2.1. *SEM-EDX*

When an electron is kicked out an inner shell of an atom, this vacant position can be filled by an electron of a higher orbital under release of energy in form of X-ray radiation. This X-ray radiation is element-specific and can be detected by an EDX detector giving insight into the chemical composition of a sample. SEM-EDX analysis has been used for identification of sodium impurities during reduction experiments (section 6.2).

3.3.2. **Optical spectroscopy**

The following sections will cover three different methods of optical spectroscopy: diffuse reflectance, Raman and infrared spectroscopy.

In optical spectroscopy, energy (e.g. in form of photons from a light source) is absorbed by the sample under investigation leading to deviations between the initial and the detected energy. Different transitions are excited depending on the

Chapter 3 – Methods & Procedures

energy, e.g. light source, used for analysis. Figure 3-6 shows the different energy transitions that are possible in a molecule between different discrete states, i.e. rotational, vibrational and electronic transitions. As known from quantum mechanics, rotational energy levels are the lowest in their energy, followed by the vibrational levels, while electronic transitions require the most energy.¹⁹⁵

Diffuse reflectance spectroscopy investigates absorption in a material through electronic transitions and gives information about the optical band gaps of semiconductor and general light absorption behavior of a material.¹⁹⁶

In Raman and infrared spectroscopy rotational-vibrational transitions are studied and are widely used for structural analysis (e.g. fingerprinting) and quantification of materials. As the mechanistics behind initiating transitions differ between these two methods, they are often used complementary. While in infrared spectroscopy the absorption of infrared light by vibrational transitions is investigated, Raman spectroscopy uses intense laser beams in the UV-visible light region.

In the following the different methods of absorption spectroscopy will be discussed in further detail with an emphasis on IR spectroscopy.

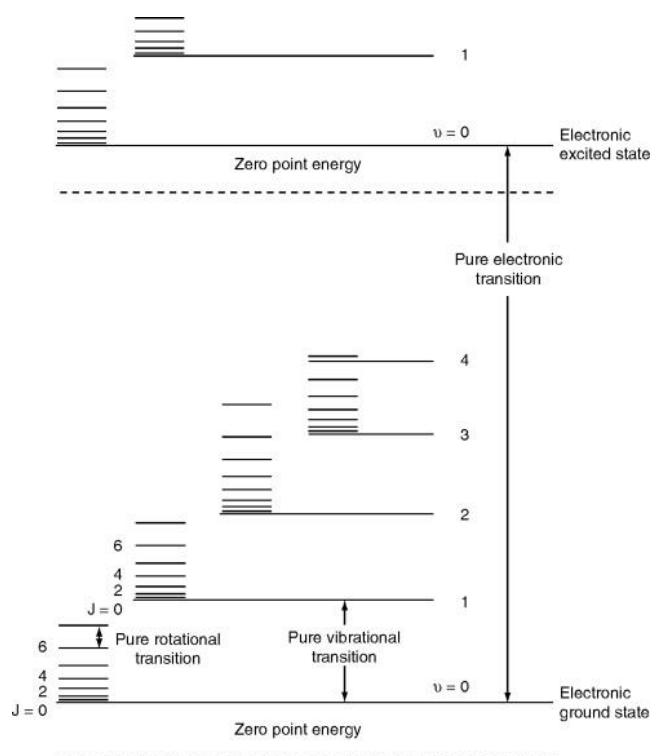


Figure 3-6. Schematic energy levels of a diatomic molecule. Reprinted from ref. 195, Copyright 2003, with permission from Elsevier .

3.3.2.1. Diffuse reflectance spectroscopy (DRS)

DRS is a type of optical spectroscopy in which light absorption by electronic transitions is measured. For liquid materials, absorption is often measured indirectly by the transmission of the incident beam through a sample. For solid materials, the absorption can be measured by detecting how much light is reflected by a surface. Both techniques are dispersive, meaning that they use a monochromator to measure transmission/reflectance for each wavelength by grating.¹⁹⁶

Diffuse reflectance – in contrast to regular or specular reflectance on for example mirrors – occurs on dull and mat surface with powder-like texture. Per definition, the angle of incidence light does not equal the angle of reflection for diffuse reflectance due to refraction, diffraction, and reflection processes (Figure 3-7). Thus, for samples that do not allow for transmission mode or do not have a polished surface (e.g. powders), diffuse reflectance measurements are used to obtain optical absorption data.¹⁹⁶

These measurements are commonly performed using an integrating sphere that has a fully reflective inner surface and a pinhole through which light enters and is diffusely reflected back to the walls off the sphere by the sample. After multiple reflections, the reflected beams reach the detector (Figure 3-8).¹⁹⁶⁻¹⁹⁷

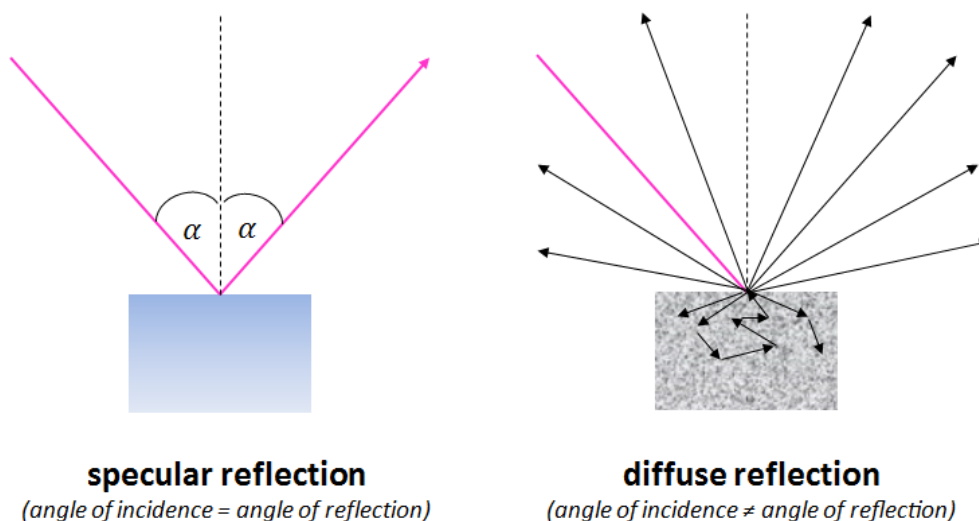


Figure 3-7. Specular versus diffuse reflection. In specular reflection the angle of incidence equals the angle of reflection. In diffuse reflection additional refraction and diffraction processes occur.

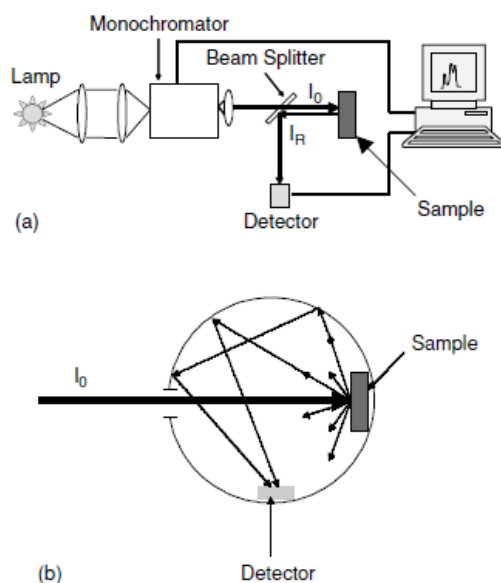


Figure 3-8. Experimental arrangement for measuring direct reflectivity spectra (a) and scheme of a typical integrating sphere used for diffuse reflectance measurements (b). Reprinted with permission from ref. 197. Copyright 2005 John Wiley and Sons.

In this work, diffuse reflectance of powders was measured on a Jasco V-670 UV-vis photospectrometer that is equipped with an Ulbricht-sphere inside a diffuse reflectance unit. The sample was positioned in a micro sample holder ($\varnothing = 3\text{mm}$).

3.3.2.1.1. Kubelka-Munk Theory & Tauc plots

The Kubelka-Munk theory correlates absorption and scattering during diffuse reflectance measurements by the following equation:¹⁹⁸

$$(3.8) \quad F(R_{\infty}) = \frac{(1 - R_{\infty})^2}{2R_{\infty}} = \frac{K}{S}$$

where R_{∞} is the reflectance of a sample of infinite thickness (or in practical applications: so that increasing the thickness does not influence the measured signal), K is the absorption coefficient, S is the scattering coefficient, and $F(R_{\infty})$ is the remission function. The Kubelka-Munk equation is now widely used to describe absorption for powders and can be further used in determination of the optical band gap of semiconductors through establishing a Tauc plot. In a Tauc plot – first developed by Jan Tauc in 1968 – a modified remission function, $(F(R_{\infty}) h\nu)^{1/r}$, is plotted against the photon energy, $h\nu$.¹⁹⁹ The exponent, $1/r$, depends on the nature of the electronic transition, i.e. direct or indirect and allowed or forbidden. The energy of the band gap can then be determined by the

intersection of the extrapolated linear fit of the absorption onset with the x-axis. Here, an exponent of $\frac{1}{2}$ is chosen for both anatase and rutile, as they have been shown to both have a direct band gap and values for the band gap as determined by the Tauc plots agree with literature (section 1.2.4).

3.3.2.2. *Infrared spectroscopy*

Infrared (IR) spectroscopy is a type of rotational-vibrational spectroscopy that is used in the qualitative and quantitative analysis of molecules and functional groups. Absorption of IR radiation induces transitions in the rotational and vibrational energy levels, which are characteristic for certain functional groups. The energy of the IR radiation determines which state is excited, i.e. the far IR region (FIR; $\tilde{\nu} = 400\text{-}10\text{ cm}^{-1}$; $\lambda = 25\text{-}1000\text{ }\mu\text{m}$) mainly induces rotation in molecules, while the mid IR region (MIR; $\tilde{\nu} = 4000\text{-}400\text{ cm}^{-1}$; $\lambda = 2.5\text{-}25\text{ }\mu\text{m}$) and near IR region (NIR; $\tilde{\nu} = 12500\text{-}4000\text{ cm}^{-1}$; $\lambda = 0.8\text{-}2.5\text{ }\mu\text{m}$) results in vibrations of a molecular bond.

Classical IR spectroscopy deals with the MIR region and vibrational transitions within a molecule. Requirements for the allowed transitions between the different energy states are that a) the selection rule, $\Delta v_i = \pm 1$, is fulfilled and b) the dipole moment μ changes during the vibration (thus, symmetric molecules such as O_2 , N_2 do not absorb IR radiation and do not appear in an IR spectrum).

3.3.2.2.1. *Fourier transform infrared (FTIR) spectroscopy*

FTIR spectroscopy is the conventional method for IR measurements nowadays.

In contrast to dispersive techniques in which light absorption of a sample at each wavelength is measured separately using a monochromatic light source, in FTIR a polychromatic spectrum is systematically modified and characteristic absorption by the sample is calculated from a data set by a common algorithm, the Fourier transform.

The modifications of the incident light are controlled by an interferometer. A common example is the Michelson interferometer depicted in Figure 3-9: here, incoming light is split into two beams of ideally 50% intensity by a beam splitter (e.g. KBr). The two split beams are directed towards two mirrors; one is fixed in position, the other can be moved. The two beams are reflected back to the beam splitter and recombine, directed towards the sample. If both mirrors are fixed at exactly the same parameters away from the beam splitter, we should obtain (in an ideal case) the same beam as first emitted from the light source. If, however, the position of the movable mirror is changed, so will the incoming beam reflected

Chapter 3 – Methods & Procedures

back from the mirror. The two beams (also called “arms”) – from the fixed and movable mirror – will interfere either constructively (if in phase) or destructively (if out of phase) with each other, thus resulting in modulations of the original beam and different absorption spectra. The obtained data is recorded by a computer and transformed using the Fourier transform, giving the known absorption or transmission spectra as output.

Due to a better signal-to-noise ratio, higher optical throughput and short analysis times, FTIR methods are now a standard analysis tool in any lab and have replaced dispersive techniques.^{197, 200-201}

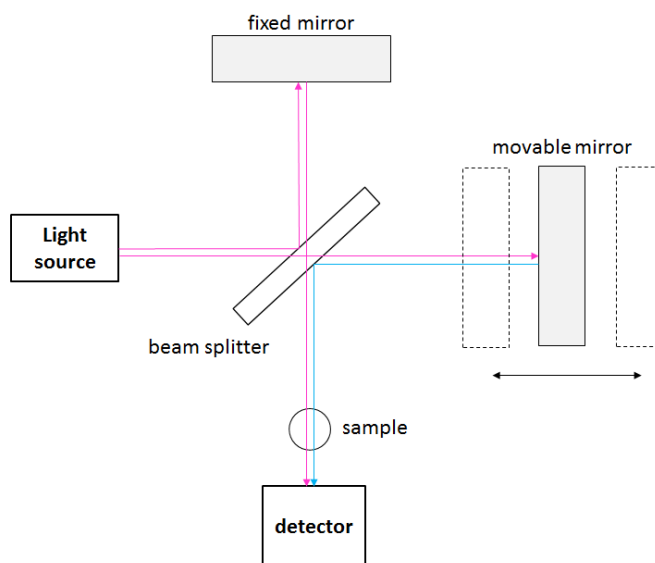


Figure 3-9. Schematic setup of a Michelson interferometer.

3.3.2.2.2. *Attenuated Total Reflection (ATR)*

ATR is the most common amongst all IR sampling techniques and is based on the principle of total internal reflection, which generates an evanescent wave (Figure 3-10). Total internal reflection means that light travelling through a medium is completely reflected at the interface to another medium if the latter is optically less dense, i.e. has a lower refractive index. Although the light is completely reflected, it can still interact with a sample placed at the interface by an evanescent wave that is created upon reflection and extends slightly above the outer limits of the optically dense medium (between 0.5 and 2 μm). This interaction modulates the light beam, so that absorption can be measured and absorption spectra are recorded. Ramer and Lendl published a concise overview with historical, physical and practical aspects of FTIR and ATR methods.²⁰⁰⁻²⁰¹

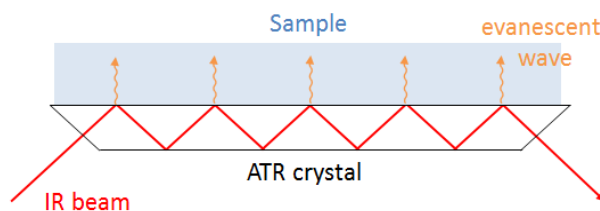


Figure 3-10. Working principle of an ATR measurement. The incident IR beam reflects on the internal surface of the ATR element. An evanescent wave penetrates the sample, which absorbs energy and modifies the exiting beam. Modification in form of absorbance spectra can be recorded by a detector.

A large advantage of ATR is the ease of sample handling and versatility in its applications. Materials for the ATR element have to meet measurement requirements, i.e. they need to show good transmission in the spectral range of interest, be optically more dense than the sample to allow for total internal reflection, and chemically inert. Common materials are, for example, Ge or Si crystals. Furthermore, a good contact with the ATR element is important for the measurement. For solid samples this can be achieved with different strategies, i.e. pressure, melting, spin-coating. Liquid samples can be measured in troughs or flow cells, while flow cells have the advantage of avoiding evaporation of the sample and possibilities of flow measurements and cleaning in between measurements. Important for measurements is to avoid gas bubbles in the liquid, which would disturb the evanescent wave.²⁰¹

3.3.2.2.3. *In situ ATR-FTIR with light irradiation*

In this work, an in situ flow cell for ATR-FTIR measurements under UV light irradiation has been developed in collaboration with the Institute of Chemical Technologies and Analytics at Vienna University of Technology. Technical details of the optical setup are provided by Bettina Baumgartner:

Optical setup (Figure 3-11): Adapted from Karabudak et al.,²⁰² Si ATR crystals (10 mm × 20 mm) are cut from standard low resistivity ca. 525 μm thick, double-side polished CZ Si wafers by using a dicing machine. The narrow facets are polished to a defined angle of 45°. This angle of incidence allows for 20 active internal reflections within the ATR crystal.²⁰¹ The ATR crystal is inserted into a home-built PMMA flow cell (700 μL) with a 2 mm-thick sapphire window as lid. A 200 W super-pressure Hg lamp (Superlite SUV DC-P deep UV, Lumatec) is placed above the window for UV illumination. A FKM O-ring formed a watertight seal around the edges of the ATR crystal. The flow cell setup is placed in the sample compartment of a Bruker Vertex 80v spectrometer equipped with a liquid N₂-cooled MCT de-

Chapter 3 – Methods & Procedures

tector (InfraRed Associates, $D^* = 4 \times 10^{10} \text{ cm Hz}^{0.5} \text{ W}^{-1}$ at $9.2 \mu\text{m}$). Two gold mirrors direct the IR beam onto the angled facets and detector, respectively (compare Figure 3-11). IR spectra are acquired with a spectral resolution of 4 cm^{-1} and a total of 8-32 scans (1-4 s, double-sided, backward forward acquisition mode) are averaged per spectrum. The beam diameter is optimized for maximum signal at the MCT detector and minimal noise resulting in an optimal beam aperture of 8 mm. The noise level is evaluated as the root-mean-square (RMS) of 100% lines, which are obtained by calculating the absorbance spectrum of two subsequent single beam spectra of the same sample under identical conditions. The RMS noise between $2200\text{-}2000 \text{ cm}^{-1}$ is determined to be $4 \times 10^{-5} \text{ AU}$ from 32 averaged scans (4 s scan time).

Spectra analysis is performed using the software package OPUS 7.5 (Bruker Corp., Ettlingen, Germany) and a Matlab script that is used for linear baseline subtraction and integration of absorption bands.

Spin-coating of TiO_2 onto Si: For the P25 paste, first a 10 wt.% ethyl cellulose (EC, 48.0-49.5% (w/w) ethoxyl basis, Sigma-Aldrich) ethanoic solution is prepared. Then 2.0 g of P25 (Aeroxide® P-25 by Acros Organics) and 8.1 g terpeneol (anhydrous, mixture of isomers, Sigma-Aldrich) are added to 10 g of the EC-ethanoic solution. After 10 minutes stirring, 35 mL of ethanol are added. The mixture is sonicated 3 times for 5 min each with a sonication finger (20 kHz, 10% amplitude, SONOPLUS HD3200, Bandelin) and stored in the fridge for future use.

Before spin-coating, the viscous paste is stirred overnight at room temperature

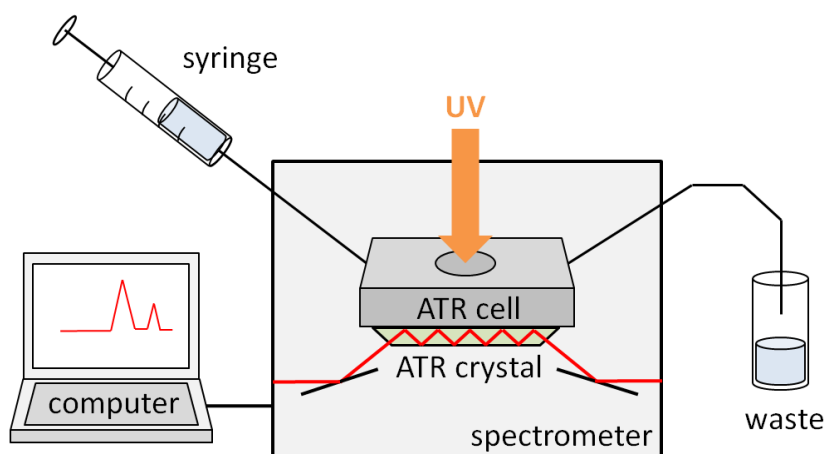


Figure 3-11. Optical setup consisting of a flow cell placed on a Si ATR crystal within a commercial FTIR spectrometer

and the Si substrates are rinsed with ethanol and iso-propanol. The P25 paste is then spread onto Si substrate before the rotation starts. For one Si wafer (10 mm × 20 mm), 100 µL P25 paste is spin-coated at 6000 rpm for 45 s (ramp time: 2.5 s). After spin-coating, the film is first pre-heated at 100 °C for 20 min and then annealed at 500 °C for 30 min.

ATR-FTIR measurements of photocatalytic oxidation of methanol and in situ photodeposition of Pt: A reaction solution of 50 vol.% methanol with H₂PtCl₆ precursor solution (7.2×10^{-5} M and 5.8×10^{-4} M) is applied to the cell containing the TiO₂-coated Si crystal manually via a syringe. Spectra are recorded in the dark for several minutes to ensure a flat baseline, after which the UV light is turned on for 60 min. Spectra are recorded every minute. No flow is applied during the measurement. UV irradiation results in a strong and curved baseline shift that has been assigned to electronic excitation in the ATR element. Thus, all spectra have to be manually baseline-corrected.

3.3.2.2.4. Diffuse reflectance infrared Fourier transform spectroscopy (DRIFTS)

DRIFTS measurements combine the principles of diffuse reflectance and FTIR discussed above (see sections 3.3.2.1 and 3.3.2.2.1). In contrast to DRS which works with UV-visible light, IR irradiation is used for a DRIFTS setup. Figure 3-12 shows a schematic setup of a DRIFTS cell in which the incident IR beam gets reflected on- to the sample and into the detector by a set of parabolic mirrors.²⁰³

The technical details of the DRIFTS measurement are provided by Dr. Litke formerly at TU Eindhoven:

The IR measurements and sample treatment are carried out in an *in-situ* DRIFTS low temperature reaction chamber (Harrick Scientific) equipped with two KBr and one fused silica windows for the IR signal collection and sample irradiation, respectively. The cell is connected to a home-built gas delivery system. During all experiments, the temperature of the cell exterior was maintained at 20 °C by cooling water. A Bruker Vertex 70v FTIR spectrometer equipped with a Praying Mantis diffuse-reflectance accessory (Harrick Scientific) and a liquid N₂-cooled MCT detector was used for the DRIFTS measurements. The sample compartment of the spectrometer is purged by dry nitrogen during all experiments. The spectra are recorded at 4 cm⁻¹ resolution in the spectral range 3950–600 cm⁻¹. Steady-state spectra reported in this study are averages of 100 scans. A low-pass IR filter (cut-off frequency 3950 cm⁻¹) is placed in front of the detector compartment, also to block stray light and reflected laser irradiation. KBr (Sigma Aldrich, IR grade)

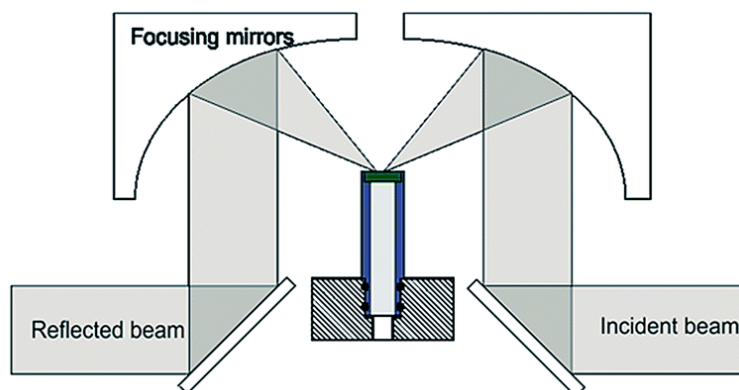


Figure 3-12. Setup of a DRIFTS measurement cell. Reprinted from ref. 203 - Published by The Royal Society of Chemistry.

was used as reference for the survey DRIFT spectra. Typically, the spectrum of the sample in the dark was used as the reference for obtaining difference spectra and time-resolved measurements. O_2 ($\geq 99.95\%$), H_2 ($\geq 99.999\%$) and Ar ($\geq 99.999\%$) gasses were supplied by Linde and passed through moisture and/or oxygen filters (Agilent technologies). CO (the Linde Group, $\geq 99.99\%$) is used as delivered without further purification. The 409 nm continuous-wave diode laser was used to irradiate the sample.

The following oxidation procedure was used to remove substantial part of the organic adsorbates. As-delivered material is evacuated at room temperature with a turbomolecular pump to the lowest stable pressure ($< 10^{-3}$ mbar) and kept under dynamic vacuum for 0.5 h. Then the sample is heated to 100 °C and irradiated with 50 mW 409 nm laser line in the presence of 100 mbar O_2 . The samples are treated in this way for 2–3 h until spectral changes become stable. Formation of gaseous CO_2 is evident from the formation of a new band at 2349 cm^{-1} . Formation of this band is accompanied by the intensity loss in the $2980\text{--}2840\text{ cm}^{-1}$ and $1700\text{--}1600\text{ cm}^{-1}$ spectral regions. These spectral changes can be attributed to oxidation of organic compounds present on the sample.

3.3.2.3. Raman spectroscopy

Like IR spectroscopy, Raman investigates rotational and vibrational transitions in a system and is a widely used tool for structural analysis. However, in contrast to IR in which a vibrational transition is induced by absorption of a matching amount of IR light, Raman spectroscopy is based on the inelastic scattering of light (Figure 3-13). In Raman, a monochromatic laser beam excites a molecule into a virtual

energy state from which it can either return to the initial energy state (elastic or Rayleigh scattering, photon energy remains unchanged) or to a state higher or lower in energy (inelastic scattering, photon energy decreases or increases) (Figure 3-13). A decrease in the energy of the photon (higher final energy state) results in a shift to a lower frequency. This downshift is also called Stokes shift. On the other side a shift to a higher energy of the photon is called upshift or Anti-Stokes shift. The main scattering event is the Rayleigh scattering, while the described Raman scattering has a much lower probability to occur (signal intensities are $\sim 10^{-5}$ of the incident beam). Thus, filters are used in a spectrometer to isolate the Raman scattering signals. The excitation of the molecule occurs through an oscillating polarization induced by the laser beam. Therefore, Raman scattering depends on the polarizability of a molecule in contrast to IR spectroscopy, where the change in dipole moment is critical. These two differing selection criteria for whether a transition is allowed, make Raman and IR two complementary techniques. Transitions that are not IR active, may be analyzed by Raman and vice versa.^{195, 204}

In this work, a LabRam 800HR evolution spectrometer with edge filter, Nd:YAG laser (532 nm, max. intensity: 55 mW), a CCD detector and an optical microscope (Olympus BX40) to focus the laser beam is used for Raman measurements.

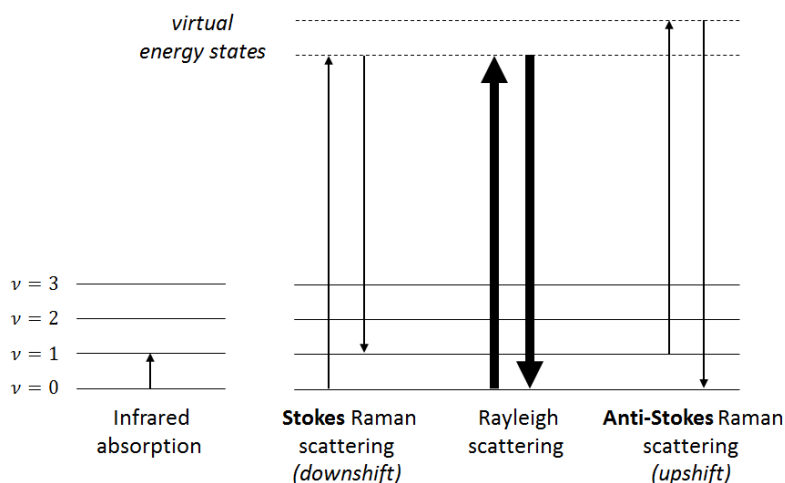


Figure 3-13. Comparison of different light interaction for infrared absorption and Raman scattering. Based on ref. 197.

3.3.3. Adsorption studies

The following section covers physisorption and chemisorption methods that are used to characterize the surface of the photocatalyst with respect to the specific surface area (physisorption according to BET theory) and number of active sites on the co-catalyst (CO chemisorption experiments).

3.3.3.1. Physisorption (*Brunauer-Emmett-Teller theory*)

In physisorption, a molecule adsorbs onto a material by weak van-der-Waals-bonding. In contrast to chemisorption no chemical bond is formed between adsorbate (adsorbing molecule) and adsorbent (material onto which the adsorbate adsorbs). Gas adsorption is a tool to characterize the texture, i.e. surface and porosity, of a material. The fundamental idea is that if one knows a) the space that is occupied on a surface by one molecule of an adsorbate and b) the total number of adsorbed molecules, one can deduct the actual surface area of the adsorbent.²⁰⁵⁻²⁰⁶

If we assume that a gas adsorbs as a monolayer onto a surface, one can deduct the surface area of a material by knowing the cross-section of the space needed per adsorbed molecule and the volume of gas that has been adsorbed (equation (3.9)).

$$(3.9) \quad A_s = n_m N_A a$$

Where A_s is the surface area, a the cross-sectional area of the adsorbate molecule, n_m the number of moles of adsorbate in a monolayer, and N_A is Avogadro's number. Usually, the specific surface, a_s , with respect to the mass of the material, m , are is given as output from physisorption measurements (equation (3.10)).

$$(3.10) \quad a_s = \frac{A_s}{m}$$

While a can be inferred from the molecular size of the gas adsorbate, the amount of adsorbed molecules needs to be determined experimentally. There are two common methods to determine how much gas is adsorbed by a material: 1) manometrically (by measuring pressure differences upon adsorption and deducting the adsorbed volume) and 2) gravimetrically (by measuring the weight gain of the adsorbent upon adsorption). The manometric (also volumetric) method is much less expensive, however, also less accurate than the gravimetric approach. Still, it is the most widely-used and is also the method of choice in this work.²⁰⁵⁻²⁰⁶

During a manometric measurement, the outgassed sample is exposed to known volumes of adsorbing gas (e.g., N₂ at 77 K – the boiling point) either in a static (step-wise) or dynamic (continuous) fashion and the pressure changes are recorded at a constant temperature giving an adsorption isotherm as output. In the adsorption isotherm, the amount of adsorbed gas is plotted against the relative pressure which is the equilibrium pressure divided by the vapor saturation pressure, p/p^o . After adsorption, desorption isotherms are recorded in the same fashion. Adsorption and desorption isotherms may differ, resulting in a hysteresis between the two curves which can give information about the porosity of a material. As I did not study any porous materials, I will not go into further detail, but Thommes et al. give a very clear and concise overview over the different isotherm types and hysteresis loops that enable us to distinguish between different porosities of a material.²⁰⁵⁻²⁰⁶

The most widely-used theory that correlates the measured relative pressure, p/p^o , to n_m is still that by Brunauer, Emmett and Teller (BET theory). Although based on an oversimplified adsorption model, the obtained value for a surface area can be seen as “effective” surface area accessible to the probe molecule. The BET equation is as follows:

$$(3.11) \quad \frac{p/p^o}{n(1 - p/p^o)} = \frac{1}{n_m C} + \frac{C - 1}{n_m C} (p/p^o)$$

where n is the specific amount adsorbed at the relative pressure, p/p^o , and C is a parameter that is exponentially related to the energy of monolayer adsorption.²⁰⁵⁻²⁰⁶

In this work, physisorption measurements are carried out on ASAP 2010 and ASAP 2020 (Micromeritics GmbH, Aachen, Germany) instruments. Samples were outgassed at 100 °C under vacuum for 6 hours. The measurement itself was carried out at a temperature of $T = 77$ K using N₂ as adsorbate. Specific surface areas were calculated according to BET theory.

3.3.3.2. Chemisorption

Chemisorption of a probe molecule (e.g. H₂ or CO) onto a catalyst can give information about parameters such as metal dispersion and number of available active sites. Measurements are based on the same basic principles as discussed for physisorption, i.e. measuring of pressure differences at a constant temperature.^{205, 207}

Chapter 3 – Methods & Procedures

Chemisorption experiments were conducted at the Ruhr-Universität Bochum, Germany, by Dr. V. Hagen:

Measurements were performed in an automated BELCAT-B chemisorption analyzer (BEL Japan, Inc.). Samples (0.02 – 0.03 g) were purged overnight with He gas at room temperature and either treated reductively and oxidatively at 200 °C for surface cleaning or this pretreatment step was omitted to avoid changes in the photocatalysts. A pulse loop with a volume of 0.3 mL and CO (10%) as probing gas was used. Detection was performed at „high sensitivity“ settings. For calculations of dispersion and the active surface, a binding stoichiometry of 1:1 between CO and Pt („on top“ position of CO) is assumed. If a “bridged” binding position of CO should be assumed, values are simply multiplied by 2.

3.3.4. X-ray diffraction (XRD)

XRD is a powerful tool for structural analysis of a sample. In particular, it gives information about the spatial arrangement of atoms in a material, and thus its crystal phase, deduced from diffraction of an X-ray beam. In contrast to TEM that allows for microstructural analysis, XRD is an averaging bulk technique giving information about the whole sample.^{193, 208}

Basically, in a diffraction experiment of a polycrystalline sample, a monochromatic beam gets directed onto the sample, where it is diffracted by atoms and finally collected at a detector (Debye-Scherrer method). In order for diffraction to occur, the incident beam has to have a wavelength in the dimensions of atomic distances, which is fulfilled by X-rays (also by electron and neutron beams). In crystalline

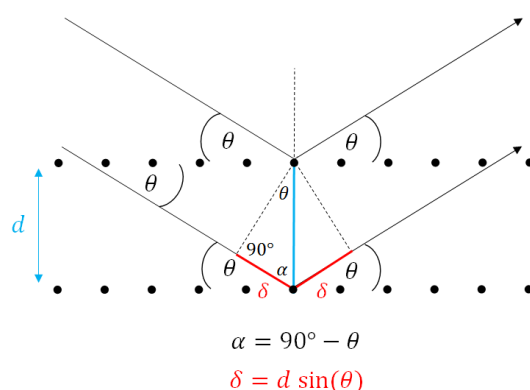


Figure 3-14. Geometrical construction for derivation of Bragg's Law: Two parallel beams are diffracted at two different atoms in a crystal lattice. The path difference can be described as $2\delta = 2d \sin\theta$. Constructive interference (Bragg diffraction) occurs when the path difference equals an integer multiple of the wavelength of the incident radiation.²⁰⁹

samples, atoms are arranged in a periodic long-range order, so that the diffraction at atomic positions results in diffracted waves that interfere with each other. The detected signal in XRD stems from constructively interfering waves.^{193, 208}

Bragg's Law gives a direct relation between constructive interference and the interlayer lattice spacing, d , in a crystal. Figure 3-14 is a geometrical construction from which Bragg's Law can be derived. It combines the requirements that 1) constructive interference occurs if the path difference between parallel, incident X-ray waves are an integer multiple of their wavelength ($2\delta = n\lambda$) and 2) that the half the path difference equals $\delta = d \sin(\theta)$. Overall this results in the Bragg equation.²⁰⁹

$$(3.12) \quad n\lambda = 2d \sin(\theta)$$

Where n is an integer, λ is the wavelength of the incident X-ray, d is the interlayer distance and θ is the angle of incidence of the X-ray beam at which diffraction occurs (Bragg angle). Thus, different facets (i.e. different interlayer spacing) correspond to different peaks (reflexes) in the resulting diffractogram, which allows for phase analysis of a crystalline material. Conventionally, the reflexes of a diffractogram can be indexed with the Miller indices of a crystal facet for assignment. Figure 3-15 shows an exemplary diffractogram of P25 with the indexed anatase (A) and rutile (R) crystal facets.²¹⁰ In this work, indices may have been omitted at times if they disturbed the clarity of an illustration and were not critical for the

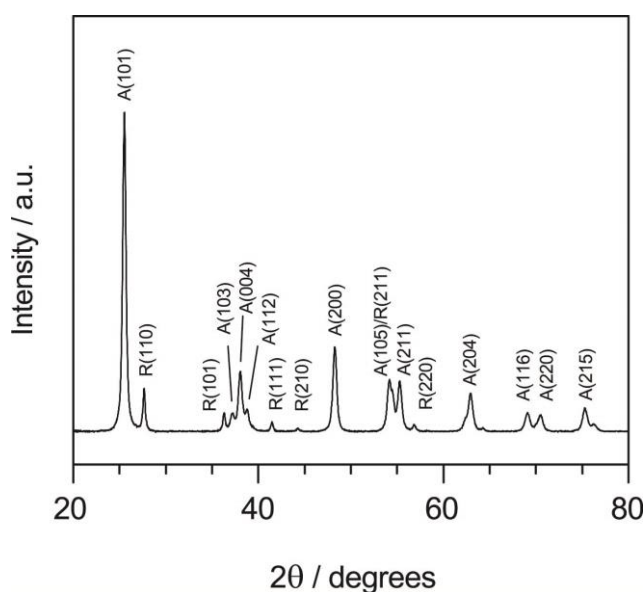


Figure 3-15. Exemplary diffractogram of P25 with the indexed anatase (A) and rutile (R) crystal facets.²¹⁰

argument. The peak width of the recorded signal depends on the crystallite size and orientation as well as strain effects, such as defect incorporation through vacancies or dopants.^{193, 208}

In this work, measurements were carried out on a Bruker D8 Advance with Lynx-Eye detector (Bruker AXS GmbH, Germany) and Cu K α radiation ($\lambda=1.5406$ Å). Samples are spread homogeneously on a Si single crystal wafer and rotated during the measurement.

3.3.4.1. Scherrer equation

Ideally, Bragg diffraction only occurs at the Bragg angle, as signals at other angles would be eliminated by destructive interference. However, the smaller the crystal size, the broader the recorded reflexes due to incomplete destructive interference.²⁰⁸ The Scherrer equation can be used to calculate the mean crystallite size in spherical systems with random orientation from the observed reflex width:^{208, 211}

$$(3.13) \quad \tau = \frac{K\lambda}{\beta \cos(\theta)}$$

Where τ is the mean crystallite size (in Å), K is a dimensionless shape factor usually taking on a value of 0.9,²¹² λ is the wavelength of the X-ray irradiation (in Å), β is the line broadening of the reflex at full-width half-maximum (fwhm, in rad) corrected for instrumental line broadening (here, 0.0627 rad) and θ is the detected Bragg angle (in °).

3.3.5. X-ray photoelectron spectroscopy (XPS)

XPS is a surface-sensitive analytical tool that is used to study the electronic environment and oxidation state of elements in a sample. XPS is based on the external photoelectric effect, i.e. photoemission of electrons upon irradiation with photons.

3.3.5.1. General

Figure 3-16 gives a schematic overview over the setup of a spectrometer. A sample is irradiated with monochromatized X-rays (e.g. Al-K α), which leads to emission of electrons from the core levels of an atom. The photoelectrons are guided into a detector through a hemispherical analyzer that can separate different energy levels by electromagnetic lenses.²¹³⁻²¹⁴ The quantity measured in an X-ray photoelectron spectrometer is the number of electrons (in counts per second) for a certain kinetic energy (KE) of the photoelectrons when they arrive at the detec-

tor of the spectrometer. However, KE depends on the energy of the X-ray and is not specific to the material unlike the binding energy (BE) of an electron, which is characteristic to the material and state of the electron. The BE can be calculated from the detected KE, if the energy of the incident photons (i.e. the X-ray source wavelength) and the work function of the spectrometer are known.²¹³⁻²¹⁴

Figure 3-17 shows a scheme illustrating the correlation between KE, BE and the work function of the sample and the spectrometer: A conductive sample and the spectrometer are in contact, which leads to alignment of their respective Fermi level. For an electron to be ejected from the atom, some energy of the incident beam is invested in order to overcome BE and the work function of the sample, ϕ_{sample} (energy needed by the electron in order to be released into vacuum, i.e. $E_{vac}-E_F$). The KE of the ejected photoelectrons is measured at the detector of the spectrometer. Some additional energy is lost when the photoelectron is absorbed, since the detector has a different work function than the sample. This causes a difference in the measured and the actual KE that corresponds to the work function of the spectrometer, ϕ_{spec} (as ϕ_{sample} cancels out), which is measurable and constant. This gives us the following relationship between the BE, KE, incident radiation, and ϕ_{spec} :

$$(3.14) \quad E = h\nu - BE - (\phi_{sample} + (\phi_{spec} - \phi_{sample}))$$

$$(3.15) \quad BE = h\nu - KE - \phi_{spec}$$

Generally, XPS is a surface-sensitive technique with analysis depths between 1-10 nm depending on the material and the electron takeoff angle.²¹⁵ Short mean

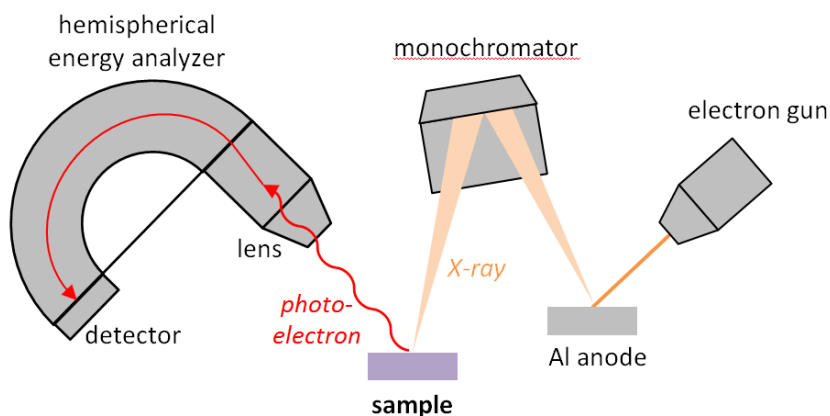


Figure 3-16. Setup of a X-ray photoelectron spectrometer.

free paths of electrons in solids ($\sim 1\text{nm}$) are the main limiting factor for XPS analysis depth. Detection limits range from 0.1 to 1 at.%; can, however, be much higher (up to 0.01 at.%) or lower (up to 3 at.%) depending on the matrix measured.²¹⁵ Heavy elements are usually easier to detect than lighter, e.g. H and He cannot be detected practically in XPS due to their low photoelectron crosssections. Furthermore, UHV conditions are required to avoid collision of the photoelectrons with other gas molecules. Additionally, samples need to be conductive in order to avoid charging effects although there are several strategies for charge compensation that can counteract these effects (e.g. flood gun).²¹³⁻²¹⁴

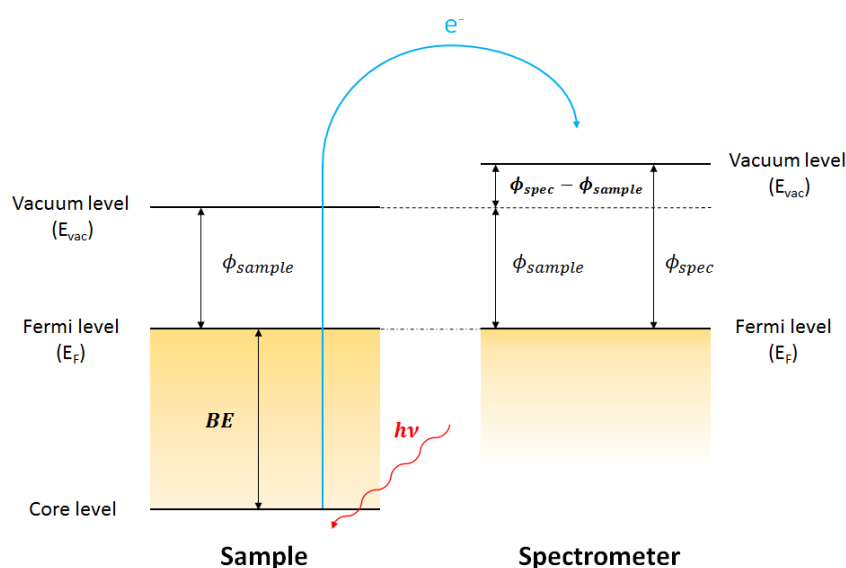


Figure 3-17. Correlation between kinetic energy (KE), binding energy (BE) and the work function of the sample and the spectrometer

3.3.5.2. Instrumentation

All measurements were carried out on a custom-built SPECS XPS spectrometer equipped with a monochromatized Al- K_{α} X-ray source (μ Focus 350) and a hemispherical WAL-150 analyzer (acceptance angle: 60°). All samples are mounted onto the sample holder using double-sided carbon tape. Pass energies of 100 eV and 30 eV and energy resolutions of 1 eV and 100 meV are used for survey and detail spectra, respectively (excitation energy: 1486.6 eV, beam energy and spot size: 70 W onto $400\ \mu\text{m}$, angle: 51° to sample surface normal, base pressure: 5×10^{-10} mbar, pressure during measurements: 2×10^{-9} mbar).

Data analysis was performed using CASA XPS software, employing transmission corrections (as per the instrument vendor's specifications), Shirley and Shirley Tougaard backgrounds,²¹⁶⁻²¹⁷ and Scofield sensitivity factors²¹⁸. Charge correction

is applied so that the adventitious carbon peak (C-C peak) is shifted to a BE of 284.8 eV.

All content values shown are in units of relative atomic percent (at.%), where the detection limit in survey measurements usually lies around 0.1-1 at.%, depending on the element. The accuracy of XPS measurements is around 10-20% of the values shown. Assignment of different components is primarily done using references²¹⁹⁻²²⁰.

Calculations of the oxygen stemming from the actual metal oxide and not from adsorbed carbonaceous species are used to calculate O:Ti ratio based on Biesinger et al.'s work.²²¹

3.3.5.3. *VB-XPS vs. UPS*

For XPS, soft X-ray (200-2000 eV) is used to generally examine the core-levels of a material but is also commonly applied to obtain VB spectra. On the other side, ultraviolet photoelectron spectroscopy (UPS) is a different branch of photoelectron spectroscopy. UPS is based on the same principles as XPS but uses UV light (10-45 eV) instead of X-rays as irradiation source. This means lower photon energies and shallower penetration depth (about 3 nm), so that UPS is mainly used for investigations of the VB of a material. Both UPS and XPS can be used to investigate the VB of a sample.²²²⁻²²³

VB investigations in this work were performed to observe VB modifications for reduced TiO₂. As literature references mainly used XPS for these studies, I also decided for this method.

4 Preliminary studies and characterization

The following chapter covers reference experiments as well as preliminary characterization studies. In particular, TEM and Raman have been proven to be ambiguous in the analysis if not measured at specific conditions. An example for an XPS spectra interpretation for TiO_2 is given at the end of the chapter, including a discussion about the VB measurements and reported values using XPS.

4.1. HER: Blank experiments

Blank experiments are carried out in the absence of TiO_2 (pure water and 50 vol.% methanol solutions) as well as in the absence of Pt as co-catalyst (TiO_2 in pure water and 50 vol.% methanol solution). No H_2 and only a negligible amount of CO_2 was detected for the irradiated water solution with and without TiO_2 present ($<1 \mu\text{mol h}^{-1}$). Irradiation of aqueous methanol resulted in small amounts of H_2 ($5\text{--}8 \mu\text{mol h}^{-1}$) and CO_2 ($<2 \mu\text{mol h}^{-1}$) that is likely due to a slight decomposition of methanol under UV irradiation. However, these rates are negligible compared to gas evolution in the presence of Pt as co-catalyst. Furthermore, O_2 was not detected in any of my experiments, although the paramagnetic detector was sensitive to pressure variations in the system.

4.2. TEM: Electron beam-induced damage of TiO_2 during TEM imaging

At certain measuring conditions, I observed an electron beam-induced damage of TiO_2 crystals during TEM imaging. Figure 4-1 shows a series of TEM images of P25 recorded at a) 0 min b) 2 min and c) 5 min at a fixed sample position. Even before the first image is recorded, a clearly not crystalline surface of roughly 1-2 nm thickness is observed. Within only 5 min, this layer grows to a thickness of 4-6 nm resulting in a growth rate of 0.5 nm min^{-1} . Electron beam-induced damage on metal oxides, including TiO_2 , has previously been reported in literature and is attributed to two dominating pathways: ballistic or radiolytic damage. Ballistic or “knock-on” damage is an elastic scattering event in which transfer of momentum and kinetic energy of an incident electron kicks out an atom. Radiolytic damage, on the other side, occurs when an electron beam-generated hole in the cation of

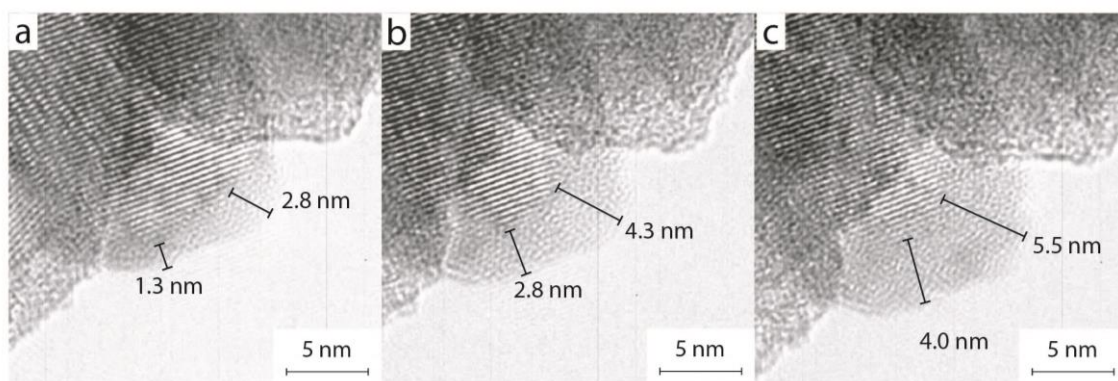


Figure 4-1. TEM images of P25 recorded at a) 0 min b) 2 min and c) 5 min at a fixed sample position.

the metal oxide is filled by an interatomic electron transfer from the anion. A subsequent repulsive potential leads to desorption of the anion, i.e. oxygen, and formation of lower valency oxides (Knotek-Feibelman mechanism¹³⁶). This desorption can be induced by electrons as in the case of electron beam-induced phenomena or by photons.^{137, 224-226} Buckett et al. showed that damage in TiO_2 is dominated by radiolytic processes rather than ballistic pathways as evidenced by the lack of pitting and a relative insensitivity to the acceleration voltage of the TEM. Crystal orientation proved to be more important for the extent of damage that could be observed.²²⁵ A recent and comprehensive review on electron beam-induced damage has been published in 2015 by Nan Jiang.¹³⁷

The beam-induced, disordered layer appears to be clearly amorphous, although further investigations of its true nature have been out of the scope of this work. This is highly relevant for investigations of black TiO_2 . In Chapter 6, I compare several different synthesis routes to obtain black TiO_2 . One key characteristic of this material is the creation of an amorphous or disordered outer layer of TiO_2 nanocrystals and a key characterization technique in evidencing the formation of this layer is TEM imaging. However, issues corresponding to electron beam-induced damage have not been addressed in literature at all. I already observe surface amorphization immediately upon recording an image and measuring conditions that are not particularly harsh in beam intensity. Thus, I want to raise sensitivity for this issue so that measuring artefacts due to beam damage are not confused with actual surface amorphization.

Decreasing the beam intensity by using different aperture and lens settings, leads to a strong reduction in the beam-induced damage as illustrated in Figure 4-2. Over a time period of 7 min, only a 0.5-1 nm thick disorder is generated. Unfortunately, I experience a significant loss in image brightness and quality at these set-

tings. Still, “low intensity” settings are used for all investigations regarding amorphous surface layers.

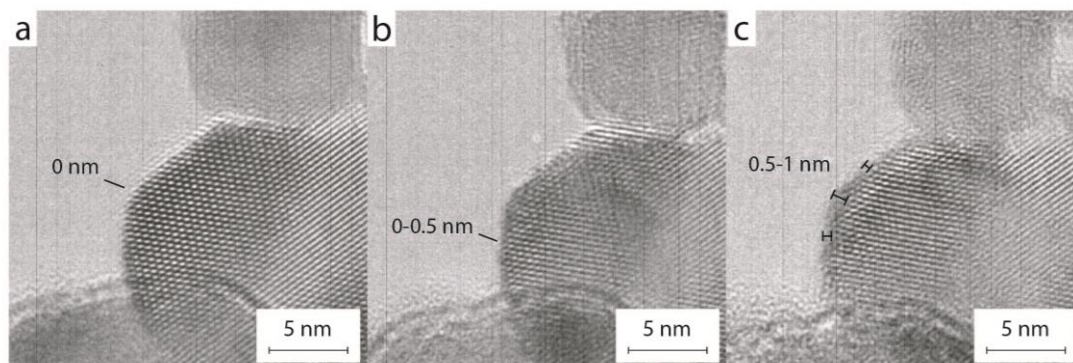


Figure 4-2. TEM images of P25 recorded at a) 0 min b) 2 min and c) 7 min at a fixed sample position and reduced electron beam intensity.

4.3. Raman: Laser-induced phase transformation & defect formation

Laser-induced phase transformation and damages have been observed during Raman measurements of the TiO_2 samples. A P25 reference sample, which would usually show the typical anatase modes at E_g (146 cm^{-1} , 198 cm^{-1} , 639 cm^{-1}), B_{1g} (398 cm^{-1}), and an A_{1g} mode (515 cm^{-1} superimposed by 519 cm^{-1}),^{178, 187} locally transformed to rutile upon increasing the laser intensity (Figure 4-3). Furthermore, shifts in the E_g mode of rutile and strong peak broadening indicates lattice strain either due to defect creation or crystal size changes (e.g. sintering).²²⁷⁻²²⁸ Camera images show a clear darkening of the measured spot.

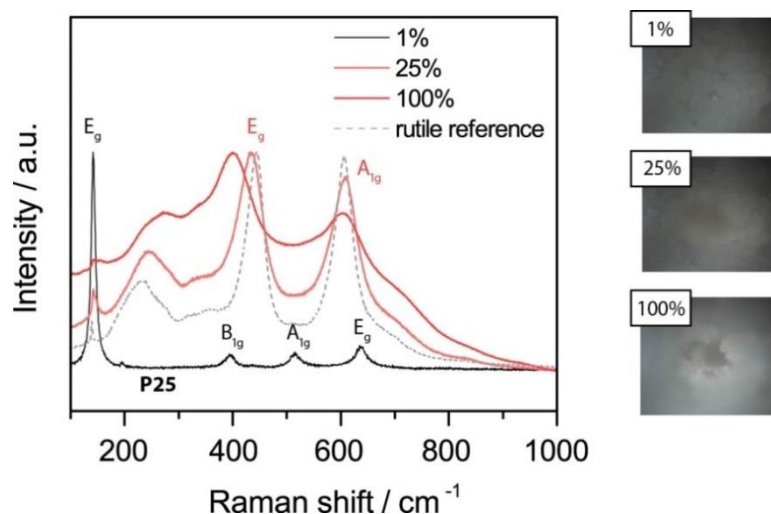


Figure 4-3. Laser-induced phase transformation and damages as observed during Raman measurements of TiO_2 samples at different laser intensities. A dark spot appears at the measuring position with

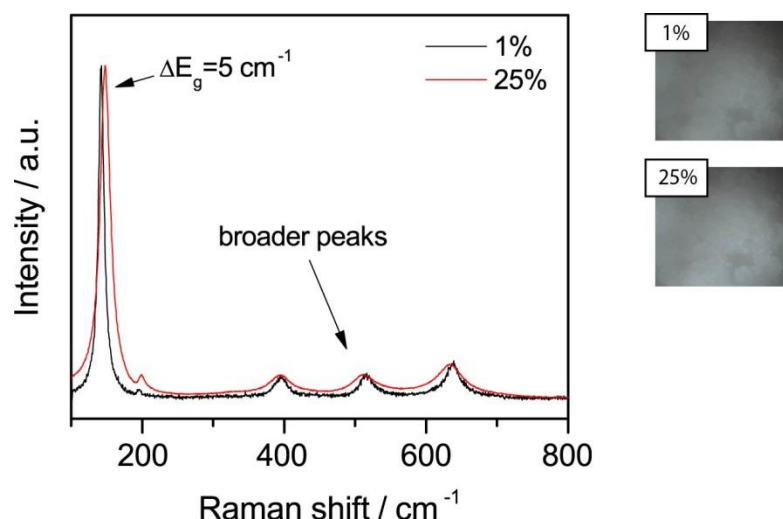


Figure 4-4. Laser-induced shift and peak broadening as observed during Raman measurements of TiO_2 samples at different laser intensities. Samples did not appear damaged in the camera images (right side).

Even when camera images did not reveal a “burn” or damage during the measurements, Raman spectra of P25 measured at 1% and 25% laser intensity showed a shift and peak broadening as well, again indicating the introduction of crystal lattice strain (Figure 4-4). This is highly relevant for my work, as I am investigating possible oxygen vacancy formation and Raman is a widely used method to correlate defect creation in materials to observed shifts and broadening of peaks.

Thus, Raman spectra are measured at “soft” conditions with the lowest intensities and acquisition times possible in order to obtain good spectra but also avoid laser beam-induced damage. Furthermore, conditions are kept as constant as possible between different measurements.

4.4. XPS: Interpretation of typical XPS detail spectra for TiO_2 at the example of P25

For a better understanding of the discussion of XPS results and avoidance of redundancy, XPS spectra of P25 will be discussed exemplary in the following section.

4.4.1. C 1s

The C 1s spectrum of P25 shows the expected shape of adventitious carbon that adsorbed onto the surface of TiO_2 (Figure 4-5). Adventitious carbon is a thin layer of carbonaceous species that physically adsorbs onto the surface of a sample immediately upon air exposure. It consists of mainly polymeric hydrocarbon spe-

cies (C-C, C-H; approx. 70-90%) as well as oxygen-containing compounds (C-O-C, C-OH, C=O, O-C=O; approx. 10-30%).²²⁹ The main peak of C-C bonds is usually used as reference point in order to correct for charging of samples and is set to 284.8 eV for all measurements. Table 4-1 lists the atomic percent of the different components fit for adventitious carbon adsorbed on P25 and their respective BE.

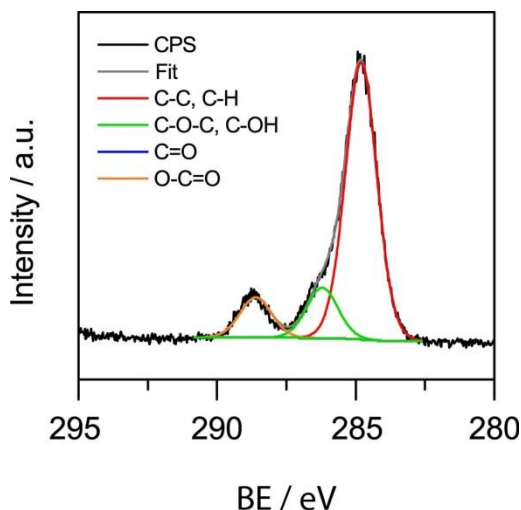


Figure 4-5. C 1s detail spectrum of P25.

Peak	C-C, C-H	C-OH, C-O-C	C=O	O-C=O
BE / eV	284.8	286.2	-	288.6
fwhm / eV	1.32	1.32	-	1.32
%	72.4	15.2	-	12.5

Table 4-1. BE values, fwhm and area % of the individual components of the C 1s detail spectrum of P25.

4.4.2. O 1s

The O 1s spectra of TiO₂ typically consist of a major peak centered at 529.5 eV that stems from the metal oxide and several components at higher BE that are due to hydroxyl groups, defects, or organic surface groups (Figure 4-6). Literature values for metal hydroxides and carbonates are overlaying at 531.3 eV with a BE for Ti³⁺-O at 531.1 eV.^{220, 230-231} A variety of organic compounds (e.g. alcohols, acids, ether, esters) can be found in the range between 532 and 534 eV. Literature values for common BE of organic compounds can be found in reference²²⁰. The exact assignment of a certain species without further knowledge about the chemical composition of the adventitious carbon layer as well as surface groups on the TiO₂ is not possible. Still, changes between samples can be investigated and give

information about the surface composition of different samples. Table 4-2 lists the atomic percent of the different components fit in the O 1s spectrum of P25 together with their respective BE.

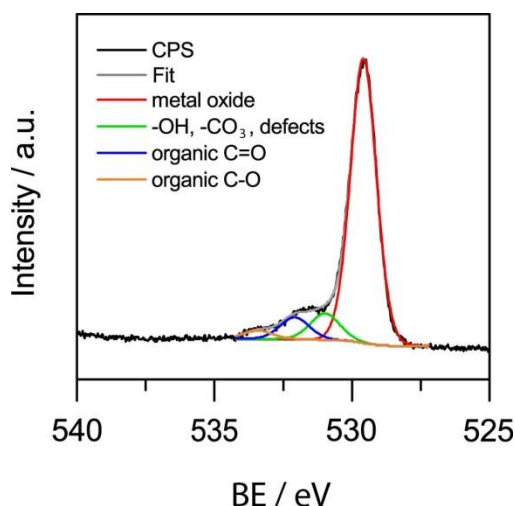


Figure 4-6. O 1s detail spectrum of P25.

Peak	<i>metal oxide</i>	<i>-OH, -CO₃, vacancies</i>	<i>organic, C=O</i>	<i>organic, C-O</i>
BE / eV	529.5	531.0	532.0	533.4
fwhm / eV	1.13	1.70	1.70	1.70
%	64.6	8.7	17.0	9.7

Table 4-2. BE values, fwhm and area % of the individual components of the O 1s detail spectrum of P25.

4.4.3. Ti 2p

The Ti 2p spectrum of TiO₂ is split into the 2p_{3/2} (458.3 eV) and 2p_{1/2} (464.0 eV) orbitals due to spin-orbit coupling, typically with an area ratio of 2:1 and a splitting value between the peaks, Δ_{oxide} , of 5.7 eV. Due to the lower oxidation state and thus lower BE, Ti³⁺ is usually expected at ~457 eV ($\Delta_{\text{oxide}} = 5.2$ eV).²³² For P25, the Ti³⁺ component is not necessary to obtain a good fit. However, it is included in the fit to give a value for comparison to samples with possibly increased Ti³⁺ centers after reduction treatments. Still, the small component of 0.5 at.% could also be due to some background signal that could not be accounted for by the standard Shirley-type background curve.²¹⁶ Table 4-3 lists the area percent of the Ti⁴⁺ components (total of 99.5%) and the Ti³⁺ or background components as well as the BE of the different orbitals and splitting values.

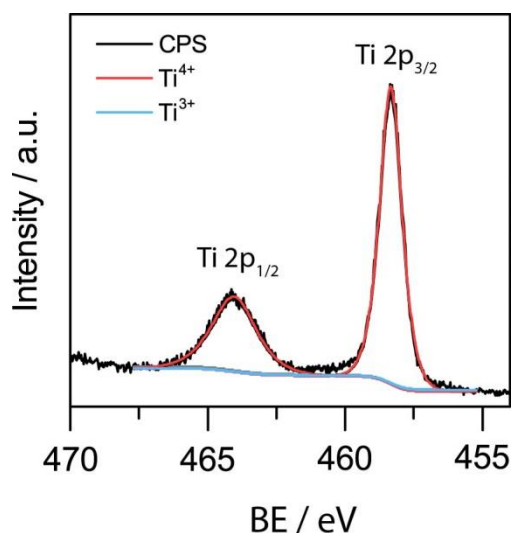


Figure 4-7. Ti 2p detail spectrum of P25.

Peak	$Ti^{4+} 2p_{3/2}$	$Ti^{4+} 2p_{1/2}$	Δ_{oxide}	$Ti^{3+} 2p_{3/2}$ or background	$Ti^{3+} 2p_{1/2}$ or background	Δ_{oxide}
BE / eV	458.3	464.0	5.7	457.3	462.5	5.2
fwhm / eV	0.96	1.89		2.00	3.97	
%	66.3	33.3		0.3	0.2	

Table 4-3. BE values, fwhm and area % of the individual components of the Ti 2p detail spectrum of P25.

4.4.4. VB

The band structure of TiO_2 has been investigated in theoretical studies and can schematically be depicted in a molecular orbital (MO) diagram.^{172, 233}

Figure 4-8 shows the molecular-orbital (MO) diagram of anatase TiO_2 , the main component in P25, as constructed by Asahi et al..¹⁷² In their work, the authors calculated that the lower VB is mainly of O 2s character, while the upper VB is made up of O 2p and Ti 3d orbitals. In its solid form, a Ti atom can be seen to be at the center of a distorted octahedral ligand field of oxygen atoms (TiO_6), which splits the Ti 3d states into two energy levels, namely the doubly-degenerate e_g ($d_{x^2-y^2}$, d_{z^2}) and the triply-degenerate t_{2g} state (d_{xy} , d_{xz} , d_{yz}). Due to the distortion of the ligand field the t_{2g} states are further discriminated in energy according to the Jahn-Teller effect. For a complete representation of the crystalline TiO_2 network, the O atom is also considered as being at the center of Ti_3O clusters (section 1.2.4). The 2p orbitals of O are split into σ (in the TiO_3 cluster plane, lower energy) and π states (out of the TiO_3 cluster plane, higher energy).

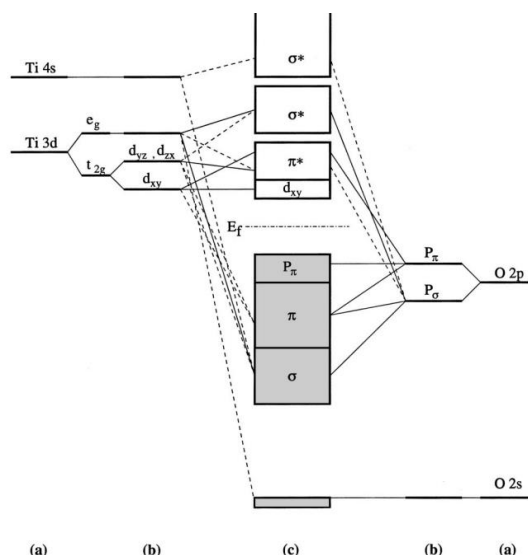


Figure 4-8. Molecular-orbital diagram for anatase. Reprinted with permission from ref. 172. Copyright 2001 American Chemical Society.

The VB can now be distinguished into 1) a σ bonding region at the lowest energy, consisting mainly of O 2p $_{\sigma}$ states, 2) a π bonding region between the t_{2g} and the O 2p $_{\pi}$ states at a middle energy level and 3) a non-bonding region where hybridization between O 2p $_{\pi}$ states and the metal d orbitals is negligible.

The CB is then composed of the respective anti-bonding states, where the d_{yz} and d_{zx} are the main contributors. In contrast to rutile, anatase has isolated d_{xy} orbitals at the bottom of the CB due to the less dense structure.¹⁷²

Figure 4-9 shows the VB-XPS spectra of P25 with a) individual components of the VB states based on the fit by Luciu et al. and b) determination of the valence band maximum (VBM).¹³³ BE, fwhm, and composition agrees very well with the reported values and are listed in Table 4-4. Additionally to the diverse VB states, a peak due to either hydroxyl groups (OH3 σ) or molecular water (a_1) occurs at 10.5 eV. Furthermore, the VB maximum (VBM) can be determined by the intersection of the background with the tangent of the VB edge at the point with the maximum slope. Due to the often noisy signal for the VB spectra, this kind of determination cannot be considered to be exact, but still gives a solid base for comparison, in particular between samples of the same kind.

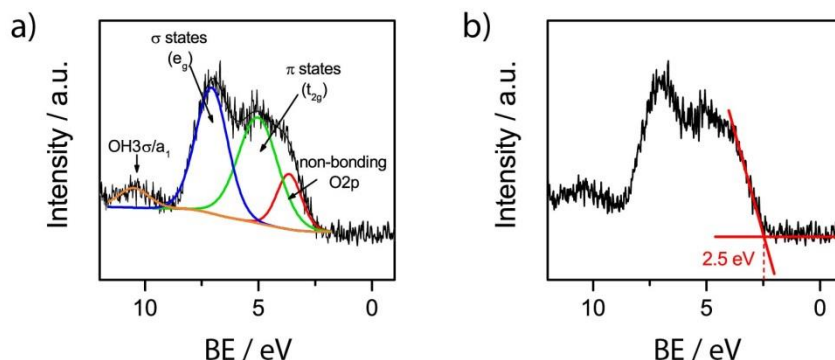


Figure 4-9. VB spectrum of P25 with a) individual components as suggested by ref. 133 and b) determination of the valence band maximum (VBM).

Peak	<i>non-bonding O2p</i>	<i>π states</i>	<i>σ states</i>	<i>OH3σ/a₁</i>
BE / eV	3.7	5.0	7.1	10.5
fwhm / eV	1.28	2.06	1.67	1.58
%	13.4	41.2	39.6	5.9

Table 4-4. BE values, fwhm and area % of the individual components of the VB spectrum of P25.

Reported literature values for the VB maximum (VBM) of TiO_2 are quite widespread with 1.2 eV at the lower end and 3.2 eV at the higher end of the range. In the following, I listed literature values for the VB edge for commercial P25 and rutile (Table 4-5), self-synthesized TiO_2 with the respective phase and synthesis method (Table 4-6) and black TiO_2 (Table 4-7). Clearly, there is a large range for the reported values even for commercial powders for which the slight variations to which BE the C-C signal is calibrated cannot account for. This could be explained by different work functions of different spectrometers. These could result in slight variations in the Fermi level alignment between TiO_2 and a spectrometer. The VB states would be more sensitive to changes in the Fermi levels, which could explain that I find deviations in literature with respect to VBM values but not for core-level values measured with XPS. However, I could not find any literature yet that discussed these varying results. Still, it seems not correct to speak of a “typical” or “characteristic” VB values, e.g. ref. 129.

Chapter 4 – Preliminary studies and characterization

TiO ₂ phase	how is the material obtained?	VB edge / eV	C-C calibration	reference
P25	commercial	3.2	285.1	49
P25	commercial	2.58	284.6	181
P25	commercial	1.2	284.6	187
P25	commercial	1.26	not given (also not in SI)	191
P25	commercial	2.05	not given (also not in SI)	188
P25	commercial	2.05	not given (also not in SI)	186
rutile	commercial	2.05	not given (also not in SI)	308
rutile	commercial	2.42	284.8	309

Table 4-5. Reported VBM values in literature for commercial TiO₂ samples.

TiO ₂ phase	how is the material obtained?	VB edge / eV	C-C calibration	reference
anatase	TTIP sol-gel	1.26	not given (also not in SI)	129
anatase	TTIP sol-gel	2.8*	not given (also not in SI)	181
anatase	TBOT sol-gel	~2	284.8	310
anatase	TBOT sol-gel	1.23	284.8	311
anatase	TiCl ₄ sol-gel	1.27	not given (also not in SI)	312
anatase	anodization	3.1	not given (also not in SI)	313
brookite	hydrothermal	2.37	not given (also not in SI)	314
rutile	"liquid-mix" method	3.2?	284.6	315
rutile	hydrothermal	1.2	284.6	316

Table 4-6. Reported VBM values in literature for self-synthesized TiO₂ samples.

TiO ₂ phase	how is the material obtained?	VB edge / eV	C-C calibration	reference
anatase	high P H ₂ reduction	-0.92	not given (also not in SI)	129
anatase	high P H ₂ reduction	1.25*	not given (also not in SI)	181
anatase	annealing in N ₂ an decarbonization	1.19	284.8	311
anatase	high P H ₂ reduction	2.45	284.6	177
anatase	electrochemical doping	3.6	not given (also not in SI)	313
brookite	aluminum-reduction	2.04	not given (also not in SI)	314
P25	ultrasonication	3.09-3.18	285.1	49
P25	ultrasonication	2.25 (tail 0.75)	284.6	317
P25	H ₂ fast cooling	0.6 + tail	284.6	187
P25	NaBH ₄ reduction	band tail 0.76	not given (also not in SI)	191
P25	aluminum-reduction	2.05	not given (also not in SI)	186
P25	H ₂ plasma	2.05	not given (also not in SI)	188
rutile	hydrothermally + H ₂ thermal annealing	1.2	284.6	316

Table 4-7. Reported VBM values in literature for black TiO₂ samples.

5 Deactivation

In this chapter, I will discuss deactivation of Pt-loaded TiO₂ during photocatalytic HER experiments under UV light irradiation in methanolic solutions, which is characterized by a sudden and unexpected drop in the H₂ evolution rate within the first hour of an experiment.

In the following sections, I will first briefly give a general impression of what I mean when I talk about deactivation. Following to this introduction, I will show that deactivation depends on several parameters that will be discussed in the consequent sub-sections (e.g. pretreatments, UV intensity, Pt loading, methanol concentration). The observed drop in rate was correlated to the amount of defects present in the system as well as a possible switch in mechanism for the photooxidation of methanol. Part of this work has been published by me in ACS Catalysis and in my master thesis.²³⁴⁻²³⁵

5.1. Deactivation in general

Figure 5-1 shows exemplary graphs for a stable (a), a gradual deactivating (b), and a fast deactivating (c) HER experiment of Pt-loaded P25 under UV light irradiation. The rates in all cases show the expected steady increase of the detected gas evolution rates during the first 20-30 min, which is the time that is needed to fill the dead volume of the tubing until the gas detector is reached. For the stable photocatalyst, gas evolution rates remain at a stable level until the end of the experiment as expected. In case of a gradually deactivating sample, a slow but distinct decrease in the gas evolution rate (here, -7% of the maximum H₂ evolution rate) during the course of the experiment is observed. Later, I will show that samples exhibiting gradual deactivation are prone to suddenly deactivate after prolonged

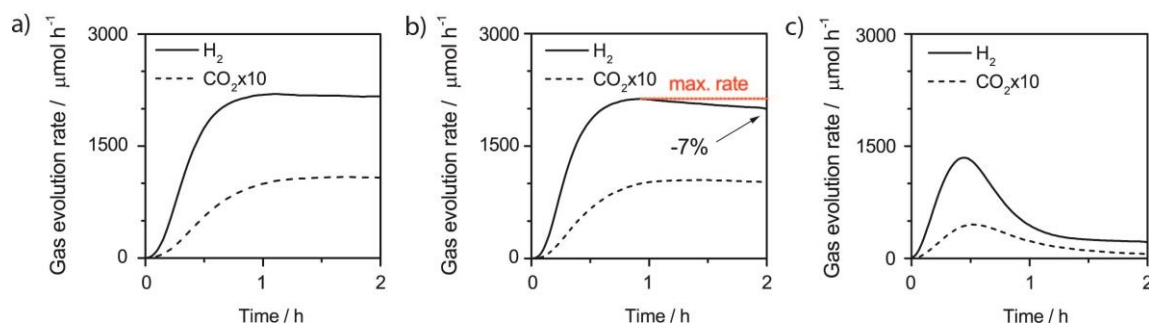


Figure 5-1. Exemplary graphs for a stable (a), a gradual deactivating (b), and a fast deactivating (c) HER experiment of Pt-loaded P25 under UV light irradiation.

UV exposure. Therefore, these rates should be seen as metastable. The fast deactivation type usually occurs during the first hour of an HER experiment and levels off to values that are comparable to reported literature values at similar conditions.

While both TiO_2 and Pt are benchmark materials in photocatalysis, these types of deactivation have not been discussed in the context of photooxidation of methanol. A few literature examples mention a decreasing rate during photocatalytic HER (section 1.2.4.3). For example, Kandiel et al. show strong variations in their H_2 evolution rate at very low methanol concentrations, which they assigned to different kinetics for intermediate formation. However, this was not discussed or investigated thoroughly.⁶⁶ Other reported losses in activity could be explained by active site poisoning with oxygen which is unlikely here, as I work under inert gas, or an increasing back reaction.^{51, 54}

Looking closer at reaction systems that operate at conditions and with materials comparable to ours, I note that our combination of online gas analysis and in situ photodeposition is quite unique: Usually, the Pt deposition step is separated from the actual photocatalytic reaction. I, however, look at the HER immediately when all active ingredients, i.e., the co- and photocatalyst, are put together resulting in a unique insight into the initial proceedings of this reaction. An overview of literature on HER with comparable reaction conditions can be found in Table 1-2 on p.24.

5.2. Role of defects

This chapter investigates the influence of defects, in particular oxygen vacancies, on the stability of HER. I will show that oxygen vacancies formed prior or during the reaction may have a detrimental effect on the stability of HER at certain conditions. I investigate the impact of different pretreatments, such as ultrasonication and calcination, as well as the influence of UV intensity changes and variations in the Pt loading. Characterization of recovered photocatalysts has been conducted by a wide array of characterization techniques, including DRS, TEM, Raman, XRD, and XPS as well as physi- and chemisorption measurements.

5.2.1. Photocatalytic experiments

5.2.1.1. Influence of ultrasound (US) on HER of Pt-TiO₂

Figure 5-2 shows the ultrasound(US)-dependent differences during a photocatalytic HER experiment under UV light in aqueous methanol solutions of P25 loaded with 0.4 wt.% Pt. The rates in both cases show the expected steady increase of the detected H₂ evolution rates during the first 20-30 min, which is the time that is needed to fill the dead volume of the tubing until the gas detector is reached. Afterwards, the pretreatment with US resulted in distinctly different H₂ evolution rates- H₂ evolution for the sample without pretreatment can be divided into three regimes: 1) a gradual decrease over approximately 10 h during which almost 45% of the maximum activity is lost (slow deactivation), 2) a sudden drop of activity within 3 h, which I refer to as fast deactivation, and 3) leveling off to a relatively stable value (4.7 mmol h⁻¹ g⁻¹) that is approximately 10 times lower than the maximum activity. Gradual declining H₂ evolution rates have been explained by pressure build ups and an increasing back reaction in batch reactors.⁵⁴ However, a gradual accumulation and blockage of reaction sites by intermediate products cannot fully explain the observed pretreatment dependence of the reaction or the Pt loading dependence as discussed in a later section (section 5.2.1.4). I explain the slow deactivation by an increasing degree of reduction through UV irradiation during the photocatalytic experiment that reaches a critical degree resulting in the unusual fast deactivation. The influence of UV will be discussed in more detail in the following section (see section 5.2.1.2). Interestingly, the rates after the fast deactivation and after leveling off to an again more or less stable value of roughly 5 mmol h⁻¹ g⁻¹ compare much better to literature reports at similar conditions than the maximum activities reached prior to deactivation (Table 1-2, p. 24).^{57, 103} Thus, I suggest, that deactivation actually may have happened in the cited literature already before the HER during the deposition step or it was not observed

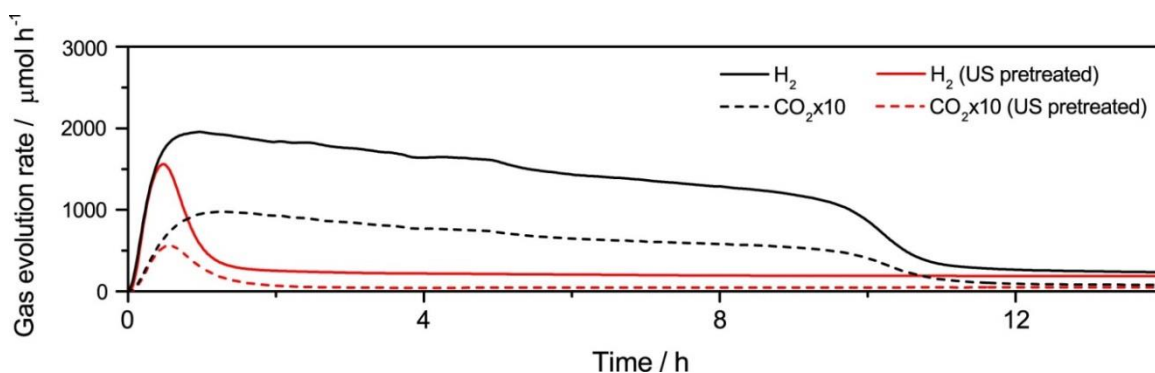


Figure 5-2. Photocatalytic HER experiment under UV light in aqueous methanol solutions of P25 loaded with 0.4 wt.% Pt. The red trace is for a sample that was pretreated with ultrasound (US, 1 min) prior to the experiment.²³⁴

during the reaction due to the chosen method of analysis.

I observe a distinctly different behavior for H₂ generation after a short US pretreatment. The pretreatment of only 1 min occurs prior to the experiment and before addition of the Pt precursor solution, so that only P25 is suspended in the reaction solution of aqueous methanol. Deactivation is observed within the first hour of an experiment and reaches a level comparable to that of the untreated sample of 4.2 mmol h⁻¹ g⁻¹. US irradiation creates a rough chemical environment through acoustic cavitation: Rapid implosion of cavitation bubbles results in approximate pressures and temperatures of several 100 bar and up to 5800 K inside the cavities, while the surrounding liquid may still approach 2400 K.²³⁶⁻²³⁹ Various mechanical effects such as microjets and shock waves invoked from the imploding cavities can damage the surface of a solid, while radicals, such as H• and OH• in water, form through the heat dissipated during cavity implosion and may oxidize or reduce inorganic compounds such as metal oxides.²³⁹⁻²⁴⁰

Creation of oxygen vacancies through mechanical or radical pathways (or both) has been reported in literature for various metal oxides including TiO₂ (e.g. ZnO, ZrO₂, Fe₂O₃, SnO₂,¹⁵¹ SiO₂,¹⁴⁷⁻¹⁴⁸ MoO₃,¹⁵⁰ Nb₂O₅¹⁴⁹). For example, Osorio-Vargas et al. showed that a low-frequency US treatment of TiO₂ creates oxygen vacancies, whereas Bellardita et al. found that oxygen vacancies generated by US (at comparable frequencies as in this work) were almost irreversibly formed in the bulk of TiO₂ and increased the photocatalytic activity for glucose conversion under visible light due to an increased light absorption.^{49, 146} As discussed in the introduction chapter, oxygen vacancies can have a large impact on the photocatalytic activity depending on the concentration, type and distribution (section 1.3.4). Therefore, it seems like there is a clear correlation between the US pretreatment, the creation of oxygen vacancies and the observed enhanced fast deactivation.

Increasing the duration of US treatment from 1 to 30 min, only results in a comparably small change in observed H₂ rates from ~1900 μmol h⁻¹ to ~1500 μmol h⁻¹ (-20%) (Figure 5-3.a). The general timing and shape of the deactivation is not changed by prolonging the US treatment. Thus, short treatments are conducted for all experiments investigating the effect of US pretreatment. Furthermore, to exclude a detrimental effect from methanol during US pretreatment, I also performed the ultrasonication of P25 in pure water adding the methanol only afterwards (Figure 5-3.b). Pt-loaded P25 still deactivated, but much earlier and with overall lower activities, showing that methanol might even have a protective effect during ultrasonication by acting as radical scavenger.

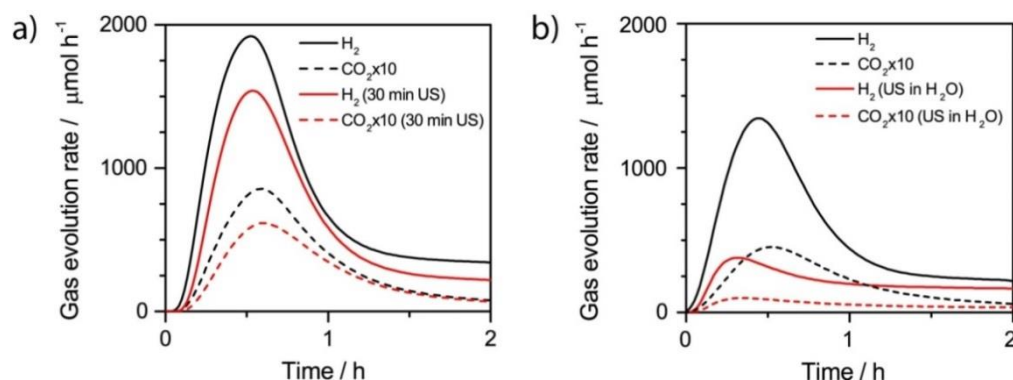


Figure 5-3. Investigation of different US treatments on HER: a) increasing the duration of the US pretreatment from 1 (black) to 30 min (red), b) performing the US pretreatment in water (red) instead of aqueous methanol solution (black).

In conclusion, US pretreatment of P25 in water or aqueous methanol solutions results in a sudden deactivation during HER under UV irradiation. As US is known to be able to reduce TiO₂ and create oxygen vacancies, these results suggest a defect-dependence of the observed deactivation.

5.2.1.2. Influence of UV intensity on HER of Pt-TiO₂

The effect of the US pretreatment discussed in the previous section suggests that deactivation depends on the concentration of oxygen vacancies in TiO₂. Another possible source of reduction during the reaction is UV irradiation. Reduction of metal oxides, e.g. TiO₂, surfaces by photons is a known process called “photoreduction”, in which defect formation is induced by trapping of charge carriers and excitons.^{56, 141-145} For example, photogenerated holes can oxidize either lattice oxygen or surface hydroxyls and thereby create an oxygen vacancy and a trapped electron at a Ti³⁺ site as shown in FTIR studies.¹⁴²⁻¹⁴³

Figure 5-4 shows the effect of different UV intensities on the deactivation behavior during HER of Pt-loaded TiO₂. In a first set of experiments, I chose a Pt loading that is sensitive to the US pretreatment at a UV light intensity of ~30 mW cm⁻², i.e. the HER only shows a slow type of deactivation without US pretreatment but deactivates fast after US pretreatment (section 5.2.1.1, see section 5.2.1.4). When decreasing the UV light intensity by a factor of 10, the slowly deactivating sample shows a 4-fold decrease in the HER rate, while exhibiting a now completely stable curve (Figure 5-4a). The decrease in activity is not linearly correlated to the decrease in the light intensity. Previous reports show, that depending on the light intensity kinetics can change from a linear to square-root dependence. At low light intensities (absolute values not mentioned), band bending dominates charge separation and a linear dependence of the rate is usually observed, while band

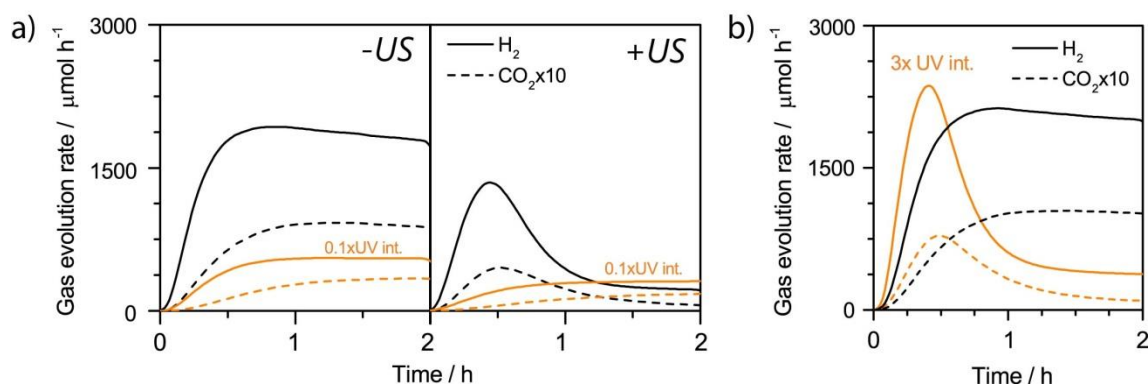


Figure 5-4. HER experiments at varying UV intensities and fixed Pt loadings. a) 10-fold decrease of UV intensity (orange) of 0.4 wt.% Pt-loaded P25 with and without US pretreatment. b) 3-fold increase of UV intensity (orange) for 0.75 wt.% Pt-loaded P25.²³⁴

bending is not as pronounced at higher intensities and surface reactions start to dominate the rate resulting in a square-root dependence. For example, Nomikos et al. showed a linear dependence of the rate at an intensity of 3 mW cm^{-2} , which would correspond well to the low intensity experiment, while we can assume that a 10-fold higher light intensity may already be in the regime of a square-root dependence.¹⁰⁵ Changes in the order of dependence between kinetics and light intensity, may therefore explain the observed non-linear correlation between the rate and changes in UV intensity.

Even more interesting in the context of deactivation, decreasing the UV intensity can completely prevent the rapid deactivation in the US pretreated sample and results in stable H_2 generation rates. Indeed, I can trigger deactivation in formerly stable conditions, when I increase the UV intensity by a factor of 3 at otherwise fixed conditions (Figure 5-4b).

This is in line with my argumentation that deactivation is triggered by oxygen vacancies, which in this case are photoinduced during the HER itself. Reducing the UV intensity would simultaneously decrease the degree of reduction, which might be the reason for the prevention of deactivation. If we reverse the way of thinking, increasing the degree of reduction (as, for example, by the US pretreatment) should thus lead to a destabilization of the H_2 evolution rate.

5.2.1.3. Calcination of P25 prior to HER experiments

Calcination is a common method to heal oxygen vacancies in a metal oxide. Thus, treating TiO_2 in oxygen or air should have a positive effect on the stability of the photocatalyst according to this line of logic. Indeed, calcination of P25 at 400°C for 5 h in air prior to the HER experiments, results in a stable HER rate at condi-

tions that otherwise lead to a fast deactivation of the photocatalyst (Figure 5-5). This experiment further supports the importance of oxygen vacancies for the stability of photodeposited Pt on TiO_2 . Interestingly, a positive effect of precalcination of TiO_2 during incipient wetness impregnation of $\text{TiO}_2(\text{B})$, another less known and metastable polymorph of TiO_2 , has been reported before for H_2 production in ethanol and was attributed to less strong interactions between the noble metal and TiO_2 .⁶²

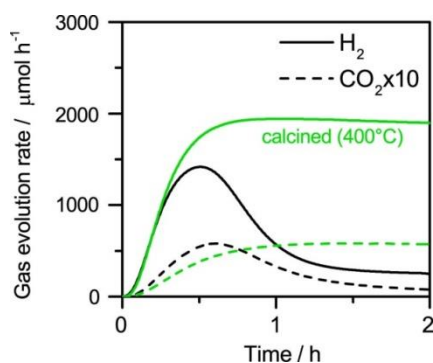


Figure 5-5. HER for pristine P25 (black) and P25 oxidized in air at 400 °C for 5 h (green).²³⁴

5.2.1.4. *Pt loading dependence of deactivation*

During my investigations of the different effects of pretreatment and UV intensity, I already noticed differences in the stability of the photocatalysts depending on the Pt loading. Therefore, I performed two sets of experiments in which I varied the Pt loading from 0 to 1.5 wt.% with and without US pretreatment at otherwise fixed conditions (Figure 5-6).

Generally, an increase in Pt loading results in an increase of available active sites for the HER, which results in higher H_2 evolution rates as I also observe for loadings up to 0.75 wt.% Pt. I do not obtain higher maximum rates when increasing from 0.75 wt.% to 1.5 wt.%, which shows that the number of active sites is no longer the rate-limiting factor at these loadings, but rather diffusion limitations and reaction kinetics control the H_2 production. Clear differences in the stability depending on the Pt loading and US pretreatment are observed, that can be divided into three different loading regimes:

- 1) At low loadings (here: 0.25 wt.% Pt), fast deactivation always occurs independent of whether US was applied or not prior to the experiments. Note, that in the absence of Pt, I only observe minor activity that is in the same

range as that for pure methanol reforming as observed in the absence of TiO_2 . Thus, deactivation is clearly related to the co-catalyst.

- 2) At intermediate loadings (here: 0.4 wt.% Pt), stability depends on the US pretreatment. Deactivation can be triggered by ultrasonication prior to the HER experiment, while in the absence of such a pretreatment I observe a relatively stable rate with a slow deactivation as described previously (section 5.2.1.1).
- 3) At high loadings (here: >0.75 wt.% Pt), the HER is again independent of the US pretreatment and I do not observe fast deactivation anymore. This regime could be subdivided further, as I still observe a slow type of deactivation at 0.75 wt.% Pt, while rates are completely stable at loadings higher than 1.0 wt.% Pt. The absolute H_2 generation values as well as quantum efficiencies are listed in Table 5-1.

These three different loading regimes (low, intermediate, high) may differ in their absolute values between the type of TiO_2 (see section 5.7) as well as other reaction parameters such as UV intensity. In order to explain the different stabilities, I need to consider the changes that are induced by increasing the amount of Pt on TiO_2 . Increasing the amount of Pt may result in an increase in particle size or number. Thus, I either observe a size effect or the number of particles is critical for stable H_2 evolution rates. Pt particles have been shown to be stable in size up to 2 wt.% in previous work by Kiwi and Grätzel, which – while using a different deposition technique and conditions – would render the number effect more likely.⁴³ From my previous experiments, I suggested that oxygen vacancies trigger deactivation. Oxygen vacancies are also the preferred nucleation site of Pt.¹⁶⁸ Thus, I suggest that rates stabilize due to an increase in the Pt particle number

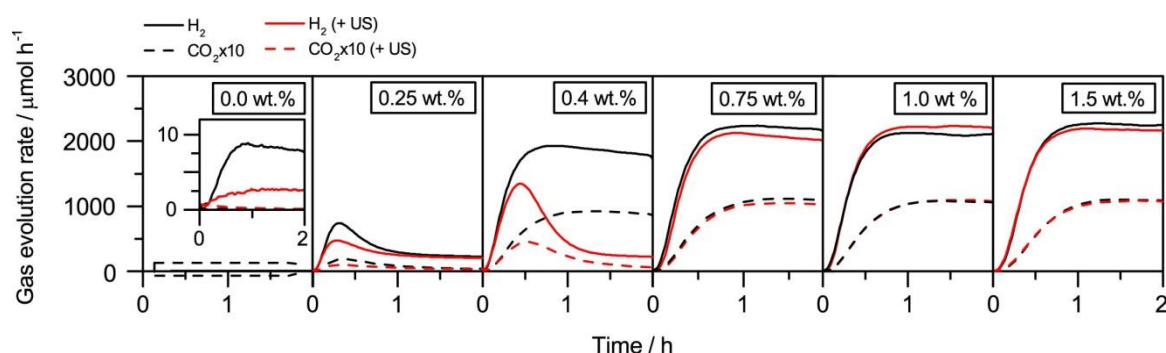


Figure 5-6. Gas evolution rates during photocatalytic HER for a series of P25 loaded with different amounts of Pt. Black traces represent experiments without US pretreatment. Red traces represent experiments with US pretreatment. Deactivation is observed at low Pt loadings independent of the pretreatment with US (e.g., 0.25 wt %) but not at high Pt loadings (≥ 0.75 wt %).²³⁴

that also quench or stabilize oxygen vacancies on the metal oxide surface. This is supported mainly by TEM and Raman studies as will be discussed in the following section that covers a thorough characterization of photocatalysts recovered after the photocatalytic experiments.

Pt loading	US? (Y/N)	Deactivation? (Y/N)	max. H ₂ rate/after deactivation ($\mu\text{mol h}^{-1}$)	max. H ₂ rate/after deactivation ($\text{mmol h}^{-1} \text{g}^{-1}$)	QY ($\lambda = 280 - 500 \text{ nm}$)	QY ($\lambda < 400 \text{ nm}$)
0.0 wt. %	N	N	8.8	0.17	0.13	0.26
0.0 wt. %	Y	N	2.8	0.056	0.04	0.08
0.25 wt. %	N	Y	739 / ~235	14.8 / ~4.7	11 / 3	22 / 7
0.25 wt. %	Y	Y	472 / ~210	9.4 / ~4.2	7 / 3	14 / 6
0.4 wt. %	N	N	1930	38.6	28	56
0.4 wt. %	Y	Y	1345 / ~235	26.9 / ~4.7	19 / 3	39 / 7
0.75 wt. %	N	N	2238	44.8	32	65
0.75 wt. %	Y	N	2128	42.6	30	62
1.0 wt. %	N	N	2127	42.6	30	62
1.0 wt. %	Y	N	2233	44.7	32	65
1.5 wt. %	N	N	2277	45.5	33	66
1.5 wt. %	Y	N	2196	43.9	31	64

Table 5-1. Overview on the photocatalytic activities and corresponding quantum yields (QY) for all materials shown in this work correlated to their pretreatment using ultrasound (US) and (if applicable) the observed deactivation.²³⁴

5.2.1.5. Brief summary & conclusions of photocatalytic experiments

I observe an unusual deactivation of the H₂ evolution rates of the benchmark photocatalyst P25 onto which Pt is photodeposited in situ during the reaction. Experiments with different pretreatments, i.e. US or calcination, as well as changes in the UV light intensity suggest that oxygen vacancies trigger this deactivation. Furthermore, the stability of H₂ generation is governed by the Pt loading at otherwise fixed conditions and may be due to an increase in either Pt particle size or number, which will be discussed in the following section.

5.2.2. Ex situ characterization

I investigated P25 loaded with Pt and recovered after photocatalytic experiments for morphological and structural changes using TEM, DRS, physi- and chemisorption, Raman, FTIR, XRD and XPS as discussed in the following subsections. With this set of characterization techniques I am able to further narrow down the rea-

son for deactivation by excluding major structural changes in phase composition or surface area and obtaining evidence for possible strong metal-support interactions during the reaction.

5.2.2.1. BET

BET measurements of pure P25 treated with US, UV, a combination of both as well as the pre-calcined P25 does not show any differences in the specific surface areas.

BET surface areas vary slightly with average value of $57 \pm 10 \text{ m}^2 \text{ g}^{-1}$ for the Pt-loaded samples. The large error is due to some exceptions: For example, a surface area of only $41 \text{ m}^2 \text{ g}^{-1}$ of 0.25 wt.% Pt-loaded P25 and a surface area of $83 \text{ m}^2 \text{ g}^{-1}$ of a 1.0 wt.% Pt-loaded sample compared to the characteristic $55 \text{ m}^2 \text{ g}^{-1}$ of pristine P25. However, there are no trends or correlations between surface area variation and US treatment or deactivation. Specific surface area values can be found in Table 5-2 (p. 98).

5.2.2.2. XRD

There are no changes in the XRD patterns between the P25 reference, UV/US-treated P25, and Pt-loaded P25 recovered after HER experiments (Figure 5-7, Table 5-2 (p. 98)). The phase composition as computed by an empirical equation by Myers and Spurr gives approximate values of 82% anatase and 18% rutile phase for all samples (equation (5.1)).²⁴¹

$$(5.1) \quad \chi_a = \frac{1}{1 + 1.26 \frac{I_R}{I_A}}$$

, where χ_a is the anatase fraction in the sample, and $\frac{I_R}{I_A}$ is the ratio of the intensity of the strongest rutile reflection to the strongest anatase reflection. This equation gives approximate values of 82% anatase and 18% rutile phase for all samples but does not account for the amorphous fraction that is inherent to P25 as shown by Ohtani et al. through selective dissolution of P25, so that the absolute values for anatase and rutile phase will deviate in reality.⁹⁴ Nevertheless, Myers' equation can be used as tool for comparing relative phase changes in reference to P25.

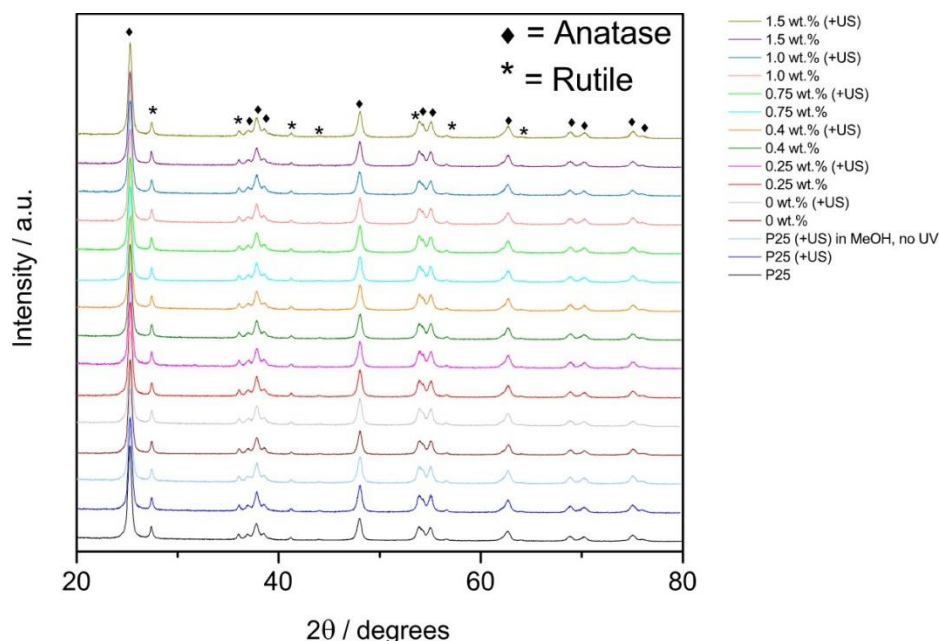


Figure 5-7. Powder XRD patterns of Pt-loaded P25, pristine P25 as well as P25 subjected to US in water and methanol solution for reference.²³⁴

5.2.2.3. DRS

DRS spectra of P25, P25 treated with US/UV as well as the pre-calcined P25 were recorded (all without Pt). As the US and UV-treated samples are recovered from aqueous solutions, I also measured the DRS spectra of pristine P25 and the calcined P25 after simply dispersing the powders in aqueous methanol solutions and recovering them by filtration.

Figure 5-8 shows the Tauc plots of these samples for band gap estimations. The dry powders of P25 and P25 calcined at 400 °C show the typical band gap of 3.18 eV.^{38, 242-243} Interestingly, the DRS absorption spectra after the dry powders have been exposed to water or aqueous methanol solution red-shifts significantly by 0.16 eV from 3.16 eV to 3.00 eV independent of whether UV or US has been applied or not. This type of red-shift is generally attributed to the creation of Ti^{3+} centers.¹²⁶ The red-shift seems to occur only in the anatase fraction of the sample, which agrees with literature suggesting that anatase is more easily reduced than rutile.²⁴⁴ While the US treated samples seem to show a slightly more pronounced red-shift, these differences are too small to strongly support a real effect by the US treatment.

As there are no clear differences between the treated samples (UV, US, calcined) and pristine P25 exposed to the aqueous solutions, the red-shift more likely results from surface hydroxylation than from oxygen vacancy creation by any of my treatments. This is not completely surprising as I assume that defects generated by US or UV form on the surface and would likely reoxidize immediately upon exposure to air (especially in absence of Pt that may act as a stabilizer for defects). Transient defect species may still have a large impact on the reaction mechanism in the dynamic environment of the HER. In line with BET, Raman, XRD and XPS measurements, DRS spectra do not change between samples being treated with US in pure water or aqueous methanol solution, which further excludes a detrimental effect by methanol and corroborates that the observed deactivation stems from the metal oxide surface.

Figure 5-9 shows the DRS spectra of P25 recovered after HER experiments with Pt loadings increasing from 0-1.5 wt.%. Absorption in the visible light range increases while the optical band gap slightly decreases with an increasing Pt loading, which is in agreement with literature.^{58-59, 245} There are no differences between samples treated with and without US. Band gap values as estimated from Tauc plots are listed in Table 5-2. The clear red-shift that has been attributed to surface hydroxylation above can be observed between pristine P25 and P25 loaded with 0 wt.% Pt, which corresponds to P25 irradiated with UV in the aqueous methanol solution.

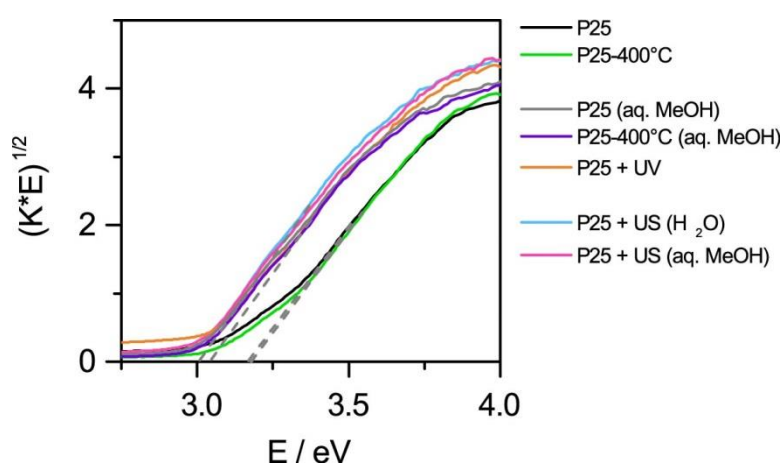


Figure 5-8. Tauc plots of dry P25 (black), P25 treated with US in methanol (magenta) and water solutions (blue), P25 treated with UV (orange) as well as the dry pre-calcined P25 (green) (all without Pt). As the US and UV-treated samples are recovered from aqueous solutions, pristine P25 and the calcined P25 are also measured after dispersion in aqueous methanol solutions (violet, grey).

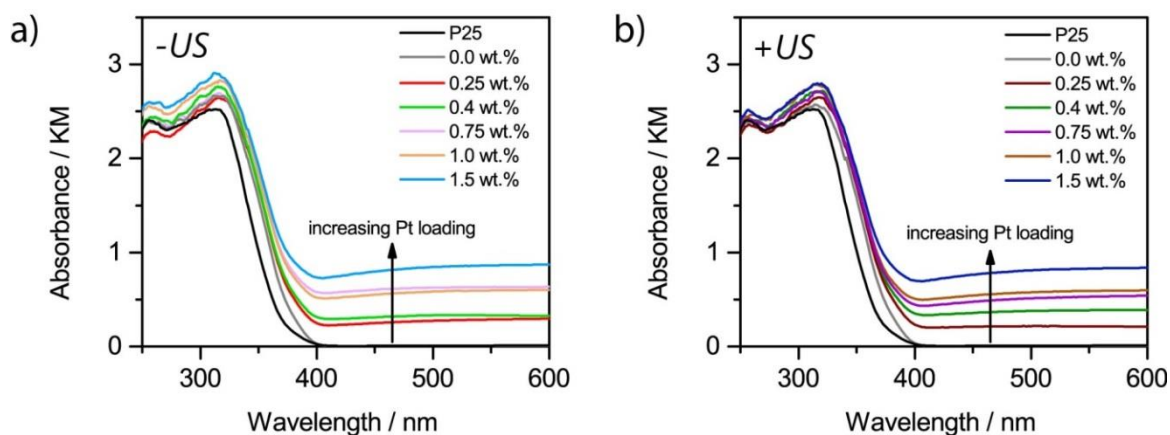


Figure 5-9. Absorption spectra for P25 and P25 loaded with different amounts of Pt recovered after HER experiments: a) no US pretreatment, b) US pretreatment.

5.2.2.4. Overview: BET, XRD, DRS

Pt / wt. %	US / min	MeOH:H ₂ O / v:v	UV / h	Deactivation?	BET / m ² g ⁻¹	E _g / eV	I _R /I _A
0.0 (pristine P25)	---	---	---	---	55.3	3.18	0.18
0.0	30	0:1	---	---	53.2	2.99	0.18
	30	1:1	---	---	52.6	3.00	0.17
0.0	0	1:1	2	---	55.6	3.03	0.16
	1	1:1	2	---	45.8	3.03	0.18
0.25	0	1:1	2	Y	41.1	3.03	0.17
	1	1:1	2	Y	41.2	3.03	0.20
0.4	0	1:1	2	N	64.3	3.02	0.17
	1	1:1	2	Y	59.5	3.00	0.18
0.75	0	1:1	2	N	62.9	2.92	0.17
	1	1:1	2	N	60.2	2.98	0.18
1.0	0	1:1	2	N	61.9	2.94	0.18
	1	1:1	2	N	82.9	2.96	0.18
1.5	0	1:1	2	N	56.4	2.88	0.18
	1	1:1	2	N	60.1	2.91	0.19

Table 5-2. Overview of BET measurements, band gap calculations from DRS, and phase composition from XRD patterns for the different Pt-loaded P25 samples and their references.

5.2.2.5. FTIR

FTIR measurements of recovered photocatalysts further support that defect sites, i.e. oxygen vacancies, act as adsorption sites for Pt as already described in previous work of the author (Figure 5-10). Characteristic methanol bands at 2978 and 2891 cm^{-1} due to the symmetric and antisymmetric stretching of the CH_3 -group of adsorbed methoxy species, respectively, appear for all samples exposed to methanolic solutions.⁵⁵ The bands decrease with increasing Pt loading as more Pt particles deposit at defect sites, which are in turn unavailable for methanol adsorption. I also observe an increase in the CO_2 (2360 and 2338 cm^{-1})²⁴⁶ and $\delta\text{-OH}$ bands (1620 cm^{-1})²⁴⁷, which I correlate to atmospheric CO_2 and H_2O adsorbed onto Pt, likely due to exposure to atmosphere (not shown). Otherwise, I did not observe an increasing surface hydroxylation or other changes in the IR spectra that could explain deactivation during HER.

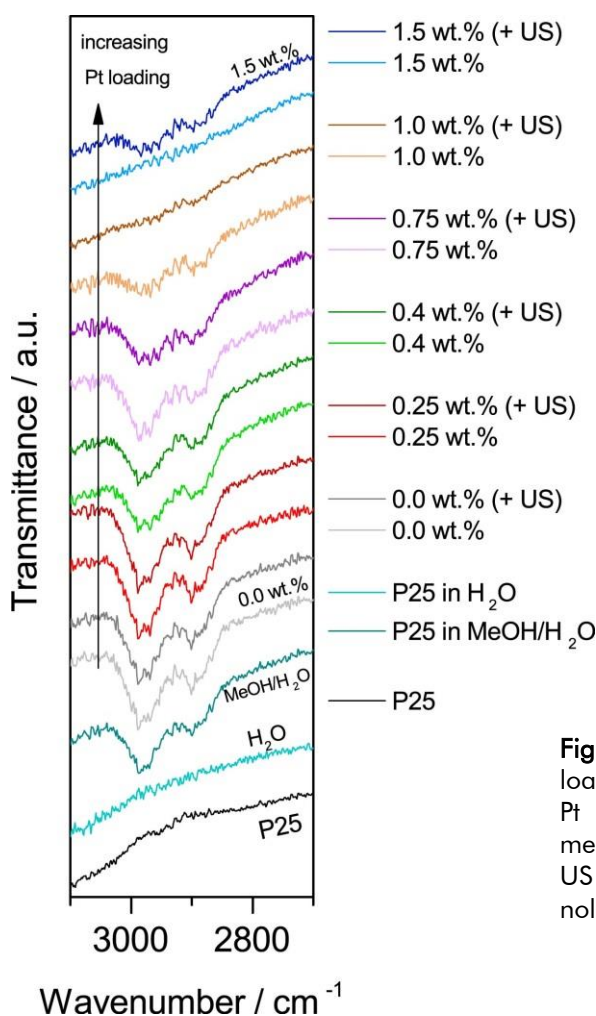


Figure 5-10. FTIR spectra of P25 loaded with different amounts of Pt recovered after HER experiments, as well as P25 subjected to US in water and 50 vol.% methanol solution for reference.

5.2.2.6. Raman

Raman spectra of P25, and P25 treated with US, UV, or a combination of both does not show any differences in the band positions or widths indicating no permanently induced crystal lattice strain by the different treatments (Figure 5-11).

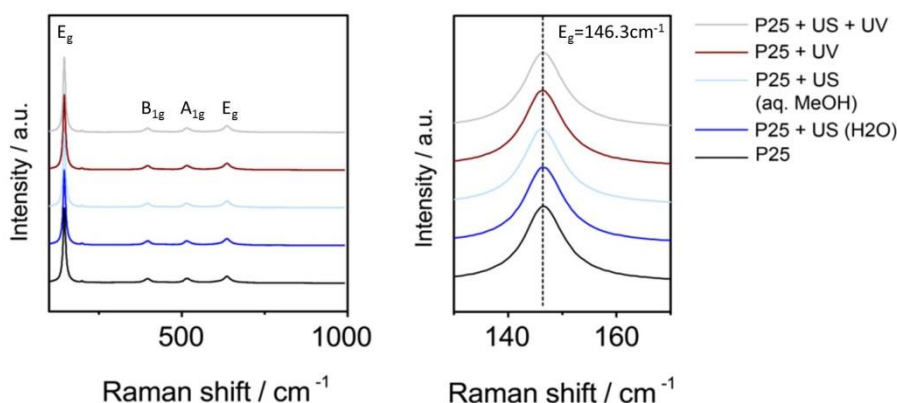


Figure 5-11. Raman spectra of P25 and UV and/or US irradiated P25: complete Raman spectra (left) and close-up of E_g mode (right).

Figure 5-11 shows the Raman spectra of Pt-loaded P25 recovered after HER experiments compared to pristine P25. Typical Raman modes of anatase TiO_2 – the main phase in P25 – are observed: E_g (146.3 cm^{-1} , 200.5 cm^{-1} , 641.5 cm^{-1}), B_{1g} (399.6 cm^{-1}), and an A_{1g} mode (515 cm^{-1} superimposed by 519 cm^{-1}).^{170, 179} I observe a significant peak broadening and shift of the E_g mode at 146 cm^{-1} , contra-

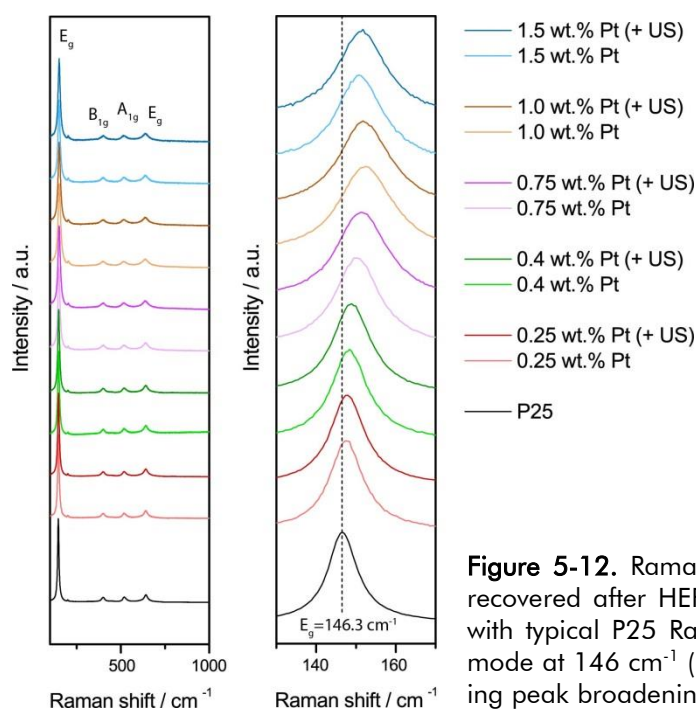


Figure 5-12. Raman spectra of P25 and Pt-loaded P25 recovered after HER experiments: (left) complete spectra with typical P25 Raman modes (left) and close-up of E_g mode at 146 cm^{-1} (right). The E_g modes show an increasing peak broadening and shift with an increasing Pt load-
--- 233

ry to P25 in absence of Pt. Peak shift and broadening can be attributed to lattice strain or size effects. Šćepanović et al. showed that at low temperatures, phonon-confinement due to a small grain size and nonstoichiometry have a large impact on observed broadenings and shift.²²⁸ As I do not observe any changes in the crystallite size, I attribute the observed broadenings and shifts to the increased presence of oxygen vacancies. The broadening and shift is more pronounced with increasing Pt loadings, which I attribute to a stabilization of defect sites by Pt as oxygen vacancies are the preferred adsorption site for Pt.¹⁶⁸ This is in line with my argumentation that there is a critical ratio of oxygen vacancies to Pt particle and stabilization of defect sites by Pt particles has a stabilizing effect on the H₂ evolution rate as observed in the photocatalytic experiments (see section 5.2.1.4).

5.2.2.7. XPS

XPS studies of the recovered Pt-loaded P25 compared to pristine P25 can give insight into possible changes in the oxidation states of Ti (e.g. due to Ti³⁺ formation) and Pt. I chose the previously observed three different Pt loading regimes with and without prior ultrasonication for a more detailed investigation (section 5.2.1.4): 1) 0.25 wt.% for the low loading that deactivated independent of the US pretreatment, 2) 0.4 wt.% Pt for the intermediate loading that shows a dependence on the US pretreatment, and 3) 1.5 wt.% that shows a stable H₂ evolution

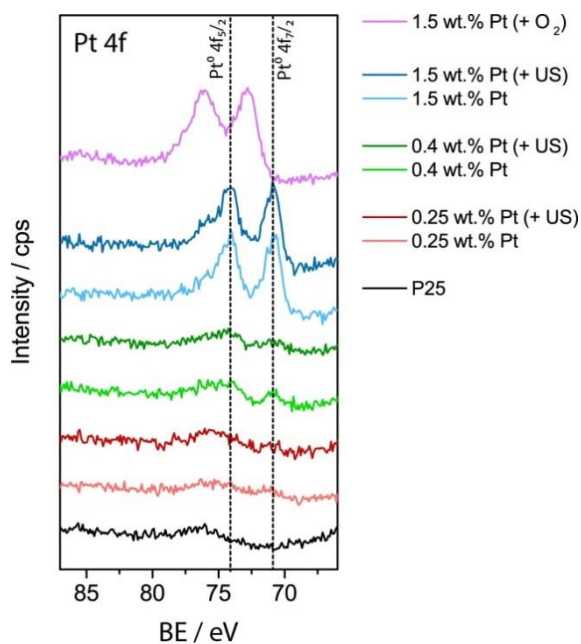


Figure 5-13. XPS Pt 4f spectra of pristine P25 and Pt-loaded P25 recovered after photocatalytic HER experiments. Pt-loaded P25 poisoned with O₂ is given as reference for a higher Pt oxidation state.²³³

rate again independent of prior ultrasonication.

The C 1s, O 1s, and Ti 2p detail spectra show typical shapes of adventitious carbon and TiO₂ as described in an earlier section ((4.4.1)-(4.4.3)). There are no signals stemming from Ti³⁺ which would evidence the presence of oxygen vacancies in my samples. Also no increased surface hydroxylation can be observed as suggested by DRS results.

The Pt 4f detail spectra show some differences between the different loading regimes, although signal intensities at the low loadings are too low to draw hard conclusions (Figure 5-13). Compared to P25, samples loaded with 0.25 and 0.4 wt % Pt show a faint signal that lies in the range of metallic Pt⁰ (Pt 4f_{7/2} = 70.8 eV; Pt 4f_{5/2} = 74.1 eV).²⁴⁸⁻²⁴⁹ Interestingly, also pristine P25 has a weak signal at 76.0 eV. As there are no other elements besides Ti, O and C (from adventitious carbon) in this sample, this could be caused by a 3s shake-up of Ti. While Pt signals for 0.25 and 0.4 wt.% are very low in intensity, the Pt 4f_{7/2} signal clearly evidences the presence of Pt and deviates from the background shake-up signal. At 1.5 wt % Pt (=stable), I see the distinct signal of metallic Pt, while also observing a clear shoulder towards higher BE, i.e. a higher oxidation state of Pt, that the 3s shake-up signal can only partially account for.^{248, 250-251} As reference for a higher oxidation state, I oxidized Pt to Pt²⁺ by bubbling O₂ gas through the reaction solution during photodeposition of Pt. The Pt 4f signals for this sample shift by about 2 eV to higher BE in agreement with literature (Pt²⁺: Pt 4f_{7/2} = 72.8 eV; Pt 4f_{5/2} = 76.1 eV) and with the shoulder of 1.5 wt.% Pt-loaded P25. Pt signals at low loadings (=deactivated) are very weak, but seem to also lie in the range of oxidized Pt. As I work in an otherwise O₂-free environment, oxidation of Pt during a regular HER experiment would likely be caused by adsorption of other oxygen-containing species onto Pt.

5.2.2.8. TEM

I use TEM in order to investigate Pt particle size distribution at the various Pt loadings discussed in a previous section (section 5.2.1.4) as well as possible morphological changes in the photocatalyst between a stable and a deactivating sample as well as the.

5.2.2.8.1. Particle size distribution (PSD) of Pt

Particle size distributions from TEM images show that the average particle size of Pt does not differ much between loadings of 0.25 (=deactivating) and 0.75 wt.% (=stable), while particles are roughly 0.5-1 nm larger in diameter at higher loadings (1.0 and 1.5 wt.% Pt) (Table 5-3). The stable size at lower loadings is in line with previous literature reports.^{43, 250} For example, Kiwi and Grätzel stated that the Pt particle size was stable at roughly 3.4 nm up to a loading of 2 wt.%.⁴³ As I already see a clear increase in stability of the H₂ generation rate at 0.4 and 0.75 wt.%, differences in Pt particle sizes are not the reason for different stabilities. As US pretreatment is suggested to introduce more defects in the form of oxygen vacancies, Pt particle sizes might be smaller for US-treated samples of the same theoretical loading as there would be more nucleation sites at the same amount of Pt. However, there is also no significant difference between the particle sizes of Pt on P25 with and without US treatment. The amount of oxygen vacancies introduced during the short ultrasonication treatment is likely not large enough to cause a size effect that is observable by TEM. In any case, changes in the size of Pt do not seem to be critical for whether H₂ generation is stable or not.

It seems like the number of Pt particles is more important in establishing a stable H₂ generation rate than the particle size. As sizes do not vary significantly, while the input amount of Pt increases, the overall number of particles has to increase as also evidenced by TEM. Furthermore, the absolute number of Pt particles cannot be the sole reason for deactivating or stable rates as, for example, an increase in UV intensity leads to deactivation or precalcination of P25 to stable rates at the same Pt loading as demonstrated in an earlier section (5.2.1.2). Thus, oxygen vacancies still seem to play an important role. Pt preferably deposits at vacancy

Pt / wt.%	US / min	Deactivated?	Median / nm
0.25	0	Y	3.03
	1	Y	3.46
0.4	0	N	3.08
	1	Y	3.05
0.75	0	N	3.06
	1	N	3.13
1.0	0	N	3.76
	1	N	3.53
1.5	0	N	4.35
	1	N	3.89

Table 5-3. Data from the particle size distribution for different Pt loadings on P25

sites. This means that the higher the Pt loading and thus number of particles the more vacancy sites are stabilized or quenched by Pt and unavailable for other reactions, e.g. decoration, adsorption of other reactants.

I conclude that there is a critical ratio between Pt particles and oxygen vacancies in TiO_2 at which deactivation is triggered. This ratio can be tuned by controlling the light intensity during HER as well as the pretreatments before HER (e.g., US, calcination).

5.2.2.8.2. Evidence for strong metal-support interactions (SMSI)

Figure 5-14 shows TEM images of a stable (a) and deactivated (b) Pt-loaded P25 sample recovered after photocatalytic HER experiments. The stable sample shows the typical TiO_2 crystals of P25 with crystal sizes between 15 and 25 nm for anatase ($d = 0.37 \text{ nm}$) onto which $\sim 3 \text{ nm}$ large Pt nanoparticles are deposited. Interestingly, in case of the deactivated Pt-P25 sample, Pt particles seem to be surrounded by a ca. 3 nm-thick shell of the same contrast as TiO_2 . The core of the 6 nm large particles on top of TiO_2 is darker in contrast and 3 nm in size which corresponds to the free Pt observed in the stable sample. The phenomenon of Pt being covered by titania species is well-known in classical heterogeneous catalysis under the name of “strong metal-support interactions” (SMSI).

While the influence of the support on the catalytic properties of noble metals was already reported before by Schwab²⁵² and Solymosi²⁵³, it was the work by Tauster et al. in 1981 that coined the term of SMSI.²⁰⁷ They showed a suppressed H_2 and CO chemisorption ability of H_2 activated catalysts that proved to be beneficial in

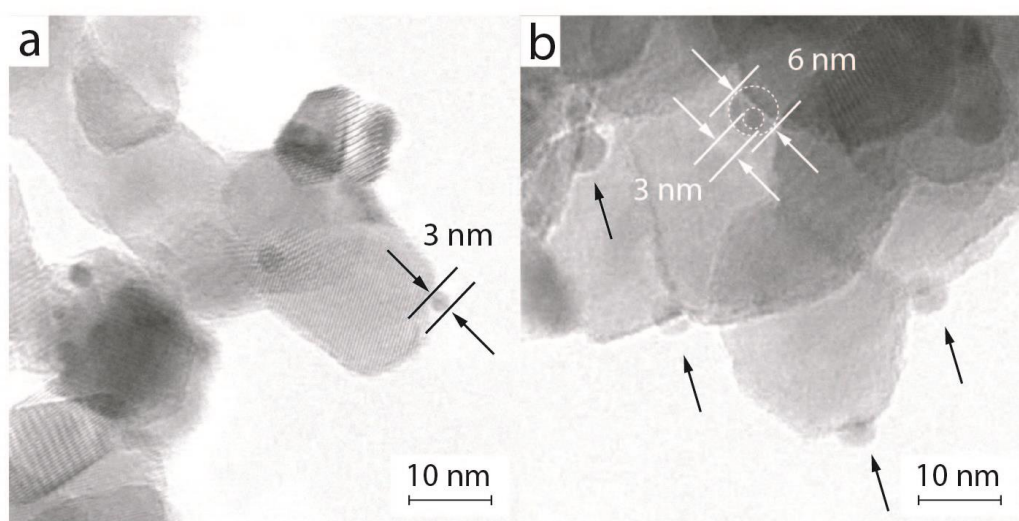


Figure 5-14. TEM images of a stable (a) and deactivated (b) Pt-loaded P25 sample recovered after photocatalytic HER experiment.

Fischer-Tropsch synthesis and was found to be a general phenomenon for noble metals on reducible metal oxide treated in reducing conditions.²⁰⁷ SMSI generally occur for noble metals that are supported on a reducible metal oxide support and exposed to reducing conditions such as H₂ treatment and are comprised of two major contributing factors: 1) decoration of the noble metal by suboxide species and 2) charge transfer between the support and the metal.²⁵⁴⁻²⁵⁶ The decoration or encapsulation model was first introduced by Simeons et al. and assumes that upon reduction of the metal oxide and creation of oxygen vacancies, substoichiometric TiO_{2-x} becomes highly mobile and is capable of decorating the surface of metal nanoparticles in order to satisfy its valency.²⁵⁷ In this way, active sites are blocked and the adsorption abilities at the metal surface are suppressed. Decoration or encapsulation is, however, generally only observed in vacuum or reducing atmospheres at high temperatures (>700 K). The interfacial charge transfer between the MO and the noble metal can occur at temperatures as low as 473 K. Electrons transfer from the reduced MO to the noble metal and accumulate, resulting in a decreased H₂ adsorption ability.²⁵⁴ The "shell" observed in Figure 5-14b would correspond to the decoration model, but has rarely been observed in the dried photocatalysts, maybe due to easy reoxidation of the suboxide shell. Thus, at this point in time it is not clear whether it is a measuring artifact induced by the TEM measurement itself or an actual feature of deactivation and due to the reducing experimental conditions.

5.2.2.9. *Chemisorption of CO*

A common technique to investigate the active sites and dispersion of noble metals on a support are chemisorption experiments, in which a probe molecule, e.g. CO or H₂, is adsorbed onto the noble metal, here Pt. Chemisorption is also a standard technique for investigations of SMSI effects: Depending on whether Pt is encapsulated or not, the probe molecule can adsorb or not. The following results were obtained in collaboration with the Ruhr-Universität Bochum, Germany. CO pulse experiments were performed after purging samples in He gas overnight in the hope that weakly adsorbed species would desorb. However, I did not obtain any meaningful value for the Pt dispersion and active surface area, e.g. no active surface area is measured for a clearly active photocatalyst. Catalysts are usually treated with an oxidative and/or reductive pretreatment to allow for a clean surface, as organic species from the reaction or atmosphere may still be adsorbed. Usually catalysts already experienced these conditions during the catalytic experiments or deposition of the noble metal, so that the cleaning step does not affect the measurement, or an additional H₂ reduction step is applied before the chemi-

sorption measurement in order to invoke SMSI. Since the experiments are all conducted at room temperature, a high temperature pretreatment would have nullified any observed result. However, the overnight purge is apparently not sufficient to obtain valid results.

CO adsorption studies coupled with IR conducted in a DRIFTS cell were conducted in collaboration with TU Eindhoven. DRIFTS spectra show the presence of large amounts of organic substances that are present on the photocatalysts as evident from very strong bands in the 2980–2840 cm^{-1} region ($-\text{CH}_3$, $-\text{CH}_2$ -stretching) as well as the broad band(s) in the 1700–1600 cm^{-1} region characteristic for C=O vibrations of oxygenates (ketones, aldehydes, carboxylic acids) (Figure 5-15).²⁵⁸⁻²⁶¹ Adsorption of CO on recovered samples is rather slow and not very efficient. Mild ‘activation’ of the recovered samples (removal of substantial part of organic adsorbates) results in a much higher intensity of the carbonyl bands (see 3.3.2.2.4). Activated (oxidized) samples equilibrate with gaseous CO much faster than recovered material (5–10 min vs. 1–1.5 h). Moreover, the structure of the CO bands changes after the treatment: a component at 2115 cm^{-1} appeared assigned to CO adsorbed on atomically dispersed Pt, while the main band maximum shifted from 2064 cm^{-1} to 2071 cm^{-1} .^{258, 262} Oxidation conditions were chosen, so that the different response of the material to the CO exposure can be attributed to the removal of organic contaminants. Still, differences between deactivated and non-

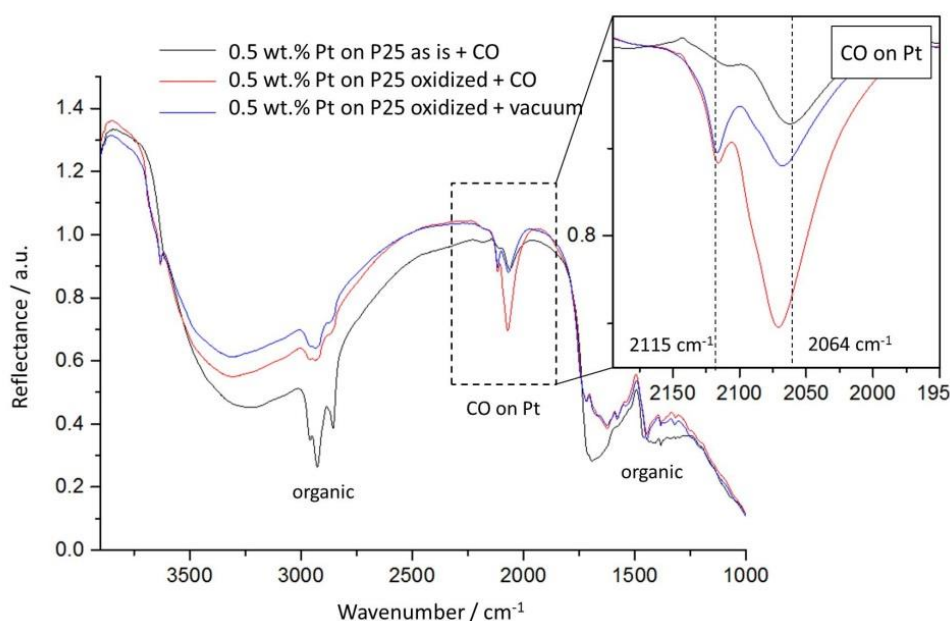


Figure 5-15. DRIFTS study for CO adsorption on 0.5 wt.% Pt loaded P25 recovered after a HER experiment. Insert: close-up of the Pt-CO bonding region.

deactivated samples are subtle and insufficient to draw hard conclusions about the deactivation mechanism. Moreover, all samples have a similar structure of the carbonyl bands.

5.2.3. Role of defects: discussion & conclusions

Generally, very few reports have discussed SMSI in the broader context of photocatalysis and it would not be considered as likely in a liquid-phase environment as the surrounding water should be able to reoxidize surface vacancies immediately. However, previous work by Ohyama et al. showed that photodeposition of Rh and Pt in thick slurries of TiO_2 in methanol (125 g L^{-1}) resulted in disorganized and diffuse metal deposits that were only clearly in nanoparticle form after heat treatment in vacuum at 400°C . They suggested that defect sites inherent to the metal oxide surface as well as induced by UV illumination drive the SMSI-like behavior, which would be in line with my observations.²⁶³ My experiments give strong, although indirect, support for the importance of oxygen vacancies in the context of the observed deactivation. Additionally, with the creation of H_2 in my reaction, the incident irradiation and possible pretreatments by ultrasound, I seem to be able to create defects in situ that have a detrimental effect on the H_2 generation rates of Pt-loaded P25. I have a dynamic system in which vacancies are also created in situ during the on-going reaction that may be close enough to cause a SMSI-like effect.

Additionally to the TEM images, XPS Pt 4f spectra of various recovered photocatalysts at different Pt loadings in some cases show a shoulder that corresponds to a higher oxidation state of Pt than in metallic Pt^0 , which might be caused by suboxide species encapsulating the particle. Indeed, Pt-O-Ti formation has previously been correlated with a positive BE shift²⁶⁴. However, while positive shifts have been occasionally mentioned in the context of SMSI,²⁶⁵ a negative shift of the BE of Pt due to an electron transfer from the Ti 3d orbital to Pt atoms after diffusion of Pt into the TiO_2 lattice is more often reported.^{249, 255, 266} As the high Pt loadings correspond to stable samples, only a partial encapsulation could explain that there is not a complete shift in the Pt signal and that there are still enough "free" Pt active sites that allow for stable H_2 generation.

In conclusion, photocatalytic experiments and ex situ characterization suggest that deactivation of TiO_2 during in situ photodeposition and HER active sites is

mediated by oxygen vacancies that are inherent to the metal oxide or photoinduced during the reaction. A possible mechanism for deactivation is a SMSI-like encapsulation of Pt by suboxides invoked by an increasing degree of reduction during HER as suggested by TEM and XPS.

However, evidencing defect creation and encapsulation by characterization of recovered photocatalysts has remained relatively inconclusive, while proper in situ characterization techniques have not yet been available to us. I excluded changes in the phase composition, surface area or general Pt and TiO₂ crystal morphology as source of deactivation.

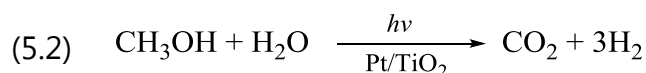
As I do not have strong evidence for the decoration model, I also have to consider other possible pathways by which oxygen vacancies may inhibit HER and other sources for deactivation of the photocatalyst. Another cause for the positive shift in the BE is that other reactants and organic byproducts generated during the HER adsorb onto the Pt. Active site poisoning by adsorbants onto Pt (\neq decoration) is a common issue in (photo-)catalysis, that I have not yet addressed. In the following section, I will discuss the mechanism and possible side reactions that can occur during photooxidation of methanol and further elucidate deactivation pathways.

5.3. Role of carbon monoxide

In the previous sections, I have been focusing on the activities for H₂ evolution of my reaction, while somehow neglecting the oxidation reaction that is happening simultaneously. Whenever a sacrificial agent is used for H₂ evolution, the HER experiment is simultaneously a photocatalytic oxidation of the organic molecule, in my case: methanol. Active site poisoning of Pt by one of the byproducts during the photocatalytic oxidation of methanol will be discussed as another possible reason for the observed deactivation in the following section.

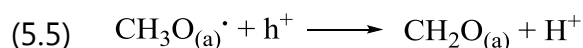
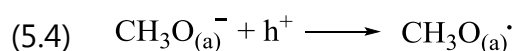
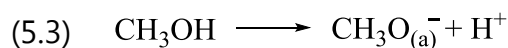
5.3.1. Mechanistic perspective

The main pathway for the photocatalytic decomposition of methanol follows a step-wise oxidation of methanol: under consumption of four holes and an equivalent of water, one equivalent of CO₂ gas and three equivalent of H₂ are generated. This results in an overall reaction as in equation (5.2).



Several studies have been conducted in order to investigate the pathway and intermediate compounds in this reaction, mostly using FTIR as identification method.^{15, 50, 61, 105, 258} The following pathway can be seen as generally accepted across literature:

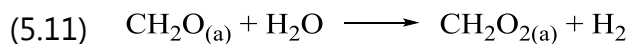
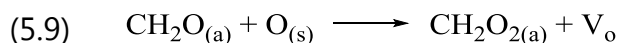
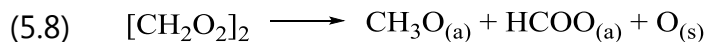
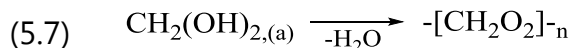
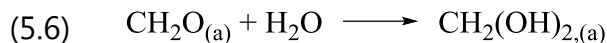
- 1) *Methanol deprotonates and a methoxy group adsorbs onto the TiO₂ surface.* An oxygen vacancy will be the preferred adsorption site.¹⁶⁷⁻¹⁷¹ The adsorbed methoxy group consumes a hole and forms a methoxy radical that can further deprotonate upon consumption of another hole to form formaldehyde ((equations (5.3)-(5.5)).



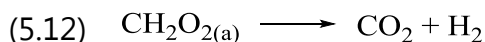
- 2) *Formaldehyde oxidizes to CH₂O₂.* This intermediate has been identified as both formic acid and the polymeric species dioxomethylene (DOM), which are identical in their sum formula but differ in their structure and adsorption.^{15, 258} Two possible pathways for the oxidation of formaldehyde to formate or formic acid were identified from literature:

- a. Firstly, DOM can be formed from formaldehyde through a first hydration step to methanediol followed by a partial dehydration (equation (5.6)-(5.7)). Following a Cannizzaro disproportionation, DOM can further decompose into adsorbed methoxy and formate species (or in their hydrated form: formic acid) (equation (5.8). Thus, DOM can be seen as a possible intermediate in the formation of formates and formic acid and both formic acid and DOM will be expected to be a product of the oxidation step of formaldehyde.^{15, 258, 267}
- b. Secondly, the oxidation of formaldehyde was suggested to occur through consumption of a lattice oxygen creating an oxygen vacancy which in turn is reoxidized by H₂O from the reaction solution (equations (5.9)-(5.10)).¹⁰⁵

In both cases – either by direct hydration of formaldehyde (path a) or by dissociative adsorption at an oxygen vacancy site (path b) – one water molecule would react with one formaldehyde molecule generating one formate or formic acid and one H₂ molecule (equation (5.11)).

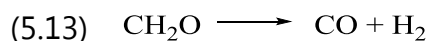


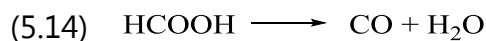
3) *In a final step, formic acid decomposes to CO₂ and H₂ by consuming another two holes (equation (5.12)).* Nomikos et al. suggested a photo-Kolbe reaction mechanism for this step.¹⁰⁵



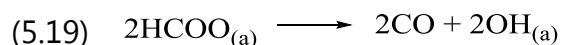
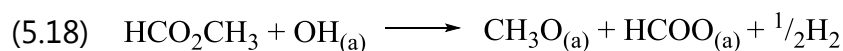
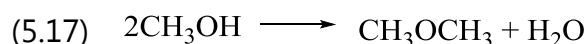
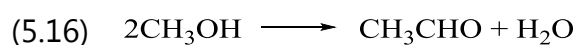
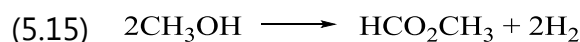
In this work, I see that the CO₂ and H₂ curves run in parallel in all photocatalytic experiments, which shows their direct correlation according to equation (5.11). Detected CO₂ amounts were approximately 6 times lower than expected from stoichiometry, which points towards either an incomplete decomposition of methanol or dissolution of CO₂ into the reaction solution.

Next to the described main pathway, various side reactions may occur that result in the generation of CO, a known catalyst poison. For example, formaldehyde could theoretically decompose into H₂ and CO (equation (5.13)), while formic acid and the corresponding formate can decompose into CO following a reverse WGS reaction (equation (5.14)). In a vapor-phase study of the methanol decomposition products over Pt-loaded TiO₂, Chiarello et al. found that CO generation seems to be more correlated to formic acid production rather than stemming from formaldehyde.¹⁵ Furthermore, the authors found that CO is not generated by the direct decomposition of methanol but rather through the oxidation intermediates.





In the same study by Chiarello et al., the occurrence of bimolecular side reactions was discussed, i.e. the reaction of two molecules of methanol can result in different side products such as methyl formate (equation (5.15)), acetaldehyde (equation (5.16)) and dimethyl ether (equation (5.17)).¹⁵ Only the formation of methyl formate may contribute to the overall H_2 generation rate. These bimolecular side reactions start to strongly influence the overall reaction at methanol fractions above 40%, which applies to my reaction conditions. Furthermore, in a comparative study on the vapor-phase decomposition of formic acid and methyl formate, Schubert et al. found that methyl formate generates larger amounts of CO and has slower overall kinetics than in the case of formic acid.⁶¹ CO was generated from methyl formate by a disproportionation step into a methoxy and formate group followed by the same reverse water-gas shift pathway as discussed above for formic acid by decomposition of formate species under formation of surface hydroxyl groups (equation (5.18)-(5.19)).



From the mentioned side reactions, it is already evident that CO seems to be a highly relevant side product during HER from methanol solutions. This is especially interesting in the context of deactivation, since CO is a known catalyst poison. However, literature reports have been inconclusive about the actual amounts of CO that are generated during photooxidation of methanol and a possible detrimental influence of CO has not been reported up to now. As the general aim of photocatalytic degradation of methanol is the production of H_2 , the presence (or absence) of CO is often neglected – especially, when no unexpected behavior of the photocatalyst is observed. While there is a number of reports, that explicitly report that CO was not detected,^{30, 54-55, 59, 66, 268-269} there are also groups including those discussed above that investigated mechanism and side reactions during

photocatalytic methanol oxidation that were able to observe CO generation.^{15, 46, 56, 61, 270}

In a study by Highfield et al., Pt deposition onto TiO₂ was investigated using a DRIFTS cell.²⁵⁸ They observed CO formation but did not see a correlation to the photocatalytic performance, leading to an assignment of CO as “spectator species”. However, I noticed that they applied a relatively high Pt loading of 1 wt.%, which could be in the stable regime of H₂ generation that I discussed previously (section 5.2.1.4). The observation of Pt-CO by Highfield and Schubert also infers that oxidation reactions either have to occur in close proximity to the metal nanoparticle, e.g., at the TPB, or there has to be a surface shuttle-mechanism that results in CO adsorbing onto Pt.

Another recent DRIFTS study by Fontelles-Carceller noted a correlation between decreasing bands of CO bonded to Pt and an increasing CO₂ concentration, which led them to the conclusion that Pt is critical in the activation and mineralization of methanol by allowing full oxidation of CO to CO₂.²⁷¹ While not specifically mentioning a poisonous effect of CO on the reaction, the authors suggest that differences in the CO adsorption properties of the noble metal are critical in the complete conversion of methanol.

Concluding from these reports, CO is a likely and relevant by-product during my reaction as well as a known catalyst poison. Thus, I employed an additional detector to the gas analyzing unit to investigate the role of CO during the photooxidation of methanol as discussed in the following section.

5.3.2. HER experiments with CO detection

I employed an additional IR detector to the on-line gas analyzer in order to investigate possible CO generation during the HER experiments. Figure 5-16 shows the gas evolution curves for H₂, CO₂ (multiplied by 10) and CO (multiplied by 100) of a deactivating (a) and a stable sample (b). No ultrasonication was applied as pre-treatment. The fact, that a loading of 0.4 wt.% Pt deactivates without US pre-treatment is due to a higher light intensity in these experiments and thus assumed higher defect to Pt ratio (section 5.2.1.2). Indeed, I observe CO generation in the deactivating sample that is inversely correlated to the H₂ generation rate, meaning that with an increasing CO generation, I observe the drop in H₂ evolution rates, while stable samples show no CO generation at all. These experiments show a clear correlation between deactivation and CO generation. Since the observed amounts of CO are very small (up to 30 ppm) and in order to exclude any

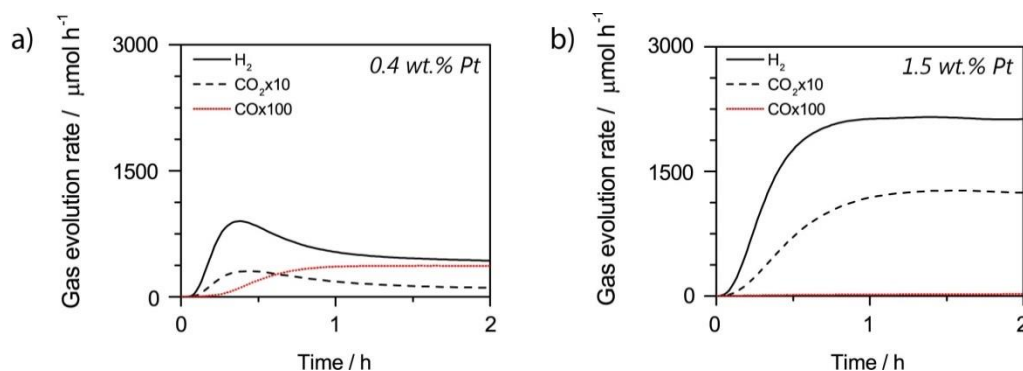


Figure 5-16. Gas evolution curves for H_2 , CO_2 (multiplied by 10) and CO (multiplied by 100) of a deactivating (a) and a stable sample (b).

cross-detection of the IR-based detector in the gas analyzer, we coupled an on-line micro-GC to the outlet of the gas analyzer. The GC results confirm the presence of H_2 , CO_2 and CO and agree well with the values measured by the gas analyzer, confirming the precision and validity of the gas analyzing unit. The drop in H_2 and CO_2 rates indicates that less formic acid is decomposed into H_2 and CO_2 , while the increase in the CO generation rate suggests that more CO is generated through either a reverse WGS reaction of formic acid or via a methyl formate intermediate (equation (5.14), (5.15), (5.18), p.111). The parallel run of the H_2 and CO_2 curves during the deactivation suggests that methanol oxidation is already inhibited during the first steps of the reaction. If only the last, CO_2 -generating step of formic acid decomposition was inhibited, we would expect to see a smaller percent-wise drop in the H_2 generation than for CO_2 generation as the first deprotonation steps still result in H_2 (equations (5.3)-(5.11)). Thus, I suggest that the methyl formate pathway through a bimolecular side reaction of methanol in the very beginning of methanol oxidation might be the main pathway that generates the CO observed in my experiments. This is also in line with Chiarello et al., who suggested an increasing influence of bimolecular side reactions at methanol percentages above 40%. Interestingly, the authors observed a strong dependence on the Pt loading for the selectivity of the side reactions that they could not explain¹⁵, which is in line with the previously observed dependence of deactivation on the Pt loading.

These findings suggest that fast deactivation is caused by a change in reaction kinetics and mechanism, in which there is a stronger influence from methyl formate formation and decomposition reaction accompanied by an increased CO generation. The decrease in H_2 generation may be due to either blockage of metal active sites by CO adsorption onto Pt or generally slower reaction kinetics due to the stronger influence of the methyl formate pathway or a combination of

both. An adsorption of CO onto Pt can also explain the observed shift to a higher oxidation state of Pt in the XPS Pt 4f spectra (section 5.2.2.7, Figure 5-13).²⁷²

I previously proposed a dependence of deactivation on the oxygen vacancy concentration during the HER relative to the amount of Pt as corroborated by various HER experiments. In an ab initio study of CO on TiO₂ surfaces, Kobayashi and Yamaguchi show that oxygen vacancies have an enhanced interaction with CO on a TiO₂ surface by electron back-donation from the electrons in the Ti 3d orbitals of surface Ti³⁺ into the π^* -orbital of molecular CO.²⁷³ This could render CO generation more favorable in the presence of an increasing amount of oxygen vacancies. Furthermore, oxygen vacancies serve as adsorption sites. Thus, the more adsorption sites are present on the surface, the higher the likelihood that two methanol molecules adsorb next to each other and proceed via the methyl formate pathway. To prove this working hypothesis that deactivation is caused by a switch in the reaction pathway going through a methyl formate intermediate, a novel in situ ATR-FTIR cell was developed in collaboration with the Institute of Chemical Technologies and Analytics at TU Vienna, which we can use to identify intermediates formed during the liquid-phase photodeposition of Pt and correlate them to the reaction pathways and byproducts that lead to deactivation (section 5.3.3).

5.3.2.1. *Variation of methanol concentration*

A positive effect of higher water concentrations in the reaction solution on the H₂ generation rate has been reported by several studies.^{15, 61, 258} An increasing water content strongly accelerates the kinetics of the forward WGS reaction from formic, resulting in a lesser generation of CO. Figure 5-17 shows a set of experiments, in which I vary the methanol concentration between 10 to 100 vol.% during HER experiments. A methanol concentration of 50 vol.% corresponds to the concentration used in previous experiments and exhibits fast deactivation-type behavior independent of the US pretreatment. Lowering the methanol concentration results in much better stability and slow deactivation-type behavior with a maximum rate value of 1335 $\mu\text{mol h}^{-1}$ achieved for the sample in 25 vol.%. At a methanol concentration of 10 vol.%, the maximum rate is slightly lower than for 25 vol.%, maybe due to less availability of methanol and consequent diffusion limitations of the oxidation side of the reaction. Concentrations above 50 vol.% all show a more or less pronounced drop in the H₂ rate during the first half hour and generally decrease in the maximum observed rates with an increasing methanol concentration. Interestingly, the value after deactivation is more or less the same for all of the high methanol concentrations.

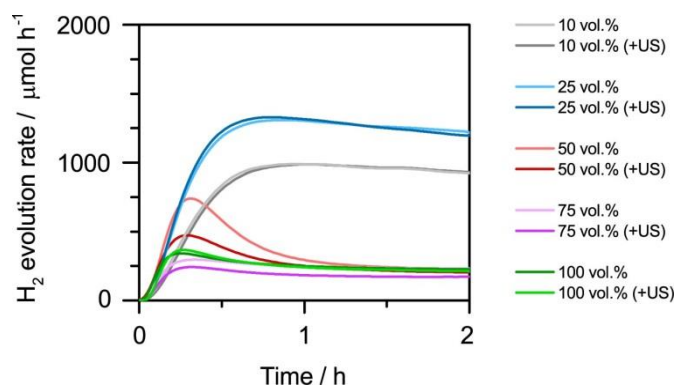


Figure 5-17. H₂ generation rates for different methanol concentrations for Pt-loaded P25 (0.25 wt %).

This is in agreement with Chiarello et al.'s work, in which H₂ generation reaches maximum values in an intermediate regime of methanol concentration (20–60%) performing best at a methanol concentration of around 40%.¹⁵ First, H₂ generation increases with the methanol concentration due to deprotonation of intermediates during oxidation reactions. In the intermediate range, equilibrium is reached between the main reactions for methanol oxidation, while the decrease at higher methanol concentrations is due to an increased influence of the bimolecular side reactions. They found that bimolecular reactions are significant at higher methanol fractions (e.g. over 40%). This agrees very well with my experiments, in particular with the fact, that I only observe fast deactivation at methanol concentrations between 50 and 100 vol.%, which further supports that the deactivation observed in this work is due to a shift in mechanism that involves the formation and stepwise decomposition of methyl formate resulting in generation of CO. This can also explain the similar post-deactivation rates, indicating that the disproportionation of methyl formate is a rate-limiting step resulting in similar kinetics and rates at a certain saturation level of methanol.

5.3.3. In situ ATR-FTIR – first experiments

(The following results were obtained in collaboration with Bettina Baumgartner and Christopher Herzig, TU Vienna)

In situ IR spectroscopy is a powerful tool in mechanistic studies enabling the detection of surface radicals and reaction intermediates as well as supplying information about adsorption modes of molecules on surfaces during a reaction.^{258, 271, 274} Generally spoken, gas-phase DRIFTS cells are easier to handle with respect to controlling reaction parameters compared to liquid-phase setups and are thus usually favored as tool for analysis. However, we aim at being as close to my reaction system as possible and decided for a liquid-phase ATR cell. ATR spectroscopy

is the preferred IR measurement method for monitoring liquid reactions on interfaces as the bulk reaction solution is not probed by the evanescent wave that only shallowly penetrates the liquid film.²⁷⁴

Here, we modified an ATR flow cell made of PMMA by introducing a sapphire window that allows for top irradiation of the ATR crystal (see 3.3.2.2.3). Cell design (i.e. cell volume, area of the window) proved to be crucial in obtaining meaningful ATR signals as, for example, a cell volume that is too small does not allow for sufficient soaking of the P25 film by the reaction solution and the illuminated area through the sapphire window needs to be maximized. Furthermore, gas evolution during the reaction in cells that are too small leads to gas bubbles that displace the liquid from the P25 film and disrupt the measurement.

A Si single crystal is spin-coated with a uniform film of P25 of roughly 700-1000 nm as evidenced by SEM (Figure 5-18). The ATR cell is loaded with a reaction solution containing 50 vol.% methanol as well as a certain concentration of H_2PtCl_6 , which completely covers the TiO_2 -coated Si crystal.

In order to correlate the results from ATR spectra to my photocatalytic experiments regarding deactivation, I need to be able to control the key parameters that seem to affect stability of H_2 evolution in the ATR cell, i.e. light intensity and Pt loading. While the light intensity can be adjusted through the choice and position of the light source, the Pt loading proves more difficult to control. The reaction solution containing the Pt precursor cannot be confined only to the irradiated area due to design constraints. Therefore, the assumption that we deposit 100% of the Pt precursor as in the photocatalytic experiment is not applicable in the ATR setup and we do not know how much of the Pt actually deposits onto the

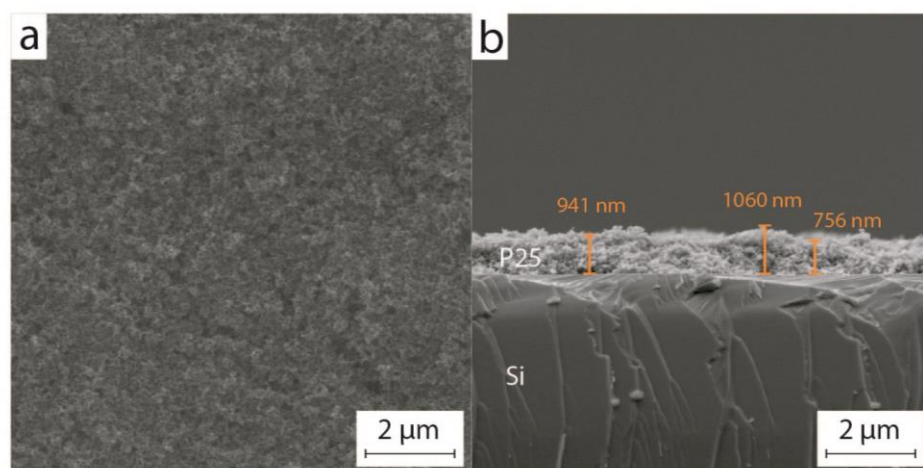


Figure 5-18. SEM images of P25 film spin-coated onto a Si single crystal: a) top view b) profile view.

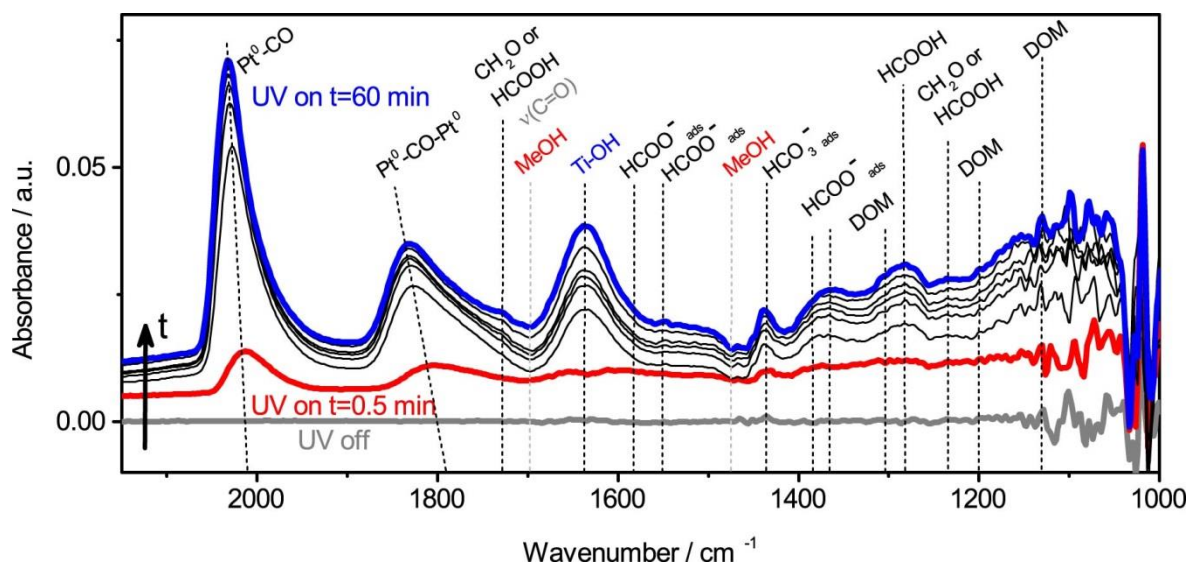


Figure 5-19. Time-dependent absorbance difference spectra of Pt-loaded P25 films on Si crystals (8 wt.%, as determined by ICP-MS) during 60 min UV irradiation.

TiO₂ film. Therefore, we recently developed a method to determine the actual Pt loading of the TiO₂ film by post-mortem ICP-MS. First results clearly showed that there is a discrepancy between the applied Pt precursor concentration and the actual Pt loading, rendering ICP-MS a crucial method for systematic investigations.

Figure 5-19 shows the time-dependent absorbance difference spectra of Pt-loaded P25 films on Si crystals (8 wt.%, as determined by ICP-MS) during 60 min UV irradiation. In the absence of UV irradiation, we obtain a flat baseline (grey trace), which shows that any changes in the spectra are invoked by light and thus of photocatalytic nature. Upon illumination, we see an expected decrease of bands at 1697 cm⁻¹ and 1473 cm⁻¹ attributed to the $\delta_{as}(\text{CH}_3)$ vibration of methanol indicating its decomposition.²⁶⁰ Furthermore, a band at 1637 cm⁻¹ attributed to Ti-OH surface hydroxyl groups increases, which is in line with dissociative adsorption of water molecules upon UV irradiation.^{247, 275} Prominent bands at wavenumbers <1500 cm⁻¹ that can be assigned to formic acid ($\nu(\text{C-O})$: 1283 cm⁻¹)²⁶¹, adsorbed formate ($\nu_s(\text{O=C=O})$: 1384, 1365 cm⁻¹)²⁵⁹⁻²⁶⁰ and DOM ($\tau(\text{CH}_2)$: 1304, 1200, 1130 cm⁻¹)^{55, 259} appear almost immediately after starting UV irradiation and remain stable after 10 min until the end of the experiment. Weaker bands from the asymmetric stretch of adsorbed formate ($\nu_{as}(\text{O=C=O})$: 1583, 1551 cm⁻¹)²⁷⁶⁻²⁷⁷ appear only after about 20 min of irradiation. Bands at 1728 and 1234 cm⁻¹ can be assigned to the $\nu(\text{C=O}_{ads})$ and $\omega(\text{CH}_2)$ of either formaldehyde or formic acid.^{259, 261, 277-278} Interestingly, after less than 1 min of UV irradiation (red line), bands at 2014 and 1808 cm⁻¹ appear which can be assigned to CO adsorbed onto

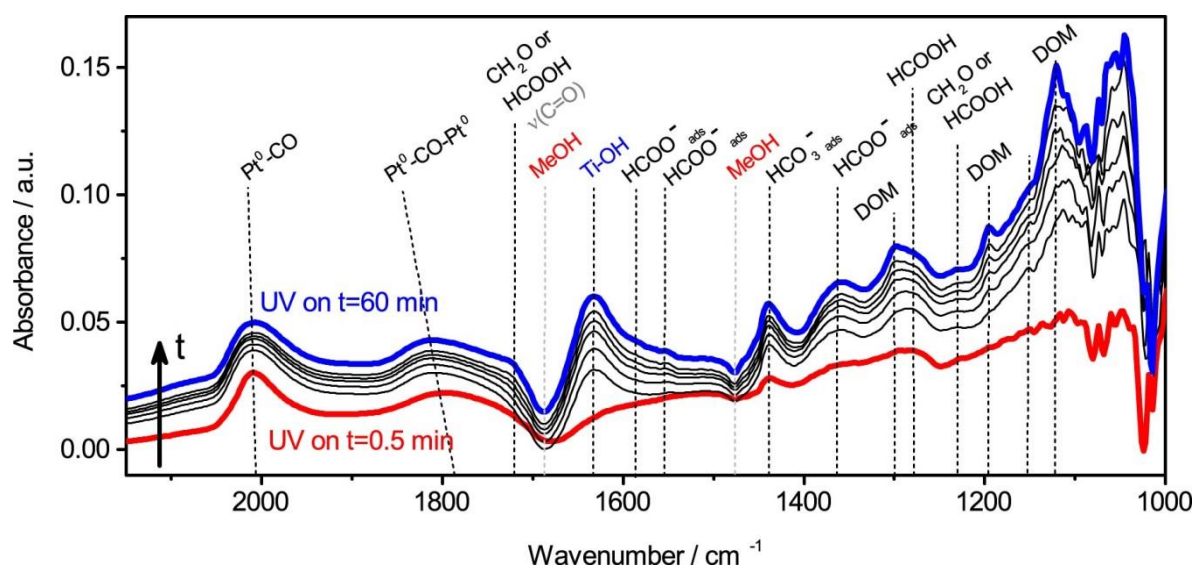


Figure 5-20. Time-dependent absorbance difference spectra of Pt-loaded P25 films on Si crystals (4 wt.%, as determined by ICP-MS) during 60 min UV irradiation.

metallic Pt in an “on top” and “bridged” position, respectively.^{50, 258, 279} Only a band for adsorbed bicarbonate ($\nu_{\text{as}}(\text{O}=\text{C}=\text{O})$: 1436 cm^{-1})²⁵⁸ also appears immediately after less than 1 min of UV irradiation and slowly increases during the UV irradiation. After ten minutes, the CO-Pt^0 and $\text{Pt}^0\text{-CO-Pt}^0$ signals are clearly pronounced. During the 60 minutes of UV irradiation, these bands show a drastic shift to 2034 and 1833 cm^{-1} , for the on top and bridged position, respectively. This has previously been attributed to either a larger Pt particle size or a higher coverage of Pt with CO.^{258, 279} An increasing CO coverage seems to be the more likely cause as previous TEM analyses showed that Pt particles deposit within the first ten minutes of an experiment and do not further grow in size. TEM analysis shows that Pt deposits in a similar – if not identical – fashion as in the case of the reactor experiment. The fact that bands for CO adsorbed onto Pt^0 and HCO_3^- immediately appear upon illumination, shows that 1) deposition of metallic Pt is immediate and fast, and 2) that either CO and CO_2 are dissolved in the reaction solution from the beginning or the reactions leading to their generation are very fast.³¹

These observed trends are similar for a Pt loading of 4 wt.% (Figure 5-20). The CO-Pt^0 (2008 cm^{-1}) and $\text{Pt}^0\text{-CO-Pt}^0$ (1798 cm^{-1}) bands are less intense, broader and shifted to slightly lower wavenumbers compared to a loading of 8 wt.%, likely due to the lower amount of Pt and possibly smaller particle size.²⁷⁹ A shift to higher wavenumbers is still observed (i.e., to 2011 and 1814 cm^{-1} , respectively), again indicating a growing Pt particle or increasing CO coverage. Bands stemming from the oxidation intermediates are more distinct at 4 wt.% Pt than for

8 wt.% Pt. Still, they are mostly stable in intensity after 10 min at wavenumbers below 1500 cm^{-1} , while some weaker bands appear later during the experiment for either formic acid or formaldehyde at 1721 cm^{-1} ($\nu(\text{C}=\text{O}_{\text{ads}})$) and the asymmetric stretch of adsorbed formate at 1587 and 1554 cm^{-1} .^{259, 261, 276-278} The relative intensity ratio between the intermediate and CO-Pt^0 bands increases at the lower Pt loading. This could be a measurement feature due to a not yet ideally fixed position of the light source and thus fluctuating light intensities. The exact band positions and their assignments for both loadings can be found in Table 5-4.

Thus, these experiments can be seen as proof of concept: I am able to follow the photocatalytic oxidation of methanol in the liquid phase with simultaneous in situ photodeposition of Pt, while correlating it to parameters used in previous photocatalytic experiments. I see a clear CO signal during this reaction and will be able to follow possible different pathways as I am now able to control the Pt loading by post mortem ICP-MS analysis. I have not yet observed any signal stemming from methyl formate species. However, I am also in a Pt loading range in which I would not expect deactivation. As mentioned before, controlling the parameters has been a challenge in the cell and experimental design. However, I am now capable of a proper and reproducible experimental design that will allow for systematic studies of my system and a direct correlation to the photocatalytic exper-

		<i>Pt loading</i>	
		<i>8 wt. %</i>	<i>4 wt. %</i>
assignment		cm^{-1}	cm^{-1}
CO on Pt	$\text{Pt}^0\text{-CO}$	2014-2034	2008-2011
	$\text{Pt}^0\text{-CO-Pt}^0$	1808-1833	1798-1814
methanol		1697	1687
	$\delta_{\text{as}}(\text{CH}_3)$	1473	1476
Ti-OH		1637	1632
CH₂O/HCOOH	$\nu(\text{C}=\text{O}_{\text{ads}})$	1728	1721*
	$\omega(\text{CH}_2)$	1234*	1230
HCOOH	$\nu(\text{C-O})$	1283	1279
HCOO⁻_{ads}	$\nu_{\text{as}}(\text{O}=\text{C}=\text{O})$	1583*, 1551	1587, 1554
	$\nu_{\text{s}}(\text{O}=\text{C}=\text{O})$	1384*, 1365*	1364
DOM	$\tau(\text{CH}_2)$	1304*, 1200*	1300, 1196, 1151
	$\tau(\text{CH}_2)$ or $\rho(\text{CH}_2)$	1130	1122
HCO₃⁻_{ads}	$\nu_{\text{as}}(\text{O}=\text{C}=\text{O})$	1436	1438

Table 5-4. IR absorbance band positions and assignments for in situ ATR-FTIR measurements of Pt-loaded P25 in aqueous methanol solution. Faint bands are labeled with an asterisk (*).

iments in my reactor system.

This in situ liquid-phase ATR-FTIR system will be a powerful tool in understanding the mechanism behind deactivation of Pt-loaded TiO_2 . Moreover, it can be applied to a variety of systems and research questions, for example, investigating different materials for photocatalysts and co-catalysts, as well as investigating effects of nanostructuring of photocatalysts or the impacts of changing sacrificial agents with respect to deactivation.

5.3.4. Conclusions

I discovered a clear correlation between the previously discussed deactivation of the photocatalysts and CO generation during HER. Decreasing H_2 generation rates are accompanied by an increasing CO generation rate, while stable samples do not show CO generation without exception. Considering possible mechanistic pathways and reactions for the photocatalytic oxidation of methanol on TiO_2 leads us to the hypothesis that reaction conditions for deactivating samples favor the formation of a methyl formate intermediate that is accompanied by slower reaction kinetics and CO generation through a reverse water-gas shift reaction. In order to investigate the mechanism, we developed a novel liquid phase ATR-FTIR cell and obtained first promising results that will allow for systematic studies of the mechanism at parameters that can be clearly correlated to my photocatalytic reactor setup.

5.4. Reversibility of deactivation

In order to test the reversibility of deactivation, I filtrated and dried deactivated samples (0.4 wt.% Pt) in air before conducting a second HER experiment. These recycled samples again deactivate indicating that deactivation is – to a certain extent – reversible (**Figure 5-21a**). The curve shape of the H_2 generation rate and deactivation of the recycled samples is softer than in the preceding experiments: the maximum activity is reached at a later point in time and reaches a lower absolute value overall ($500 \mu\text{mol h}^{-1}$ compared to $644 \mu\text{mol h}^{-1}$ in the first run). After deactivation, recycled photocatalysts level off to an almost identical steady state value as their precursors. I do not add additional Pt precursor for these recycling experiments, as Pt is already photodeposited in the first HER experiment. Therefore, these experiments exclude that deactivation is caused by the Pt precursor, that is present during the first experiment, as it is assumed to be removed during

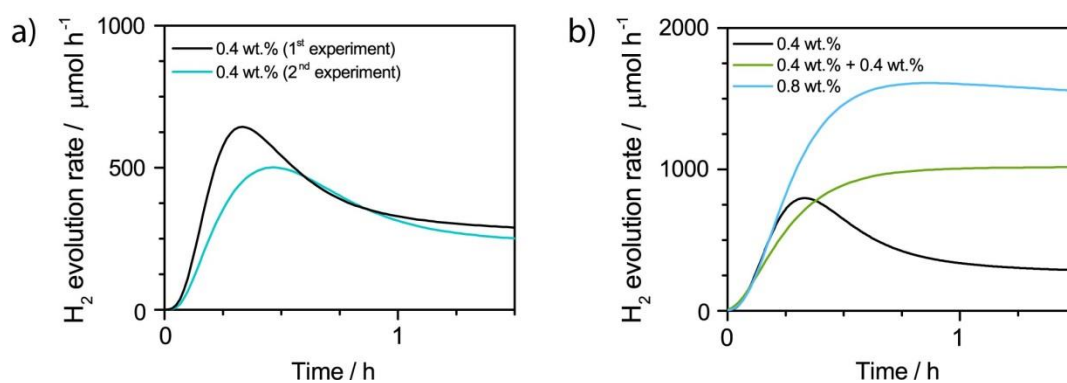


Figure 5-21. Investigations of reversibility of deactivation: a) recycled experiment (teal) b) recycled experiment with additional Pt deposition (green) and one-step photodeposition of corresponding Pt amount (blue). The black trace represents the first experiment.

the filtration and drying step. For example, the possibility that metastable Pt²⁺ complexes could be the source of the higher activation prior to the sudden drop in rate is excluded, as these complexes would be destroyed during the recovery step. I still investigated a possible influence by the presence of the acid precursor in the following section (section 5.5).

In another set of experiments, I added another 0.4 wt.% of Pt to a formerly deactivating sample in the second HER experiment (0.4+0.4 wt.%) and compared this to P25 loaded in one step with 0.8 wt.% of Pt. Interestingly, the 0.8 wt.% sample has a ~35% higher maximum H₂ evolution rate than the 0.4+0.4 wt.% sample. However, it shows a slow deactivation trend, while rates for the 0.4+0.4 wt.% – though lower – are stable.

Assuming that the maximum activity before deactivation of the 0.4 wt.% Pt-loaded P25 roughly corresponds to the maximum potential H₂ generation rate at this loading, then 0.4 wt.% Pt on P25 can generate 797 μmol H₂ per h (maximum of black curve, (Figure 5-21b). Furthermore, assuming a linear correlation between Pt loading and activity, a two-fold increase in H₂ generation would be expected between P25 loaded with 0.4 wt.% and 0.8 wt.% Pt, so that 0.8 wt.% Pt on P25 would generate 1594 μmol H₂ per h. This calculated value is in very good agreement with the observed maximum H₂ generation rate of 1611 μmol h⁻¹ for 0.8 wt.% Pt-loaded P25. In case of 0.4+0.4 wt.%, this potential maximum value for a loading of 0.8 wt.% is not reached. However, if I add the assumed maximum potential rate of 0.4 wt.% Pt on P25 if it does not deactivate (797 μmol h⁻¹) to the activity of deactivated 0.4 wt.% (276 μmol h⁻¹), I obtain a value of 1073 μmol h⁻¹. Again, this is in very good agreement with the observed H₂ generation rate of 1022 μmol H₂ per h for 0.4+0.4 wt.% Pt on P25.

Chapter 5 – Deactivation

In summary, recycling a deactivated sample without adding more Pt in the consecutive experiments leads to a recurring but slower or less pronounced deactivation. Addition of more Pt to a recycled deactivated photocatalyst leads to a stable H_2 generation rate that has, however, a lower maximum value compared to when the equivalent amount of Pt precursor is added at once without the recycling step.

Concluding from these previous experiments, the higher ratio of surface vacancies that is generated in situ during a HER experiment to the number of Pt particles the more likely deactivation is to occur. Here, I see that a deactivated photocatalyst deactivates again in a slower or less pronounced fashion, unless more Pt precursor is added, which results in a very stable rate for H_2 generation. During filtration and drying of the photocatalysts, surface vacancies are likely to reoxidize. These reoxidized surfaces now seem to be less prone to create new defects again or previously generated defects are less mobile, which results in the slow kinetics of the second deactivation. This would be in line with my experiment with pre-calcined P25 that shows a stable H_2 evolution rate contrary to untreated P25 at equivalent conditions (section 5.2.1.3). The oxidized surface seems to be resistant against defect formation. A sort of immobilization of the TiO_2 surface or higher defect resistance would also explain, why the addition of more Pt precursor results in neither a fast nor slow deactivation but a solid H_2 generation rate. The few defects that can be formed or are still available are used as deposition sites and are, in this way, quenched by the additional Pt. So the before-mentioned defect to Pt particle ratio is lower than in the case of 0.8 wt.% Pt on P25. Also, a higher resistivity against defect formation of (re-)oxidized TiO_2 surfaces would explain the different stabilities of 0.4+0.4 wt.% and 0.8 wt.% Pt-loaded P25. In the latter case, the dynamics of the surface during the reaction are not slowed by an additional (re-)oxidation steps.

Still, I have not explained yet why the activities between the 0.4+0.4 wt.% and 0.8 wt.% sample differ this much. Since deactivation is not observed, as in the case of recycled 0.4 wt.% without adding additional Pt, I should add up two times the assumed potential rates of active 0.4 wt.% Pt instead of those of deactivated 0.4 wt.% and active 0.4 wt.% Pt on P25. Possibly, some of the fresh 0.4 wt.% deposits on top of previously deposited Pt, which diminishes the total number of Pt particles and thus active site, while deactivation is still inhibited due to the "quenching" by Pt. In this case, it would be more a coincidence that the values deactivated and active 0.4 wt.% add up so well.

More recycling experiments with different Pt loadings would help in elucidating whether activities indeed always add up between deactivated and active Pt on P25. However, what is much more needed is an in situ characterization technique to measure defect generation during the reaction as I can clearly see in my HER experimental results, that recovering the photocatalysts already alters their surface chemistry. Also the absence of clear evidence for the presence of oxygen vacancies in my recovered photocatalysts, while my HER experiments at different conditions strongly suggest their influence on deactivation, shows the urgent need for a characterization technique that is able to monitor the formation of oxygen vacancies in situ. However, standard techniques such as XPS or HRTEM that would identify the presence of Ti^{3+} or a possible encapsulation are UHV techniques that will not allow for my experimental conditions.

5.5. Role of pH and anions

The unique feature of our setup is the combination of an on-line detection system with the in situ photodeposition of Pt onto the TiO_2 surface. However, this also results in a reaction solution in which I do not have a pure aqueous methanol solution but – depending on the Pt loading – varying amounts of the corresponding H^+ and Cl^- ions. Thus, differences in pH or the concentration of Cl^- ions may influence the stability of H_2 generation rates. Ex situ XPS analysis shows that Cl is present in all (also pristine) P25 samples. Cl is a common impurity in P25 due to the TiCl_4 precursor used during flame-spray pyrolysis and I do not see a trend with respect to deactivation. Furthermore, I did not detect any Cl_2 gas evolution, so that all ions can be assumed to remain in solution during the HER reaction.

Different pH environments in the context of photocatalytic oxidation of alcohols or organic compounds have previously been investigated and are usually separated into a low and high pH regime. Often formic acid degradation was studied in varying pH environments with a range between roughly 3.5 and 5 being reported as optimum.^{42-44, 54} Methanol and formaldehyde are not easily ionized, rendering formic acid the intermediate of interest for investigations of pH dependence of methanol oxidation. The pH dependence of photocatalytic reactions is governed by two main points: 1) the dissociation grade of reactants as indicated by the respective pK_a (e.g., 3.75 for formic acid) and 2) the surface charge of TiO_2 which governs the adsorption behavior of reactants and can be defined by the isoelectric point (IEP). The IEP of TiO_2 lies between a pH of 4-6.²⁸⁰ At a pH below the IEP, the TiO_2 surface is positively charged, which would favor the adsorp-

tion of negatively charged species, such as formate, while at a pH above the IEP, the TiO_2 surface is negatively charged, which would lead to less favored adsorption of deprotonated species like formate. While formic acid is more easily deprotonated and oxidized to CO_2 at high pH, previous work has shown that the mineralization of formic acid is inhibited at alkaline pH due to the repulsive force of the negatively charged TiO_2 surface and competitive adsorption with OH^- and carbonate.^{31, 281} I am well within the optimum reported range, so I should not expect a significant influence due to pH variations.

This leads us to also investigate a possible effect by a change of chloride ion concentration. Generally, chloride ions have either been reported to have an inhibitive or neutral effect on photocatalytic reaction. Inhibition usually occurs through blockage of active sites by adsorption of chloride ions onto the TiO_2 surface. In my case of increased stability at higher Pt loadings – assuming that pH variations do not have a large impact – increasing the amount of chloride ions would rather have a beneficial effect. A promoting effect of chloride ions has only been reported in the context of pollutant photooxidation (hexane, toluene) that is mediated by a chloride radical mechanism.²⁸² However, the rates for photooxidation of 1-butanol and acetone again experienced a detrimental effect by prechlorination of the TiO_2 surface. Thus, on first sight neither a decreasing pH nor an increasing chloride ion concentration is expected to have such a large impact on the stability of the photocatalyst.

I still conducted several sets of experiments in order to elucidate the role of ions and pH in the reaction solution. I conducted three different sets of additions to account for pH and Cl^- concentration changes to the reaction solution with P25, aqueous methanol and the H_2PtCl_6 for a theoretical loading of 0.4 wt.% Pt (deactivates):

- 1) HCl is added, which is the closest approximation to the addition of additional H_2PtCl_6 precursor without depositing more Pt and affects both the Cl^- concentration and pH
- 2) NaCl is added in order to investigate difference in the Cl^- concentration, while the pH is kept constant
- 3) HI is added in order to investigate difference in the pH, while the Cl^- concentration is kept constant

Exact experimental procedures can be found in the experimental section (3.1.2.1.3). Shortly, in a first experiment, I add the acid or salt to a reaction solu-

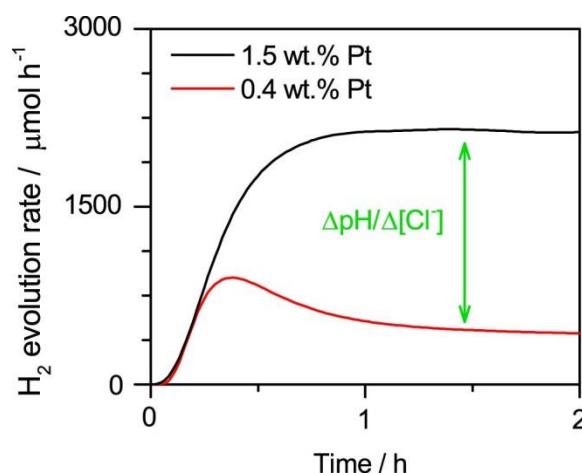


Figure 5-22. Difference in chloride ions and pH between a deactivating (e.g. 0.4 wt.%, red trace) and a stable Pt loading (e.g. 1.5 wt.%, black trace) at otherwise fixed parameters.

tion that already contains the H_2PtCl_6 precursor for nominally 0.4 wt.% Pt (deactivates) and proceed with the HER as usual. The acid or salt is added in an equivalent amount to the difference in pH or chloride concentration between the deactivating (e.g. 0.4 wt.%) and stable Pt loading at otherwise fixed parameters (e.g. 1.5 wt.%), $\Delta[\text{Cl}^-]/\Delta\text{pH}$ (Figure 5-22). In a second experiment, I add an excess amount ($10 \times \Delta[\text{Cl}^-]/\Delta\text{pH}$) to exaggerate possible effects by pH and anion concentration changes.

Measuring the pH of all solutions confirms that the addition of the acids correspond to the same drop in pH as that of the H_2PtCl_6 precursor: P25 in the methanolic solution was at a pH of ~ 4.5 , dropping to ~ 4 upon addition of 0.4 wt.% equivalent H_2PtCl_6 solution and further to ~ 3.8 for an equivalent of 1.5 wt.% Pt. In each experiment, I also added an excess ($\times 10$) amount of the additional agent (HCl, NaCl, or HI) to enhance possible effects reaching a pH of ~ 2.8 . The pH of the NaCl solution remained stable at 4.2 as expected.

Figure 5-23 shows the rates for H_2 , CO_2 , and CO generation for 0.4 wt.% Pt-loaded P25 with addition of either HCl, NaCl, or HI. In all experiments, CO_2 and CO generation curves follow the same trends as observed in the previous experiments and were not influenced by the additional acids or salt. When adding $\Delta[\text{Cl}^-]/\Delta\text{pH}$ for HCl, the maximum activity is significantly increased and deactivation is slightly delayed (Figure 5-23a). Adding an excess amount of HCl results in a change from the usual fast deactivation at these conditions to a slow and gradual deactivation over the course of the experiment. While there seems to be a beneficial effect of increasing the concentration of either H^+ or Cl^- in the reaction, the

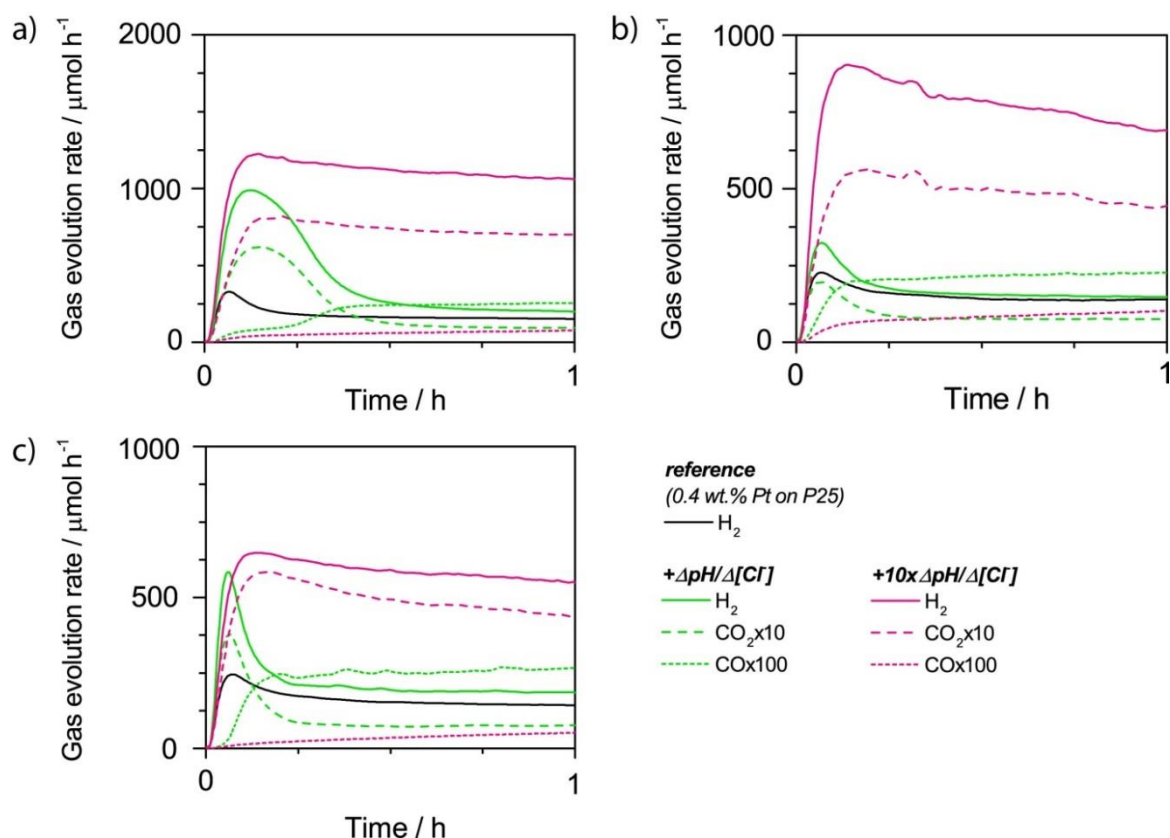


Figure 5-23. H_2 (solid), CO_2 (dash), and CO generation (dots) for 0.4 wt.% Pt-loaded P25 with addition of either (a) HCl, (b) NaCl, (c) or HI. Green traces correspond to $\Delta[\text{Cl}^-]/\Delta\text{pH}$. Magenta traces correspond to a 10-fold excess of $\Delta[\text{Cl}^-]/\Delta\text{pH}$.

concentration difference in HCl between a deactivating and stable sample during regular HER experiments is not enough to account for the different stabilities further supporting that it is the actual Pt loading that influences stability in these cases.

Addition of $\Delta[\text{Cl}^-]$ equivalent of NaCl only results in a slightly increased maximum activity, while the deactivation behavior remains unchanged. On first sight, this would infer that it actually is the pH difference that affects activity. However, when adding an excess amount of NaCl, I observe a very similar behavior to when excess amounts of HCl are added. Deactivation changes from fast to slow and activities are almost as high as in the case of excess HCl suggesting that rather Cl^- ions play a critical role.

Addition of ΔpH equivalent of HI resulted in a significantly increased maximum activity for H_2 evolution but an unchanged sharp drop and fast deactivation of the photocatalyst. Again, upon addition of excess acid, this fast deactivation was inhibited and transformed into a slow and gradual deactivation over the course of the experiment. Maximum activities, however, are much lower compared to HCl

and NaCl additions. On first sight, these experiments would again infer that differences in pH might have an effect on deactivation. However, the excess NaCl experiment clearly disagrees with this hypothesis. Furthermore, while I keep the concentration of Cl^- constant, when adding HI, I still increase the anion concentration in form of I^- . Iodide ions can be expected to behave at least similarly to chloride, while they are apparently not as effective in preventing deactivation. As the ionic radius of I^- is larger than that of Cl^- , iodide ions might not adsorb as easily as chloride.

Generally, all additions result in an improved activity for H_2 evolution. NaCl addition experiments suggest that the difference in pH is not significant enough to explain the different stabilities, which is in line with literature. While I see an apparent beneficial effect of increasing the anion concentration in the reaction solution on the stability of the photocatalysts, the added amounts are ten times higher than the concentration difference between 0.4 wt.% (deactivating) and 1.5 wt.% (stable) Pt-loaded P25. Thus, chloride ions may have a positive effect on the activity, but they do not appear to be the (sole) source of stability. A beneficial effect of increasing concentration of halides in the reaction solution is unusual and not clarified yet. One option is that, indeed, some radical mechanism is involved in my reaction as described by d’Hennezel et al.²⁸² However, the authors worked in aerated systems and clearly stated a detrimental effect of prechlorination of TiO_2 on alcohol photooxidation. Another option is, that Cl^- or I^- indeed block some adsorption sites on the TiO_2 surface, which decreases the likelihood of two methanol molecules reacting in the bimolecular side reaction to methyl formate, which I currently think is the intermediate during the observed deactivation.

5.6. Incipient wetness impregnation

In some first experiments, I used incipient wetness impregnation of P25 with 0.4 wt.% Pt from H_2PtCl_6 (IW04- TiO_2) in order to investigate whether the deactivation effect is specific to the photodeposition technique. Indeed, I found that at a Pt loading at which I observe deactivation of P25 loaded with in situ photodeposition, the corresponding IW04- TiO_2 sample is more stable and shows an overall higher activity. I attribute this to the oxidative treatment during the incipient wetness procedure, which has previously shown to be beneficial for the stability of the photocatalysts (section 5.6). TEM analysis shows a slightly smaller median Pt particle size for the IW sample (2.5 nm) compared to photodeposition (3.1 nm).

However, further experiments and investigations need to be conducted in order for better statistics.

5.6.1. Induced SMSI

In an additional experiment, I aimed to investigate the effect of induced decoration of Pt particles on the gas evolution rates. If deactivation is caused by encapsulation of Pt particles during the HER, then already deactivated Pt particles should be possible to synthesize by an ex situ reductive treatment of the IW-TiO₂ samples.

Here, I deposited 0.75 wt.% Pt onto TiO₂ via incipient wetness impregnation (IW075-TiO₂) from H₂PtCl₆ and subdued the Pt-loaded TiO₂ to H₂ treatment at 500 °C, which is in the temperature regime at which decoration of Pt by suboxide species is expected to happen. Figure 5-24 shows TEM images of (a) photodeposited Pt, (b) IW075-TiO₂ and (c) IW075-TiO₂ followed by H₂ treatment. Note, that in case of the photodeposited Pt, the sample was exposed to aqueous methanol and UV irradiation. The surface of the TiO₂ seems rougher than in the case of IW075-TiO₂, which would be in line with the reported creation of photoinduced defects. However, I did not see a very clear trend regarding surface amorphization of TiO₂ in my samples. The Pt particle in the photodeposited case already seems partially covered with some surrounding material, while the Pt particles for IW075-TiO₂ is clearly defined. H₂-treated IW075-TiO₂ shows clear signs of decoration of the Pt particle.

Photocatalytic experiments show a slow deactivation in all cases, that is most pronounced for IW075-TiO₂. In contrast to the experiment at lower Pt loading, the photodeposition sample performs at the highest H₂ rate at these conditions (Figure 5-25). The H₂ treatment of IW075-TiO₂ resulted in a decreased rate, that is however still higher than for photodeposition samples after deactivation. While

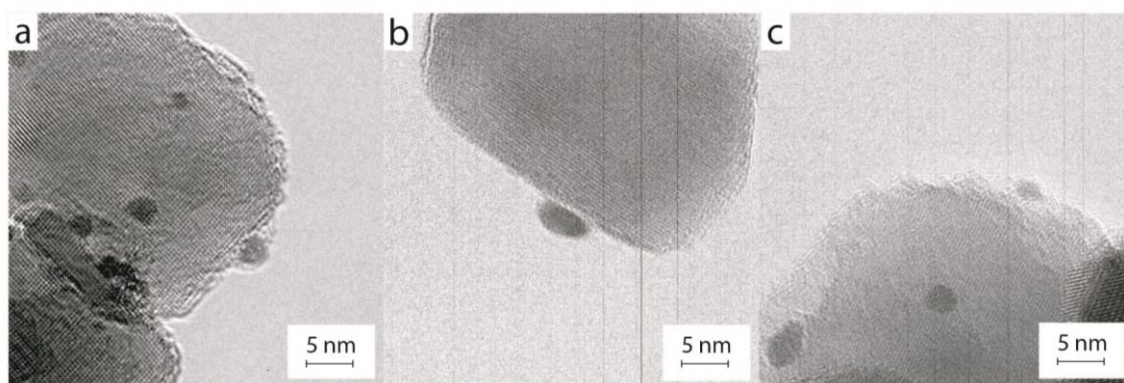


Figure 5-24. TEM images of (a) photodeposited Pt, (b) IW075-TiO₂ and (c) IW075-TiO₂ followed by H₂ treatment.

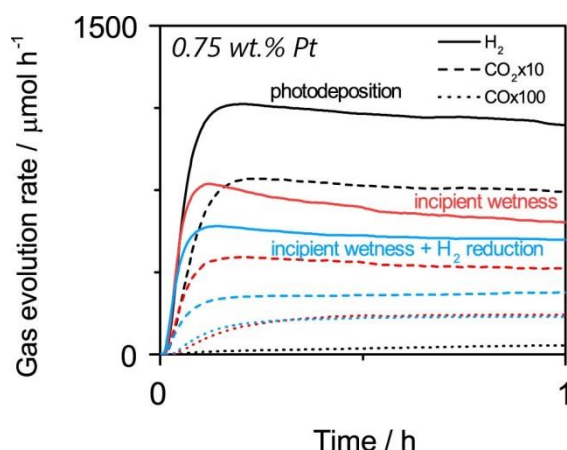


Figure 5-25. Photocatalytic HER experiments for P25 with Pt deposited with different methods: photodeposition (black), incipient wetness impregnation (IW075-TiO₂, red) and (c) incipient wetness impregnation followed by H₂ treatment (blue).

the CO₂ and CO curves follow the same general trends as discussed before, CO generation is significantly higher for both IW samples.

I have not yet thoroughly investigated other characteristics such as Pt particle size and distribution (although after first analyses, these seem to be very comparable between both deposition techniques) as well as chemisorption differences between the H₂-treated and untreated IW-TiO₂. Therefore, these results can only be seen as preliminary. Moreover, H₂ treatment of a recovered stable photodeposited sample as well as oxidative treatment of a recovered deactivated sample are possible experiments to further investigate possible SMSI effects.

Still, one important observation of my experiments is, that deactivation is not specific to photodeposition technique but may also be observed – although so far much less pronounced – for Pt loaded by incipient wetness. My results show that depending on the reaction parameters photodeposition or incipient wetness may be the preferred method for deposition of Pt. Overall, photodeposition shows the highest maximum activities. Deactivation induced by H₂ treatment seems to have a clearly detrimental effect and activities are within the range of deactivated samples, while further studies have to be completed before drawing a clear correlation between the observed deactivation during HER and encapsulation of Pt nanoparticles during this reaction.

5.7. Deactivation of pure TiO₂ polymorphs and a mixture

(The following results were obtained in collaboration with Dr. Alexey Cherevan, Sreejith P. Nandan, Antony Litovoiis, TU Vienna)

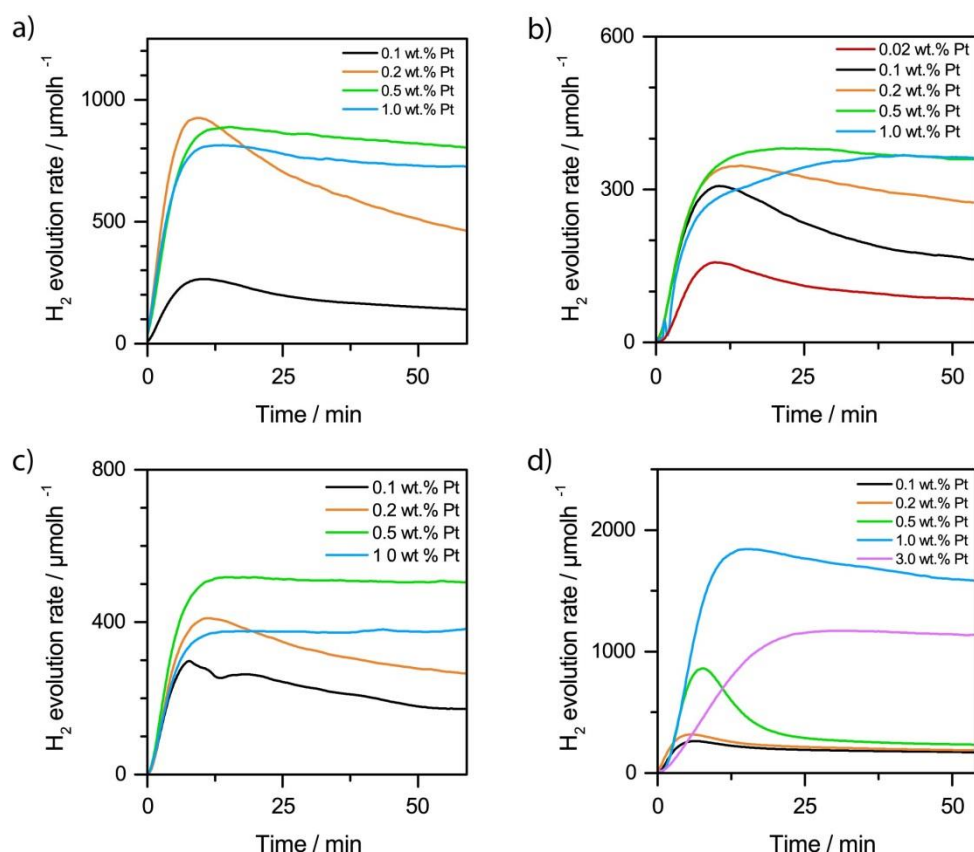


Figure 5-26. H₂ evolution rates for (a) anatase, (b) rutile, (c) a 80:20 mixture of anatase and rutile, and (d) P25 under UV irradiation at loadings ranging between 0.1 wt.% (exception 0.02 wt.% Pt for rutile) and 1.0 wt.% Pt (exception 3.0 wt.% Pt for P25).

Up to now, I have only investigated P25-type TiO₂ for HER. As P25 is the standard benchmark in photocatalysis, it was a reasonable choice in the beginning of my studies. However, in order to further elucidate the origins of the observed deactivation and to find out whether this phenomenon is specific to P25 I also investigated the pure polymorphs of TiO₂, anatase and rutile. In several sets of experiments, commercial anatase and rutile nanopowders as well as a physical mixture of both powders are compared to P25 for different Pt loadings mainly ranging between 0.1 and 1.0 wt.% of Pt. The ratio of the mixture of anatase and rutile was 80:20, which roughly corresponds to the ratio of these phases in commercial P25.⁹⁴

Figure 5-26 shows the H₂ evolution rates for anatase, rutile, a 80:20 mixture of anatase and rutile, and P25 under UV irradiation at loadings ranging between 0.1 wt.% (exception 0.02 wt.% Pt for rutile) and 1.0 wt.% Pt (exception 3.0 wt.% Pt for P25). Deactivation is observed for all TiO₂ polymorphs at certain conditions and is thus not specific to P25. Still, there are clear differences between the pure polymorphs, the mixture of anatase and rutile, and P25 synthesized by flame-

spray pyrolysis. The following sections will discuss the differences in stabilities and H₂ evolution rates in more detail.

5.7.1. Stability

I observe three different levels of stability for all materials: 1) fast deactivation (D) during the first hour (sometimes taking longer to level off completely) 2) gradual, linear deactivation (d) over the whole course of the experiment (may suddenly deactivate) 3) stable rate (s) with sometimes slow initial kinetics (s*). As observed before for P25, higher Pt loadings result in more stable rates for photocatalysts (although not necessarily higher maximum rates), while deactivation is observed at lower loadings. The Pt loading range, in which fast deactivation changes to slow and finally to a stable H₂ generation rate, differs between the two polymorphs, the mixture and P25. When I compare the two pure polymorphs, rutile – while lower in absolute H₂ generation values – is more stable compared to anatase at the same Pt loadings, e.g. at 0.5 wt.% Pt. Additionally, rutile reaches a stable rate at 1.0 wt.%, whereas anatase loaded with 1.0 wt.% Pt still shows slow deactivation type behavior. Furthermore, rutile loaded with 1.0 wt.% Pt not only shows a stable H₂ generation rate, but also slower initial kinetics, i.e., reaching the maximum rate for H₂ generation needs longer than at other loadings. One reason for these slow initial kinetics might be saturation of the surface with Pt as rutile has the lowest specific surface area of all TiO₂ samples with ~25 m² g⁻¹ compared to, e.g., 55 m² g⁻¹ for P25 and 90 m² g⁻¹ for anatase. Furthermore, while Pt particle size does not increase below ~1 wt.% as evidenced by my own TEM PSD studies on P25 as well as literature, this behavior might be different on rutile. Higher Pt loadings may result in larger particle sizes, which may need more time to grow than at lower loadings.

Interestingly, the anatase and rutile mixture is more stable than both anatase and rutile at the same loadings. This can be explained by a previously reported preferential deposition of Pt on rutile and a corresponding higher specific loading on rutile in this mixture as discussed in the following section (section max act).

In contrast, P25 is less stable than anatase and rutile or their mixture, while showing the highest absolute rates. Scanlon et al. previously investigated the band alignment of rutile and anatase and the charge separation between the two polymorphs (section 1.2.4.1).⁹⁶ They found that anatase has a higher electron affinity, which in the case of P25 could lead to a larger availability of electrons for the photoreduction of the Pt precursor to metallic Pt and thus a less significant preference for Pt deposition between anatase and rutile. As P25 is synthesized by

flame-spray pyrolysis, anatase and rutile particles can be assumed to be in a closer contact than after the physical mixing procedure that was applied for the anatase and rutile mixture, making these charge separation processes more likely in the case of P25 than for the physical mixture, explaining that the deposition onto rutile is more preferred in the case of the mixture.

This means that for P25 at the same overall loading as in the case of pure anatase or rutile, the phase-specific loadings are lower, which may lead to the lesser overall stability. This would mean that the deactivation is indeed phase-specific and stability for P25 is only reached if both components, anatase and rutile, are loaded with Pt loadings that allow for stable H₂ generation rates. This also explains, that P25 only reaches the same stable rate as 1.0 wt.% Pt-loaded rutile at a loading of 3.0 wt.% Pt.

5.7.2. Maximum activity values

Table 5-5 lists the different maximum H₂ generation rates as well as the stability of photocatalysts as indicated in the brackets. When looking at maximum activity values, anatase, rutile, and their mixture follow the same general trend for Pt loading dependence, i.e. an increase in rate is observed until some maximum value (at 0.5 wt.% Pt) is achieved after which the maximum values achieved for H₂ generation decline. The optimum loading in case of P25 is higher than for the polymorphs at 1.0 wt.% Pt in line with the previous argumentation on preferred deposition (section stability). This occurrence of a maximum Pt loading has been observed in literature before.^{54, 58, 283} The first increase in rate with increasing Pt loading can be easily explained by a simultaneous increase of active sites for H₂ evolution. After a certain optimum Pt loading, the number of Pt particles and corresponding active sites is no longer the rate-limiting factor for reduction of

Pt / wt.%	H ₂ / $\mu\text{mol h}^{-1}$			
	A	R	A+R	P25
0.02	-	150 (<i>D</i>)	-	-
0.1	250 (<i>D</i>)	300 (<i>D</i>)	300 (<i>D</i>)	250 (<i>D</i>)
0.2	900 (<i>D</i>)	350 (<i>D</i>)	400 (<i>D</i>)	300 (<i>D</i>)
0.5	900 (<i>d</i>)	400 (<i>d</i>)	500 (<i>s</i>)	850 (<i>D</i>)
1.0	800 (<i>d</i>)	400 (<i>s</i> *)	400 (<i>s</i>)	1850 (<i>d</i>)
3.0	-	-	-	1150 (<i>s</i> *)

Table 5-5. H₂ evolution rates for HER experiments of anatase (A), rutile (R), a 80:20 mixture of anatase and rutile (A+R), and P25. Values are rounded to steps of 50 $\mu\text{mol h}^{-1}$. *D*-quick deactivation, *d*-slow deactivation, *s*-stable, *s**-stable with slow initial kinetics.

protons and an increasing amount thus does not further increase the rate for H₂ evolution. Furthermore, a Pt loading that is higher than necessary for the HER reaction may block active sites on the TiO₂ surface as well as shield photons from exciting the metal oxide, hence resulting in a decreased rate.

Based on the highest observed H₂ generation rate, P25 is most active, followed by anatase, the mixture of anatase and rutile, and at last rutile. The better performance of anatase compared to rutile can be explained by the lower rate of recombination as well as other factors such as a possible different surface properties and differences in the band gaps (section 1.2.4).¹⁰¹⁻¹⁰² The improved performance of P25 has been assigned to a synergistic effect between anatase and rutile, in which the band alignment allows for better charge separation (section 1.2.4.1). While P25 can reach the by far highest overall activities, anatase may be the better choice as photocatalyst depending on the Pt loading, as we see that it achieves better stability and a higher maximum rate at lower Pt loading (e.g. 0.5 wt.% Pt). This should be kept in mind, when designing photocatalytic experiments. Also it should again be noted that deactivation depends on many different parameters such as concentration and type of sacrificial agent, light intensity etc. so that there is no universal solution to this problem.

Comparing the maximum activity values of anatase, rutile to their mixture shows an interesting trend: the observed maximum rates of the mixture correspond more to the maximum activities of rutile than of anatase. Thus, the influence of rutile seems to be larger in the mixture, although it is less abundant than anatase. Previous work showed that Pt preferably deposits onto rutile.²⁸⁴ I can use the data set on the activities of pure anatase and rutile at a specific loading to estimate the percentage of Pt that deposits onto rutile compared to anatase in the mixture under the assumption that there is a roughly linear relationship between Pt loading and the H₂ generation rate. For example, at a loading of 0.5 wt.% Pt, we record H₂ generation rates of 900 and 400 μmol h⁻¹ for pure anatase and rutile, respectively. Then, for the mixture I have to a) account for the mass fraction of anatase (0.8) and rutile (0.2) in the mixture and b) multiply by a factor to account for the fraction of the 0.5 wt.% Pt that is actually deposited onto either anatase or rutile. The sum of both activities is assumed to add up to the activity observed for the mixture at 0.5 wt.% Pt (500 μmol h⁻¹). Overall this gives us the following equation:

$$(5.20) \quad 0.8xA + 0.2(1 - x)R = 500 \mu\text{mol h}^{-1} \quad (\text{at } 0.5 \text{ wt.\% Pt})$$

, where A and R are the respective activities of anatase and rutile at 0.5wt.% Pt (in $\mu\text{mol h}^{-1}$), x is the percentage of Pt deposited onto the anatase phase, and 1-x is the percentage of Pt deposited onto the rutile phase. Solving the equation gives $x=0.65$, meaning that 65% of the deposited Pt deposits on anatase and 35% on rutile. Related to the mass percentages of anatase and rutile phase this gives an anatase-specific loading of 0.41 wt.% Pt and a rutile-specific loading of 0.88 wt.% Pt. From these calculations, I can infer that rutile attracts Pt two times stronger than anatase. The high Pt loading on the rutile phase can also explain the better stability of the mixture compared to pure anatase, which is the main component of the mixture and shows a slow deactivation type at 0.5 wt.%, while rutile is stable at 1.0 wt.% Pt, further supporting that the activity of the mixture is governed by rutile. As mentioned before, these calculations can – for now – only be considered with caution as I assume a linear relationship between the H_2 that is produced per hour and the Pt loading, which I actually do not observe. For example, at 0.02 wt.% the activity of rutile would be $3000 \mu\text{mol h}^{-1} \text{ wt.\%}^{-1}$, at 0.1 wt.% it would be $1750 \mu\text{mol h}^{-1} \text{ wt.\%}^{-1}$ and at 0.5 wt.% it would be $800 \mu\text{mol h}^{-1} \text{ wt.\%}^{-1}$. TEM analysis and complementary photocatalytic experiments will help to elucidate the actual affinities of Pt to anatase or rutile. Still, it seems clear from the observed stabilities and activities, that Pt-loaded rutile is the dominating component in the anatase and rutile mixture. As discussed above, this effect seems to be reduced in case of P25 due to the close interface between anatase and rutile in this material and an according charge separation effect that might reduce the preference of Pt to deposit onto rutile and leads to a less stable rates.

5.7.3. Conclusions

Deactivation is not specific to P25, but is also observed in the phase-pure polymorphs. Three levels of stabilities can be distinguished that are dependent on the Pt loading and TiO_2 type. Stabilities increase with an increasing Pt loading. Interestingly, the Pt loading for the most stable rate does not equal that for the highest observed maximum rate. Furthermore, observations of stabilities and maximum rates in the physical mixture of anatase and rutile as well as P25 suggest a preferential deposition of Pt onto the rutile phase.

5.8. Deactivation of Pt-loaded TiO₂ during photocatalytic HER and methanol oxidation: conclusions & outlook

I investigated an unusual and previously undiscussed deactivation of TiO₂ loaded with Pt during photocatalytic H₂ evolution from aqueous methanol solutions under UV irradiation. This deactivation seems to be mediated by oxygen vacancies that are inherent to the metal oxide or photoinduced during the reaction as suggested by photocatalytic experiments and ex situ characterization. The ratio of Pt particles to oxygen vacancies seems to be a critical factor for the stability of the H₂ generation rate. Three levels of stability (stable, slow deactivation, fast deactivation) can be distinguished, where stability increases with an increasing Pt loading. The most stable rates are not observed at the same loading as the highest activity. HER with phase-pure polymorphs and mixtures of thereof suggest a preferential deposition of Pt onto the rutile phase. Deactivation is not specific to the photodeposition method but has also been observed to a lesser extent for TiO₂ loaded with Pt by incipient wetness. Furthermore, it has been found to be – to a certain extent – a reversible process.

A possible SMSI-like encapsulation of Pt by suboxides invoked by an increasing degree of reduction during HER is suggested by TEM and XPS. Furthermore, monitoring the CO generation during the photooxidation of methanol shows an evident correlation between an increasing CO concentration and decreasing H₂ rates. I suggest that certain reaction conditions lead to a switch in mechanism to favor the formation of a methyl formate intermediate that is accompanied by slower reaction kinetics and CO generation through a reverse water-gas shift reaction. Electron back-donation by surface Ti³⁺ from oxygen vacancies might have a stabilizing impact on the CO generation. Furthermore, an increasing amount of oxygen vacancies may increase the probability of bimolecular site reactions of methanol due to a higher number of adsorption sites. A novel liquid phase ATR-FTIR cell has been developed that will allow for systematic studies at controlled parameters in order to identify possible different reaction pathways.

However, what is much more needed is an in situ characterization technique to obtain direct evidence for the oxygen vacancy creation during my reaction. However, standard techniques such as XPS or HRTEM that would identify the presence of Ti³⁺ or a possible encapsulation are UHV techniques that will not allow for my experimental conditions. Still, recent technical progress may allow for in situ XPS

illumination of certain samples. In situ photo-EPR is another possible analysis method.

The observed behaviors may explain varying reports on H₂ activities or previous findings that could not be explained by authors. For example, Ohtani et al. noticed a decreased photocatalytic activity of TiO₂ samples after washing that included an ultrasonication step they could not explain but fits with the US-dependence that I observe.⁹⁴ In another example, Chiarello et al. found a more than linear increase in H₂ evolution when they increased their doubled their Pt loading, which fits the Pt loading-dependence described above.¹⁵ Pan et al. showed a continuous decrease in H₂ evolution in a series of photooxidation experiments of benzyl alcohol and suggested an increases concentration of oxygen vacancies to be the cause.¹⁰⁸ This fits with the observed slow-type of deactivation. Thus, the observed results are highly relevant when considering Pt-loaded TiO₂ as a reference system.

My studies show that although Pt-loaded TiO₂ is a benchmark system, there are still many open questions to the reaction mechanism and influence of certain parameters on this complex and dynamic system. Understanding individual steps will help in designing better photocatalysts.

6 Black TiO₂

In this chapter, four different approaches from highly-cited literature references to synthesize black TiO₂ are reproduced in order to identify key characteristics that influence the photocatalytic performance of this material. Properties of black TiO₂ have shown a wide variance and an exact definition of black TiO₂ is diffuse up to now. Two H₂ thermal treatments and two chemical reductions were chosen for comparison. One H₂ thermal treatment is the original first report on black TiO₂ and is meant to serve as a reference for the remaining methods.¹²⁹ The second is a method published by Naldoni et al. in 2012, in which an amorphous TiO₂ precursor was treated with H₂ and then cooled rapidly in order to “freeze” the metastable disordered outer layer.¹⁸⁷ The two chemical reductions are conducted with aluminum¹⁸⁶ and NaBH₄¹⁹¹, respectively. The aluminum reduction is conducted in an evacuated two-zone furnace with aluminum serving as reductant by reacting with oxygen, lowering the oxygen partial pressure in the system and triggering reduction of the outer layers of P25 in the lower temperature compartment.¹⁸⁶ NaBH₄ is a simple solid mixing approach in which H₂ is set free upon heating and reduces the outer layers of P25.¹⁹¹ Thus, it can be seen as being a combination of both chemical reduction and H₂ thermal treatment.

A comprehensive set of characterization techniques is used to thoroughly characterize all synthesized materials. A short summary of what is the purpose of each characterization technique is given below in order to allow for a better overview:

DRS: check for extended visible light absorption and possible decrease in the optical band gap as well as possible interband gap states.

HRTEM: check for the presence of a disordered outer shell. All images were recorded at specific conditions to avoid electron beam-induced damage (section 4.2).

BET: check for surface area changes. Generally, not well-investigated in the context of black TiO₂.

Raman: check for indications of strain or defects in form of peak broadenings and shifts as well as possible additional modes that have been observed in the context of black TiO₂. All spectra are measured at conditions for highest possible intensity while trying to minimize effects due to sample heating or reoxidation (Section 4.3).

XRD: check for changes in phase composition and strain induced by disorder.

(VB-)XPS: check for possible Ti³⁺ generation, changes in Ti-OH and creation of VB tail states as observed in the original report and some other literature reports on black TiO₂.

Photocatalytic activities for the HER were investigated under UV and visible light at high Pt loadings of 1.0 wt.% in 50 vol.% aqueous methanol solutions to avoid possible deactivation events. 10 mg of photocatalysts were used in each experiment except for the aluminum reduction, where only 4 mg was used due to sometimes low amounts of synthesized material.

Each section of a specific synthesis will be concluded with a short discussion and comparison to the literature reference. An overall comparison between all references and my work is listed in Table 6-9 at the end of this chapter.

6.1. TiO₂ reduced at high H₂ pressure

Prolonged reduction of TiO₂ in a high pressure H₂ atmosphere at 200 °C is the original method to obtain black TiO₂ as reported by Chen et al.¹²⁹ The authors suggested hydride formation that stabilized an approximately 1 nm thick disordered outer layer in anatase nanocrystals of about 8 nm in size. The disordered outer layer led to extended visible light absorption as well as reduced recombination and an overall higher photocatalytic performance (section 1.3.5).

The following section covers the characterization and photocatalytic performance for the HER of four different TiO₂ materials reduced in a high pressure H₂ atmosphere: anatase nanocrystals that were made according to Chen et al., commercial anatase nanopowder, commercial rutile nanopowder, and P25.

6.1.1. Color

High pressure-reduced TiO₂ (40 bar) changes its color from white to different shades of brown depending on the phase and crystal size of the starting material (Figure 6-1). The color change is most drastic for the self-made anatase nanocrystals (aNC), which turned from an off-white tone to dark brown. Commercial anatase nanopowder turned from pure white to a medium brown tone, while P25 and commercial rutile turned from pure white to beige. Rutile showed the smallest change in coloration.

This color change is unexpected in the conventional reduction of TiO₂ by H₂ which creates oxygen vacancies and Ti³⁺ color centers, that result in a blue color of reduced TiO₂ (section 1.3.1.1). However, in the recent literature on the synthesis of black TiO₂, a sudden variety of colors has been reported, including brown TiO₂ (section 1.3.5.2). For example, Xin et al. oxidized TiH₂ with H₂O₂ to obtain TiO₂ that was ranging in color from light brown to black depending on the annealing



Figure 6-1. Images of different TiO₂ samples before (top) and after (bottom) treatment in 40 bar H₂ atmosphere for 5 days at 200 °C.

temperature. NaOH and NaBH₄ were used for pH control and as antioxidant and eliminated from the final products by washing with HCl, water and ethanol.²⁸⁵ The annealing step in the post-treatment resulted in a stoichiometric surface layer but defective core as evidenced by XPS and EPR, respectively. The absorption in visible light range was thus ascribed to bulk Ti³⁺ defects and a continuous vacancy band. Additionally, Lu et al. conducted a high pressure hydrogenation of P25 at 35 bar H₂ pressure and room temperature for 3-20 days.²⁸⁶ Depending on the time of H₂ treatment P25 turned from light beige as observed in this work to dark brown similar to my H₂-treated nanocrystals, which they assign to be black TiO₂. While the authors did not explicitly discuss the origin of the color, they observed a disordered outer shell and correlated their work to Chen et al., so it can be assumed that they as well attribute the color to new VB states generated by the introduced surface disorder.

Furthermore – not correlated to black TiO₂ – Wang et al. synthesized brown P25 via reduction with NaH under inert gas at temperatures between 120 and 150 °C.²⁸⁷ The absorption edge was attributed to Ti³⁺ and oxygen vacancies, as supported by shifts in the XPS Ti 2p spectra. The authors did not discuss why they did not observe the typical blue coloration for reduced TiO₂. Some trace amounts of Na⁺ remained, which may explain a different coloration. Sodium is present in both syntheses that resulted in brown TiO₂, which might make one suspecting it to be the cause of the unusual coloration. Sodium titanates have been reported to be white, yellowish-green but also blue to black in color.²⁸⁸⁻²⁸⁹ However in my experiments, I did not come into any contact with Na so that I could correlate the color with possible Na⁺ incorporation. Additionally, in a later section, I will show that the presence of sodium impurities results in blue colored TiO₂ reduced using NaBH₄ resulted in blue products (section 6.2).

The darkening of the color could therefore be correlated to the degree of hydrogenation. One conclusion would be that the degree of hydrogenation is phase-dependent and that anatase reacts more easily than rutile and P25. The difference in the anatase nanocrystals (ca. 8-15 nm in TEM) and the commercial nanopowder (ca. 15 nm in TEM) suggests that crystal size effects are more important. Rutile the lightest material has the largest crystals, followed by P25, the mixture of rutile and anatase, with the second lightest color. This observation agrees with the formation mechanism suggested by Liu et al., in which H₂ acting as a scissor molecule is favored at the surface (section 1.3.5.1), smaller particles with a higher surface-to-bulk ratio will experience a higher relative degree of hydrogenation per crystal than larger crystals.¹⁸⁰

6.1.2. DRS

All samples reduced with high H₂ pressure exhibit a higher absorption in the visible light range (400-800 nm, 3-1.5 eV) resulting in the different brown tones discussed above. Figure 6-2 shows the Tauc plots of (a) high-pressure reduced self-made aNC, (b) anatase, (c) rutile and (d) P25 and their pristine precursors.

The untreated, self-made aNC have an estimated band gap of 2.88 eV which is already significantly below the typical band gap of anatase (3.20 eV).⁹⁶ Upon H₂ treatment, the nanocrystals do not have a well-defined band gap anymore – similar to NaBH₄-reduced samples that are discussed in a later section (6.3) – rendering a band gap estimation from the Tauc plot unreasonable. The band gap of commercial anatase decreases from the characteristic 3.20 eV to 2.70 eV when treated in H₂. While the onset of the absorption edge remains unchanged for the H₂-treated anatase, the slope of the edge flattens and visible light absorption increases. The estimated band gaps for rutile and P25 were 3.03 and 3.15 eV, respectively, in complete agreement with literature.^{38, 242-243} Upon H₂ treatment, only

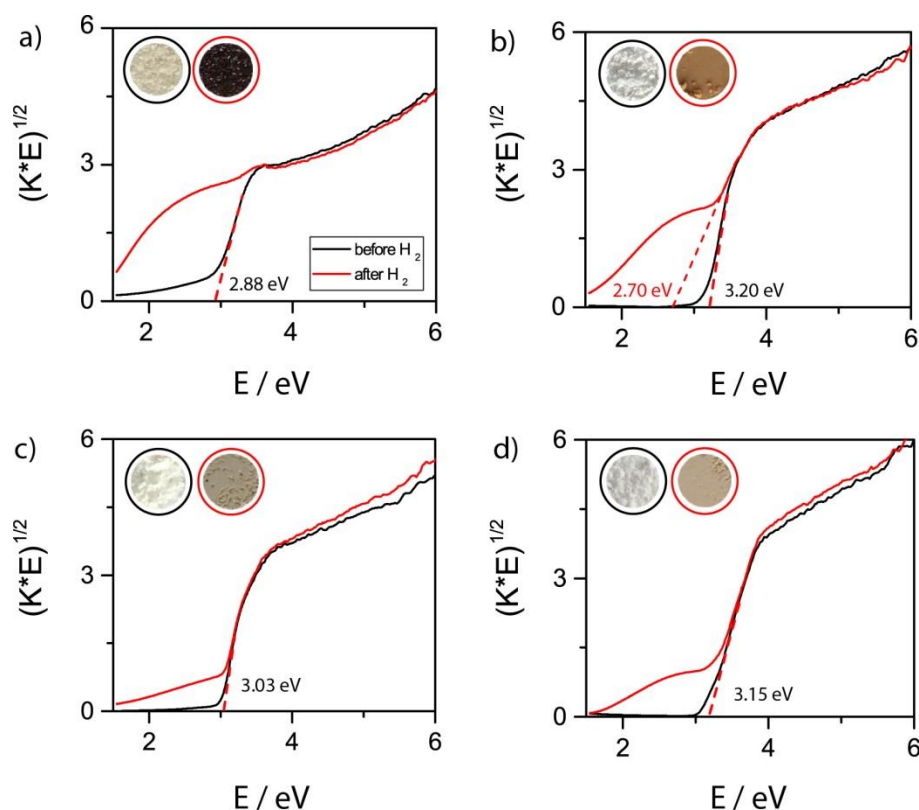


Figure 6-2. Tauc plots of (a) high-pressure reduced self-made aNC, (b) anatase, (c) rutile and (d) P25 and their pristine precursors.

the visible light absorption increases for rutile and P25, while the absorption onset and slope remain unchanged.

The observed band gap of 2.88 eV for the self-made aNC does agree with the reported value of 3.30 eV by Chen et al. (Figure 6-2b).¹²⁹ Reduction of the band gap can be attributed to defect states. Following Chen et al., I used F127 as an organic template during synthesis of aNC. Possibly some organic rests are still present in the sample, that result in the reduced band gap. However, the absorption spectra of the self-made aNC and reduced aNC seem to be in good agreement with Chen et al.

In conclusion, DRS did not show a red-shift usually attributed to the creation of Ti³⁺ centers in reduced TiO₂, but an increased visible light absorption in accordance with Chen et al. Absorption increased in the order of reduced rutile > reduced P25 > reduced anatase (commercial) > reduced anatase (self-made), which is also reflected in the increasingly darker color. The anatase samples additionally show a flatter absorption edge that – in the case of aNC – make a band gap estimation from Tauc plots unreasonable.

6.1.3. BET

Table 6-1 shows the BET surface areas for aNC, anatase, rutile and P25 before and after H₂ treatment of one specific sample batch. The sample amount for H₂-treated rutile was not large enough for correct measurements and will be measured in the future.

Still, a clear trend can be seen: upon H₂ treatment, the surface areas of all samples

Sample type	BET surface area / m ² g ⁻¹
aNC	50.2
aNC + H ₂	30.4
anatase	89.3
anatase + H ₂	69.6
rutile	26.9
rutile + H ₂	-
P25	54.7
P25 + H ₂	46.7

Table 6-1. BET surface areas for aNC, anatase, rutile and P25 before and after 40 bar H₂ atmosphere for 5 days at 200 °C of one specific sample batch.

show a clear decrease. The difference in surface areas before and after H₂ treatment is most pronounced for H₂-treated aNC (ca. –40 %, which also shows the darkest) and least pronounced for P25 (ca. –15 %).

6.1.4. TEM

TEM images of the reduced TiO₂ samples and their precursors were recorded to check for morphological changes, in particular, to investigate the possible formation of a disordered outer shell as it has been observed by Chen et al.. Figure 6-3 shows the TEM images of a) aNC b) H₂-treated aNC, c) commercial anatase, d) H₂-treated commercial anatase. The self-made aNC show crystal sizes in the range of 8 to 12 nm with lattice spacings of 0.36 nm that are typical for the anatase(101)facet.²⁹⁰⁻²⁹¹ The aNC tend to form dense clusters that do not separate well on the TEM grid. Thus, isolated crystals are difficult to observe. Furthermore, the self-made aNC show a rougher surface than the commercially obtained anatase. The commercial anatase arranged in flower-like clusters, differently from rutile and P25. Crystallite sizes were in the range of 20 by 30 nm ($d = 0.35$ nm).

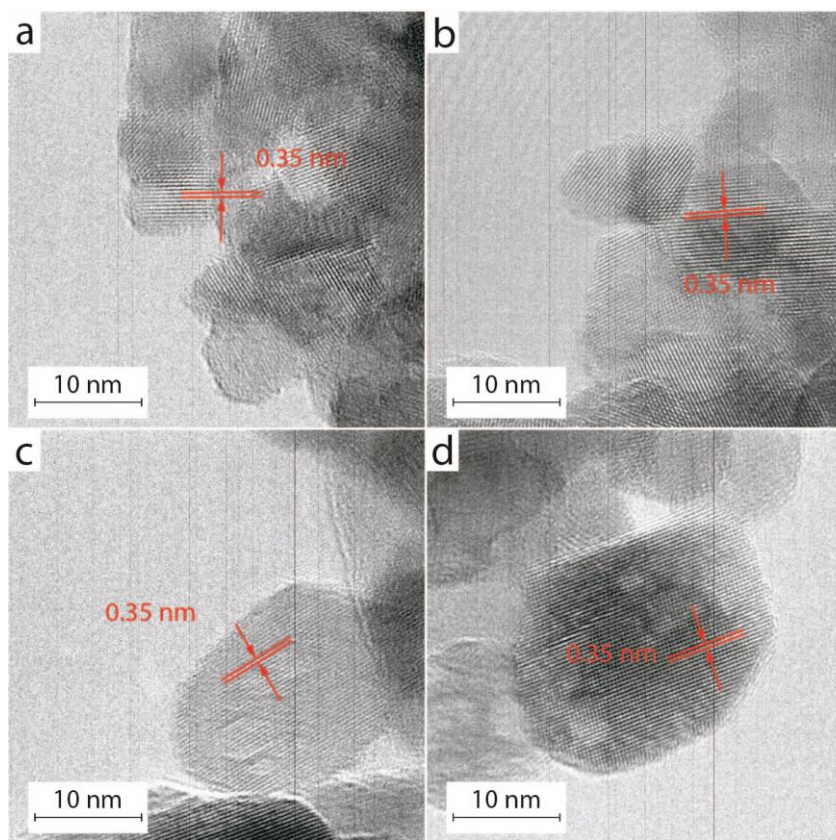


Figure 6-3. TEM images of a) aNC b) H₂-treated aNC, c) commercial anatase, d) H₂-treated commercial anatase.

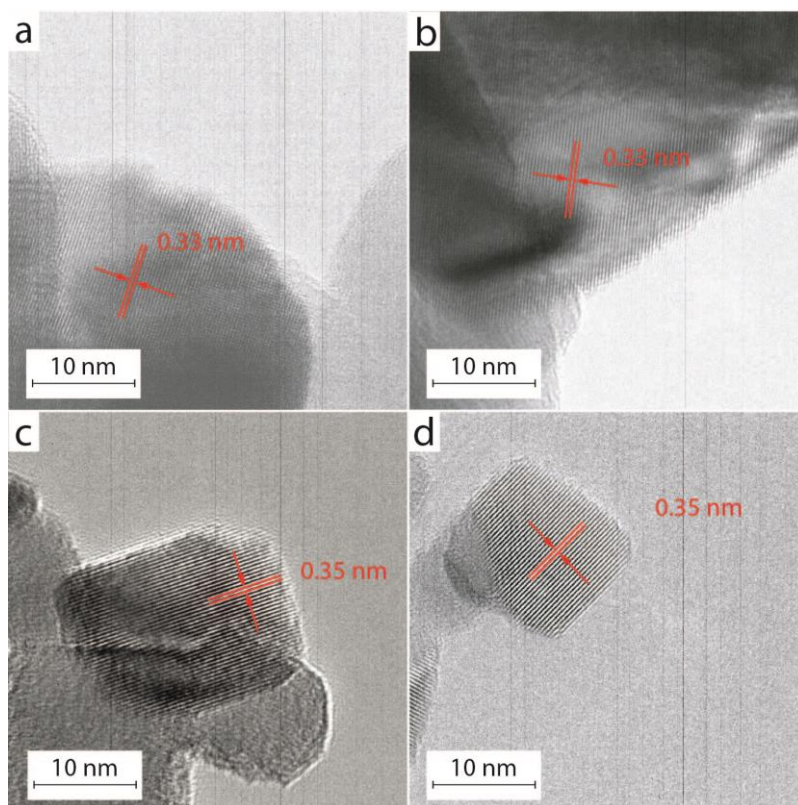


Figure 6-4. TEM images of a) commercial rutile b) H₂-treated rutile, c) P25, d) H₂-treated P25.

Figure 6-4 shows the TEM images of a) commercial rutile b) H₂-treated rutile, c) P25, d) H₂-treated P25. As expected, rutile shows larger crystals than the anatase samples with sizes ranging from 50 by 30 nm to comparably very large crystals of almost 100 nm in size. The lattice spacing is slightly lower with 0.33 nm which correlates to the (110) facet of rutile. The images of P25 show typical anatase and rutile crystallites with no apparent changes upon H₂ treatment.

Overall, the TEM images showed no significant differences between the pristine TiO₂ and TiO₂ reduced in a high pressure H₂ atmosphere. While in some cases surfaces look like they might have been roughened upon reduction (e.g. anatase, Figure 6-3c-d), TEM images were not consistent enough to give real evidence for this observation. In addition, even the pristine TiO₂ samples showed thin amorphous outer layers in some of the images (see section 4.2). Thus, the high pressure H₂ treatment of TiO₂ did not result in a formation of a clearly visible amorphous outer layer in this case. Also, lattice disorder was not observed as in the case for other reduction methods (section 6.2).

6.1.5. Raman

Figure 6-5 shows the Raman spectra of all high P-reduced samples with their corresponding references. The anatase and P25 samples show typical bands for E_g (145 cm⁻¹, 198 cm⁻¹, 640 cm⁻¹), B_{1g} (398 cm⁻¹), and an A_{1g} mode (516 cm⁻¹ superimposed by 519 cm⁻¹) with some slight variations between P25 and anatase.^{170, 179} Rutile shows typical bands at 144 (B_{1g}), 447 (E_g) and 611 cm⁻¹ (A_{1g}).²²⁷ Samples were measured in a way that obvious damage due to the laser beam was avoided (section 4.3). Still, the commercial anatase and P25 proved to be quite vulnerable to laser-induced damages even at very low laser intensities (e.g. 1%). Rutile proved to be very robust towards laser-induced damages. If the damage is attributed to reduction or oxidation processes, this different behavior is not as surprising as rutile is the thermodynamically most stable phase of TiO₂ (section 1.2.4).

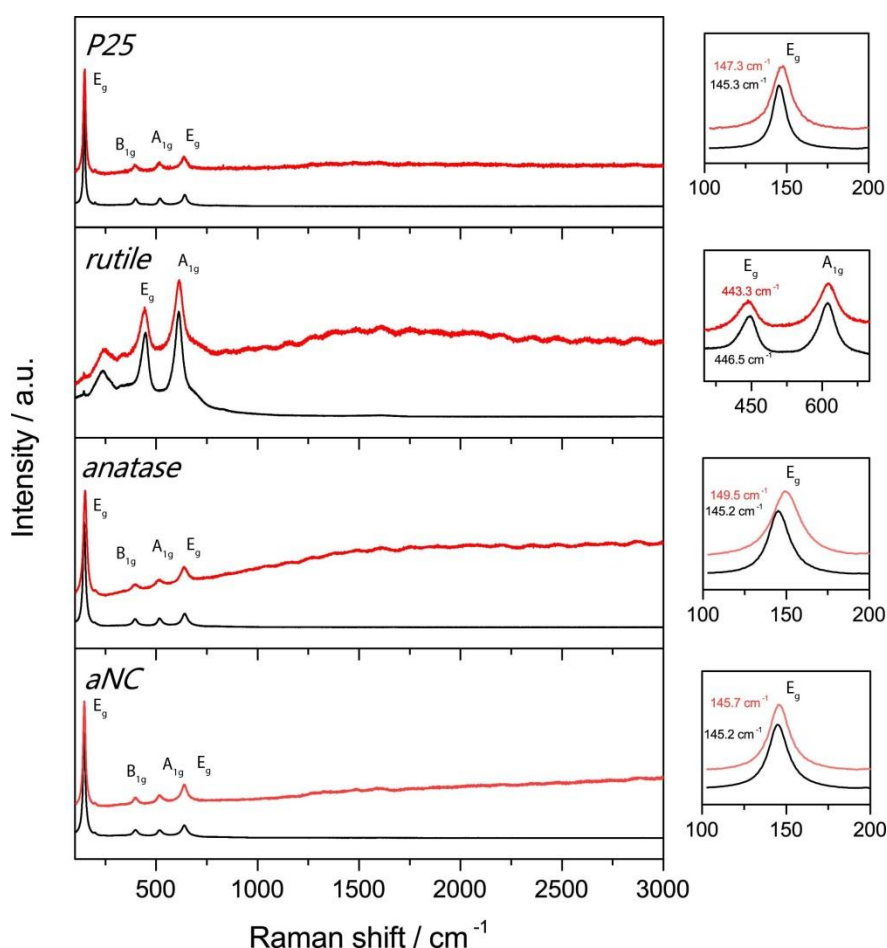


Figure 6-5. Raman spectra of P25, rutile, anatase, aNC before (black) and after (red) H₂ treatment at 40 bar for 5 days at 200 °C. Right: Close-ups of the E_g modes.

The E_g mode of the reduced samples is shifted compared to the references (Figure 6-5 close-up). The anatase samples and P25 show a blue-shift between approximately 0.5 and 4 cm⁻¹, which is most pronounced in the commercial anatase sample. Rutile shows a red-shift by 3 cm⁻¹. Additionally, peaks are broadened after H₂ treatment. Generally, peak shift and broadening can be attributed to lattice strain by phonon-confinement due to a small grain size and nonstoichiometry.²²⁸ Furthermore, all reduced samples show a dramatic decrease in signal intensity compared to their references indicating a different scattering behavior. This might be caused by defects as parameters such as sample concentration or laser source remain constant between measurements. Additionally, Raman spectra for reduced samples show periodic irregularities in the range between 1000 and 3000 cm⁻¹, that are quite pronounced in some cases and are combined with an upward slope in those samples. This kind of background has been previously assigned to fluorescence.²⁹² Fluorescence in TiO₂ has been shown to be caused by the presence of defect states like oxygen vacancies.²⁹³⁻²⁹⁴ I, therefore, attribute the increased background to an increased amount of oxygen vacancies in H₂-treated TiO₂.

In conclusion, the observed background together with the mode shifts and broadenings are strong evidence for the presence of defects, i.e. oxygen vacancies, in TiO₂ samples reduced under a high pressure H₂ atmosphere.

6.1.6. XRD

Figure 6-6 shows the XRD patterns of the high pressure reduced samples and their references. None of the reduced samples showed changes in the diffraction pattern, i.e. peak broadening, shifts or emergence of new phases that could be correlated to structural strain or changes – such as suboxide formation. Also averaged crystallite sizes remained basically unchanged. The self-made aNC are of pure anatase phase, just as the commercial anatase powder. However, reflexes are slightly broader – indicating a smaller crystallite size of the nanocrystals

Average crystallite sizes of aNC, anatase, rutile and P25 before and after 40 bar H₂ atmosphere for 5 days at 200 °C as calculated from the Scherrer equation (equation (3.13)) are listed in Table 6-2. The average crystallite size of the aNC is calculated using the average of two reflexes (25.5° and 48.0°) and is found to be 13.4 ± 1.4 nm, which does not differ much from commercial anatase with a calculated average crystallite size of 14.5 ± 0.9 nm. However, TEM images revealed crystals that were significantly smaller compared to commercial anatase and about 8 nm in size. As XRD is an averaging technique, these contradicting obser-

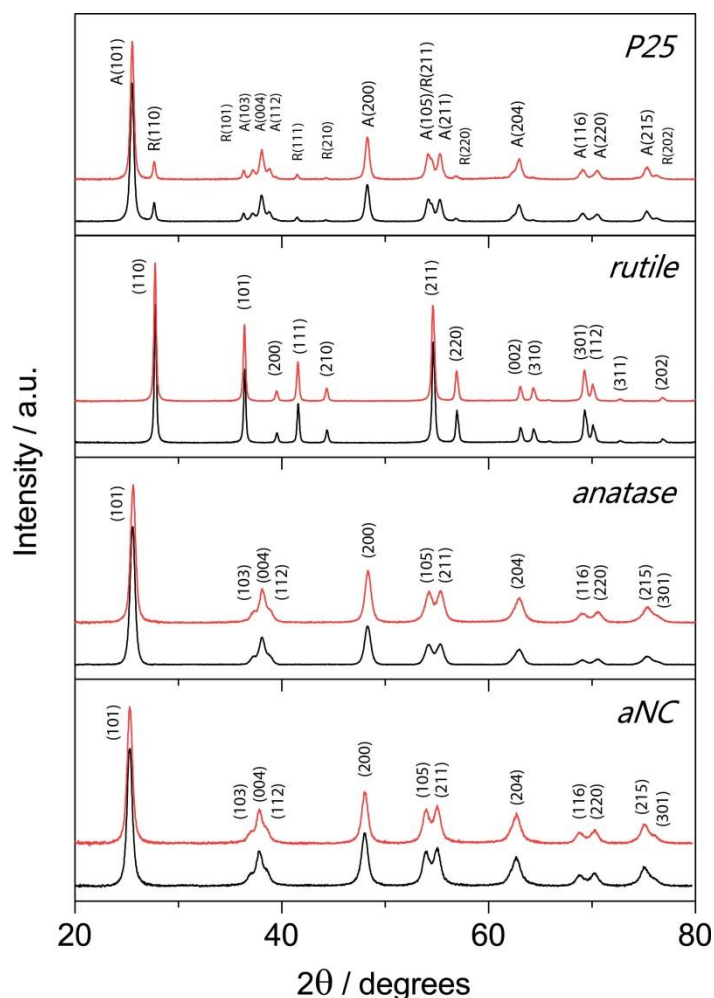


Figure 6-6. XRD patterns of P25, rutile, anatase, aNC before (black) and after (red) H₂ treatment at 40 bar. for 5 days at 200 °C.

variations indicate that a broader size distribution in the self-made nanocrystals than in commercial anatase. Commercial rutile is of pure phase as well (size by Scherrer: 44.3 ± 0.3 nm for $2\theta = 27.7^\circ$ and 36.4°), while P25 shows the expected mixture of anatase and rutile reflexes (size by Scherrer: anatase = 21.4 ± 1.4 nm (25.5° , 48.3°); rutile = 26.7 ± 1.5 nm (27.7° , 41.5°)).

In conclusion, XRD did not show any structural changes of the reduced samples which is in agreement with Chen et al.'s work. Crystallite sizes for the self-made anatase nanocrystals following Chen et al.'s procedure were higher than reported, although TEM images showed 8 nm crystals. Contrary to other reduction methods, I did not observe the formation of suboxide phases.

Sample	Phase	average crystallite size / nm
aNC	A	13.4 ± 1.4
aNC + H ₂	A	12.8 ± 0.9
anatase	A	14.5 ± 0.9
anatase + H ₂	A	14.4 ± 1.6
rutile	R	44.3 ± 0.3
rutile + H ₂	R	40.8 ± 0.7
P25	A	21.4 ± 1.4
P25 + H ₂	A	33.5 ± 2.5
P25	R	26.7 ± 1.5
P25 + H ₂	R	37.2 ± 2.4

Table 6-2. Average crystallite sizes aNC, anatase, rutile and P25 before and after 40 bar H₂ atmosphere for 5 days at 200 °C as calculated from the Scherrer equation. A – anatase, R – rutile.

6.1.7. XPS

Survey spectra of the high-P reduced TiO₂ do not show any impurities. There is also no significant change in the O:Ti ratio that would point towards suboxide formation. The C 1s spectra show the typical shape for adventitious carbon (C-C = 284.8 eV) (section 4.4.1) (Figure 6-7). However, the reduced anatase nanocrystals showed a slightly broadened C 1s signal and an increase in the component stemming from organic C=O bonds at 287.7 eV. This is in line with the O 1s spectrum of this sample, as it showed a clearly increased signal at 532.1 eV that was assigned to organic C=O bonds (Figure 6-8). This could be due to a higher number of defect sites that can act as adsorption sites. The remaining O 1s spectra of the reduced TiO₂ show slight variations, but were mainly of similar shape as the precursors and also did not vary much between the different types of TiO₂. Chen et al. did not comment on the C 1s spectra, but noticed a dramatic increase in the Ti-OH signal in the O 1s spectra of their reduced black nanocrystals.¹²⁹ I cannot observe the same behavior here.

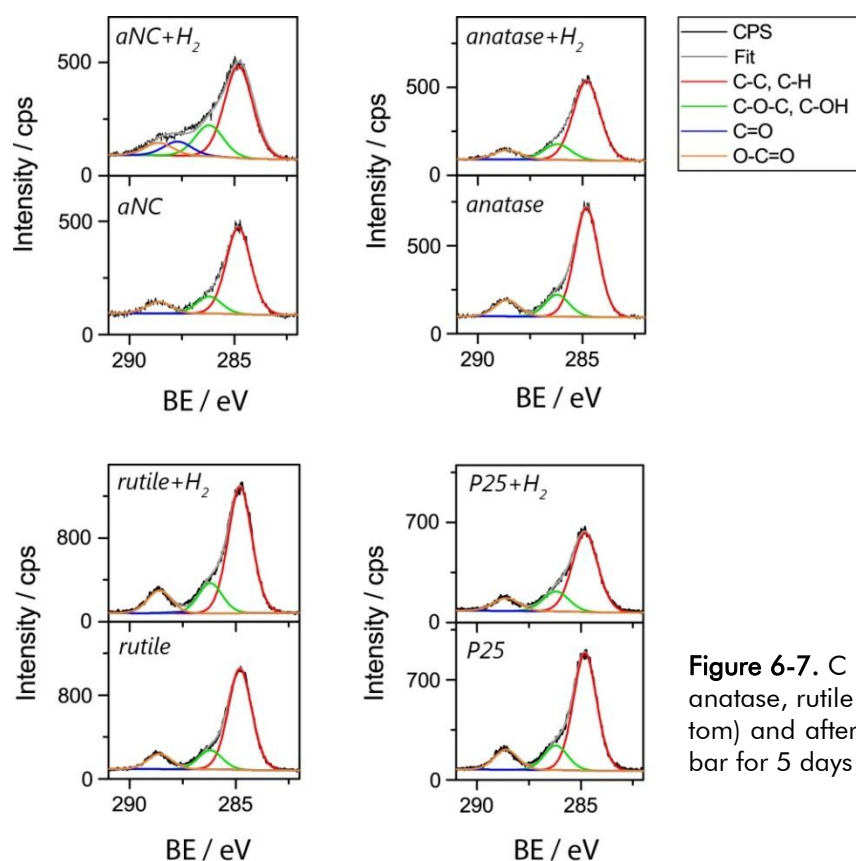


Figure 6-7. C 1s detail spectra of aNC, anatase, rutile and P25 before (bottom) and after (top) H₂ treatment at 40 bar for 5 days at 200 °C.

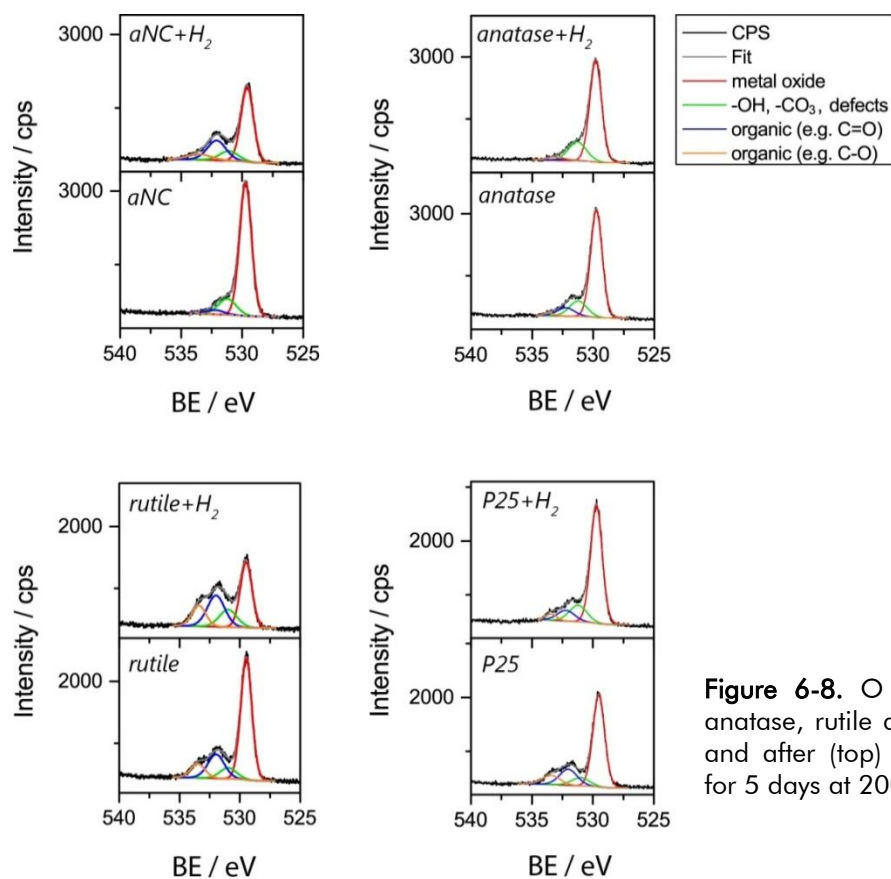


Figure 6-8. O 1s detail spectra aNC, anatase, rutile and P25 before (bottom) and after (top) H₂ treatment at 40 bar for 5 days at 200 °C.

Figure 6-9 shows the Ti 2p spectra of the H₂-treated samples and their references. All samples show the typical split 2p orbital of Ti⁴⁺ with the Ti 2p_{3/2} at 458.3-5 eV and $\Delta_{\text{oxide}} = 5.7$ eV (section 4.4.3). Very interestingly, the H₂-treated aNC show a split component at 460.8 eV and 466.5 eV ($\Delta = 5.7$ eV). Generally, charging of a sample can result in a shift to higher BE due to a higher positive charge. This shift is usually seen in form of a distorted and broad signal with a shoulder at the higher BE side of the peak and is observed in the C 1s and O 1s spectra as well. Neither is the case here. This makes it difficult to argue that the extra signal in the Ti 2p spectra of the H₂-treated aNC results from a charging effect. However, as Ti⁴⁺ is already the highest oxidation state of Ti, a Ti 2p_{3/2} signal that is at a 2 eV higher BE than 458.5 eV does not seem to be physically sensible as it would correspond to an even higher oxidation state.

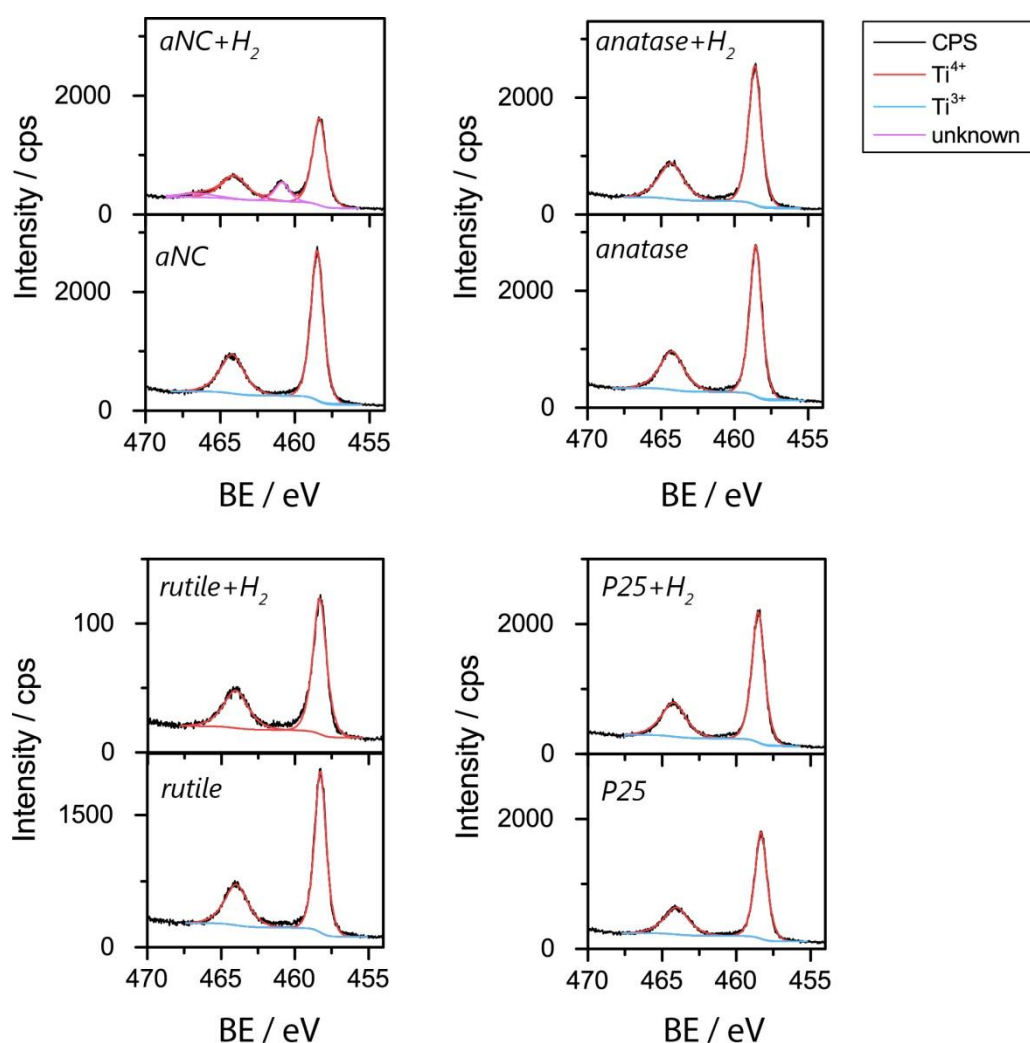


Figure 6-9. Ti 2p detail spectra of aNC, anatase, rutile and P25 before (bottom) and after (top) H₂ treatment at 40 bar for 5 days at 200 °C. H₂-treated rutile was measured second time because of some charging effects, a little different intensity due to measurement.

A strong characteristic of the black TiO₂ reported by Chen et al. is a distinct VB tail in the VB-XPS spectra of black nanocrystals that resulted in a largely decreased band gap of this material due to hydrogenation. Figure 6-10 shows the VB-XPS spectra of my samples. We observed neither a VB tail as described by Chen et al. nor a decrease in the VBM in the H₂-treated TiO₂. However, when I fit the VB orbitals as described in section 4.4.4, I see a slight increase in the contribution from the non-bonding O 2p orbitals as well as in the σ state component (predominantly O 2p _{σ} states). The contribution from the π states (t_{2g} and the O 2p _{π} states) decreased in all cases. This points towards a higher influence of the oxygen in the metal oxide bonding and, vice versa, a lower influence by the electrons from titanium. No split of the σ states was observed as in other reduction methods discussed in later sections (section 6.2.7.3). The H₂-treated aNC and rutile additionally showed an increase in the component stemming from hydroxyl groups or molecular water. This is consistent with the C 1s and O 1s spectra, which also showed an increased contribution from adsorbed species for these samples.

In conclusion, XPS measurements confirm the absence of Ti³⁺ as reported by

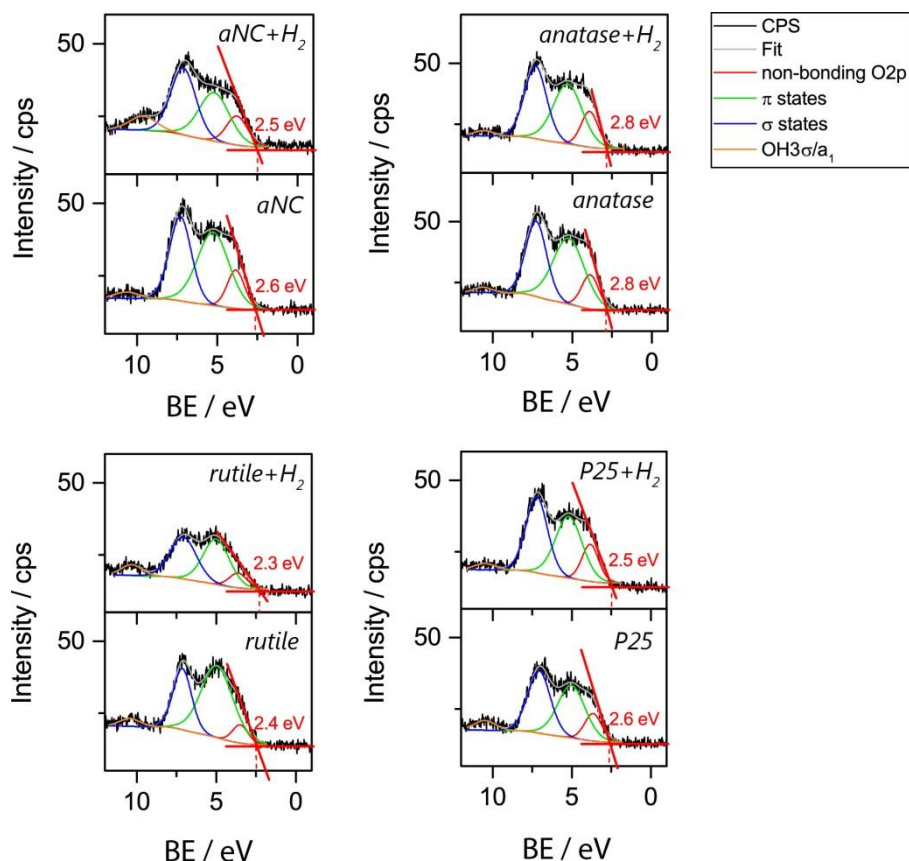


Figure 6-10. VB detail spectra of aNC, anatase, rutile and P25 before (bottom) and after (top) H₂ treatment at 40 bar for 5 days at 200 °C.

Chen et al. I can neither observe a VB tail nor a drastic increase in –OH groups as reported. However, since I also do not observe the formation of a disordered outer shell in TEM, this could be seen as indirect proof that the shell is the cause of the VB tail. Furthermore, I see an additional signal at 460.8 eV for Ti 2p_{3/2} that cannot be explained up to now.

6.1.8. HER

Photocatalytic H₂ evolution of the different H₂-treated TiO₂ types and their precursors has been investigated under UV and visible light irradiation.

6.1.8.1. *UV irradiation*

Figure 6-11 shows the HER experiments of aNC, anatase, rutile and P25 before (black) and after (red) H₂ treatment at 40 bar for 5 days at 200 °C under UV light. The different pristine TiO₂ polymorphs show clear differences in their performances. P25 – the known benchmark photocatalyst – outperforms the single-phase polymorphs rutile and anatase by far with a maximum activity of about 1200 $\mu\text{mol h}^{-1}$ (120 $\text{mmol h}^{-1} \text{ g}^{-1}$). The commercial anatase shows a significantly lower but still good activity (480 $\mu\text{mol h}^{-1}$; 48 $\text{mmol h}^{-1} \text{ g}^{-1}$). The activity of the commercial rutile lies in a similar range as the self-made anatase nanocrystals (ca. 100 $\mu\text{mol h}^{-1}$; 10 $\text{mmol h}^{-1} \text{ g}^{-1}$). Besides the maximum activity, there are also some differences in the stability of the rates that could be observed. P25 shows a gradual decrease that has been observed before in all previous experiments and seems to be specific for the material (Chapter 5). This instability is less pronounced in the pure commercial anatase, whereas the commercial rutile shows a stronger decrease. While this is not exactly the “sudden” deactivation as discussed in the previous chapter, it might also have origins in an increasing degree of reduction under UV irradiation. However, the precise origin is not yet understood. The self-made aNC display a slow but steady increase during the course of the experiment suggesting that some platinum is still being deposited. Absolute rates are quite low compared with the commercial anatase. Band gap estimation by DRS gave a much significantly smaller value for the aNC than for commercial anatase, while the VB-XPS measurements showed no deviation from the VBM of the commercial anatase and P25 (mainly anatase). This suggests, that the CB for the aNC is at a potential that is too low to be a good driving force for H₂ evolution.

The H₂-treated samples all show a strongly reduced performance. H₂ evolution rates are all in a similar range – between 25 and 50 $\mu\text{mol h}^{-1}$ – independent of the precursor.

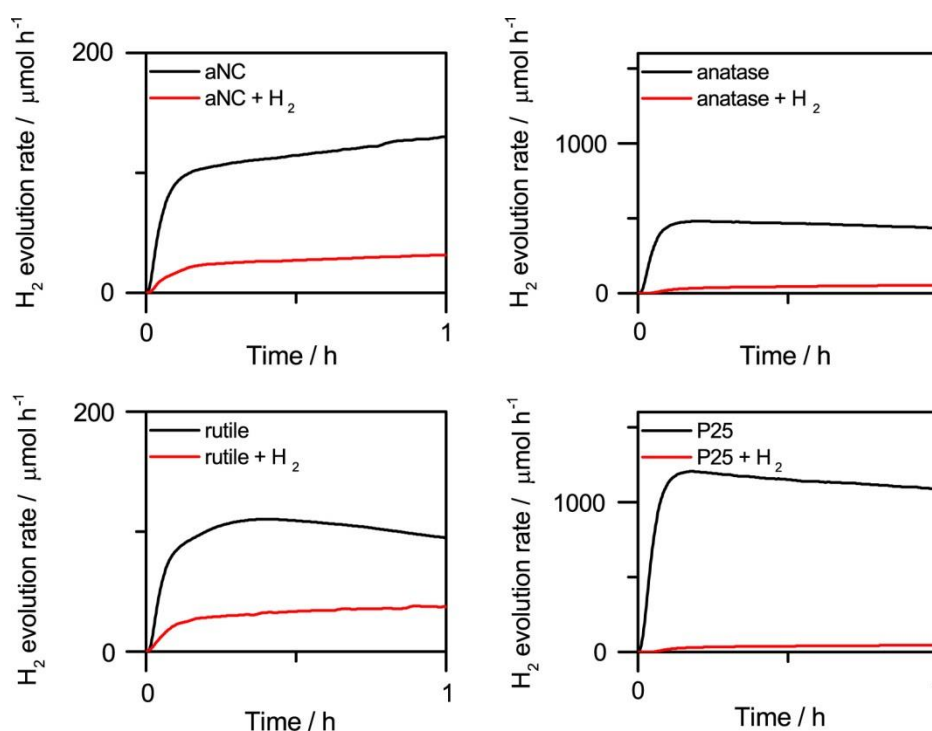


Figure 6-11. HER experiments under UV light of aNC, anatase, rutile and P25 before (black) and after (red) H₂ treatment at 40 bar for 5 days at 200 °C.

6.1.8.2. Visible light irradiation

Figure 6-12 shows the HER experiments under visible light of aNC, anatase, rutile and P25 before (black) and after (red) H₂ treatment. P25, rutile and – to a very small extent – commercial anatase show visible light activity. The band gap of rutile (3.0 eV/415 nm) lies at the lower limit of the visible light range which explains the small but steady activity (8.4 μmol h⁻¹, 0.84 mmol h⁻¹ g⁻¹). P25 outperforms rutile with a 3-fold increase in activity (26 μmol h⁻¹, 2.6 mmol h⁻¹ g⁻¹), although the percentage of rutile in P25 is only about 15 %.⁹⁴ This higher activity is in agreement with previous findings and was attributed to a synergy between rutile and anatase: Rutile takes on the role of a visible light sensitizer (section 1.2.4.1). It can get excited in the visible light range and deliver charge to the more active anatase. Overall, this leads to a higher rate of H₂ generation under visible light for P25. In comparison, very low (0.2 mmol h⁻¹ g⁻¹) but present hydrogen evolution for commercial anatase can be explained by the fact, that our visible light source ranges from 400 to 700 nm which can still excite anatase to a very small extent as it has a very slight absorption up to about 420 nm. The aNC show no activity under visible light irradiation, which is in line with the lower band gap compared to the commercial anatase as observed by DRS.

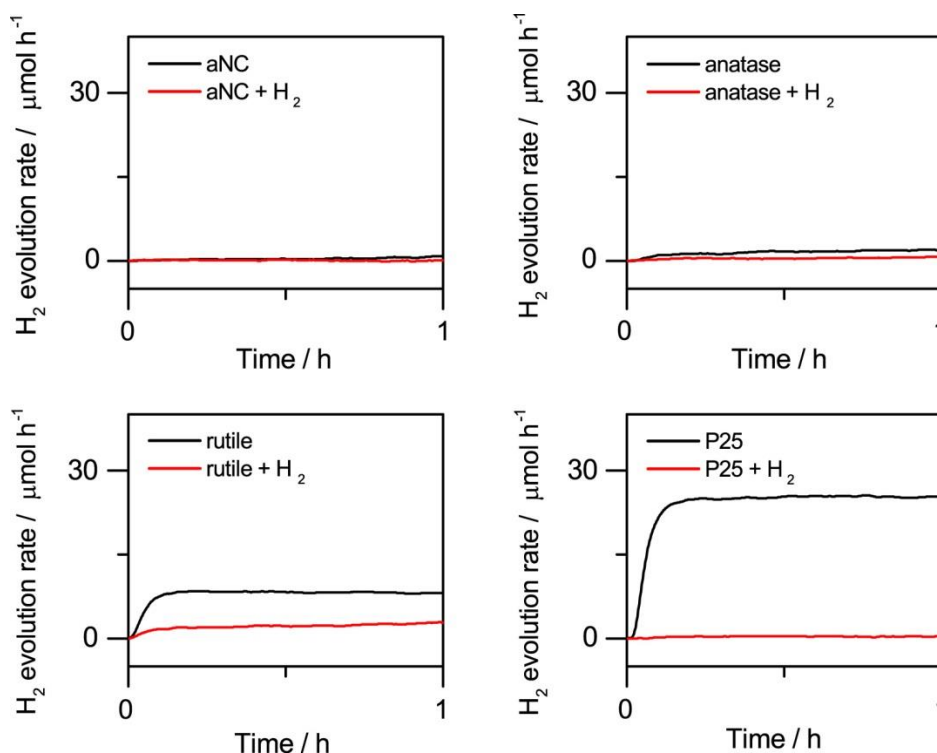


Figure 6-12. HER experiments under visible light of aNC, anatase, rutile and P25 before (black) and after (red) H₂ treatment at 40 bar for 5 days at 200 °C.

6.1.9. Discussion & Conclusions

Chen et al. show that during high pressure H₂ treatment at elevated temperatures a disordered outer shell is created. The disordered surface layer results in VB tail states that reduce recombination by hole trapping and led to high photocatalytic activities under simulated solar light. Furthermore, their black TiO₂ exhibits extended visible light absorption, additional Raman modes and an increase in Ti-OH groups, while Ti³⁺ is not observed.

Here, high H₂ pressure treatment of P25, commercial rutile and anatase nanopowders as well as self-made anatase nanocrystals results in beige to dark brown materials. DRS shows the expected extended visible light absorption and a decrease in the optical band gap as well as the loss of a diffuse absorption edge in some cases. The darkening of the brown tones with decreasing TiO₂ crystal size is attributed to a higher surface-to-bulk ratio and thus higher relative degree of the altered surface layer. However, I do not observe an amorphous outer shell in TEM or VB modification using XPS, which poses the question about the origin of the dark coloration of the material. XPS shows an additional peak for the H₂-treated aNC that cannot be assigned so far but might be due to incorporation of

hydrogen into the crystal lattice. Thus, the incorporation of hydrogen atoms might be the cause for the brown appearance of TiO₂.

Furthermore, DRS does not show a red-shift as expected if Ti³⁺ color centers would be introduced into the material. The absence of Ti³⁺ is confirmed by XPS, while Raman spectroscopy suggests the presence of oxygen vacancies in the form of peak broadening and shifts accompanied by a fluorescence background in the H₂-treated TiO₂. As the penetration depth of the Raman measurements using a 532 nm laser is several hundred nanometer, Raman can be considered a bulk technique for my applications.²⁹⁵ I therefore attribute the observed fluorescence to bulk oxygen vacancies that are not observable by XPS. I do not observe additional Raman modes, or the formation of suboxide species using XRD as for other techniques or previous literature reports.

In contrast to literature, my materials show a greatly decreased photocatalytic performance for HER under both UV and visible light irradiation.

For now, I can only assume that I created defects, maybe in form of incorporated hydride species or oxygen vacancies, during high pressure H₂ treatment that quench the photocatalytic activity by providing recombination centers for electron-hole pairs. The similar H₂ evolution rates after H₂ treatment indicate that the rate-limiting step for hydrogen evolution is governed by the defect states and not as much by the phase composition in these reduced samples anymore.

A comparison between my results and the literature reference can be found in Table 6-9 at the end of this chapter together with the following three synthesis routes.

6.2. Aluminum-reduced TiO₂

Aluminum reduction of TiO₂ has been reported by Wang et al. as an easy, large scale approach to create black TiO₂ and falls into the category of chemical reductions as listed in Chen et al.'s review on black nanomaterials.^{182, 186} The reduction is performed in an evacuated two-zone furnace at elevated temperatures with aluminum as reducing agent. The working principle is that aluminum takes up oxygen that is released by TiO₂, thereby forming aluminum oxide and reducing the outer shell of TiO₂. In the following sections, I will first discuss and critically assess the physical background of aluminum reduction in more detail. This is followed by the comprehensive characterization and photocatalytic evaluation of the synthesized materials analogous to the previous section.

TEM measurements were conducted in order to investigate if an amorphous outer layer has been formed upon reduction as reported by Wang et al. They observed a disordered outer layer of aluminum-reduced P25 that was increasing in thickness with an increasing reduction temperature of the TiO₂ compartment.

6.2.1. Theoretical background

In the original paper on aluminum reduction of P25, the authors base their process on the principle that the ease of reduction for different metals and their oxides depends on the surrounding partial oxygen pressure as well the temperature and Gibb's free energy of formation.

Ellingham diagrams are the graphical depiction of the change in Gibb's free energy, ΔG , for an oxidation reaction of a metal in dependence of temperature:

$$(6.1) \quad \Delta G = \Delta H - T\Delta S$$

They can easily be used to deduct whether a metal or its oxide will be reduced or oxidized in a reaction. The amount of oxygen used for the oxidation reaction has to be the same for all reactions in one Ellingham diagram (generally used 1 or ½ mole of O₂). This renders the change in entropy, ΔS , basically constant across all oxidation reactions, as it is governed by the amount of consumed gas. The change in enthalpy, ΔH , is the y-intercept and – as expected – a fixed value for a specific reaction (unless a phase change of the metal/oxide occurs with a change in T). Thus, the plot can be considered to be dependent on ΔG and T only, with the slope being equal to the negative change in entropy (equation (6.2)).²⁹⁶

$$(6.2) \quad \frac{d\Delta G}{dT} = -\Delta S$$

From the Ellingham diagrams, it can be seen that aluminum and its oxide have ΔG values below those of titanium and its (sub-)oxides (Figure 6-13). This means that in a reaction system with Al/Al₂O₃ and Ti/TiO_{2-x} at a certain T, the titania is more easily reduced, while the aluminum gets oxidized.^{186, 297}

Additionally, the authors elaborate on the oxygen partial pressure during the reaction. The equilibrium oxygen partial pressure can be calculated from:

$$(6.3) \quad \Delta G^0 = -RT \ln p_{O_2}$$

If the oxygen partial pressure of the surrounding system, $p_{O_2,sys}$, is larger than the equilibrium oxygen partial pressure, p_{O_2} , the metal will be oxidized. Vice versa, when the oxygen partial pressure of the surrounding system, $p_{O_2,sys}$, is smaller than the equilibrium oxygen partial pressure, p_{O_2} , the metal will be reduced. So:

$$(6.4) \text{ Oxidation: } p_{O_2,sys} > p_{O_2}$$

$$(6.5) \text{ Reduction: } p_{O_2,sys} < p_{O_2}$$

The authors state that due to the fact, that aluminum is molten at 800 °C it can effectively decrease the oxygen partial pressure much below the equilibrium partial pressure for TiO₂, so that a reduction of TiO₂ can occur easily.

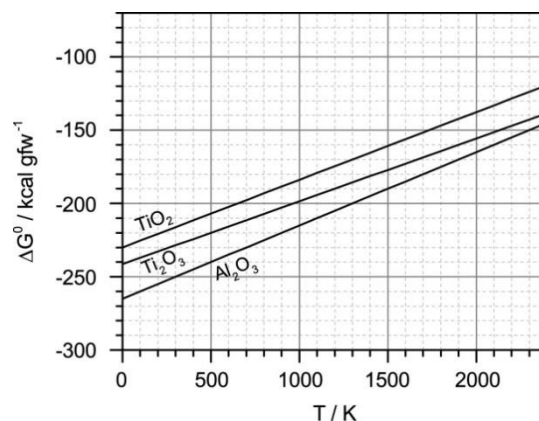
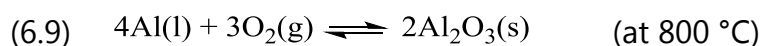
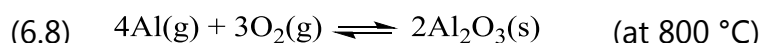
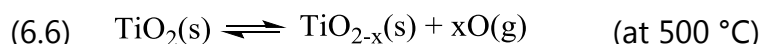


Figure 6-13. Ellingham diagram for TiO₂, Ti₂O₃ and Al₂O₃ based on data shown in ref. 297.

6.2.1.1. Discussion of applicability of Ellingham diagrams

In the Ellingham diagram, we consider ΔS to be basically constant, because a fixed amount of oxygen reacts with a metal to a metal oxide ($M(s) + O_2(g) \rightarrow MO_2(s)$). The fact, that aluminum is present in a different aggregate state adds another level of complexity to the reaction system as we have to consider the vapor pressure of liquid aluminum as well. Since we work in vacuum, gas-phase aluminum would now be a significant factor for considering changes in entropy and, thus, the eligibility of Ellingham diagrams is questionable.

For the aluminum reduction, the following equilibria should therefore be considered: 1) the equilibrium of gas phase oxygen and lattice oxygen of TiO₂ at (here) 500 °C; 2) the equilibrium between liquid and gaseous aluminum at 800 °C; 3) the reaction between gas-phase aluminum and oxygen to aluminum oxide at 800 °C; 4) the reaction between liquid-phase aluminum and oxygen to aluminum oxide at 800 °C.



This means that in vacuum at 500 °C, small amounts of lattice oxygen of TiO₂ are set free and react with Al in its liquid state but also its gas phase.

Looking at the glass tube after synthesis confirms that the presence of gas-phase Al in the system (Figure 6-14): At the outlet of the oven, where the glass tubes cools down again, I clearly see deposition of a thin, dark, metallic film, presumably Al. At the position where the aluminum powder is placed during reduction, a white film is covering the glass walls. In the middle of the tube – between the two temperature zones – a brownish/oscillating thing film deposits, mixed with some very thin white film.

From the involved chemicals, I can deduct, that the white deposit is very likely an aluminum oxide that forms from the reaction of gas phase aluminum and oxygen (equation (6.8)). The darker areas are likely either pure aluminum (in particular, at the tube outlet), or a mixture of aluminum and its oxide. After the reduction process, the aluminum powder has merged to larger silver-metallic "drops" (likely Al maybe mixed with alumina) covered by a darker layer.

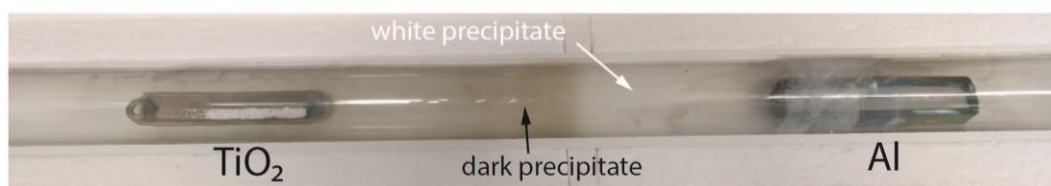


Figure 6-14. Quartz glass reaction tube with TiO₂ and aluminum powder after aluminum reduction process.

The fact, that elemental aluminum also seems to deposit suggests, that aluminum is present in excess and formation of white (presumably) aluminum oxide occurs in the gas phase. Assuming that oxygen stems from TiO₂ – which is supported by the various characterization methods that show the formation of sub-oxide phases and defects (e.g. sections 6.2.4, 6.2.5, 6.2.6) – the amount of oxygen present in the reaction could be increased by either raising the temperature of the TiO₂ compartment or by providing a better vacuum. However, I already see a strong reduction at some of the parameters I used (e.g. 24 h reduction, high Al:P25 ratio) and a corresponding decreasing photocatalytic activity. This renders experiments that would result in even more oxygen vacancies and disorder undesirable. The reported amorphous outer shell and black coloration could not be observed at my parameters. This could be due to a highly sensitive system that needs a lot of fine tuning.

In the following sections, I will present the results from characterization and photocatalytic experiments for my materials.

6.2.2. Color & DRS

Figure 6-15 shows the Tauc plots of P25 and Al-reduced P25. The band gap of 3.16 eV for P25 agrees with literature.^{38, 242-243} The reduced P25 shows only a slight reduction of the band gap that is more pronounced in the darker materials (Table 6-3). The band gap of the light blue P25 remains basically unchanged, while blue P25 shows a distinct red-shift of the absorption edge similar to those discussed previously (section 5.2.2.3). This red-shift is associated with the formation of oxygen vacancies and Ti³⁺ color centers, which have previously reported to result in the classical blue coloration of reduced TiO₂.¹²⁶ Grey P25 shows a similar band gap value as blue P25. Here, the red-shift of the absorption edge is not parallel to the pristine P25 but the reduced band gap seems to result more from a “flattened” slope of the absorption edge. Dark blue P25 shows a distinctly different behavior from the other reduced P25. The onset of the absorption edge is less distinctive and significantly blue-shifted. All reduced samples show a higher

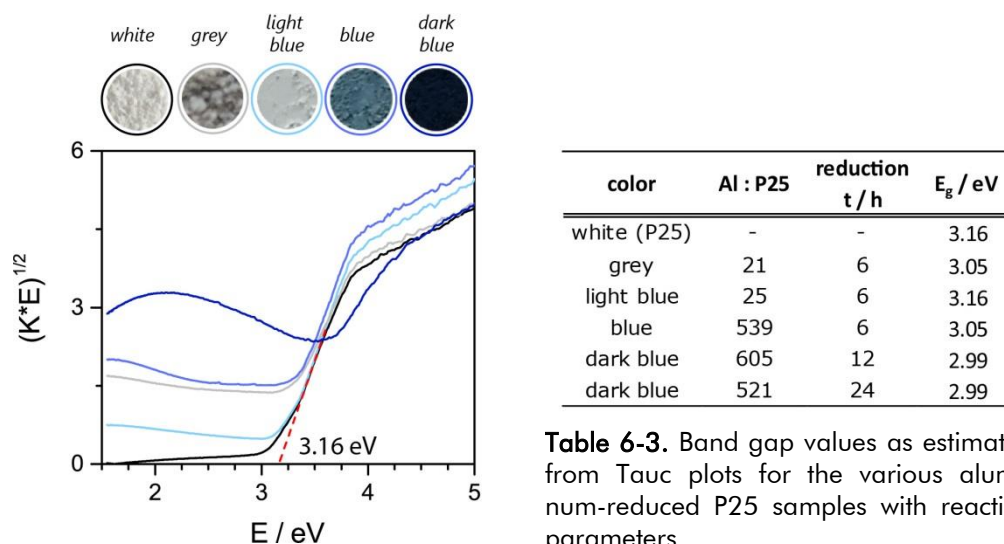


Figure 6-15. Tauc plots and images of P25 and Al-reduced P25.

Table 6-3. Band gap values as estimated from Tauc plots for the various aluminum-reduced P25 samples with reaction parameters.

visible light absorption than P25, increasing in the following order: light blue < blue ≈ grey < dark blue.

Interestingly, some samples – especially the dark blue P25 – appeared black before air exposure. Upon air contact, an immediate lightening of the material can be observed. Attempts to slowly air the evacuated synthesis tube or restore atmospheric pressure under inert gas have not proven beneficial for retaining the black color so far. Overall, Al-reduction of P25 led to a range of different blue tones as well as to a grey coloration in some cases. The darkness of the blue color increased with a) an increasing ratio of the aluminum to P25 and b) with an increased time of reduction (e.g. 12, 24 h).

6.2.3. BET

BET measurements have not been conducted yet due to the low sample amounts.

6.2.4. TEM

Figure 6-16 shows TEM images of pristine P25 (a), grey (b), light blue (c), blue (d) and dark blue P25 (e-f). Interestingly, grey P25 shows a partially very thick layer of an amorphous material (up to 10 nm). However, this is likely not amorphous TiO₂ because: 1) the contrast of this layer is much lighter compared to TiO₂, which hints towards an overall lighter material (section 3.3.1.1) 2) there is a very sharp, and distinct edge between the TiO₂ crystal and the amorphous shell, which disagrees with a diffuse amorphization of the outer TiO₂ layers but rather indicates that a different material deposited on top of the TiO₂. Raman shows the presence

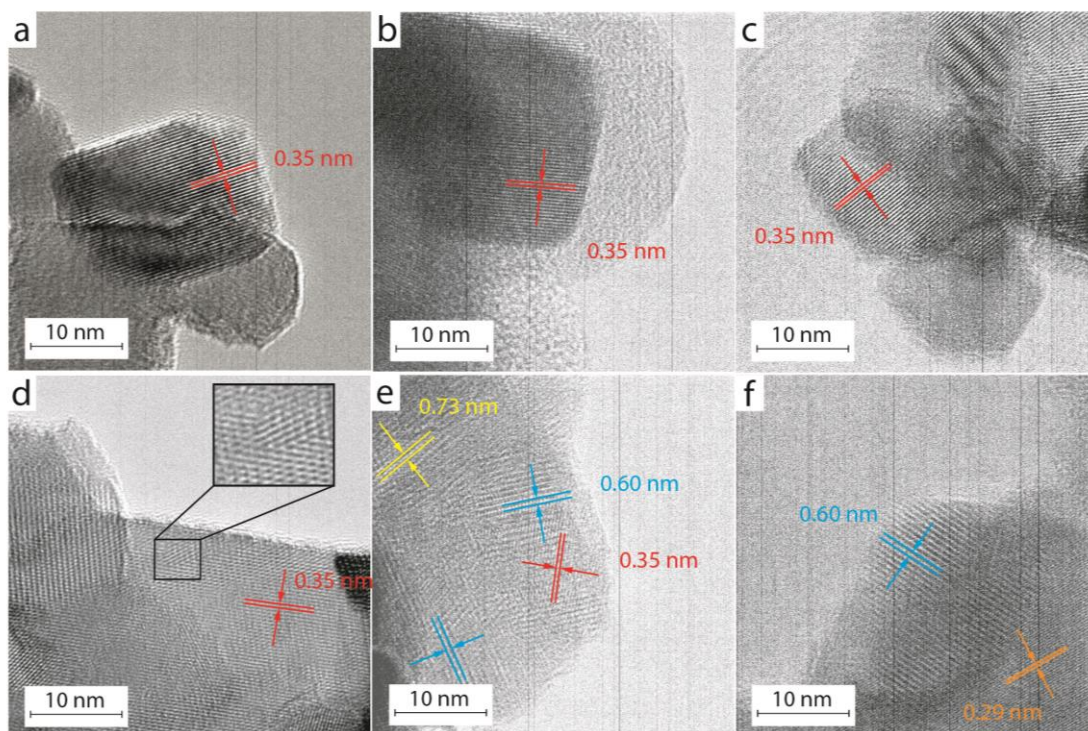


Figure 6-16. TEM images of pristine P25 (a), grey (b), light blue (c), blue (d) and dark blue P25 reduced for 12 h (e) and 24 h (f).

of carbon in this sample (section 6.2.5). Therefore, the observed layer is very likely a carbon film on top of TiO₂.

While there is no amorphous outer layer for any of the other samples, I observe an increasing degree of disorder within the TiO₂ crystals with an increasing Al:P25 ratio and/or reduction time. Lattice spacings of 0.35 nm are predominantly observed in P25, corresponding to the (101) facet of anatase.²⁹⁰⁻²⁹¹ Light blue P25 shows no significant changes compared to pristine P25. Blue P25 shows very small irregular regimes within the TiO₂ crystals (insert, Figure 6-16d). This disorder is very pronounced in the dark blue P25 with lattice spacings that do not conform with rutile or anatase facets but result in diffraction reflexes at 2θ values of about 12°, 14° and 30° (section 6.2.6).

6.2.5. Raman

Figure 6-17 shows the Raman spectra of pristine P25 and aluminum- reduced samples for a) the typical spectral range from 110 cm⁻¹ to 1000 cm⁻¹ with close-up of the E_g mode and b) between 1000 cm⁻¹ and 3000 cm⁻¹. Peaks are increasingly broadened and an increasing peak shift of the E_g mode is observed with an increasing Al:P25 ratio and/or longer reduction times during synthesis. Light blue P25 shows almost no change to pristine P25. As for DRS, the blue and grey sam-

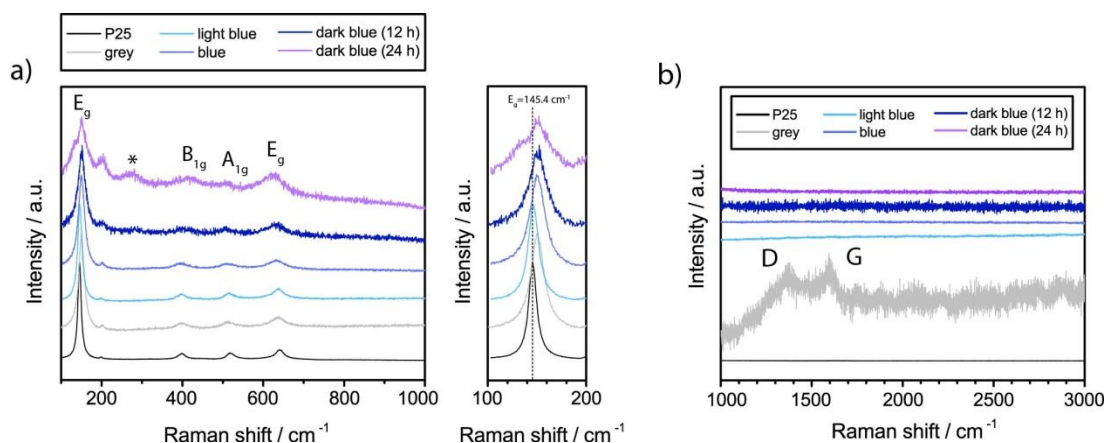


Figure 6-17. Raman spectra of pristine P25 and aluminum-reduced samples. a) typical spectral range from 110 cm⁻¹ to 1000 cm⁻¹ with close-up of the E_g mode. b) spectra between 1000 cm⁻¹ and 3000 cm⁻¹.

ples are also quite similar in their Raman spectra. The dark blue samples show the strongest peak broadening. Signal intensities are significantly lower for blue and dark blue P25 compared to P25, which points towards a loss of order in these samples (see also 6.2.6). The dark blue P25, reduced for 24 h, shows a shoulder to lower wavenumbers for the E_g mode and a yet unassigned band at 274.3 cm⁻¹ (labeled with an asterisk) that indicates the formation of an additional phase, as also observed in TEM.

Usually, for TiO₂ it suffices to look at the vibrational modes up to 1000 cm⁻¹. I decided to look at higher wavenumbers to confirm the absence of additional modes due to, for example, carbon impurities, in particular in the context of high pressure-reduced TiO₂ in which an organic template was used for TiO₂ synthesis. None of the blue Al-reduced samples have a signal in the range between 1000 and 3000 cm⁻¹. However, the grey P25 shows very faint but distinctive bands at 1360 and 1605 cm⁻¹, which corresponds to the D and G bands of carbonaceous species and explains the grey color of the sample and the apparent “shell” around the crystals that is observed in TEM images (section 6.2.4).²⁹⁸

6.2.6. XRD

Figure 6-18 shows the XRD patterns of Al-reduced P25. The pattern of light blue P25 is nearly identical to the untreated P25, which agrees with DRS, TEM and Raman results that showed little to no changes between these samples and P25. Unlike for Raman and DRS, the grey and blue P25 now clearly show different characteristics: While the grey P25 only shows a decrease in the rutile fraction within the sample, blue and dark blue P25 show additional reflexes that grow in intensity and resolution with increasing Al:P25 ratio and reduction time. For blue

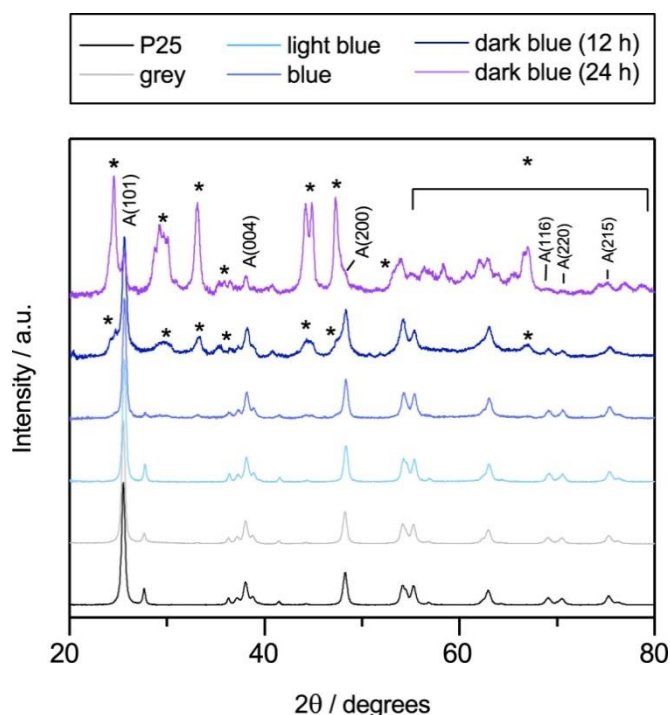


Figure 6-18. XRD patterns of pristine P25 and aluminum-reduced samples.

P25, shoulders appear at 24.7° and 47.5° right next to the reflexes from the anatase (101) and (200) facets at 25.7° and 48.3° , respectively. Also a broad signal in the range of $29.3\text{--}30^\circ$ and more distinct reflexes at 33.1° , 44.8° are observed. These new phases are even more pronounced and many more additional reflexes are emerging in dark blue P25 reduced for 12 h. Furthermore, rutile reflexes completely vanish (e.g. (110) at 27.8°). After 24 h reduction, the new phase dominates the diffraction pattern being even more intense than anatase reflexes and more resolved than for the 12 h sample. These new reflexes are in line with the disorder and corresponding lattice spacings in the blue and dark blue samples observed in TEM measurements (section 6.2.4).

Looking at the phase changes as progressing from light blue over blue to dark blue P25, it is noticeable that, first, the intensity of rutile reflexes decreases while the new phase is forming, followed by a decrease in the anatase phase and a continuing emergence of the new phase. Grey P25 did not show growth of any new reflexes, but a decrease of the rutile phase similar to blue P25. Table 6-4 lists the calculated fractions of anatase and rutile for pristine, light blue, grey and blue P25. For the dark blue P25, there was no clear rutile peak identifiable anymore to calculate any ratios. Calculations are based on the empirical formula by Spurr and Myers and do not account for the inherent amorphous fraction present in P25 as described by Ohtani et al. (equation (5.1), section 5.2.2.2).^{94, 241} Therefore, they do

Sample	x_A	x_R
P25	0.85	0.15
light blue	0.84	0.16
grey	0.90	0.10
blue	0.94	0.06
dark blue	n/a	n/a

Table 6-4. Calculated fractions of anatase and rutile for pristine and aluminum-reduced P25. Based on ref. 241.

not represent the accurate percentages of rutile and anatase phase but can still be used as an indication for whether the relative ratios of rutile and anatase change.

Identification of the new reflexes was not straight-forward. I expected a possible growth of suboxide phases due to reduction and considered possible contamination by aluminum and the formation of Al₂O₃ phases. However, none of these structures match the observed reflexes. I used XPS and SEM-EDX to confirm the absence of aluminum in my sample. Indeed, no aluminum was found, but – surprisingly – I found a strong sodium signal using both techniques. Sodium titanate (e.g. Na_{0.23}TiO₂ or NaTi₄O₈) provides a very good match with the newly grown phase. These titanates are also known to be blue-black in color. Thus, I conclude that during the aluminum reduction process, sodium was incorporated into the crystal lattice of TiO₂ leading to the formation of titanate phases that cause the dark coloration of the material. XRD of photocatalysts recovered before and after HER experiments were identical. This shows, that the sodium titanate phase are stable under photocatalytic conditions.

6.2.7. XPS

6.2.7.1. Surveys

Figure 6-19 shows the XPS surveys of P25 and aluminum-reduced samples, while absolute values for the elemental composition are listed in Table 6-5.

No aluminum is found in any of the samples. However, very surprisingly, sodium is present in the blue and dark blue samples. The Na 1s signal coincides with the Ti LMM edge (both at ca. 1071 eV) making an exact quantification difficult: about 2 at.% can be subtracted from the Na 1s signal to account for the Ti LMM edge signal, which gives a rough estimate of the actual sodium content. Because of the ambiguity due to the signal overlay and the apparent absence of Na in my synthesis route, SEM-EDX were conducted measurements to confirm whether, in-

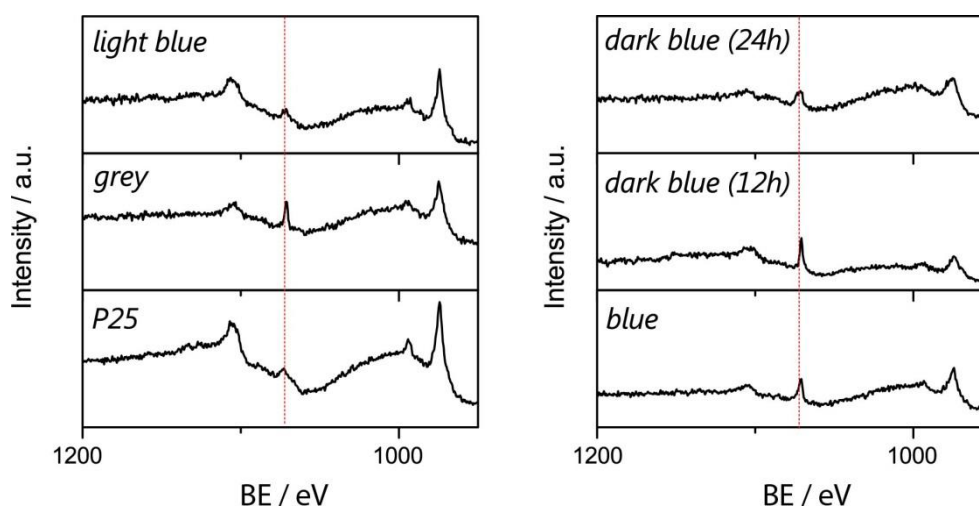


Figure 6-19. XPS survey spectra of P25 and aluminum-reduced P25. The red line marks Ti LMM edge and Na 1s signal.

deed, sodium is present in the reduced samples. EDX confirmed the absence of aluminum and the presence of sodium in the reduced samples. Sodium was also found in dark blue P25 (24 h), whereas in the XPS survey the signal would have still been in an acceptable range for the Ti LMM edge signal. No sodium was found in pristine P25, confirming that it is incorporated only during the aluminum reduction process.

The Ti:O ratios were constant 0.6 for almost all samples, including the P25 reference. This suggests an oxygen deficiency in all samples. However, since the pristine P25 reference exhibits the same calculated ratio, I attribute this deviation from the stoichiometric ratio of 1:2 to inherent errors during fitting and calculating. Dark blue (12h) P25 was an exception with a significantly lower ratio of 0.4. This sample, i.e. the spot measured, also shows the highest content of Na. While XRD and TEM confirmed the presence of sodium titanate, patterns of NaTiO₃ and other titanates with a higher Ti:O ratio than TiO₂ did not match well with the observed diffractograms of the aluminum-reduced P25 (sections 6.2.4, 6.2.6) The detail spectra also do not give further information about the origin of this deviating Ti:O ratio. It might be within the inherent variance of the estimation method.

Sample	at. % from survey					metal oxide
	C	O _{total}	O _{metal oxide}	Ti	Na/Ti LMM	Ti:O
P25	28.2	47.2	41.0	23.0	1.6	0.6
grey	50.3	34.5	22.9	12.9	2.4	0.6
light blue	38.5	41.5	32.6	18.6	1.4	0.6
blue	32.3	43.1	35.8	19.7	4.9	0.5
dark blue (12h)	38.1	40.1	33.1	14.5	7.3	0.4
dark blue (24h)	61.4	29.5	12.3	6.8	2.4	0.5

Table 6-5. Quantifications from survey spectra for P25 and aluminum-reduced P25.

6.2.7.2. Detail spectra

C 1s detail spectra of the aluminum-reduced samples exhibit the expected general shape for adventitious carbon: the typical major peak for C-C/C-H bonds set to 284.8 eV and various organic species adsorbed at higher binding energies (Figure 6-20) (section 4.4.1). Interestingly, some of the reduced samples show additional signals at ~293 eV and ~296 eV. These BEs are too high for adsorbed organic species and most other carbon compounds. Only a few possibilities for these chemical shifts can be found in literature: 1) the 2p_{2/3} of KCl with a BE of 292.9 eV and a spin-orbit splitting of $\Delta_{\text{chloride}} = 2.8$ eV,^{213, 299-300} 2) CF₂ and CF₃ with BE of ~292 eV and ~294 eV, respectively,³⁰⁰⁻³⁰² 3) π - π^* and σ - σ^* shake-ups in compounds with extended delocalized electrons from, for example aromatic rings, result in signals at ~291 eV and ~294 eV.³⁰²⁻³⁰³ Since I do not have any aromatic compounds or graphitic carbon in my samples, I exclude the last point. The first two would be equally surprising, because neither potassium nor fluorine are found in the samples including the P25 reference or are used during synthesis. Also, SEM-EDX did not show the presence of potassium or fluorine. Thus, the origin of these signals remains unclear.

O 1s spectra of P25, grey, light blue and blue P25 were very similar and in accordance with the expected shape for TiO₂ with a dominant signal at around 530 eV stemming from the lattice oxygen of the metal oxide and a shoulder that could be deconvoluted into signals of hydroxyl groups and adsorbed organic species (Figure 6-21) (for more detailed discussion of XPS interpretation see section 4.4.2). The O 1s spectra of the dark blue P25 show a much decreased signal intensity compared to all other samples and pristine P25, while the general shape of the spectrum for the 12h-reduced P25 was still analogue to that of the P25 refer-

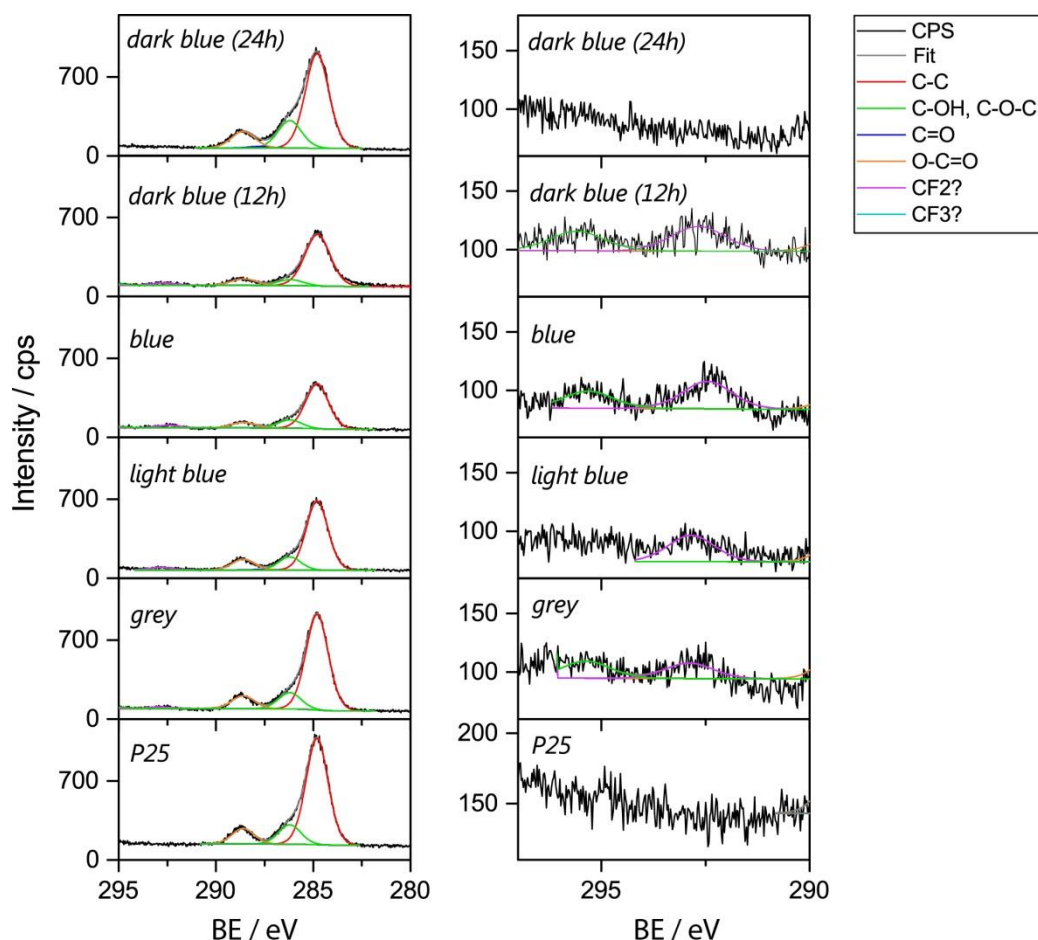


Figure 6-20. C 1s detail spectra of P25 and aluminum-reduced P25. Right: close-up of BE region between 290 and 296 eV.

ence. The lower signal intensity can have several causes, i.e. a lower conductivity of the samples, or an increased amount of defects that trap electrons.²¹³ The 24h-reduced P25 showed a significantly higher percentage of adsorbed organic species and hydroxyls or defects. From previous characterization, I know that the dark blue P25 – and in particular the 24 h long reduced sample – show a high degree of disorder and the emergence of new sodium titanate phases. A highly defective surface can allow for a larger number of adsorbents at defect sites and thus explain the higher percentage of these species in the dark blue P25 (24 h).

Figure 6-22 shows the Ti 2p detail spectra of P25 and Al-reduced P25. The Ti 2p spectra of all samples show the typical peaks of the Ti 2p_{3/2} and Ti 2p_{1/2} at 458.1-458.4 eV and 463.8-464.1 eV, respectively (section 4.4.3). Signals from Ti³⁺ centers were not observed in any of the samples. Dark blue P25 had to be charge compensated during measurement, which results in a slight tail on the lower BE side, possibly overlaying a Ti³⁺ signal. However, since none of the other samples (e.g. the 24 h-reduced sample) showed a lower oxidation state of Ti⁴⁺, it could be ex-

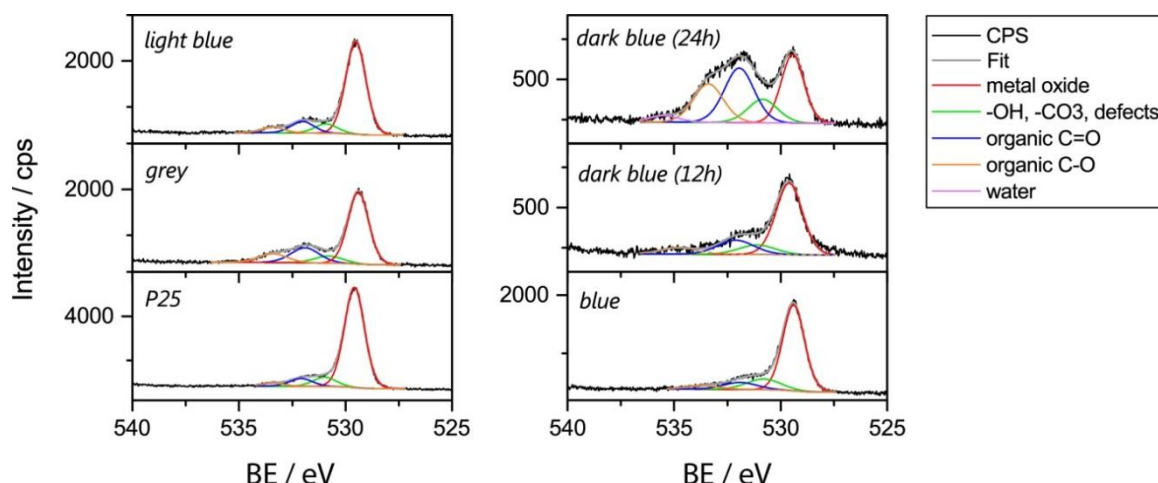


Figure 6-21. O 1s detail spectra of P25 and aluminum-reduced P25.

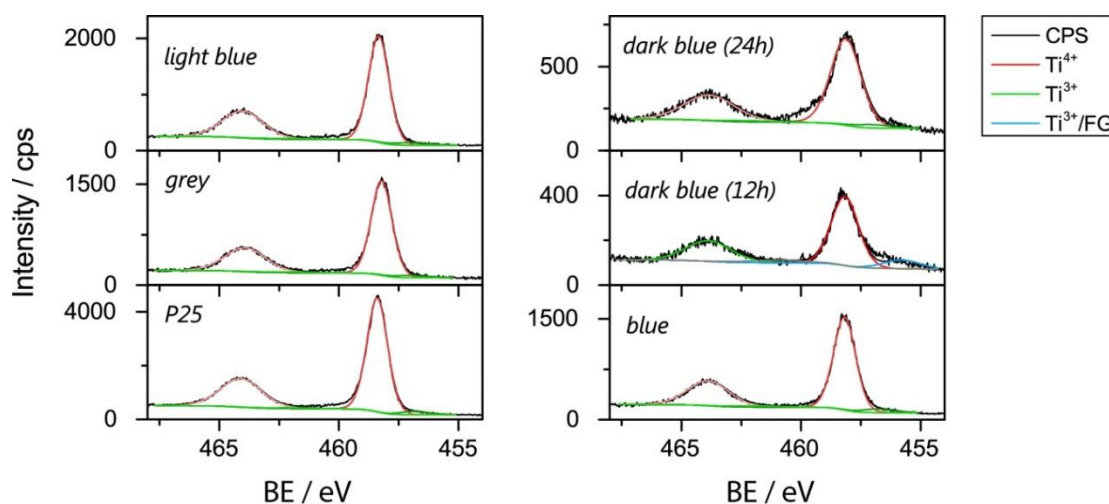


Figure 6-22. Ti 2p detail spectra of P25 and aluminum-reduced P25.

trapolated that also in this sample there is likely no Ti³⁺. Thus, the Ti 2p spectra did not give any evidence on major structural changes in the reduced samples.

6.2.7.3. VB

Figure 6-23 shows the VB spectra of P25 and Al-reduced samples. There is a slight decrease in the VBM values from 2.47 eV for pristine P25 to 2.25-2.41 eV for the reduced samples with exception of the light blue one. Fitting the VB according to reference, I see a splitting of the σ state-component into two peaks. This has been observed previously and was attributed to either distortion of the TiO₆ octahedron or due to interactions of Ti with the second neighbor shell.³⁰⁴ Also, as the main contributor to the σ state is the O 2p orbital a decrease of this component might stem from a decrease in electron density coming from oxygen, i.e. by the creation of oxygen vacancies. However, I do not observe a signal at ~2 eV associ-

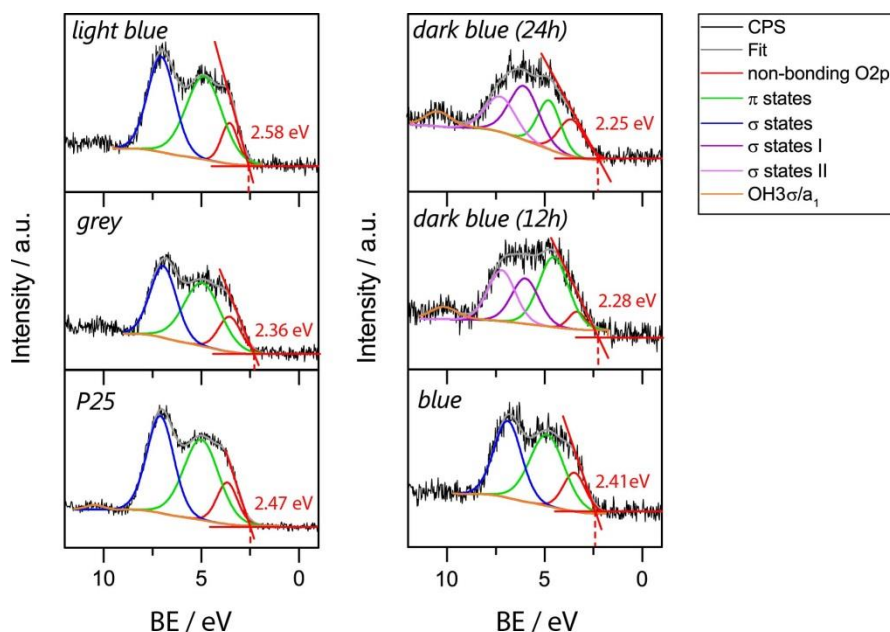


Figure 6-23. VB spectra of P25 and aluminum-reduced P25.

ated with Ti³⁺ centers that would usually be created with oxygen vacancies. The signal at 10.5 eV stemming from hydroxyl groups or molecular water is increased in relation to the other signals for the dark blue P25. This could be due to the higher degree of disorder in these samples resulting in a higher number of adsorption sites.

Wang et al. also investigated their aluminum-reduced P25 with (VB-)XPS. They did not observe any signals stemming from Ti³⁺ centers or changes in the VB for their sample and attributed this to an easy re-oxidation of the disordered layer upon air exposure. Their VBM was at 2.05 eV, which differs from my value. However, as discussed previously, there is a wide range in reported literature values for the VBM of TiO₂ (section 4.4.4). Furthermore, it is not clearly discussed which spectra are shown in the paper. However, I assume that the authors did not find any differences and chose representative spectra. Overall, my VB-XPS measurements are in line with the strong increase in disorder in the TiO₂ as observed by TEM, Raman, and XRD. Possible signals from Ti³⁺ centers are not observed, while a very slight decrease in the VBM value is observed.

6.2.8. HER

Photocatalytic experiments under UV and visible light exposure at 1.0 wt.% Pt with methanol as sacrificial agent were conducted (Figure 6-24). The aluminum-reduced P25 performs increasingly worse with an increasing Al:P25 ratio and/or reduction time. P25 remains the best photocatalyst. Previous characterization

confirmed the incorporation of sodium into the crystal lattice of TiO₂ under formation of sodium titanate phases for the reduced samples. The incorporated Na⁺ very clearly has a detrimental effect on the H₂ evolution capability of these photocatalysts, which has also been reported before in literature.³⁰⁵ The same trend is observed for visible light activity. Although, clearly, higher visible light absorption is possible in the reduced samples, the disorder and defect states are likely to impede H₂ evolution by serving as recombination centers and are outweighing possible benefits from increased absorption.

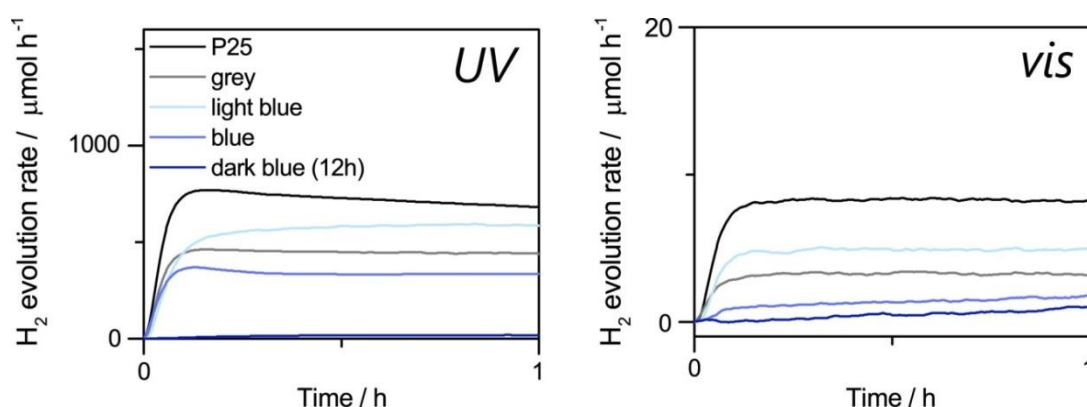


Figure 6-24. HER experiments for P25 and aluminum-reduced P25 under UV (left) and visible light irradiation (right).

6.2.9. Discussion & Conclusions

Wang et al. were able to synthesize black TiO₂ with a shell that is tunable through the applied reduction temperature. While the authors did not observe changes in the VB, Ti³⁺ creation is suggested by XRD line broadening (although this was not very clearly depicted in the given supporting information) and Raman peak broadening and shifts (Table 6-9).

I, on the other side, am not able to create core-shell TiO₂ with my setup, although TiO₂ is clearly altered and changes color to grey, blue, and dark blue. The darkness of the blue color increased with a) an increasing ratio of the aluminum to P25 and b) with an increased time of reduction (e.g. 12, 24 h). TEM, Raman and XRD show that this is due to the incorporation of impurities like C (grey P25) and Na (blue P25). The presence of defects is further confirmed by peak broadening in both XPS and Raman. No VB modifications have been observed.

While Wang et al. show strongly enhanced photocatalytic dye degradation and HER activities of their Al-reduced P25, I only observed detrimental effects of my

treatment on the photocatalytic performance which is not surprising in the presence of a lot of impurities that may serve as recombination centers.

The source of the impurities is not clear yet. In particular, accidental contamination with sodium during sample handling is unlikely as the results are very reproducible. Thus, the sodium source must come from the actual procedure and/or setup. SEM-EDX analysis of the aluminum powder does not show any sodium impurities. However, what is clear is that there are several key parameters (e.g. type of aluminum, Al:TiO₂ ratio, surface areas, heating/cooling rates, influence of vacuum level) that are not mentioned in the reference paper, which makes reproduction of the original work tedious. Attempts to contact the authors remain without reply up to now.

6.3. NaBH₄-reduced P25

Tan et al. synthesized blue to black P25 with a tunable core-shell morphology and improved photocatalytic performance by a simple dry mixing of NaBH₄ and TiO₂.¹⁹¹ The idea is that due to the loose mixing with NaBH₄ only the outer TiO₂ surface is reduced upon thermal treatment (300-400 °C) of the mixture in inert gas. The authors suggested that the disordered outer layer was accompanied by a VB tail and observed peak broadening in both Raman and XPS that indicates defect formation.

6.3.1. Color & DRS

In situ reduction of P25 with NaBH₄ leads to blue, dark blue or blue-black samples. The color distribution in a sample after the treatment is generally not as homogeneous as for other methods due to the mechanical grinding procedure. The darkness of the material – an indicator for the state of reduction – increases with increasing reduction temperature from 300 °C to 400 °C.

Figure 6-25 shows the Tauc plots for P25 and P25 treated at the three different reduction temperatures. Samples reduced at 300 °C show a consistent and highly reproducible red-shift of the band gap from 3.15 eV for pristine P25 to 2.78 eV for the 300 °C samples. As previously discussed, this shift is generally attributed to the formation of oxygen vacancies and Ti³⁺ centers (sections 5.2.2.3, 6.2.2). The band gaps for samples reduced at 350 °C and, in particular, at 400 °C are more difficult to determine exactly as these samples do not show a well-defined absorption edge anymore which is needed for extrapolation of the slope. Neverthe-

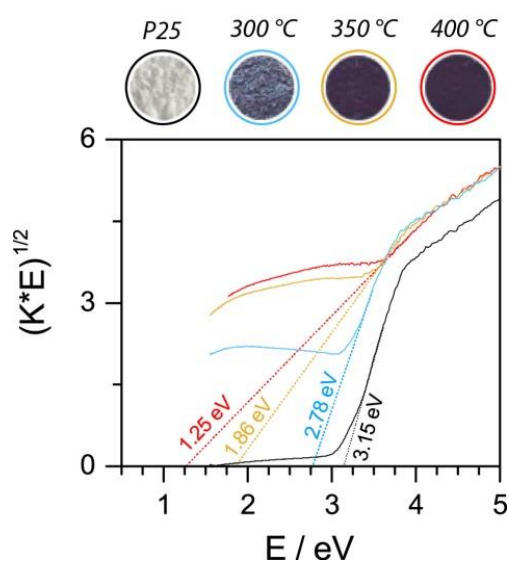


Figure 6-25. Tauc plots and images of P25 and NaBH₄-reduced P25.

less, in line with the observed color, I observe a trend towards lower band gap energies for higher reduction temperatures. Generally, the absorption across the visible light range increases with increasing reduction temperature as well, making these materials interesting candidates for visible light photocatalysis. The color and absorption of my materials agree well with the literature reference.¹⁹¹

6.3.2. BET

BET surface areas for samples reduced at 300 °C and 350 °C are 69 ± 11 and 81 ± 14 m² g⁻¹, respectively, which is higher than for pristine P25 (55 m² g⁻¹). This could be induced by surface roughening. Samples reduced at 400 °C show a similar surface area to P25 (48 ± 11 m² g⁻¹), suggesting that either the surface might be less rough or that already some sintering effects counteract the effects of the NaBH₄ treatment.

6.3.3. TEM

Figure 6-26, Figure 6-27, and Figure 6-28 show TEM images of P25 reduced at 300 °C, 350 °C and 400 °C, respectively. I did not observe an amorphous outer layer for any of the NaBH₄-reduced P25 samples as reported by Tan et al.¹⁹¹ According to literature, the disordered shell should have been especially pronounced in the dark blue samples. Instead of a uniform layer, a clear surface roughening is observed that increased in intensity with increasing reduction temperature. While the 300 °C and 350 °C samples only show this roughening in some cases (e.g. Figure 6-27), the 400 °C samples look all clearly deformed.

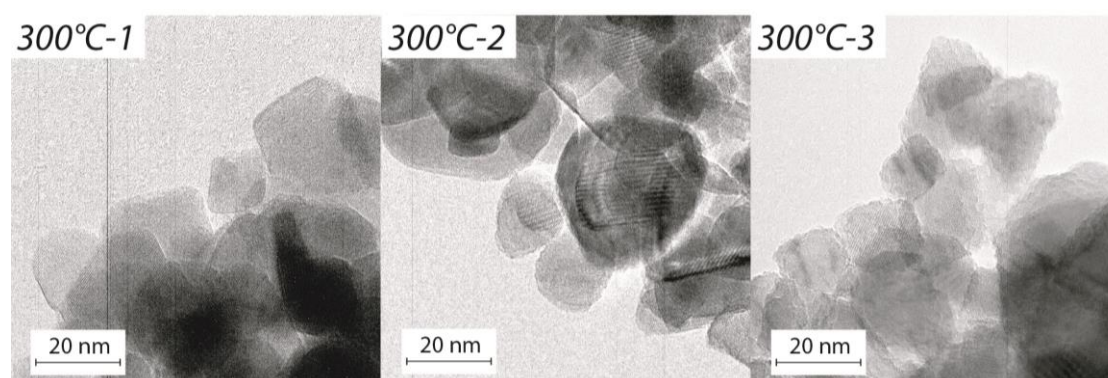


Figure 6-26. TEM images of P25 reduced with NaBH₄ at 300 °C.

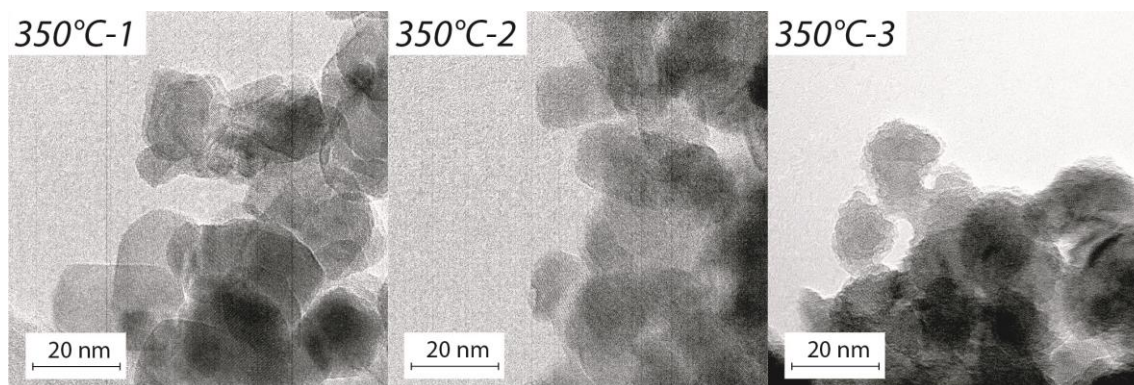


Figure 6-27. TEM images of P25 reduced with NaBH₄ at 350 °C.

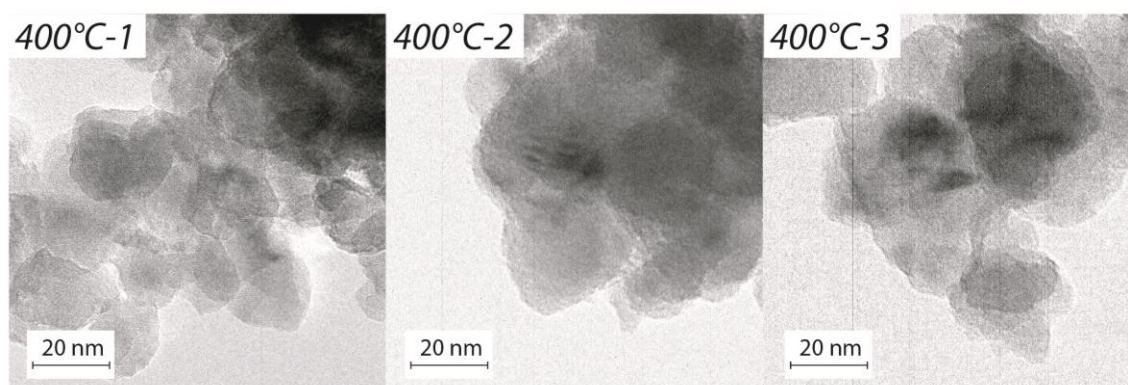


Figure 6-28. TEM images of P25 reduced with NaBH₄ at 400 °C.

6.3.4. Raman

Figure 6-29 shows the Raman spectra of all NaBH₄-reduced P25 samples as well as a reference spectrum for pristine P25 with its typical modes (e.g. section 5.2.2.6).^{170, 179} Samples treated at 300 °C shift by 5-6 cm⁻¹, samples treated at 350 °C by 7-8 cm⁻¹, while samples treated at 400 °C show the largest shift with

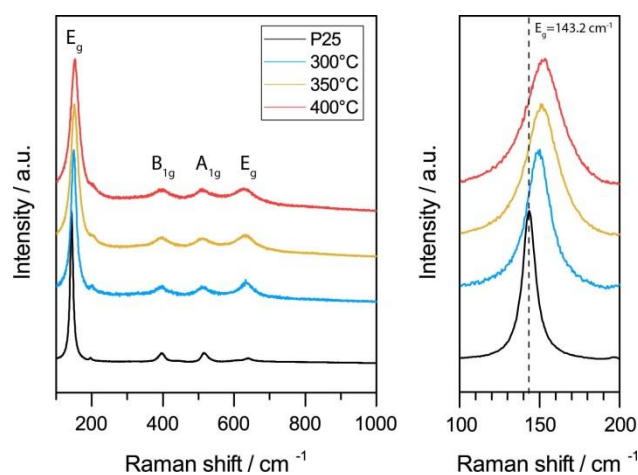


Figure 6-29. Raman spectra of P25 and NaBH₄-reduced P25. Right: close-up of E_g mode.

8-9 cm⁻¹. Peak broadening increases significantly with the reduction temperature as well with a change in the full width-half maximum of the E_g mode of 19.6 cm⁻¹ for 300 °C, 23.7 cm⁻¹ for 350 °C and 27.5 cm⁻¹ for 400 °C compared to only 10.1 cm⁻¹ for pristine P25. The broadening of all modes and the blue-shift of the E_g mode at 144 cm⁻¹ indicates the introduction of strain in form of either crystal size changes or defects in the treated samples. Thus, Raman results are in line with the increased surface roughening that is observed in TEM.

6.3.5. XRD

Figure 6-30 shows the XRD patterns of the NaBH₄-reduced samples. The 300 °C samples show no significant changes, such as additional reflexes, shifts or broadenings of reflexes. The 350 °C-treated samples show reflexes for new phases that best fit with substoichiometric TiO_{2-x} species, which is in agreement with literature.¹⁹¹ These new reflexes were distinctly different from the sodium titanate phases observed in the case of P25 reduced with aluminum (section 6.2.6). The 400 °C-treated samples show similar patterns to the 350 °C-treated samples. However, the suboxide reflexes have a higher relative intensity compared with the anatase(101) reflex at 25.5°, indicating that the structural loss was even more pronounced at this reduction temperature. While these results are in line with Tan et al.'s work, they reached a comparable extent of suboxide formation only after longer treatments or higher temperatures.

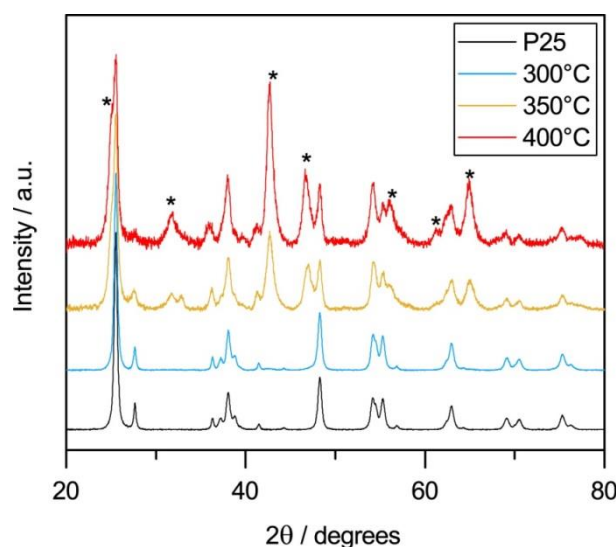


Figure 6-30. XRD patterns of P25 and NaBH₄-reduced P25. Right: close-up of E_g mode.

6.3.6. XPS

6.3.6.1. *Effect of washing*

As NaBH₄ was used as reducing agent, I checked for the presence of sodium and boron after synthesis to ensure that I obtained clean, reduced TiO₂. Directly after synthesis which already included a thorough washing step with water and ethanol, XPS surveys show the presence of sodium in all samples and the presence of boron – in form of borates – in the 400 °C-treated samples. Generally, boron has a very low sensitivity for XPS measurements and is thus difficult to detect, while exact quantification of sodium proves difficult as well, since the Na 1s peak coincides with the Ti LMM edge of TiO₂ and the 2s signal of sodium coincides with the Ti 3p signal.^{213, 219, 302, 306} However, the presence of sodium can be confirmed and amounts can be roughly estimated, when compared to the P25 reference. For my samples, I see that the amount of sodium increases with increasing reduction temperature.

XPS surveys and detail spectra of the NaBH₄-reduced samples show that Na and B/B₂O₃ can only be completely removed after I applied two additional washing steps with ethanol and warm water. Only one exception was found in which some Na signal was still observed after three washing steps. This sample was treated at 400°C and also shows the highest disorder in TEM, Raman and XRD (section 6.3.3, 6.3.4, 6.3.5). Besides Na and B, there are no additional impurities in the samples. An example for the elemental composition of a sample treated at 400 °C and measured after each washing step is shown in Table 6-6.

The first additional wash reduced the signal in the Na1s/Ti LMM region of 400 °C-treated samples from about 11 at.% to 2 at.% (note, that the listed values are slightly overestimated as they do not account for the inherent signal of Ti LMM). Borates are not detected anymore after two times of washing, although this does

Sample	At % from surveys				
	C	O	Ti	Na*	B
P25	55.2	32.9	17.2	-	-
400°C (1x wash)	9.9	53.4	23.9	11.6	4.5
400°C (2x wash)	35.8	44.6	20.6	2.5	<i>not detected</i>
400°C (3x wash)	25.8	47.9	11.8	2.4	<i>not detected</i>

Table 6-6. Elemental composition quantified from XPS survey measurements for P25 and a sample of P25 reduced with NaBH₄ at 400 °C after three washing steps.

not completely exclude its presence due to the mentioned low sensitivity of this element. A second additional wash did not further reduce the Na1s/Ti LMM region. Thus, it was assumed that no Na and no B is left in the material after two additional washing steps in all but one sample – that also shows the highest degree of reduction as observed by Raman and XRD – and remained at a level comparable to the Ti LMM signal of pristine P25 (Figure 6-31). Colors and other characteristics were not affected by the washing steps indicating that the generated defects and newly-formed phases are stable against oxidation and hydrolysis. This is supported by the fact that photocatalytic experiments do not show any significant differences amongst the different washing steps.

All results shown in this section are of samples that are washed three times in total.

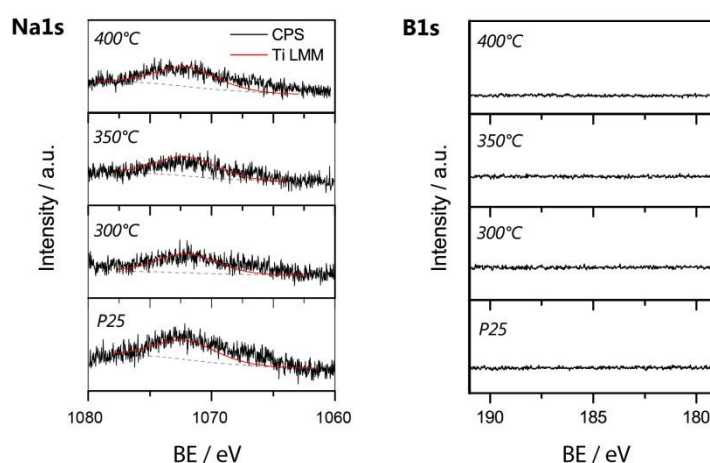


Figure 6-31. Na 1s and B 1s detail spectra for P25 and NaBH₄-reduced P25.

6.3.6.2. Surveys

Table 6-7 shows the elemental composition of P25 and the NaBH₄-treated samples from XPS survey measurements. The average value for the Ti:O ratio of the reduced samples was slightly higher than for pristine P25, which supports that suboxides have formed and is in line with an increasing degree of disorder as observed using TEM, Raman and XRD.

reduction T °C	at. % from survey					metal oxide
	C	O _{total}	O _{metal oxide}	Ti	Na	Ti:O
- (P25)	30.2 ± 15.7	46.0 ± 8.1	45.3 ± 4.7	17.7 ± 6.2	-	0.4 ± 0.2
300	50.5 ± 3.9	34.5 ± 2.2	20.2 ± 1.3	15.0 ± 1.7	-	0.7 ± 0.1
350	43.6 ± 8.4	38.6 ± 4.5	27.3 ± 7.0	17.7 ± 4.3	-	0.7 ± 0.3
400	31.7 ± 8.7	45.9 ± 4.3	38.1 ± 4.1	21.5 ± 4.0	(in one case: 0.6)	0.6 ± 0.2

Table 6-7. Elemental composition from survey spectra for P25 and NaBH₄-reduced P25.

6.3.6.3. *Detail spectra*

Figure 6-32 shows the C 1s, O 1s and Ti 2p detail spectra of the NaBH₄-reduced and pristine P25 after complete removal of Na and B. All samples show typical C 1s spectra for adventitious carbon with the C-C signal set to 284.8 eV and the various carbonaceous species in the range of 286 to 289 eV (section 4.4.1).

The O 1s spectra show the typical signal at 529.5-530.0 eV stemming from the lattice oxygen of TiO₂. Additional contributions stem from hydroxide species and adsorbed organic species in the range of 531 to 534 eV. The ratio between the O 1s signals from adsorbed species to the lattice oxygen increases for the reduced samples. The absolute signal intensities indicate that this is due to a decrease in the main signal from the lattice oxygen at 530 eV rather than to an increase of adsorbed species, which is also confirmed by the almost equivalent C 1s spectra. This is again in agreement with an increased disorder in the sample.

Ti 2p spectra show the typical features of TiO₂ with the Ti2p_{3/2} peak at 458.5 ± 0.1 eV and the Ti2p_{1/2} peak at 464.2 ± 0.1 eV ($\Delta = 5.7$ eV) (section 4.4.3). The 350°C and 400°C samples show a broadened signal plus a faint shoulder around 456 eV, which can be attributed to an increased amount of Ti³⁺ in these samples. Additionally, sometimes a shift in the Ti⁴⁺ signal was observed, that is similar to the one described for the high pressure-reduced aNC and not completely understood yet (section 6.1.7).

Tan et al. observed a small shift of the main Ti 2p signal by 0.2 eV to lower BE for some samples which they assigned to Ti³⁺ centers.¹⁹¹ Additionally, peaks were broadened for most of their reduced samples. They deconvoluted these broadened peaks into signals stemming from Ti²⁺, Ti³⁺, and Ti⁴⁺ species. However, the presence of Ti²⁺ species is questionable from the shown data and peak deconvolution as one would expect to see a 2p_{3/2} signal centered at about 455 eV to some extent. The TiO spectrum given for comparison is lacking labeling and peak assignments are not comprehensible and signal intensities between the 2p_{3/2} and 2p_{1/2} seem to be inverted. Generally, it appears as though peaks are fitted below the actual background line, unless the background is supposed to be a very broad Ti²⁺ signal. Both cases would not make sense and make it difficult to almost impossible to follow the argumentation of the authors.

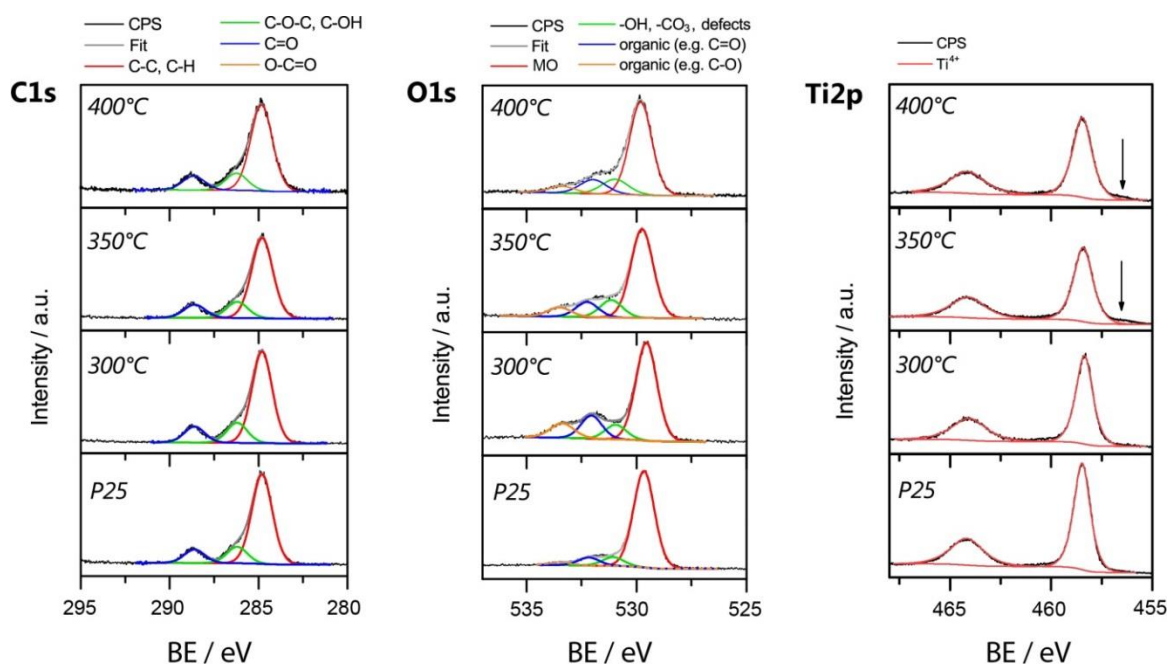


Figure 6-32. C 1s, O 1s and Ti 2p detail spectra for P25 and NaBH₄-reduced P25.

6.3.6.4. VB

Figure 6-33 shows the VB spectra for P25 and NaBH₄-reduced P25. I do not observe band tailing or decrease in the VBM for any of my samples as suggested by Tan et al. On the contrary, the 400 °C-treated samples even show a slight increase in the VBM. The increase in the VBM of the strongly-reduced 400°C samples might be caused by more electrons being located in donor states at Ti³⁺ sites

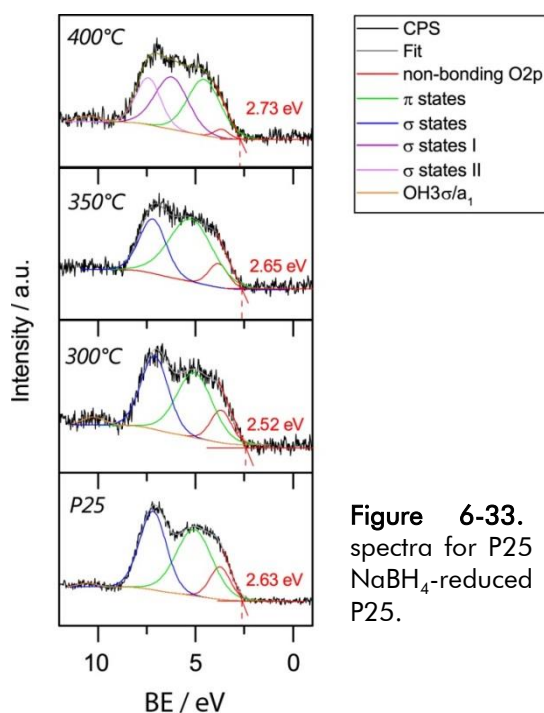


Figure 6-33. VB spectra for P25 and NaBH₄-reduced P25.

which may lead to a lower electron density and thus a more positive value in the VB states.

Tan et al. reported on blue-shift with band tail for their black sample.¹⁹¹ However, based on the published figure it is again questionable whether tail states can really be fitted into the spectrum, as the intensity of the assigned tail states seems to lie within the intensity variation of the background for this sample. Thus, while I do not want to diminish the observed performance and impact of the cited work, I do not agree with their XPS interpretation based on the published figures in main and supporting text.

6.3.7. HER

Figure 6-34 shows the HER curves for representative samples of the NaBH₄-reduced and pristine P25. Activity for H₂ evolution decreases with an increasing reduction temperature, with the samples reduced at 300 °C showing the best performance and those reduced at 400 °C the worst. Still, all reduced samples perform significantly worse than pristine P25. The activity decreased drastically between the samples reduced at 300 °C and 350 °C (about -50 %) as well as between the 350 °C-reduced and the 400 °C-reduced samples (about -65%). As discussed in Chapter 5, a gradual deactivation was observed under UV irradiation for P25 and slightly for the 300°C samples, while higher reduction temperatures had much lower but at least stable H₂ evolution rates.

Visible light activity was only observed for P25 and samples treated at 300 °C. Comparable to the experiments under UV irradiation, P25 showed a much better performance than the 300 °C-samples (2-10-fold higher) with a maximum H₂ activity of 25 μmol h⁻¹ (2.5 mmol h⁻¹ g⁻¹). Samples treated at 350 °C and 400 °C did not show any activity for H₂ evolution in the visible light, although these are the

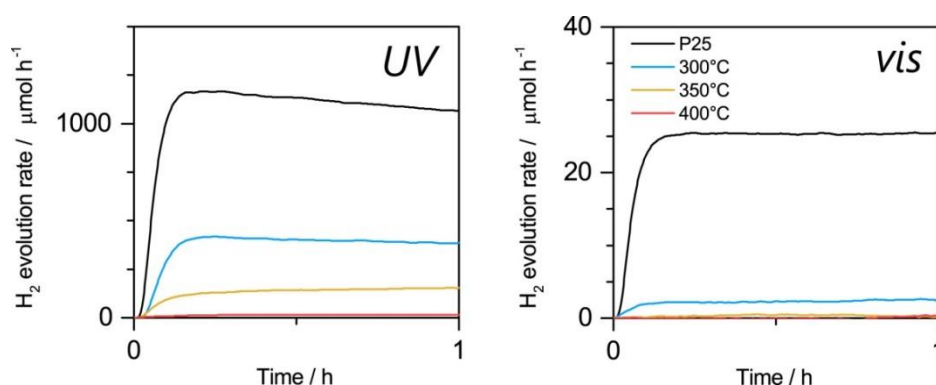


Figure 6-34. HER experiments for P25 and NaBH₄-reduced P25 under UV (left) and visible light (right) irradiation.

samples with the lowest optical band gap and, therefore, the best capability to capture energy from visible light. Hence, performance must be limited by other factors than just visible light absorption.

6.3.8. Discussion & Conclusions

Tan et al. synthesized blue to black TiO₂ with a tunable disordered outer shell and suggested VB modifications. Structural analysis by Raman, XRD and XPS showed the loss of the original TiO₂ structure and the emergence of new suboxide phases in form of peak broadenings, shifts and new reflexes.

My characterization agrees to a large extent with the reference as I observe the same broadening and shifts in Raman and the XPS Ti 2p spectra as well as broadening and the emergence of new phases in XRD that are attributed to a mixture of suboxides. The Ti 2p spectra give evidence not only for general strain in the material but also for the presence of Ti³⁺ through faint shoulders at about 456 eV for samples treated at 300 and 350 °C.

The loss of original structure together with the formation of suboxide species is accompanied by a decrease in band gap and a respective increase in absorption in the visible light range. There was no trend in the surface areas that could be correlated to changes in the phase composition.

However, in contrast to Tan et al. I do not observe an amorphous outer shell but rather a deformation or surface roughening of the original crystals. Furthermore, I do not observe VB tailing as suggested by Tan et al., although their interpretation is difficult to follow from the provided information. Moreover, I observe a slight positive shift of the VBM for the 400 °C-treated sample that points at a lower electron density for these valence states in the material. This could be due to increased localization of electrons in the Ti³⁺ donor levels in the CB.

I do not observe strong shifts in the VB, but a large decrease in the optical band gap. This suggests that the increased absorption is due to donor states below the CB that are not detected by the VB measurements.

In further contrast to the reference, I observe a decrease in the H₂ evolution rate for NaBH₄-reduced P25 with an increasing reduction temperature under both UV and visible light irradiation.

From structural analysis (Raman, XRD, XPS), I know that the degree of reduction increased with the reduction temperature and is accompanied by a loss of the

original structure of P25 along with the formation of new suboxide phases. With the introduction of new structures, defect centers, e.g. in form of grain boundaries, are created which can serve as recombination sites for electron-hole pairs. Furthermore, the newly formed suboxide phases might be less photoactive than the stoichiometric TiO₂.

Here, the structural loss and increased defect concentration resulted in a decrease in the photocatalytic performance, likely due to an increased concentration of recombination centers. Although the dark, reduced materials are capable of much more visible light absorption than white, pristine P25, they do not show an improved visible light performance. Therefore, the impact of recombination outweighs the improved absorption in these materials.

6.4. H₂ reduction followed by rapid cooling

This synthesis is based on the work by Naldoni et al. from 2012.¹⁸⁷ Amorphous TiO₂ is treated and reduced in a H₂ atmosphere at ambient pressure and elevated temperatures. Upon a very rapid cooling step, the metastable disordered outer layer is suggested to “freeze” resulting in stable and black TiO₂. On the other side, slow cooling rates resulted in reoxidation of the black materials. When already crystalline TiO₂ was treated in the same manner, it turned blue as expected during a conventional H₂ reduction.

Naldoni et al. also created a disordered outer shell that resulted in a pronounced VB tail and also shift. While XPS detail spectra did not show changes hinting at Ti³⁺, Raman spectra revealed oxygen vacancy-related photoluminescence features. Photocatalytic activity has not been reported for their material.

6.4.1. Color & DRS

Figure 6-35 shows the Tauc plots and images of sol-gel TiO₂, He-TiO₂ and H₂-TiO₂. Sol-gel TiO₂ changes color from white to grey upon H₂ treatment followed by rapid cooling. In comparison, it remains white when treated under the same conditions but in He gas. The Tauc plots show that the band gap for the sol-gel derived precursor is 3.05 eV, which is typical for rutile phase (section 6.1.2). The presence of some rutile in the sol-gel-derived precursor is also confirmed by other characterization techniques (TEM, Raman, XRD), which is likely due to a heating step during the procedure. Upon heat treatment, the absorption edge red-shifts

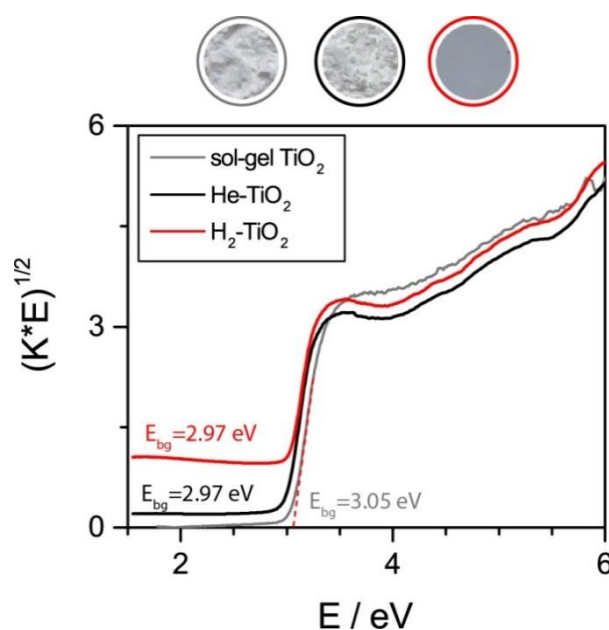


Figure 6-35. Tauc plots and images of sol-gel TiO₂, He-TiO₂ and H₂-TiO₂.

by 0.08 eV to 2.97 eV for both He- and H₂-treated TiO₂. The only difference between these two samples is the absorption in the visible light range, which is higher for the hydrogenated sample as also indicated by the grey color. Naldoni et al. also observed grey TiO₂, when the cooling rate was too slow or air exposure too fast.¹⁸⁷ Our current setup does not allow for faster cooling at this point in time and will be considered in future work.

6.4.2. BET

Sol-gel TiO₂ has a high surface area as determined by BET with a value of 126 m² g⁻¹. Upon H₂ treatment, the surface area for both He- and H₂-treated TiO₂ drastically decreases to 29 and 36 m² g⁻¹, respectively, which is comparable to values obtained for commercial rutile powder. Naldoni et al. used a commercially obtained amorphous TiO₂ powder with a BET surface area of 500 m² g⁻¹. However, this powder was not commercially available anymore.

6.4.3. TEM

Figure 6-36 shows TEM images of sol-gel TiO₂ (a,d), He-TiO₂ (b,e), and H₂-TiO₂ (c,f). All samples show particles that appear to consist of fan-like arranged rutile needles. The sol-gel sample shows large amorphous areas but also clearly crystalline areas, as also evidenced by structural characterization (XRD, Raman). However,

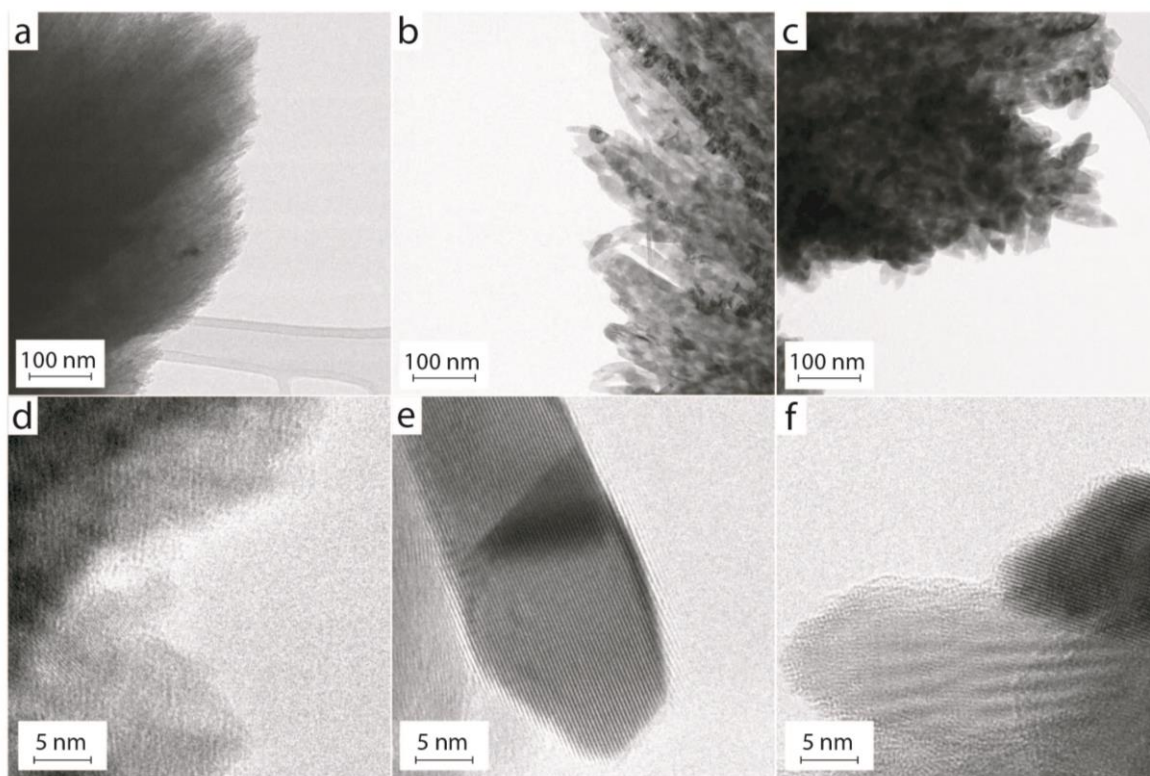


Figure 6-36. TEM images of sol-gel TiO₂ (a,d), He-TiO₂ (b,e), and H₂-TiO₂ (c,f).

er, crystallites are almost indistinguishable from the amorphous background and other crystallites but in some cases reached sizes of less than 5 nm. This is also reflected in the high BET surface area ($126 \text{ m}^2 \text{ g}^{-1}$). He-TiO₂ and H₂-TiO₂ show a needle-like morphology in all cases that is typical for rutile (section 1.2.4). Upon zooming in, distinct rutile crystals can be identified that are often roughly 50 nm by 15 nm large and are reflected in the large reduction of the surface area in these samples (29 and $36 \text{ m}^2 \text{ g}^{-1}$, respectively).

The He-treated TiO₂ shows clean and distinct crystal edges. In some cases, some thick (up to 4 nm) amorphous layer of light contrast can be observed as discussed for aluminum-reduced samples (section 6.2.4). As images were recorded at conditions where amorphization by the electron beam of the TEM is very slow or not occurring at all. Thus, these amorphous layers are indicative of the sample even in the absence of H₂. However for the H₂-treated samples, I see a different kind of amorphization that is clearly of the same contrast as the TiO₂ crystal and seems to evolve from the crystal which is indicated by a diffuse border between the crystalline core and the disordered outer layers.

I conclude that I, indeed, obtained the desired core-shell structure for H₂-treated TiO₂ in agreement with literature.

6.4.4. Raman

Raman spectra of sol-gel TiO₂, He-TiO₂, and H₂-TiO₂ show typical modes of rutile in all cases (Figure 6-37).²²⁷ The sol-gel-derived TiO₂ shows a lower signal intensity (plots normalized) and less defined bands, which suggests a lower extent of crystallinity in the precursor. There is a large red-shift in the E_g mode of rutile accompanied by a significant peak broadening between He-TiO₂ (444.4 cm^{-1}) and

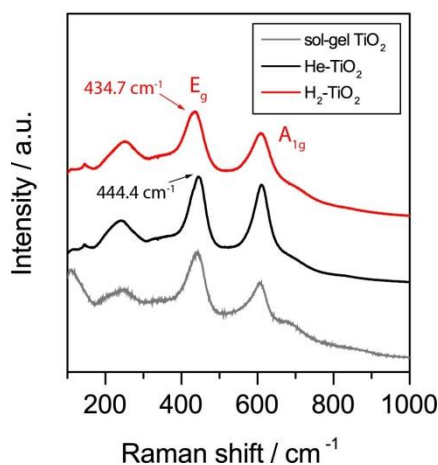


Figure 6-37. Raman spectra of sol-gel TiO₂, HeTiO₂, and H₂-TiO₂

H₂-TiO₂ (434.7 cm⁻¹) by almost 10 cm⁻¹. As discussed previously, this is usually assigned to strain in the crystal lattice. As TEM and XRD do not show obvious variations in the crystal sizes of He- and H₂-treated TiO₂, I attribute the shift and broadening to the introduction of defects into the crystal lattice upon H₂ treatment.²²⁸ H₂-TiO₂ is therefore apparently more defective than He-TiO₂, indicating a possible incorporation of oxygen vacancies. This result also agrees with Naldoni et al.'s observed strong blue-shift and peak broadening for their anatase black TiO₂.¹⁸⁷

6.4.5. XRD

XRD patterns of sol-gel TiO₂, He-TiO₂, and H₂-TiO₂ show typical reflexes for rutile in all cases (Figure 6-38).³⁰⁷ The reflexes for the sol-gel TiO₂ are less resolved, broader and lower in overall intensity (plots are normalized) than for He- and H₂-TiO₂ which indicates a lower degree of crystallinity and higher percentage of amorphous TiO₂ as expected for the precursor without heat treatment. This also agrees with the Raman spectra as discussed above. As rutile is the thermodynamically favored phase of TiO₂, it might form to some extent during the heating step of the synthesis. The patterns for He- and H₂-treated TiO₂ are identical; indicating no differences in crystal size or structure between these samples.

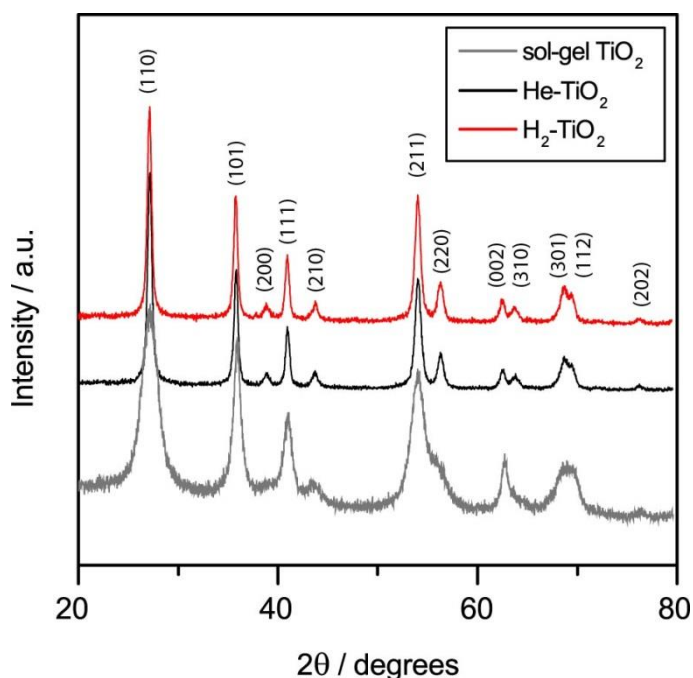


Figure 6-38. XRD patterns of sol-gel TiO₂, He-TiO₂, and H₂-TiO₂.

6.4.6. XPS

Surveys show the presence of some Cl⁻ ions (*ca.* 0.5 at.%) in the sol-gel precursor, which is not surprising as TiCl₄ is used for the sol-gel process (Table 6-8). However, this signal vanishes completely for all heat-treated samples and is thus unlikely to affect performance of these materials. There are no further impurities found in any of the samples. The Ti:O ratio is centered at 0.5 for all samples, as expected for stoichiometric TiO₂.

Sample	at. % from survey					metal oxide
	C	O _{total}	O _{metal oxide}	Ti	Cl	Ti:O
SG4_1	42.5	41.8	31.4	15.1	0.6	0.5
04-015_2	33.9	45.8	38.0	20.3	-	0.5
04-014_1	33.1	46.5	38.3	20.4	-	0.5

Table 6-8. Elemental composition of sol-gel TiO₂, He-TiO₂, and H₂-TiO₂ quantified from XPS survey spectra.

Detail spectra (C 1s, O 1s, Ti 2p) show regular signals for adventitious carbon and TiO₂ (Figure 6-39 and Figure 6-40). There is no contribution from Ti³⁺ species, which agrees with Naldoni et al.¹⁸⁷ Naldoni et al. observed a distinct shift in the VB from 1.2 eV for TiO₂ to 0.6 eV (tail up to -0.3 eV) for black TiO₂ in agreement with the first black TiO₂ report by Chen et al.¹²⁹ While not discussed, the VB spectrum of their black TiO₂ additionally showed a significantly different shape than their white reference material, indicating a different bonding environment in the black sample. In contrast, my VB spectra neither show a VB shift nor a change of shape, but agree with the typical VB shape observed for TiO₂ that has been discussed before (section 4.4.4).

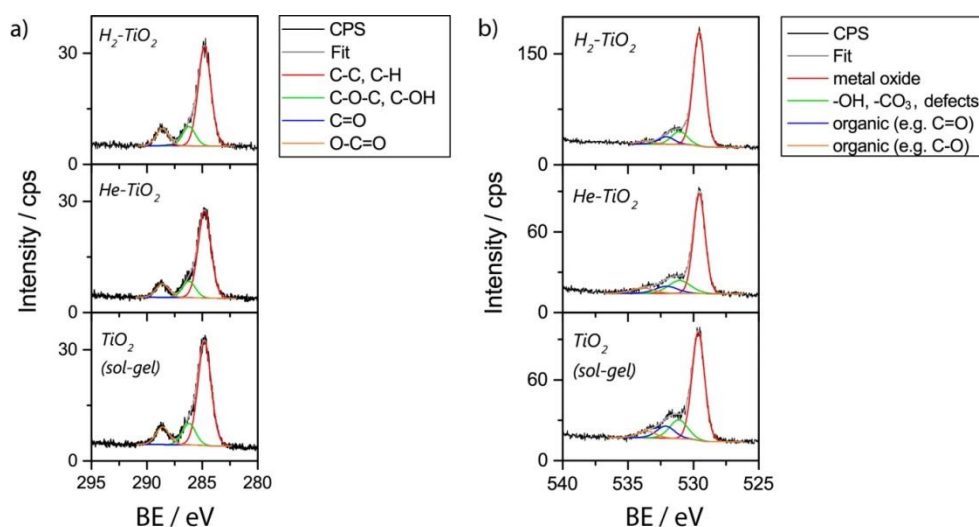


Figure 6-39. (a) C 1s and (b) O 1s detail spectra of sol-gel TiO₂, He-TiO₂, and H₂-TiO₂.

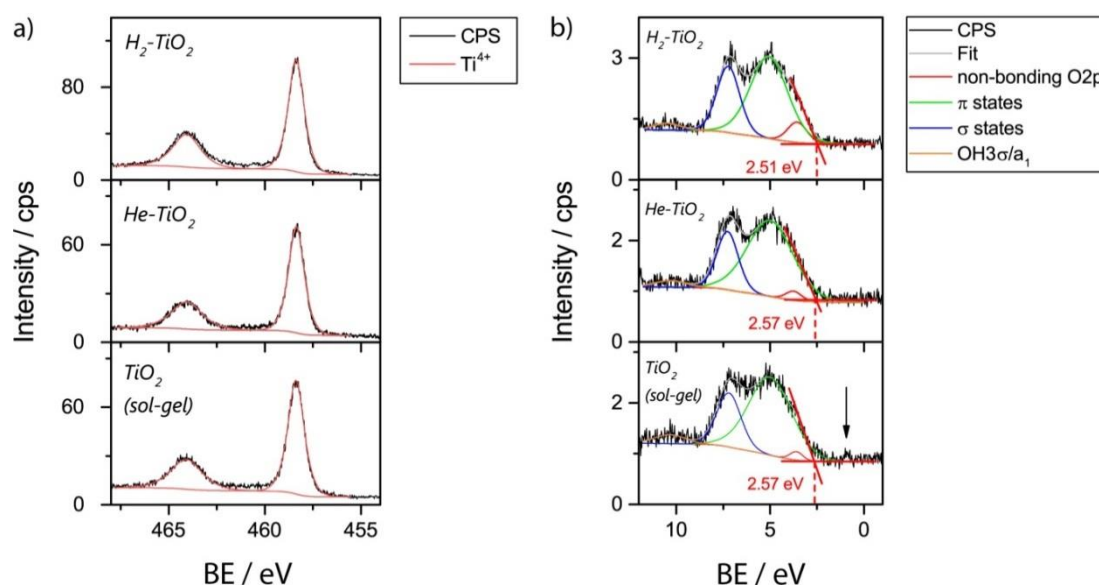


Figure 6-40. (a) Ti 2p and (b) VB detail spectra of sol-gel TiO₂, He-TiO₂, and H₂-TiO₂.

6.4.7. HER

Figure 6-41 shows the HER experiments for sol-gel TiO₂, He-TiO₂, H₂-TiO₂, and a commercial rutile reference under both UV and visible light irradiation. Additionally, a P25 reference is plotted for the visible light experiments.

Photocatalytic HER show clear differences between the precursor, He-TiO₂ and H₂-TiO₂: Under UV light, He-TiO₂ shows a comparable activity to commercial rutile (shown here as reference) with a rate of 142 $\mu\text{mol h}^{-1}$ (14.2 $\text{mmol h}^{-1} \text{g}^{-1}$) of photocatalyst. Interestingly, the sol-gel TiO₂ shows a much higher activity with a maximum at 280 $\mu\text{mol h}^{-1}$ (28.0 $\text{mmol h}^{-1} \text{g}^{-1}$). The maximum activity of sol-gel TiO₂ is reached faster than for the other samples, but is followed by a slow degradation that has been discussed in Chapter 5. I previously attributed this slow deg-

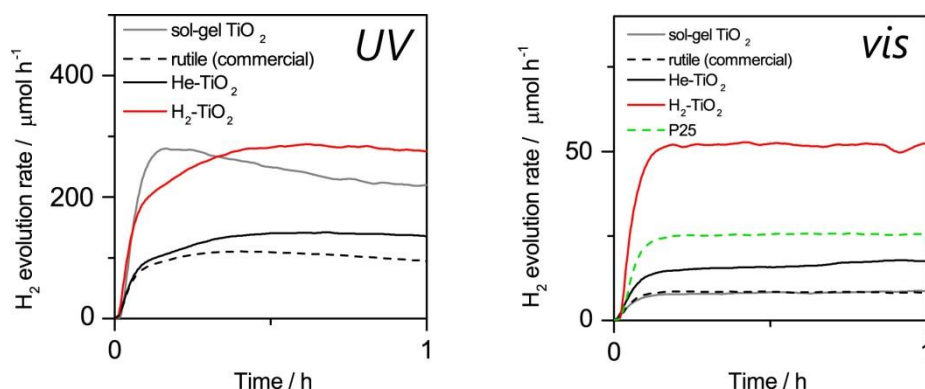


Figure 6-41. HER experiments for sol-gel TiO₂, He-TiO₂, H₂-TiO₂, and a commercial rutile reference under both UV and visible light irradiation. Additionally, a P25 reference is plotted for the visible light experiments.

radiation to a slow build-up of defects in the material due to UV irradiation. As sol-gel TiO₂ has a higher amorphous percentage than the other samples, it might be more vulnerable to defect creation, which would agree with my hypothesis. The faster initial kinetics of sol-gel TiO₂ might be caused by a faster deposition of Pt, as more defect sites could be available in a largely amorphous material. The comparably higher rate for the sol-gel TiO₂ than for the commercial rutile and He-TiO₂, might be caused by the almost 4x larger surface area, which is naturally accompanied by an increase in reaction sites on the surface. The grey H₂-TiO₂ shows a similarly high maximum rate for HER as its sol-gel precursor. However, the rate is more stable and remains at 3x higher values than for commercial rutile and the He reference, while the surface area in this case is comparable between these materials.

Under visible light, sol-gel TiO₂ and commercial rutile show almost equivalent rates around 8 $\mu\text{mol h}^{-1}$, while H₂ evolution for the He reference doubles. TiO₂ was treated at 200°C in O₂ before the He or H₂ treatment. Thus, He-TiO₂ can be assumed to be more stoichiometric than sol-gel TiO₂ and possibly commercial rutile. Less defects and higher crystallinity may lead to a higher activity under visible light due to less recombination. However, this effect should be expected to be seen under UV light as well. A reason might lie in the significantly lower light intensity and photon energy of visible light compared to UV light. A lower photon flux and thus lower density of charge carriers may render the influence of defects more important than with an excess of charge carriers, whereas under UV light the surface area effect counteracts the influence of defects to some extent, e.g. in the case of sol-gel TiO₂.

The enhancement in activity for the H₂-treated sample is highly pronounced under visible light, when even P25 is outperformed by a factor of 2 (H₂-TiO₂: 51.8 $\mu\text{mol h}^{-1}$; P25: 25.3 $\mu\text{mol h}^{-1}$). When the rate is correlated to the surface areas, this factor increases to a value of ~ 3 (H₂-TiO₂: 144 $\mu\text{mol h}^{-1} \text{m}^{-2}$; P25: 46 $\mu\text{mol h}^{-1} \text{m}^{-2}$). The most striking difference to He-TiO₂ is the disordered outer layer for H₂-TiO₂ observed in TEM. As discussed, a disordered outer layer has led to a decreased recombination rate and strongly improved photocatalytic performance in the original work by Chen et al. As is the case for He-TiO₂, the trends for H₂-TiO₂ differ between UV and visible light irradiation. Under UV light, P25 clearly remains the most active material (about 1200 $\mu\text{mol h}^{-1}$ / $2.2 \times 10^3 \mu\text{mol m}^{-2}$). This suggests that under excess amounts of charge carriers (i.e. UV irradiation), the high surface area of sol-gel TiO₂ and the synergistics between anatase and rutile

phase in P25 have a stronger influence on the performance of these materials than under visible light irradiation. On the other side, defect distribution and concentration seems to have a stronger influence under visible light irradiation.

6.4.8. Discussion & Conclusions

In the reference work by Naldoni et al., amorphous TiO₂ treated in H₂ followed by a rapid cooling step, resulted in black TiO₂ with a disordered outer shell. They reported a pronounced VB tail and shift, whereas XPS detail spectra did not show defect-related changes. Raman spectra showed photoluminescent features that were attributed to oxygen vacancies. Photocatalytic performance was not investigated for their black TiO₂.

Here, I synthesized grey TiO₂ that exhibited a disordered outer shell as well as evidenced by TEM, while I could not observe corresponding VB modifications or shifts. However, modifications of the VB have been both observed and not observed in literature in the presence of a disordered outer shell (1.3.5.2).¹⁸² The absence of a VB tail is therefore not contradicting the observed amorphous layer.

Visible light absorption increased, while no red-shift attributed to Ti³⁺ color centers could be observed.

In further agreement with the reference, I observed peak broadening and shifts in Raman that I attributed to oxygen vacancy formation. However, I could not observe a background due to photoluminescence.

XRD showed the presence of rutile in the sol-gel precursor, which may have impaired some of the synthesis as the same treatment of purely crystalline materials did not result in black TiO₂. Using a completely amorphous precursor in the future might result in a more pronounced reduction.

As the only out of the four syntheses, the H₂-treated sample shows a strongly enhanced photocatalytic H₂ generation under visible light irradiation clearly outperforming P25. As discussed in the HER section, clear differences in the performances of the materials between UV and visible light irradiation that suggest that under excess amounts of charge carriers (i.e. UV irradiation), the nature and concentration of defects is less influential than under less intense irradiation with lower amounts of charge carriers (i.e. visible light irradiation).

Characterization method	high pressure H ₂ reduction <i>Chen et al.¹²⁹ this work</i>	Aluminum reduction <i>Wang et al.¹⁸⁶ this work</i>	<i>in situ</i> NaBH ₄ <i>Tan et al.¹⁹¹ this work</i>	H ₂ reduction and rapid cooling <i>Naldoni et al.¹⁸⁷ this work</i>
color	black	black	blue to black	grey and black
DRS	increased visible light absorption no comment on optical band gap	increased visible light absorption no band gap shifts (3.20 eV) red-shift in band gap (3.16-2.99 eV)	increased visible light absorption no comment on optical band gap	increased visible light absorption red-shift in band gap (3.15-2.75 eV) red-shift in band gap (3.03-2.97 eV)
TEM	shell (1 nm)	shell (>1.5 nm; tuneable)	shell (also for blue sample; tuneable)	shell (ca. 1.5 nm, only for black)
BET	(later work calculated from XRD: increase)†	no change	no change	-
Raman	peak broadening extra modes	peak broadening + shift no extra modes C impurity for grey sample	peak broadening + shift no extra modes	peak broadening + shift no extra modes V ₀ -related PL maybe V ₀ -related PL
XRD	anatase no phase changes (later work: plane spacing analysis)†	P25 [line broadening (V ₀)] sodium titanate phases	P25 line broadening new phases (suboxides) at higher T and longer treatments	amorphous (white) 81% A and 19% R (black) synchrotron XRD: 5% V ₀ (Rietveld) amorphous/rutile (white) rutile (grey) no difference between He and H ₂ treated sample
XPS				
Ti2p	no Ti ²⁺	no changes in detail spectra or VB (explained by reoxidation)	Ti 2p: small shifts + broadening	no changes in detail spectra (explained by reoxidation)
O1p	increased Ti-OH	decrease in metal oxide signal	broadening Ti 2p, faint shoulder	no changes in detail spectra or VB
other	extra signal aNC	no Al, Na not investigated	broadening Ti 2p, faint shoulder	no changes in detail spectra or VB
VB	VB-tail	no VB-tail (VBM: slight decrease 0.2 eV) (split sigma states due to distortion)	[VB-tail] (independent of shell)	VB-tail + shift no VB-tail
photocatalysis				
dye degradation	MB + phenol (solar): enhanced activity	MO (UV-vis) + phenol (vis) degradation: enhanced activity	MO (UV): CIOMP-4/-6 (not black) outperform P25, black sample worse	-
HER	solar light: active (50 vol.% MeOH, 0.6 wt.% Pt)	UV-vis: enhanced activity (25 vol.% MeOH, 0.5 wt.% Pt)	UV-vis: all better than P25, best CIOMP-6 (not black) (25 vol.% MeOH, 1.0 wt.% Pt)	largely improved activity of grey H ₂ -treated TiO ₂ compared to rutile, outperforms P25 in visible light experiments
additional:	DFT	also EPR; PEC; DFT	EPR	also: EELS, EPR, CL

Table 6-9. Comparison of characterization results between literature and references and this work for the synthesis of black TiO₂.

† Xia, T.; Chen, X., *J. Mater. Chem. A* **2013**, 1, 2983-2989.

6.5. Discussion & Conclusions

In conclusion, four different synthesis routes of black core-shell TiO₂ were tested in order to investigate reproducibility and common key characteristics of these materials. Table 6-9 gives an overview of the characterizations and observations as reported in literature in direct comparison with my results.

6.5.1. Reproducibility and performance of the reported black core-shell TiO₂

Reproduction of the chosen literature references has proven challenging. The high pressure H₂ treatment of different types of TiO₂ at elevated temperature resulted in various brown shades that seem to be dictated by the crystal size. Characteristics such as the disordered outer shell, VB modification and additional Raman modes are not observed in my materials. The treatment was detrimental for the photocatalytic performance. Danon et al. suggested that the reactor material has a large influence on the color and characteristics of the H₂-treated TiO₂.¹⁸³ Black TiO₂ was obtained for stainless steel reactors due to chromium doping, while TiO₂ remained blue using a quartz glass reactor. Thus, there are clearly more parameters than only the H₂ pressure and temperature that need to be considered, when synthesizing black TiO₂.

The aluminum reduction resulted in grey, blue, and dark blue P25 depending on the ratio of TiO₂ to aluminum and the reaction duration. However, impurities like C and Na of currently unknown source have been identified as origin of the grey and blue color, respectively. Several key parameters such as the type of aluminum, the Al:TiO₂ ratio, surface areas, heating/cooling rates, and the influence of the vacuum level have not been mentioned in the reference paper, which makes reproduction of the original work tedious. Also in this case, photocatalytic performance was clearly hampered.

In the case of NaBH₄-reduced P25, my characterization largely agrees with the reference as I observe the same broadening and shifts in Raman as well as broadening and the emergence of comparable new phases in XRD that are attributed to a mixture of suboxides. Also, the XPS Ti 2p spectra show broadened signals that indicate the presence of defects in form of Ti³⁺ and oxygen vacancies in line with Tan et al.¹⁹¹ However, Tan et al. observe an amorphous outer shell that they can tune with the reduction temperature and time, whereas I do not see a similar

feature in my samples. Rather a deformation or degradation of the original crystals is evident in TEM. Again, the reductive treatment only resulted in decreased rates for H₂ evolution.

The H₂ reduction of an amorphous TiO₂ precursor followed by rapid cooling proved to be the most promising synthetic route for reproduction of black, core-shell TiO₂ so far. In agreement with the reference and as the only synthesis out of the four chosen routes, I observe a surface amorphization of TiO₂. While I do not observe a similar VB tail and shift, other characterization results (e.g. Raman, DRS, XPS detail spectra) are in line with the reference. The grey instead of black color can be explained by a slightly slower cooling rate or differences in the precursor and renders this method promising for further applications.

6.5.2. Identifying key characteristics

In the first report on black TiO₂, the authors identified a disordered outer layer that creates hole traps in form of additional VB tail states as the key characteristic of their material and origin of the unusual black color. Later work questions the necessity and impact of this shell as there is only a slight preference for the existence of a shell in these materials based on the evaluation of a recently published review by the original authors.¹⁸² I will summarize and discuss my findings on the various properties of my materials in the following sections in order to further elucidate key characteristics for an improved photocatalytic activity.

6.5.2.1. *Color*

In this work, all samples generally show an increased visible light absorption although the effect on the optical band gap is not always identical. My materials display a wide array of brown tones for the high pressure hydrogenation in agreement with literature beyond the original report. The remaining three approaches resulted in grey and blue to blue-black tones. The blue coloration is identified to stem from newly formed suboxide and sodium titanate phases. The grey color was due to C impurities in the case of aluminum reduction. However, the rapidly-cooled sample shows surface amorphization that might cause the color change from white to grey as suggested before for black TiO₂.

The wide array of colors reported in literature shows that the color-shell correlation is not very well understood or investigated. The chosen literature references all report on a black color that they correlate – although not always explicitly mentioned – to the introduced disordered outer layer. However, there are discrepancies regarding the origin of the color even within these four references:

some of the NaBH₄-reduced materials that also have an amorphous shell are blue. This leads to the conclusion, that either the observed shell is an artefact of the TEM measurement or that it, in fact, does not cause the black color. My work clearly shows, that the reasons for coloration can be manifold and cannot be seen as evidence that the original black TiO₂ has been obtained.

6.5.2.2. *Disordered outer shell*

As discussed above, I was only able to reproduce surface amorphization in one out of four synthesis approaches suggesting that the creation of an amorphous shell seems to need highly specific reaction conditions that are either not clearly stated or not fully understood. In three out of four approaches (high pressure hydrogenation, aluminum and NaBH₄ reduction), I observe a highly detrimental effect of the reductive treatments, likely due to 1) the creation of too many and uncontrolled recombination centers in form of defects like oxygen vacancies, 2) the formation of new, inactive phases or 3) due to incorporation of impurities. Only the sample in which surface amorphization is observed shows a strongly improved photocatalytic H₂ evolution rate under both UV and visible light that even outperforms the benchmark photocatalyst P25 under visible light by a factor of 2. Thus, my work can be seen as support for the beneficial effect of the amorphous shell, agreeing with the first report on black TiO₂.

Problematic for characterization of a disordered outer shell is that the main technique remains TEM. I found that the electron beam under standard measuring conditions is able to amorphize the outer layers of TiO₂, which can lead to the wrong conclusion that an observed shell was originating from synthesis, while it can indeed be a measuring artefact (section 4.2).

6.5.2.3. *VB tail states and stability*

The generation of VB tail states constitutes another key feature that seems to be connected to the presence of an amorphous outer shell and lead to visible light absorption by narrowing of the band gap. I did not observe any VB tail states or strong modifications, even when the disordered outer layer was introduced in the case of rapidly-cooled TiO₂.

The correlation between shell and VB tail states has been supported by DFT.¹⁸⁰ However, there are also reports where an amorphous shell has been observed but VB spectra show no modifications.^{186, 188} This is usually explained with reoxidation of the disordered shell upon exposure to air. While reoxidation may happen in many incidences, it should still be considered whether it makes sense in all cases

and why one shell should reoxidize while another does not. Furthermore, if the black color of a material is due to mid gap states above the VB and a subsequently narrower band gap as suggested by Chen et al., a color change should be observed as well upon reoxidation and vanishing of the VB states.

The presence of Ti-H might have a stabilizing role as suggested by Liu et al. (section 1.3.5.1).¹⁸⁰ However, investigations on the role of Ti-H are scarce. For example, there has been a report using a H₂ plasma treatment in which a disordered shell is clearly observed in TEM. While the authors claim the presence of Ti-H from XPS, they do not observe any changes in their VB spectra.¹⁸⁸ These differing results in literature suggest that the properties of the disordered outer layer vary between different synthesis approaches or conditions, which in turn may also affect the respective photocatalytic activity.

6.5.2.4. *Presence of Ti³⁺, oxygen vacancies, Ti-H, Ti-OH*

With any treatment, lattice strain or defects are introduced into TiO₂ as evidenced by TEM, Raman and XRD, sometimes by XPS. In the case of NaBH₄, TEM evidences deformation of TiO₂ crystals, while lattice spacings of sodium titanate phases are observed for aluminum-reduced TiO₂. Raman shows peak broadenings and shifts for all reduction treatments that increase with the intensity of reactions conditions and can be seen as an indication for the presence of strain due to oxygen vacancies as crystal sizes do not differ before and after treatments as evidenced by TEM and XRD. For the high pressure reduces samples, I see an increased fluorescence background after hydrogenation that can be correlated to oxygen vacancies. XPS shows no signs for Ti³⁺ in the hydrogenation approaches, while for the chemical reduction Ti 2p spectra were broadened indicating the presence of Ti³⁺.

The XPS signal for Ti-OH was only increased in the case of high pressure H₂-treated anatase nanocrystals, while Ti-H is not needed for any of the fits.

Overall, I did not obtain a clear picture about the impact of any of these defects. While oxygen vacancies seem to be created at least to some extent in all of the materials, they seem to rather harm the photocatalytic performance.

6.5.3. **Conclusion**

In conclusion, I obtained core-shell TiO₂ with a disordered outer layer around crystalline cores in only one out of four different synthesis approaches, namely from hydrogenation of a mostly amorphous TiO₂ precursor followed by rapid cooling. This indicates that the synthesis of black TiO₂ needs highly specific con-

ditions that are either not completely understood or not fully stated in the respective reference literature. Following the first report on black TiO₂, many groups tried to reproduce this material leading to a vast amount of differing reports and an unclear picture of the actual key characteristics of this material. This might in part be due to sometimes questionable data interpretation, e.g. dark brown materials are labeled black, line broadenings and XPS analyses that do not seem to make sense from the published data, a vague concept of reoxidation of the disordered outer shell and an unclear correlation between the presence or absence of a disordered shell and the actual color of a material.

Concluding from this work, surface amorphization seems to be the crucial parameter for the synthesis of highly active photocatalysts which is supporting the first report on black TiO₂. However, I did not observe the VB tail states, which are suggested as cause of the improved activities due to hole trapping and reduced charge recombination.

In a broader context, my investigations on deactivation in Chapter 5 show a clear impact of the amount of Pt loading and method of deposition on the activity of a photocatalyst. In the four reference papers that I used as basis for my syntheses, there was no information on the Pt deposition method. This indicates a general problem, that key parameters might be omitted in publications rendering comparison across different groups tedious or impossible.

6.6. Outlook

Future work on black TiO₂ materials should consider not only to report properties of the newly-synthesized materials but, in particular, to critically review and assess which of the properties is source of an improved activity. A comparison between different black TiO₂ materials will be key in giving insight into structure-performance relationships as well as critical reaction conditions. Once a clear picture of black TiO₂ has been formed and a reliable synthesis route is established, these materials can be used in a variety of applications and research directions, such as nanocarbon hybrids.

References

- (1) Sachs, J. D., *The age of sustainable development*. Columbia University Press: New York City, United States, 2015.
- (2) Hansen, J.; Johnson, D.; Lacis, A.; Lebedeff, S.; Lee, P.; Rind, D.; Russell, G., *Science*, **1981**, 213, 957-966.
- (3) Arrhenius, S., *Über den Einfluss des atmosphärischen Kohlensäure-gehalts auf die Temperatur der Erdoberfläche*. 1896.
- (4) Schellnhuber, H. J., *Selbstverbrennung*. Bertelsmann: Munich, Germany, 2015.
- (5) IPCC, Summary for Policymakers, In: *Climate Change 2014, Mitigation of Climate Change*. Cambridge University Press: Cambridge, UK, 2014.
- (6) Diego, S. I. o. O. o. U. S., The Keeling Curve (<https://scripps.ucsd.edu/programs/keelingcurve/>), last accessed 25 Sep 2018. 2018.
- (7) Keeling, C. D., *Science*, **1978**, 202, 1109-1109.
- (8) Stern, N., *Stern review: the economics of climate change*. N. p.: United Kingdom, 2006.
- (9) Buceti, G., *Management of Environmental Quality: An International Journal*, **2014**, 25, 5-18.
- (10) Lewis, N. S.; Nocera, D. G., *P. Natl. Acad. Sci.*, **2006**, 103, 15729-15735.
- (11) Møller, K. T.; Jensen, T. R.; Akiba, E.; Li, H.-w., *Prog. Nat. Sci.-Mater.*, **2017**, 27, 34-40.
- (12) Ni, M.; Leung, M. K. H.; Sumathy, K.; Leung, D. Y. C., *Int. J. Hydrogen Energy*, **2006**, 31, 1401-1412.
- (13) Crabtree, G. W.; Dresselhaus, M. S.; Buchanan, M. V., *Phys. Today*, **2004**, 57, 39-44.
- (14) Dutta, S., *J. Ind. Eng. Chem.*, **2014**, 20, 1148-1156.
- (15) Chiarello, G. L.; Aguirre, M. H.; Selli, E., *J. Catal.*, **2010**, 273, 182-190.
- (16) Antzara, A.; Heracleous, E.; Bukur, D. B.; Lemonidou, A. A., *Energy Proced.*, **2014**, 63, 6576-6589.
- (17) Fujishima, A.; Honda, K., *Nature*, **1972**, 238, 37-38.
- (18) Linsebigler, A. L.; Lu, G.; Yates, J. T., *Chem. Rev.*, **1995**, 95, 735-758.
- (19) Fujishima, A.; Zhang, X.; Tryk, D. A., *Int. J. Hydrogen Energy*, **2007**, 32, 2664-2672.
- (20) Fujishima, A.; Zhang, X.; Tryk, D. A., *Surf. Sci. Rep.*, **2008**, 63, 515-582.
- (21) Herrmann, J.-M., *Top. Catal.*, **2005**, 34, 49-65.
- (22) Colmenares, J. C.; Xu, Y.-J., *Heterogeneous Photocatalysis: From Fundamentals to Green Applications*. 1 ed.; Springer: Berlin/Heidelberg, 2016.
- (23) Matsuoka, M.; Kitano, M.; Takeuchi, M.; Tsujimaru, K.; Anpo, M.; Thomas, J. M., *Catal. Today*, **2007**, 122, 51-61.
- (24) Nakata, K.; Fujishima, A., *J. Photochem. Photobiol. C*, **2012**, 13, 169-189.

- (25) Ohtani, B., *Chem. Lett.*, **2008**, 37, 216-229.
- (26) Palmisano, L.; García-López, E. I.; Marcì, G., *Dalton Trans.*, **2016**, 45, 11596-11605.
- (27) Kudo, A.; Miseki, Y., *Chem. Soc. Rev.*, **2009**, 38, 253-278.
- (28) Atkins, P. W.; De Paula, J., *Physikalische Chemie*. WILEY-VCH Verlag GmbH & Co. KGaA: Weinheim, Germany, 2013.
- (29) Xu, Q.; Zhang, L.; Yu, J.; Wageh, S.; Al-Ghamdi, A. A.; Jaroniec, M., *Mater.Today*, **2018**.
- (30) Kawai, T.; Sakata, T., *Chem. Commun.*, **1980**, 694-695.
- (31) Chen, J.; Ollis, D. F.; Rulkens, W. H.; Bruning, H., *Water Res.*, **1999**, 33, 669-676.
- (32) Schneider, J.; Bahnemann, D. W., *J. Phys. Chem. Lett.*, **2013**, 4, 3479-3483.
- (33) Lin, W.-C.; Yang, W.-D.; Huang, I. L.; Wu, T.-S.; Chung, Z.-J., *Energy Fuels*, **2009**, 23, 2192-2196.
- (34) Osterloh, F. E., *ACS Energy Lett.*, **2017**, 2, 445-453.
- (35) Ong, C. B.; Ng, L. Y.; Mohammad, A. W., *Renew. Sust. Energ. Rev.*, **2018**, 81, 536-551.
- (36) Basahel, S. N.; Ali, T. T.; Mokhtar, M.; Narasimharao, K., *Nanoscale Res. Lett.*, **2015**, 10, 73.
- (37) Zhai, Y.; Zhang, S.; Pang, H., *Mater. Lett.*, **2007**, 61, 1863-1866.
- (38) Diebold, U., *Surf. Sci. Rep.*, **2003**, 48, 53-229.
- (39) ASTM G173-03(2012), Standard Tables for Reference Solar Spectral Irradiances: Direct Normal and Hemispherical on 37° Tilted Surface, ASTM International, West Conshohocken, PA, 2012, www.astm.org.
- (40) Iwasita, T., *Electrochim. Acta*, **2002**, 47, 3663-3674.
- (41) Ge, M.; Li, Q.; Cao, C.; Huang, J.; Li, S.; Zhang, S.; Chen, Z.; Zhang, K.; Al-Deyab, S. S.; Lai, Y., *Adv. Sci.*, **2017**, 4, 1600152.
- (42) Henderson, M. A., *Surf. Sci. Rep.*, **2011**, 66, 185-297.
- (43) Kiwi, J.; Graetzel, M., *J. Phys. Chem.*, **1984**, 88, 1302-1307.
- (44) Candal, R. J.; Zeltner, W. A.; Anderson, M. A., *Environ. Sci. Technol.*, **2000**, 34, 3443-3451.
- (45) Xie, S.; Zhang, Q.; Liu, G.; Wang, Y., *Chem. Commun.*, **2016**, 52, 35-59.
- (46) Naldoni, A.; D'Arienzo, M.; Altomare, M.; Marelli, M.; Scotti, R.; Morazzoni, F.; Selli, E.; Dal Santo, V., *Appl. Catal. B*, **2013**, 130-131, 239-248.
- (47) Baba, R.; Nakabayashi, S.; Fujishima, A.; Honda, K., *J. Phys. Chem.*, **1985**, 89, 1902-1905.
- (48) Bowker, M., *Green Chem.*, **2011**, 13, 2235-2246.
- (49) Bellardita, M.; Nazer, H. A. E.; Loddo, V.; Parrino, F.; Venezia, A. M.; Palmisano, L., *Catal.Today*, **2017**, 284, 92-99.
- (50) Halasi, G.; Schubert, G.; Solymosi, F., *Journal of Catalysis*, **2012**, 294, 199-206.
- (51) Rosseler, O.; Shankar, M. V.; Du, M. K.-L.; Schmidlin, L.; Keller, N.; Keller, V., *J. Catal.*, **2010**, 269, 179-190.

- (52) Pai, Y.-H.; Fang, S.-Y., *J. Power Sources*, **2013**, 230, 321-326.
- (53) Hu, C.-C.; Teng, H., *J. Catal.*, **2010**, 272, 1-8.
- (54) Bamwenda, G. R.; Tsubota, S.; Nakamura, T.; Haruta, M., *J. Photochem. Photobiol. A*, **1995**, 89, 177-189.
- (55) Chen, T.; Feng, Z.; Wu, G.; Shi, J.; Ma, G.; Ying, P.; Li, C., *J. Phys. Chem. C*, **2007**, 111, 8005-8014.
- (56) Yang, X.; Salzmann, C.; Shi, H.; Wang, H.; Green, M. L. H.; Xiao, T., *J. Phys. Chem. A*, **2008**, 112, 10784-10789.
- (57) Zou, J.-J.; He, H.; Cui, L.; Du, H.-Y., *Int. J. Hydrogen Energy*, **2007**, 32, 1762-1770.
- (58) Wei, P.; Liu, J.; Li, Z., *Ceram. Int.*, **2013**, 39, 5387-5391.
- (59) Navarro, R. M.; Arenales, J.; Vaquero, F.; González, I. D.; Fierro, J. L. G., *Catal. Today*, **2013**, 210, 33-38.
- (60) Oros-Ruiz, S.; Zanella, R.; López, R.; Hernández-Gordillo, A.; Gómez, R., *J. Hazard. Mater.*, **2013**, 263, Part 1, 2-10.
- (61) Schubert, G. b.; Bánsági, T. s.; Solymosi, F., *J. Phys. Chem. C*, **2013**, 117, 22797-22804.
- (62) Wang, F.-C.; Liu, C.-H.; Liu, C.-W.; Chao, J.-H.; Lin, C.-H., *J. Phys. Chem. C*, **2009**, 113, 13832-13840.
- (63) Yu, J.; Qi, L.; Jaroniec, M., *J. Phys. Chem. C*, **2010**, 114, 13118-13125.
- (64) Maeda, K.; Murakami, N.; Ohno, T., *J. Phys. Chem. C*, **2014**, 118, 9093-9100.
- (65) Abe, T.; Suzuki, E.; Nagoshi, K.; Miyashita, K.; Kaneko, M., *J. Phys. Chem. B*, **1999**, 103, 1119-1123.
- (66) Kandiel, T. A.; Ivanova, I.; Bahnemann, D. W., *Energy Environ. Sci.*, **2014**, 7, 1420-1425.
- (67) Yi, H.; Peng, T.; Ke, D.; Ke, D.; Zan, L.; Yan, C., *Int. J. Hydrogen Energy*, **2008**, 33, 672-678.
- (68) Sakata, T.; Kawai, T., *Chem. Phys. Lett.*, **1981**, 80, 341-344.
- (69) Zheng, Z.; Huang, B.; Lu, J.; Wang, Z.; Qin, X.; Zhang, X.; Dai, Y.; Whangbo, M.-H., *Chem. Commun.*, **2012**, 48, 5733-5735.
- (70) Herrmann, J. M.; Disdier, J.; Pichat, P., *J. Phys. Chem.*, **1986**, 90, 6028-6034.
- (71) Gerischer, H., *J. Phys. Chem.*, **1984**, 88, 6096-6097.
- (72) Zhang, Z.; Yates, J. T., *Chem. Rev.*, **2012**, 112, 5520-5551.
- (73) Michaelson, H. B., *J. Appl. Phys.*, **1977**, 48, 4729-4733.
- (74) Cabán-Acevedo, M.; Stone, M. L.; Schmidt, J. R.; Thomas, J. G.; Ding, Q.; Chang, H.-C.; Tsai, M.-L.; He, J.-H.; Jin, S., *Nature Mater.*, **2015**, 14, 1245.
- (75) Grant, F. A., *Rev. Mod. Phys.*, **1959**, 31, 646-674.
- (76) Hewitt, J., *Cosmet. Toiletries*, **1999**, 114, 59.
- (77) Siddle, G. R., *Pigm. Resin Technol.*, **1975**, 4, 4-12.
- (78) Yan, M. F.; Rhodes, W. W., *Appl. Phys. Lett.*, **1982**, 40, 536-537.
- (79) Xu, Y.; Yao, K.; Zhou, X.; Cao, Q., *Sensor Actuat. B-Chem.*, **1993**, 14, 492-494.
- (80) Marchand, R.; Brohan, L.; Tournoux, M., *Mater. Res. Bull.*, **1980**, 15, 1129-1133.

- (81) Zhang, H.; F. Banfield, J., *J. Mater. Chem.*, **1998**, 8, 2073-2076.
- (82) Lazzeri, M.; Vittadini, A.; Selloni, A., *Phys. Rev. B*, **2001**, 63, 155409.
- (83) Ramamoorthy, M.; Vanderbilt, D.; King-Smith, R. D., *Phys. Rev. B*, **1994**, 49, 16721-16727.
- (84) Fu, N.; Huang, C.; Liu, Y.; Li, X.; Lu, W.; Zhou, L.; Peng, F.; Liu, Y.; Huang, H., *ACS Appl. Mater. Interf.*, **2015**, 7, 19431-19438.
- (85) Kavan, L.; Grätzel, M.; Gilbert, S. E.; Klemen, C.; Scheel, H. J., *J. Amer. Chem. Soc.*, **1996**, 118, 6716-6723.
- (86) Lin, H.; Li, L.; Zhao, M.; Huang, X.; Chen, X.; Li, G.; Yu, R., *J. Amer. Chem. Soc.*, **2012**, 134, 8328-8331.
- (87) Zhang, J.; Zhou, P.; Liu, J.; Yu, J., *Phys. Chem. Chem. Phys.*, **2014**, 16, 20382-20386.
- (88) Landmann, M.; Rauls, E.; Schmidt, W., *J. Physics-Condens. Mat.*, **2012**, 24, 195503.
- (89) Madhusudan Reddy, K.; Manorama, S. V.; Ramachandra Reddy, A., *Mater. Chem. Phys.*, **2003**, 78, 239-245.
- (90) Reyes-Coronado, D.; Rodríguez-Gattorno, G.; Espinosa-Pesqueira, M. E.; Cab, C.; Coss, R. d.; Oskam, G., *Nanotechnology*, **2008**, 19, 145605.
- (91) Kho, Y. K.; Iwase, A.; Teoh, W. Y.; Mädlar, L.; Kudo, A.; Amal, R., *J. Phys. Chem. C*, **2010**, 114, 2821-2829.
- (92) Bickley, R. I.; Gonzalez-Carreno, T.; Lees, J. S.; Palmisano, L.; Tilley, R. J. D., *J. Solid State Chem.*, **1991**, 92, 178-190.
- (93) Ohno, T.; Sarukawa, K.; Tokieda, K.; Matsumura, M., *J. Catal.*, **2001**, 203, 82-86.
- (94) Ohtani, B.; Prieto-Mahaney, O. O.; Li, D.; Abe, R., *J. Photochem. Photobiol. A*, **2010**, 216, 179-182.
- (95) Hurum, D. C.; Agrios, A. G.; Gray, K. A.; Rajh, T.; Thurnauer, M. C., *J. Phys. Chem. B*, **2003**, 107, 4545-4549.
- (96) Scanlon, D. O.; Dunnill, C. W.; Buckeridge, J.; Shevlin, S. A.; Logsdail, A. J.; Woodley, S. M.; Catlow, C. R. A.; Powell, M. J.; Palgrave, R. G.; Parkin, I. P.; Watson, G. W.; Keal, T. W.; Sherwood, P.; Walsh, A.; Sokol, A. A., *Nat. Mater.*, **2013**, 12, 798-801.
- (97) Mills, A.; Davies, R. H.; Worsley, D., *Chem. Soc. Rev.*, **1993**, 22, 417-425.
- (98) Maness, P.-C.; Smolinski, S.; Blake, D. M.; Huang, Z.; Wolfrum, E. J.; Jacoby, W. A., *Appl. Environ. Microbiol.*, **1999**, 65, 4094-4098.
- (99) Paz, Y.; Luo, Z.; Rabenberg, L.; Heller, A., *J. Mater. Res.*, **2011**, 10, 2842-2848.
- (100) Poullos, I.; Spathis, P.; Grigoriadou, A.; Delidou, K.; Tsoumparis, P., *J. Environ. Sci. Health*, **1999**, 34, 1455-1471.
- (101) Luttrell, T.; Halpegamage, S.; Tao, J.; Kramer, A.; Sutter, E.; Batzill, M., *Sci. Rep.*, **2014**, 4, 4043.
- (102) Riegel, G.; Bolton, J. R., *J. Phys. Chem.*, **1995**, 99, 4215-4224.

- (103) Melián, E. P.; López, C. R.; Méndez, A. O.; Díaz, O. G.; Suárez, M. N.; Doña Rodríguez, J. M.; Navío, J. A.; Fernández Hevia, D., *Int. J. Hydrogen Energy*, **2013**, 38, 11737-11748.
- (104) Patsoura, A.; Kondarides, D. I.; Verykios, X. E., *Appl. Catal. B*, **2006**, 64, 171-179.
- (105) Nomikos, G. N.; Panagiotopoulou, P.; Kondarides, D. I.; Verykios, X. E., *Appl. Catal. B*, **2014**, 146, 249-257.
- (106) Abe, R. In *A two-step photoexcitation system for photocatalytic water splitting into hydrogen and oxygen under visible light irradiation*, SPIE Solar Energy + Technology, SPIE: 2011; p 13.
- (107) Kozlova, E. A.; Lyubina, T. P.; Nasalevich, M. A.; Vorontsov, A. V.; Miller, A. V.; Kaichev, V. V.; Parmon, V. N., *Catal. Commun.*, **2011**, 12, 597-601.
- (108) Pan, X.; Zhang, N.; Fu, X.; Xu, Y.-J., *Appl. Catal. A*, **2013**, 453, 181-187.
- (109) Tuller, H. L.; Bishop, S. R., *Annu. Rev. Mater. Res.*, **2011**, 41, 369-398.
- (110) Pacchioni, G., *ChemPhysChem*, **2003**, 4, 1041-1047.
- (111) Pan, X.; Yang, M.-Q.; Fu, X.; Zhang, N.; Xu, Y.-J., *Nanoscale*, **2013**, 5, 3601-3614.
- (112) Seebauer, E. G.; Noh, K. W., *Mater. Sci. Eng.-R*, **2010**, 70, 151-168.
- (113) Minato, T., *Chem. Rec.*, **2014**, 14, 923-934.
- (114) Friend, C. M., *Chem. Rec.*, **2014**, 14, 944-951.
- (115) Hooton, I. E.; Jacobs, P. W. M., *Canad. J. Chem.*, **1988**, 66, 830-835.
- (116) Bruni, Y. L.; Garrido, L. B.; Aglietti, E. F., *Proc. Mat. Sci.*, **2015**, 8, 203-210.
- (117) Kröger, F. A.; Vink, H. J., Relations between the Concentrations of Imperfections in Crystalline Solids. In *Solid State Phys.*, Seitz, F.; Turnbull, D., Eds. Academic Press: Cambridge, Massachusetts. 1956; Vol. 3, pp 307-435.
- (118) Nowotny, J.; Bak, T.; Nowotny, M.; Sheppard, L., *J. Phys. Chem. C*, **2008**, 112, 590-601.
- (119) Zhang, Z.; Rousseau, R.; Gong, J.; Li, S.-C.; D. Kay, B.; Ge, Q.; Dohnalek, Z., *Phys. Rev. Lett.*, **2008**, 101, 156103/1-4.
- (120) Li, S.-C.; Zhang, Z.; Sheppard, D.; Kay, B. D.; White, J. M.; Du, Y.; Lyubinetsky, I.; Henkelman, G.; Dohnálek, Z., *J. Amer. Chem. Soc.*, **2008**, 130, 9080-9088.
- (121) Zhang, M.; Pei, Q.; Chen, W.; Liu, L.; He, T.; Chen, P., *RSC Adv.*, **2017**, 7, 4306-4311.
- (122) Wertz, J. E.; Auzins, P.; Griffiths, J. H. E.; Orton, J. W., *Discuss. Farad. Soc.*, **1959**, 28, 136-141.
- (123) Turner, T. J.; Crawford, J. H., *Solid State Commun.*, **1975**, 17, 167-169.
- (124) Summers, G. P.; White, G. S.; Lee, K. H.; Crawford, J. H., *Phys. Rev. B*, **1980**, 21, 2578-2584.
- (125) Kotomin, E. A.; Popov, A. I., *Nucl. Instrum. Meth. B*, **1998**, 141, 1-15.
- (126) Eder, D.; Kramer, R., *Phys. Chem. Chem. Phys.*, **2003**, 5, 1314-1319.
- (127) Regonini, D.; Adamaki, V.; Bowen, C. R.; Pennock, S. R.; Taylor, J.; Dent, A. C. E., *Solid State Ionics*, **2012**, 229, 38-44.

- (128) Xiong, L.-B.; Li, J.-L.; Yang, B.; Yu, Y., *J. Nanomater.*, **2012**, 2012, 13.
- (129) Chen, X.; Liu, L.; Yu, P. Y.; Mao, S. S., *Science*, **2011**, 331, 746-750.
- (130) Diebold, U.; Lehman, J.; Mahmoud, T.; Kuhn, M.; Leonardelli, G.; Hebenstreit, W.; Schmid, M.; Varga, P., *Surf. Sci.*, **1998**, 411, 137-153.
- (131) Guillemot, F.; Porté, M. C.; Labrugère, C.; Baquey, C., *J. Colloid Interf. Sci.*, **2002**, 255, 75-78.
- (132) Liu, H.; Ma, H. T.; Li, X. Z.; Li, W. Z.; Wu, M.; Bao, X. H., *Chemosphere*, **2003**, 50, 39-46.
- (133) Luciu, I.; Bartali, R.; Laidani, N., *J. Phys. D Appl. Phys.*, **2012**, 45, 345302.
- (134) Lu, T.-C.; Lin, L.-B.; Wu, S.-Y.; Zhao, C.-P.; Xu, X.-C.; Tian, Y.-F., *Nucl. Instrum. Meth. B*, **2002**, 191, 291-295.
- (135) Nakamura, I.; Negishi, N.; Kutsuna, S.; Ihara, T.; Sugihara, S.; Takeuchi, K., *J. Mol. Catal. A*, **2000**, 161, 205-212.
- (136) Knotek, M. L.; Feibelman, P. J., *Surf. Sci.*, **1979**, 90, 78-90.
- (137) Jiang, N., *Rep. Prog. Phys.*, **2015**, 79, 016501.
- (138) Wu, Q.; van de Krol, R., *J. Amer. Chem. Soc.*, **2012**, 134, 9369-9375.
- (139) Zuo, F.; Wang, L.; Feng, P., *Int. J. Hydrogen Energy*, **2014**, 39, 711-717.
- (140) Suriye, K.; Praserthdam, P.; Jongsomjit, B., *Appl. Surf. Sci.*, **2007**, 253, 3849-3855.
- (141) Emeline, A.; Kataeva, G. V.; Litke, A. S.; Rudakova, A. V.; Ryabchuk, V. K.; Serpone, N., *Langmuir*, **1998**, 14, 5011-5022.
- (142) Takeuchi, M.; Martra, G.; Coluccia, S.; Anpo, M., *J. Phys. Chem. C*, **2007**, 111, 9811-9817.
- (143) Yamakata, A.; Ishibashi, T.-a.; Onishi, H., *J. Mol. Catal. A*, **2003**, 199, 85-94.
- (144) Emeline, A. V.; Kataeva, G. V.; Panasuk, A. V.; Ryabchuk, V. K.; Sheremetyeva, N. V.; Serpone, N., *J. Phys. Chem. B*, **2005**, 109, 5175-5185.
- (145) Murakami, N.; Prieto Mahaney, O. O.; Torimoto, T.; Ohtani, B., *Chem. Phys. Lett.*, **2006**, 426, 204-208.
- (146) Osorio-Vargas, P. A.; Pulgarin, C.; Sienkiewicz, A.; Pizzio, L. R.; Blanco, M. N.; Torres-Palma, R. A.; Pétrier, C.; Rengifo-Herrera, J. A., *Ultrason. Sonochem.*, **2012**, 19, 383-386.
- (147) Romanyuk, A.; Spassov, V.; Melnik, V., *J. Appl. Phys.*, **2006**, 99, 034314.
- (148) Romanyuk, A.; Oelhafen, P.; Kurps, R.; Melnik, V., *Appl. Phys. Lett.*, **2007**, 90, 013118.
- (149) Li, D. G., *Ultrason. Sonochem.*, **2015**, 27, 296-306.
- (150) Jeevanandam, P.; Diamant, Y.; Motiei, M.; Gedanken, A., *Phys. Chem. Chem. Phys.*, **2001**, 3, 4107-4112.
- (151) Fan, C.; Yu, S.; Qian, G.; Wang, Z., *RSC Adv.*, **2017**, 7, 18785-18792.
- (152) Haerudin, H.; Bertel, S.; Kramer, R., *J. Chem. Soc. Faraday T.*, **1998**, 94, 1481-1487.
- (153) Enevoldsen, G. H.; Foster, A. S.; Christensen, M. C.; Lauritsen, J. V.; Besenbacher, F., *Phys. Rev. B*, **2007**, 76, 205415.

- (154) König, T.; Simon, G. H.; Heinke, L.; Lichtenstein, L.; Heyde, M., *Beilstein J. Nanotechnol.*, **2011**, 2, 1-14.
- (155) Setvín, M.; Wagner, M.; Schmid, M.; Parkinson, G. S.; Diebold, U., *Chem. Soc. Rev.*, **2017**, 46, 1772-1784.
- (156) Zhang, L.; Wang, S.; Lu, C., *Anal. Chem.*, **2015**, 87, 7313-7320.
- (157) Fan, H.-B.; Yang, S.-Y.; Zhang, P.-F.; Wei, H.-Y.; Liu, X.-L.; Jiao, C.-M.; Zhu, Q.-S.; Chen, Y.-H.; Wang, Z.-G., *Chin. Phys. Lett.*, **2007**, 24, 2108.
- (158) Jaiswar, S.; Mandal, K. D., *J. Phys. Chem. C*, **2017**, 121, 19586-19601.
- (159) Howe, R. F.; Gratzel, M., *J. Phys. Chem.*, **1987**, 91, 3906-3909.
- (160) Yan, J.; Wu, G.; Guan, N.; Li, L.; Li, Z.; Cao, X., *Phys. Chem. Chem. Phys.*, **2013**, 15, 10978-10988.
- (161) Ganesan, K.; Ghosh, S.; Gopala Krishna, N.; Ilango, S.; Kamruddin, M.; Tyagi, A. K., *Phys. Chem. Chem. Phys.*, **2016**, 18, 22160-22167.
- (162) Lavrov, E. V.; Weber, J.; Huang, L.; Nielsen, B. B., *Physica B*, **2001**, 308-310, 206-209.
- (163) Londos, C. A.; Andrianakis, A.; Aliprantis, D.; Ohyama, H.; Emtsev, V. V.; Oganessian, G. A., *Physica B*, **2007**, 401-402, 487-490.
- (164) Stein, H. J.; Vook, F. L., *Radiat. Eff.*, **1969**, 1, 41-46.
- (165) Cochran, W.; Kartha, G., *Acta Cryst.*, **1956**, 9, 944-948.
- (166) Zharikov, E.; Kuz'micheva, G.; Lis, D.; Papin, Y. M.; Rybakov, V.; Smirnov, B.; Subbotin, K., *Inorg. mater.*, **2003**, 39, 151-160.
- (167) Wendt, S.; Schaub, R.; Matthiesen, J.; Vestergaard, E. K.; Wahlström, E.; Rasmussen, M. D.; Thostrup, P.; Molina, L. M.; Lægsgaard, E.; Stensgaard, I.; Hammer, B.; Besenbacher, F., *Surf. Sci.*, **2005**, 598, 226-245.
- (168) Han, Y.; Liu, C.-j.; Ge, Q., *J. Phys. Chem. C*, **2009**, 113, 20674-20682.
- (169) A. Henderson, M.; Otero-Tapia, S.; E. Castro, M., *Faraday Discuss.*, **1999**, 114, 313-329.
- (170) Schaub, R.; Thostrup, P.; Lopez, N.; Laegsgaard, E.; Stensgaard, I.; Norskov, J. K.; Besenbacher, F., *Phys. Rev. Lett.*, **2001**, 87, 266104.
- (171) Guo, Q.; Xu, C.; Ren, Z.; Yang, W.; Ma, Z.; Dai, D.; Fan, H.; Minton, T. K.; Yang, X., *J. Am. Chem. Soc.*, **2012**, 134, 13366-13373.
- (172) Asahi, R.; Morikawa, T.; Ohwaki, T.; Aoki, K.; Taga, Y., *Science*, **2001**, 293, 269-271.
- (173) In, S.; Orlov, A.; Berg, R.; García, F.; Pedrosa-Jimenez, S.; Tikhov, M. S.; Wright, D. S.; Lambert, R. M., *J. Am. Chem. Soc.*, **2007**, 129, 13790-13791.
- (174) Zaleska, A., *Recent Pat. Eng.*, **2008**, 2, 157-164.
- (175) Tan, H.; Zhao, Z.; Zhu, W.-b.; Coker, E. N.; Li, B.; Zheng, M.; Yu, W.; Fan, H.; Sun, Z., *ACS Applied Materials & Interfaces*, **2014**, 6, 19184-19190.
- (176) Kong, M.; Li, Y.; Chen, X.; Tian, T.; Fang, P.; Zheng, F.; Zhao, X., *J. Am. Chem. Soc.*, **2011**, 133, 16414-16417.
- (177) Leshuk, T.; Parviz, R.; Everett, P.; Krishnakumar, H.; Varin, R. A.; Gu, F., *ACS Appl. Mater. Interfaces*, **2013**, 5, 1892-1895.

- (178) Jiang, X.; Zhang, Y.; Jiang, J.; Rong, Y.; Wang, Y.; Wu, Y.; Pan, C., *J. Phys. Chem. C*, **2012**, 116, 22619-22624.
- (179) Liu, F.; Lu, L.; Xiao, P.; He, H.; Qiao, L.; Zhang, Y., *Bull. Korean Chem. Soc.*, **2012**, 33, 2255-2259.
- (180) Liu, L.; Yu, P. Y.; Chen, X.; Mao, S. S.; Shen, D. Z., *Phys. Rev. Lett.*, **2013**, 111, 065505.
- (181) Chen, X.; Liu, L.; Liu, Z.; Marcus, M. A.; Wang, W.-C.; Oyler, N. A.; Grass, M. E.; Mao, B.; Glans, P.-A.; Yu, P. Y.; Guo, J.; Mao, S. S., *Sci. Rep.*, **2013**, 3.
- (182) Chen, X.; Liu, L.; Huang, F., *Chem. Soc. Rev.*, **2015**, 44, 1861-1885.
- (183) Danon, A.; Bhattacharyya, K.; Vijayan, B. K.; Lu, J.; Sauter, D. J.; Gray, K. A.; Stair, P. C.; Weitz, E., *ACS Catal.*, **2011**, 2, 45-49.
- (184) Sun, C.; Jia, Y.; Yang, X.-H.; Yang, H.-G.; Yao, X.; Lu, G. Q.; Selloni, A.; Smith, S. C., *J. Phys. Chem. C*, **2011**, 115, 25590-25594.
- (185) Liu, N.; Schneider, C.; Freitag, D.; Hartmann, M.; Venkatesan, U.; Müller, J.; Spiecker, E.; Schmuki, P., *Nano Lett.*, **2014**, 14, 3309-3313.
- (186) Wang, Z.; Yang, C.; Lin, T.; Yin, H.; Chen, P.; Wan, D.; Xu, F.; Huang, F.; Lin, J.; Xie, X.; Jiang, M., *Energy Environ. Sci.*, **2013**, 6, 3007-3014.
- (187) Naldoni, A.; Allietta, M.; Santangelo, S.; Marelli, M.; Fabbri, F.; Cappelli, S.; Bianchi, C. L.; Psaro, R.; Dal Santo, V., *J. Am. Chem. Soc.*, **2012**, 134, 7600-7603.
- (188) Wang, Z.; Yang, C.; Lin, T.; Yin, H.; Chen, P.; Wan, D.; Xu, F.; Huang, F.; Lin, J.; Xie, X.; Jiang, M., *Adv. Funct. Mater.*, **2013**, 23, 5444-5450.
- (189) Cherevan, A. Nanocarbon-inorganic hybrids for photocatalytic water splitting H₂ production. University of Münster, Münster, Germany, 2014.
- (190) Maicu, M.; Hidalgo, M. C.; Colón, G.; Navío, J. A., *J. Photochem. Photobiol. A*, **2011**, 217, 275-283.
- (191) Tan, H.; Zhao, Z.; Niu, M.; Mao, C.; Cao, D.; Cheng, D.; Feng, P.; Sun, Z., *Nanoscale*, **2014**, 6, 10216-10223.
- (192) Addamo, M.; Augugliaro, V.; Di Paola, A.; García-López, E.; Loddo, V.; Marci, G.; Palmisano, L., *Colloid. Surface. A*, **2005**, 265, 23-31.
- (193) Fultz, B.; Howe, J. M., *Transmission Electron Microscopy and Diffractometry of Materials*. Springer: 2007.
- (194) Williams, D. B.; Carter, C. B., *The Transmission Electron Microscope*. In *Transmission Electron Microscopy: A Textbook for Materials Science*, Williams, D. B.; Carter, C. B., Eds. Springer US: Boston, MA, 2009; pp 3-22.
- (195) Ferraro, J. R.; Nakamoto, K.; Brown, C. W., Chapter 1 - Basic Theory. In *Introductory Raman Spectroscopy (Second Edition)*, Ferraro, J. R.; Nakamoto, K.; Brown, C. W., Eds. Academic Press: San Diego, 2003; pp 1-94.
- (196) Mirabella, F. M., *Modern techniques in applied molecular spectroscopy*. Wiley: New York, 1998.
- (197) Solé, J.; Bausa, L.; Jaque, D., *An introduction to the optical spectroscopy of inorganic solids*. John Wiley & Sons: Chichester, England, 2005.
- (198) Kubelka, P.; Munk, F., *Z. Tech. Phys.*, **1931**, 593-601.

- (199) Tauc, J., *Mater. Res. Bull.*, **1968**, 3, 37-46.
- (200) Bürgi, T.; Baiker, A., Attenuated Total Reflection Infrared Spectroscopy of Solid Catalysts Functioning in the Presence of Liquid-Phase Reactants. In *Adv. Catal.*, Gates, B. C.; Knzinger, H., Eds. Academic Press: Cambridge, Massachusetts, 2006; Vol. 50, pp 227-283.
- (201) Ramer, G.; Lendl, B., Attenuated Total Reflection Fourier Transform Infrared Spectroscopy. In *Encyclopedia of Analytical Chemistry*. John Wiley & Sons: online, 2013.
- (202) Karabudak, E.; Kas, R.; Ogieglo, W.; Rafieian, D.; Schlautmann, S.; Lammertink, R. G. H.; Gardeniers, H. J. G. E.; Mul, G., *Anal. Chem.*, **2013**, 85, 33-38.
- (203) Cumming, D. J.; Tumilson, C.; Taylor, S. F. R.; Chansai, S.; Call, A. V.; Jacquemin, J.; Hardacre, C.; Elder, R. H., *Faraday Discuss.*, **2015**, 182, 97-111.
- (204) Nafie, L. A., *Handbook of Raman Spectroscopy: From the Research Laboratory to the Process Line*. Dekker: New York, Basel, 2001; p 1054 pp.
- (205) Thommes, M.; Kaneko, K.; Neimark Alexander, V.; Olivier James, P.; Rodriguez-Reinoso, F.; Rouquerol, J.; Sing Kenneth, S. W., *Pure Appl. Chem.*, **2015**, 87, 1051.
- (206) Condon, J. B., *Surface area and porosity determinations by physisorption: measurements and theory*. Elsevier: Amsterdam, The Netherlands, 2006.
- (207) Tauster, S. J.; Fung, S. C.; Baker, R. T. K.; Horsley, J. A., *Science*, **1981**, 211, 1121-1125.
- (208) Jenkins, R.; Snyder, R. L., *Introduction to X-ray Powder Diffractometry (Volume 138)*. Wiley Online Library: 1996.
- (209) Bragg, W. H.; Bragg, W. L., *P. R. Soc. Lond.-A*, **1913**, 88, 428-438.
- (210) Yang, Y.; Liu, E.; Dai, H.; Kang, L.; Wu, H.; Fan, J.; Hu, X.; Liu, H., *Intern. J. Hydrogen Energy*, **2014**, 39, 7664-7671.
- (211) Patterson, A. L., *Phys. Rev.*, **1939**, 56, 978-982.
- (212) Holzwarth, U.; Gibson, N., *Nat. Nano.*, **2011**, 6, 534-534.
- (213) van der Heide, P., *X-Ray Photoelectron Spectroscopy: An Introduction to Principles and Practices*. John Wiley & Sons, Inc.: Hoboken, NJ, United States, p 241.
- (214) Watts, J. F.; Wolstenholme, J., *Electron energy-loss spectroscopy in the electron microscope*. John Wiley & Sons Ltd.: Chichester, England, 2011.
- (215) Strohmeier, B. R., *Surf. Interface Anal.*, **1990**, 15, 51-56.
- (216) Shirley, D. A., *Phys. Rev. B*, **1972**, 5, 4709-4714.
- (217) Neal Fairley, X. I. a. C. F., in: D. Briggs, J.T. Grant (Eds.), *Surface Analysis by Auger and X-ray Photoelectron Spectroscopy*, IM Publications, Chichester UK, 2003, p. 398.
- (218) Scofield, J. H., *J. Electron Spectrosc. Relat. Phenom.*, **1976**, 8, 129-137.
- (219) Wagner, C. D.; ANaumkin, A. V.; Kraut-Vass, A.; Allison, J. W.; Powell, C. J.; Rumble, J. R., NIST Standard Reference Database 20 , Version 4.1 (web version) (<https://srdata.nist.gov/xps/>). 2012.

- (220) Beamson, G.; Briggs, D., *High Resolution XPS of Organic Polymers: The Scienta ESCA300 Database*. Wiley: Chichester, England, 1992.
- (221) Payne, B. P.; Biesinger, M. C.; McIntyre, N. S., *J. Electron Spectrosc. Relat. Phenom.*, **2011**, 184, 29-37.
- (222) Hüfner, S., *Photoelectron Spectroscopy: Principles and Applications*. Springer-Verlag Berlin Heidelberg GmbH: New York, United States, 2003.
- (223) Thermo Fisher Scientific, I., UV Photoelectron Spectroscopy (<https://xpssimplified.com>), last accessed 24 Sep 2018. 2018.
- (224) McCartney, M. R.; Smith, D. J., *Surf. Sci.*, **1991**, 250, 169-178.
- (225) Buckett, M. I.; Strane, J.; Luzzi, D. E.; Zhang, J. P.; Wessels, B. W.; Marks, L. D., *Ultramicroscopy*, **1989**, 29, 217-227.
- (226) Smith, D. J.; McCartney, M. R.; Bursill, L. A., *Ultramicroscopy*, **1987**, 23, 299-303.
- (227) Swamy, V., *Phys. Rev. B*, **2008**, 77, 195414.
- (228) Šćepanović, M. J.; Grujić-Brojčin, M.; Dohčević-Mitrović, Z.; Popović, Z., *Sci. Sinter.*, **2009**, 41, 67-73.
- (229) Barr, T. L.; Seal, S., *J. Vac. Sci. Technol. A*, **1995**, 13, 1239-1246.
- (230) Huang, C.-N.; Bow, J.-S.; Zheng, Y.; Chen, S.-Y.; Ho, N.; Shen, P., *Nanoscale Res. Lett.*, **2010**, 5, 972.
- (231) Kumar, P. M.; Badrinarayanan, S.; Sastry, M., *Thin Solid Films*, **2000**, 358, 122-130.
- (232) Biesinger, M. C.; Lau, L. W. M.; Gerson, A. R.; Smart, R. S. C., *Appl. Surf. Sci.*, **2010**, 257, 887-898.
- (233) Sorantin, P. I.; Schwarz, K., *Inorg. Chem.*, **1992**, 31, 567-576.
- (234) Haselmann, G. M.; Eder, D., *ACS Catal.*, **2017**, 7, 4668-4675.
- (235) Haselmann, G. M. Defect engineering in semiconductor photocatalysis University of Münster, Münster, Germany, 2014.
- (236) Flint, E. B.; Suslick, K. S., *Science*, **1991**, 253, 1397-1399.
- (237) Suslick, K. S., *Sci. Am.*, **1989**, 260, 80-86.
- (238) Birkin, P. R.; Power, J. F.; Leighton, T. G., *Chem. Commun.*, **2001**, 2230-2231.
- (239) Thompson, L. H.; Doraiswamy, L. K., *Ind. Eng. Chem. Res.*, **1999**, 38, 1215-1249.
- (240) Suslick, K. S.; Casadonte, D. J.; Doktycz, S. J., *Solid State Ionics*, **1989**, 32, 444-452.
- (241) Spurr, R. A.; Myers, H., *Anal. Chem.*, **1957**, 29, 760-762.
- (242) Guayaquil-Sosa, J. F.; Serrano-Rosales, B.; Valadés-Pelayo, P. J.; de Lasa, H., *Appl. Catal. B*, **2017**, 211, 337-348.
- (243) Martins, N. C. T.; Ângelo, J.; Girão, A. V.; Trindade, T.; Andrade, L.; Mendes, A., *Appl. Catal. B*, **2016**, 193, 67-74.
- (244) Morgan, B. J.; Watson, G. W., *J. Phys. Chem. C*, **2010**, 114, 2321-2328.
- (245) Almeida, L. C.; Zanoni, M. V. B., *J. Brazil. Chem. Soc.*, **2014**, 25, 579-588.
- (246) Ogren, P. J., *J. Chem. Educ.*, **2002**, 79, 117.
- (247) Cooke, D. J.; Eder, D.; Elliott, J. A., *J. Phys. Chem. C*, **2010**, 114, 2462-2470.

- (248) Parkinson, C. R.; Walker, M.; McConville, C. F., *Surf. Sci.*, **2003**, 545, 19-33.
- (249) Koudelka, M.; Monnier, A.; Sanchez, J.; Augustynski, J., *J. Mol. Catal.*, **1984**, 25, 295-305.
- (250) Ohtani, B.; Iwai, K.; Nishimoto, S.-i.; Sato, S., *J. Phys. Chem. B*, **1997**, 101, 3349-3359.
- (251) Bashir, S.; Wahab, A. K.; Idriss, H., *Catal. Today*, **2015**, 240, 242-247.
- (252) Schwab, G.-M., *Discuss. Farad. Soc.*, **1950**, 8, 166-171.
- (253) Solymosi, F., *Catal. Rev.*, **1968**, 1, 233-255.
- (254) Jochum, W.; Eder, D.; Kaltenhauser, G.; Kramer, R., *Top. Catal.*, **2007**, 46, 49-55.
- (255) Zhang, J.; Zhang, M.; Jin, Z.; Wang, J.; Zhang, Z., *Appl. Surf. Sci.*, **2012**, 258, 3991-3999.
- (256) de la Pena O'Shea, V. A.; Consuelo Alvarez Galvan, M.; Platero Prats, A. E.; Campos-Martin, J. M.; Fierro, J. L. G., *Chem. Commun.*, **2011**, 47, 7131-7133.
- (257) Simoens, A. J.; Baker, R. T. K.; Dwyer, D. J.; Lund, C. R. F.; Madon, R. J., *J. Catal.*, **1984**, 86, 359-372.
- (258) Highfield, J. G.; Chen, M. H.; Nguyen, P. T.; Chen, Z., *Energy Environ. Sci.*, **2009**, 2, 991-1002.
- (259) Kecskés, T.; Raskó, J.; Kiss, J., *Appl. Catal. A*, **2004**, 273, 55-62.
- (260) Araña, J.; Doña-Rodríguez, J. M.; Cabo, C. G. i.; González-Díaz, O.; Herrera-Melián, J. A.; Pérez-Peña, J., *Appl. Catal. B*, **2004**, 53, 221-232.
- (261) Chuang, C.-C.; Wu, W.-C.; Huang, M.-C.; Huang, I. C.; Lin, J.-L., *J. Catal.*, **1999**, 185, 423-434.
- (262) Chen, X.; Su, X.; Duan, H.; Liang, B.; Huang, Y.; Zhang, T., *Catal. Today*, **2017**, 281, 312-318.
- (263) Ohyama, J.; Yamamoto, A.; Teramura, K.; Shishido, T.; Tanaka, T., *ACS Catal.*, **2011**, 1, 187-192.
- (264) Davidson, M. R.; Hoflund, G. B.; Niinistö, L.; Laitinen, H. A., *J. Electroanal. Chem. Interf. Electrochem.*, **1987**, 228, 471-480.
- (265) Pesty, F.; Steinrück, H.-P.; Madey, T. E., *Surf. Sci.*, **1995**, 339, 83-95.
- (266) Sexton, B. A.; Hughes, A. E.; Fogar, K., *J. Catal.*, **1982**, 77, 85-93.
- (267) Li, C.; Domen, K.; Maruya, K.-i.; Onishi, T., *J. Catal.*, **1990**, 125, 445-455.
- (268) Moon, S.-C.; Mametsuka, H.; Tabata, S.; Suzuki, E., *Catal. Today*, **2000**, 58, 125-132.
- (269) Galińska, A.; Walendziewski, J., *Energy Fuels*, **2005**, 19, 1143-1147.
- (270) Zou, Z.; Ye, J.; Abe, R.; Arakawa, H., *Catal. Lett.*, **2000**, 68, 235-239.
- (271) Fontelles-Carceller, O.; Muñoz-Batista, M. J.; Rodríguez-Castellón, E.; Conesa, J. C.; Fernández-García, M.; Kubacka, A., *J. Catal.*, **2017**, 347, 157-169.
- (272) Toyoshima, R.; Yoshida, M.; Monya, Y.; Suzuki, K.; Amemiya, K.; Mase, K.; Mun, B. S.; Kondoh, H., *Phys. Chem. Chem. Phys.*, **2014**, 16, 23564-23567.
- (273) Kobayashi, H.; Yamaguchi, M., *Surf. Sci.*, **1989**, 214, 466-476.
- (274) Pichat, P., *Catal. Today*, **2014**, 224, 251-257.

- (275) Tan, S.; Feng, H.; Ji, Y.; Wang, Y.; Zhao, J.; Zhao, A.; Wang, B.; Luo, Y.; Yang, J.; Hou, J. G., *J. Am. Chem. Soc.*, **2012**, 134, 9978-9985.
- (276) Li, Y.; Lu, G.; Li, S., *Chemosphere*, **2003**, 52, 843-850.
- (277) Popova, G. Y.; Andrushkevich, T. V.; Chesalov, Y. A.; Stoyanov, E. S., *Kinet. Catal.*, **2000**, 41, 805-811.
- (278) Busca, G.; Lamotte, J.; Claude Lavalley, J.; Lorenzelli, V., *J. Am. Chem. Soc.*, **1987**, 109, 5197-5202.
- (279) Lentz, C.; Jand, S. P.; Melke, J.; Roth, C.; Kaghazchi, P., *J. Mol. Catal. A*, **2017**, 426, 1-9.
- (280) Kim, D. H.; Anderson, M. A., *J. Photochem. Photobiol. A*, **1996**, 94, 221-229.
- (281) Wang, K.-H.; Hsieh, Y.-H.; Wu, C.-H.; Chang, C.-Y., *Chemosphere*, **2000**, 40, 389-394.
- (282) d'Hennezel, O.; Ollis, D. F., *Helv. Chim. Acta*, **2001**, 84, 3511-3518.
- (283) Dickinson, A.; James, D.; Perkins, N.; Cassidy, T.; Bowker, M., *J. Mol. Cat. A*, **1999**, 146, 211-221.
- (284) Iddir, H.; Skavysh, V.; Ögüt, S.; Browning, N. D.; Disko, M. M., *Physical Review B*, **2006**, 73, 041403.
- (285) Xin, X.; Xu, T.; Yin, J.; Wang, L.; Wang, C., *Appl. Catal. B*, **2015**, 176-177, 354-362.
- (286) Lu, H.; Zhao, B.; Pan, R.; Yao, J.; Qiu, J.; Luo, L.; Liu, Y., *RSC Adv.*, **2014**, 4, 1128-1132.
- (287) Wang, M.; Nie, B.; Yee, K.-K.; Bian, H.; Lee, C.; Lee, H. K.; Zheng, B.; Lu, J.; Luo, L.; Li, Y. Y., *Chem. Commun.*, **2016**, 52, 2988-2991.
- (288) Hobbs, D., *J. S. C. Acad. Sci.*, **2011**, 9, 8.
- (289) Akimoto, J.; Takei, H., *J. Solid State Chem.*, **1989**, 79, 212-217.
- (290) Liu, M.; Piao, L.; Zhao, L.; Ju, S.; Yan, Z.; He, T.; Zhou, C.; Wang, W., *Chem. Commun.*, **2010**, 46, 1664-1666.
- (291) Chu, L.; Qin, Z.; Yang, J.; Li, X. a., *Sci. Rep.*, **2015**, 5, 12143.
- (292) Foucher, F.; Guimbretière, G.; Bost, N.; Westall, F., Petrographical and Mineralogical Applications of Raman Mapping. In *Raman Spectroscopy and Applications*, InTech: 2017.
- (293) Zhao, Y.; Li, C.; Liu, X.; Gu, F.; Jiang, H.; Shao, W.; Zhang, L.; He, Y., *Mater. Lett.*, **2007**, 61, 79-83.
- (294) Chung, K.; Leung, Y. H.; To, C. H.; Djurišić, A. B.; Tomljenovic-Hanic, S., *Beilstein J. Nanotechnol.*, **2018**, 9, 1085-1094.
- (295) Song, J.; Yang, C.; Hu, H.; Dai, X.; Wang, C.; Zhang, H., *Sci. China-Phys. Mech. Astron.*, **2013**, 56, 2065-2070.
- (296) Hasegawa, M., Chapter 3.3 - Ellingham Diagram. In *Treatise on Process Metallurgy*, Seetharaman, S., Ed. Elsevier: Boston, 2014; pp 507-516.
- (297) Reed, T. B., (1971). Free energy of formation of binary compounds: an atlas of charts for high-temperature chemical calculations. Cambridge, Mass, MIT Press.

- (298) Saito, R.; Hofmann, M.; Dresselhaus, G.; Jorio, A.; Dresselhaus, M. S., *Adv. Phys.*, **2011**, 60, 413-550.
- (299) Chun, K.-Y.; Lee, C. J., *J. Phys.Chem. C*, **2008**, 112, 4492-4497.
- (300) Thermo Fisher Scientific, I., Thermo Scientific X-ray photoelectron spectroscopy XPS (<https://xpssimplified.com>), last accessed 24 Sep 2018. 2018.
- (301) Rolere, S.; Coulon, J.-F.; Poncin-Epaillard, F., *Eur. Polym. J.*, **2017**, 91, 61-69.
- (302) Biesinger, M. C., X-ray Photoelectron Spectroscopy (XPS) Reference Pages (<http://www.xpsfitting.com>), last accessed 25 Sep 2018
- (303) Webb, M. J.; Palmgren, P.; Pal, P.; Karis, O.; Grennberg, H., *Carbon*, **2011**, 49, 3242-3249.
- (304) Fleming, L.; Fulton, C. C.; Lucovsky, G.; Rowe, J. E.; Ulrich, M. D.; Lüning, J., *J. Appl. Phys.*, **2007**, 102, 033707.
- (305) Kurtoglu, M. E.; Longenbach, T.; Gogotsi, Y., *Int. J. Appl. Glass Sci.*, **2011**, 2, 108-116.
- (306) Ong, C. W.; Huang, H.; Zheng, B.; Kwok, R. W. M.; Hui, Y. Y.; Lau, W. M., *J. Appl. Phys.*, **2004**, 95, 3527-3534.
- (307) Thamaphat, K.; Limsuwan, P.; Ngotawornchai, B., *Nat. Sci.*, **2008**, 42, 357-361.
- (308) Yang, C.; Wang, Z.; Lin, T.; Yin, H.; Lü, X.; Wan, D.; Xu, T.; Zheng, C.; Lin, J.; Huang, F.; Xie, X.; Jiang, M., *J. Am. Chem. Soc.*, **2013**, 135, 17831-17838.
- (309) Pan, S.; Liu, X.; Guo, M.; Yu, S. f.; Huang, H.; Fan, H.; Li, G., *J. Mater. Chem. A*, **2015**, 3, 11437-11443
- (310) Quan, L. N.; Jang, Y. H.; Stoerzinger, K. A.; May, K. J.; Jang, Y. J.; Kochuveedu, S. T.; Shao-Horn, Y.; Kim, D. H., *Phys. Chem. Chem. Phys.*, **2014**, 16, 9023-9030.
- (311) Wang, S.; Zhao, L.; Bai, L.; Yan, J.; Jiang, Q.; Lian, J., *J. Mater. Chem. A*, **2014**, 2, 7439-7445.
- (312) Feng, N.; Liu, F.; Huang, M.; Zheng, A.; Wang, Q.; Chen, T.; Cao, G.; Xu, J.; Fan, J.; Deng, F., *Sci. Rep.*, **2016**, 6, 34765.
- (313) Li, H.; Chen, Z.; Tsang, C. K.; Li, Z.; Ran, X.; Lee, C.; Nie, B.; Zheng, L.; Hung, T.; Lu, J.; Pan, B.; Li, Y. Y., *J. Mater. Chem. A*, **2014**, 2, 229-236.
- (314) Zhu, G.; Lin, T.; Lu, X.; Zhao, W.; Yang, C.; Wang, Z.; Yin, H.; Liu, Z.; Huang, F.; Lin, J., *J. Mater. Chem. A*, **2013**, 1, 9650-9653.
- (315) Vásquez, G. C.; Peche-Herrero, M. A.; Maestre, D.; Cremades, A.; Ramírez-Castellanos, J.; González-Calbet, J. M.; Piqueras, J., *J. Phys. Chem. C*, **2013**, 117, 1941-1947.
- (316) Wang, G.; Wang, H.; Ling, Y.; Tang, Y.; Yang, X.; Fitzmorris, R. C.; Wang, C.; Zhang, J. Z.; Li, Y., *Nano Lett.*, **2011**, 11, 3026-3033.

- (317) Fan, C.; Fu, X.; Shi, L.; Yu, S.; Qian, G.; Wang, Z., *J. Alloy. Compd.*, **2017**, 703, 96-102.

Curriculum Vitae

Greta M. Haselmann

Date of birth: 08.08.1989
Place of birth: Münster (Germany)
Nationality: German

Education

<i>Since 10/2015</i>	PhD student in the working group for materials chemistry (Prof. Dr. Dominik Eder) at Vienna University of Technology in Vienna (Austria)
<i>10/2014 – 09/2015</i>	PhD student (Prof. Dr. Dominik Eder) at University of Münster in Münster (Germany)
<i>10/2012 – 09/2014</i>	M.Sc. in at University of Münster in Münster
<i>09/2008 – 05/2012</i>	B.Sc. <i>summa cum laude</i> in chemistry at Northeastern University in Boston, MA
<i>1999 – 2008</i>	high school: Gymnasium Paulinum, Münster

Employment

<i>Since 10/2015</i>	Research assistant at Vienna University of Technology
<i>10/2014 – 09/2015</i>	Research assistant at University of Münster
<i>08/2013 – 09/2013</i>	Internship at Durham University (England; Dr. H.C. Greenwell)
<i>10/2012 – 10/2013</i>	Student assistant at MEET battery research center (Münster; Prof. Dr. Martin Winter)
<i>09/2011 – 05/2012</i>	Student assistant in the Laboratory for Advanced Electrochemical Power (LEAP) at Northeastern University Center for Renewable Energy (Prof. Dr. Sanjeev Mukerjee)
<i>07/2010 – 12/2010</i>	Research assistant in the Molecular Cardiovascular Research Institute am Tufts Medical Center in Boston, MA (Prof. Dr. Richard Karas, MD)

List of publications

1. Haselmann, G. M.; Eder, D., "Early-Stage Deactivation of Platinum-Loaded TiO₂ Using In Situ Photodeposition during Photocatalytic Hydrogen Evolution", *ACS Catal.* **2017**, 7, 4668-4675.
2. Kemnade, N.; Gebhardt, P.; Haselmann, G. M.; Cherevan, A.; Wilde, G.; Eder, D., "How to Evaluate and Manipulate Charge Transfer and Photocatalytic Response at Hybrid Nanocarbon–Metal Oxide Interfaces", *Adv. Func. Mater.* **2018**, 28, 1704730.
3. Tan, Y.; Ma, S.; Leonhard, M.; Moser, D.; Haselmann, G. M.; Wang, J.; Eder, D.; Schneider-Stickler, B., "Enhancing antibiofilm activity with functional chitosan nanoparticles targeting biofilm cells and biofilm matrix", *Carbohyd. Polym.* **2018**, 200, 35-42.
4. Dörr, T. S.; Deilmann, L.; Cherevan, A.; Haselmann, G.; Zhang, P.; de Oliveira, P. W.; Kraus, T.; Eder, D., "Ordered Mesoporous TiO₂ gyroids: Effects of Pore Architecture and Nb doping on Photocatalytic Hydrogen Evolution under UV and VIS irradiation", *Adv. Energy Mater., accepted manuscript*, **2018**.

List of conferences

- 22nd International Conference on Photochemical Conversion and Storage of Solar Energy (IPS-22), July 29-August 3, **2018**, Hefei, China. Oral presentation: "The role of carbon monoxide during photocatalytic hydrogen evolution over Pt-loaded TiO₂ investigated by in situ ATR-FTIR spectroscopy". G. M. Haselmann, B. Baumgartner, S. P. Nandan, A. Litovolis, J. Wang, A. Cherevan, B. Lendl and D. Eder. *Funded by TU Vienna travel stipend*.
- 17th Austrian Chemistry Days, September 25-27, **2017**, Salzburg, Austria. Oral presentation: "Deactivation of Pt-loaded TiO₂ during photocatalytic H₂ evolution mediated by oxygen vacancies". G. M. Haselmann, D. Eder.
- 21st International Conference on Photochemical Conversion and Storage of Solar Energy (IPS-21), July 25-29, **2016**, St. Petersburg, Russia. Oral presentation: "Defect-induced deactivation of Pt/TiO₂ during liquid-phase photo-

catalysis under ambient conditions" G. M. Haselmann, P. Gebhardt, D. Eder. *Funded by TU Vienna travel stipend.*

- International FOXSI Conference, May 23-25, **2016**, Vienna, Austria. Poster presentation: "Strong-metal support interaction (SMSI) effects under ambient conditions in liquid-phase photocatalysis." G. M. Haselmann, P. Gebhardt, D. Dieterle, and D. Eder.
- 12th International Conference on Materials Chemistry (IMC12), July 20-23, **2015**, York, England. Poster presentation: "Deactivation of Pt-loaded TiO₂ (P25) during sacrificial water splitting". G. M. Haselmann, P. Gebhardt, D. Dieterle and D. Eder. *Funded by Ewald-Wicke stipend.*

Acknowledgments

Science is usually something quite unemotional and rational. We do not often have the opportunity to thank the people that are surrounding us and have been part of our lives and work in this format. So, I hope that the following words can somehow express the gratitude that I feel for being able to pursue my chosen career path and doing so being surrounded by great personalities.

First of all, I would like to thank my supervisor Prof. Dr. Dominik Eder very warmly for the support and encouragement that I experienced throughout my master and PhD studies. Thank you for always being enthusiastic about solving scientific questions and problems that I encountered during my work and encouraging me in my professional career. I would also like to thank Prof. Dr. Julia Kunze-Liebhäuser and Prof. Dr. Jürgen Fleig for the time they will spend reading and evaluating this thesis.

I really enjoyed (and still am enjoying) the shared projects during the time of this thesis and I would like to thank all of my collaborators and mentors very much. Especially (in no particular order): DI Bettina Baumgartner during the past year for her excellent ATR expertise and the good spirit; DI Christopher Herzig for the ICP-MS measurements; Dr. Anton Litke for DRIFTS measurements at TU Eindhoven; Dr. Volker Hagen for chemisorption measurements at the Ruhr-Universität Bochum; Dr. Torsten Reuters and Dr. Andreas Schäfer from Nanoanalytics for XPS measurements during my time in Münster; Dr. Annette Foelske-Schmitz and Dr. Markus Sauer from the Analytical Instrumentation Centers (AIC) in Vienna for the training at the XPS, their patience and helpfulness whenever I had questions and the proof-reading of parts of this thesis; the USTEM team, in particular Dr. Johannes Bernardi, Dr. Michael Stöger-Pollach, and DI Thomas Schachinger, for the training and help during TEM measurements; DI Werner Artner from the X-ray center of TU Vienna for the technical support and constant willingness to help; DI Walter Dazinger for his support with the high pressure H₂ experiments; and Dr. Alexey Cherevan, Sreejith P. Nandan, and Antony Litovolis for the work and valuable discussions with the pure-phase experiments.

Moving with the group to a new city and university has been a unique experience, but it is much less "nerve-wrecking" if a support system like this group moves with you. So, I would also like to thank all members of the Eder group that I had the opportunity to meet, work and share experiences with during my studies, especially: Paul, Oli (or is it Oli and Paul?), Alexey, Dennis, Robert M., Nina, Leonie,

Jia (thank you for spin-coating, Raman and SEM also), Paolo, Ari, Sreejith, Ralf, Jasmin, Shaghayegh (also for the BET!), Niusha, Bernhard (thank you for proof-reading) and Tushar. Also a special thank you to Martina who has become indispensable to our team. Thanks to everyone for always being open for scientific discussions and willing to support each other! You have made working in such a diverse group a very enriching experience.

Last but not least, I would like to thank my friends and family who have always supported me throughout my studies, no matter if near or far. Mentioning individuals would diminish the impact of others (except for Clare: thanks for proof-reading!). I am lucky for every single one of you in my life and I am looking forward to what the future holds for us!

